An analysis of constitutive models for peat under deviatoric loading

Master Thesis Geotechnical Engineering

for the completion of the master's track program
of Geoengineering, as a part of the
Masters of Science in Civil Engineering at
Delft University of Technology.

Author:	Alberto Camino Ríos	5594480
Committee Members:	Prof. dr. C. Jommi	TU Delft
	Dr. S. Muraro	TU Delft
	Prof. dr. Z. Li	TU Delft
	ir. P.R.M. Ammerlaan	Boskalis

Date of submission: May 31, 2023

TU Delft Delft University of Technology

Abstract

The comprehensive assessment of the deviatoric behaviour in peats is paramount in ensuring the resilience of soil structures. The understanding of this material is riddled with intricacies, given its highly complex fabric, which includes organic matter such as fibers. This thesis evaluates the capabilities of a recent constitutive model (JMC) to adequately describe the response of peat by means of a flexible combination of constitutive ingredients, such as a non-associate flow rule and mixed volumetric and distortional hardening. The JMC model capabilities are tested with respect to laboratory and field data and compared against well-established models such as the NGI-ADP and Soft Soil (SS) model in a 3D FEM environment. The framework of reference is the measured response of the Bloemendalerpolder test, as it involves long-term consolidation, deviatoric behaviour, and soil-structure interaction. The results of this thesis demonstrate, that although the deformation pattern of the measurements is emulated effectively by the JMC and SS models, all the models show an overestimation of the lateral displacement compared to field data. Despite these limitations of the formulations and the modeling environment, the work shows the potential of the JMC model to reproduce reasonably deviatoric peat behaviour.

Summary

Current practice refers to the Soft Soil (SS) model and the NGI-ADP model as the recommended tools to simulate peat behaviour in FEM environments, with the former meant to better deal with consolidation processes and the latter for deviatoric/shearing mechanisms. However, neither of these formulations purposefully ponders the contributions of organic matter, as their genesis is based on the description of clayey material. The use of this and other similar approaches has proven insufficient in the assessment of dykes and embankments.

Dealing with soft organic material in a continuum already requires the reduction of all the material's complexities in simplified models, which implicitly hides the influence of all the acting components of the soil matrix. The deficiencies of such formulations are accentuated even further when the tools do not incorporate variables meant to deal with these factors. The JMC model aims to provide a preliminary tool that grasps the effects of fibers in a framework having the required flexibility to capture results from experimental testing of peat. The comparison procedure of this model considers the SS and NGI-ADP models as the reference to prove its competence when dealing with this type of material.

This project evaluates the extent to which the capabilities of the JMC model can better simulate the recorded measurements during the Bloemendalerpolder experiment. Considering the occurring mechanisms during the construction of the test's embankments and the inclusion of structural elements, it appears as a suitable framework to visualize the effective simulation of the consolidation process, the lateral response of the material, and the soil-structure interaction.

The thesis initially explores the properties of the material through the laboratory results of isotropically consolidated undrained triaxial, oedometer, and K_0-CRS tests. The characterization of each model is based on these results, which are simultaneously compared with the *in situ* investigation (Chapter 4). Additionally, an extensive analysis aims to replicate the results of the K_0-CRS tests, as they provide a comprehensive overview of the consolidation process in a controlled set up. Moreover, this process provides a simplified framework for the definition of the state properties and the compression parameters required for each model (Appendix C).

The testing of the model migrates to the more complex field conditions in a progressive manner, by testing the models in a uniform stratigraphy and further introducing geometric variations that better simulate the test mounds (Chapter 6). The results of these calculations are compared to the measurements made during the Bloemendalerpolder field test of water pressure, settlement, and horizontal displacements. This stage of the project allowed to differentiate the sources of uncertainty, by recognizing the limitations of the models, the modeling software, and the assumptions made.

With the response of the embankment faithfully replicated, two steel piles were included to investigate soil-structure interaction (Chapter 7). Nonetheless, the piles were installed after the construction. As the platform used does not allow including new elements in a deformed mesh, a representative comparison could not be performed. Consequentially, it was decided to limit the comparison of the lateral deformation to the inclinometers located outside the embankment's footprint, as these elements were installed previous to the construction of the mound.

The results of this thesis show that the JMC model provides the best average simulation of the stress conditions due to the flexibility of the non-associative formulation. However, the resulting horizontal deformation from the simulations is systematically higher than that of the field. This could be linked to the need for additional laboratory data to fully calibrate the model parameters related to the plastic strain mechanism (plastic potential). Overall, the most accurate estimation of the Bloemendalerpolder peat is provided by the SS model, as the amorphous nature of the material and the lack of reinforcing from fibers yield a response closer to a highly compressible clay.

The implementation of the three-dimensional model was limited by the lack of a fully logarithmic equation to visualize the evolution of the void-dependent hydraulic conductivity and the lack of representation of the initial stress state of the field. These constraints and the high degree of intrinsic uncertainty of the large-scale test suggest that a better-controlled smaller experiment would be a better fit to further assess the capabilities of the constitutive models.

Contents

List of Figures

List of Tables

Nomenclature

Symbol	Parameter	Units
c	Cohesion	kPa
c_v	Consolidation coefficient	m^2/s
c_k	Permeability strain factor	m^2/s
c_M	Ratio of M_e over M_c	-
c_{RH}	Rate of evolution of anisotropy	-
C_r	Swelling index	-
C_c	Compression index	-
D_0	Magnitude of deviatoric hardening	-
D_1	Rate of evolution of deviatoric hardening	-
E	Young's modulus	MPa
e_0	Initial void ratio	-
G	Shear modulus	kPa
G_{ur}	Unloading/reloading shear modulus	kPa
k	Hydraulic conductivity	m/s
K_0	Lateral stress ratio	-
M^*	Aspect ratio of yield surface	-
M_e	Critical state line in compression	-
M_c	Critical state line in extension	-
$M_{g,c}$	Stress ratio at critical state	-
$M_{f,c}$	Stress ratio linked to the horizontal tangent of the yield locus	-
p'_c	Pre-consolidation mean effective stress	kPa
p_{atm}	Atmospheric pressure	kPa
p_{ref}	Reference pressure	kPa
p_{tmult}	Shift of means stress	-
w_0	Initial water content	%

Symbol	Parameter	Units
OCR	Over Consolidation ratio	-
POP	Pre-Overburden Pressure	kPa
$\underline{C}^T$	Coupling matrix	-
$\underline{H}$	Permeability matrix	-
$\underline{K}$	Stiffness matrix	-
$\underline{q}$	Prescribed outflow vector	-
$\underline{S}$	compressibility matrix	-
γ	Unit weight	kN/m^3
ϵ_a	Axial strain	-
κ	Cam-Clay swelling index	-
κ^*	Modified swelling index	-
λ	Cam-Clay compression index	-
λ^*	Modified compression index	-
μ^*	Modified creep index	-
ν	Poisson's ratio	-
ν_{ur}	Unloading/reloading Poisson's ratio	-
ρ_s	Specifc weight	-
ϕ	Friction angle	°
χ_f	Shape coefficient of the yield locus	-
χ_g	Shape coefficient of the plastic potential	-
ψ	Dilatancy angle	°

1 | Introduction

Adequate estimation of the mechanical behaviour of soft organic soils is a cornerstone in the proper design, construction, and maintenance of geotechnical infrastructure in deltaic environments. Considering that these materials are present in a great variety of applications in the realms of water management, transport, and flood protection, it is to be expected that failing to effectively model their response to a comprehensive array of loading conditions becomes a matter of social and economic risk. Within the Dutch context, the failure and serviceability conditions of peat structures have been a recurrent subject, as the inherent complexity that arises from its composition and sensitivity to the state of degradation introduces a high degree of uncertainty in the different mechanisms that test its competence. The shortcomings of current methodologies arise mainly in under-performing models that either fall short in grasping the long-term conditions of the material or fail to visualize the relevance of secondary components (e.g., material degradation, presence of fibers, gas production). The end result gives leeway to considerable maintenance costs and in the worst cases, the loss of human lives.

On this note, several governmental entities and institutions in the Netherlands (e.g., Rijkswaterstaat, NWO, Deltares) have systematically provided financing and development platforms to projects that can further improve the resilience of these structures. As part of this endeavor, the research performed by Muraro (2019) yielded a broad insight into the deviatoric response of peats; from their interactions in laboratory testing to their role in larger-scale dyke systems. One of the most relevant outcomes of this venture was the development of an elastoplastic modeling framework based on the experimental investigation, which could provide a reliable estimation tool for the analysis of the mechanical response of peat under deviatoric loading.

In general, the behaviour of organic soils is heavily constrained by the presence of multi-level networks of fibers, a high shrinkage potential, and a considerable susceptibility to degradation. These limitations become aggravated when natural variability is also accounted for, as this will potentially arrange the soil matrix anisotropically and favor structuration. Consequentially, the characterization of the geotechnical properties of peat is challenging, with considerable disparity and inconsistencies in the matter; a fact that becomes greatly aggravated when dealing with deviatoric stress (Muraro & Jommi, 2020).

Back in 2010, a case study was designed in the Bloemnendalerpolder to analyze some of the complexities involved in the response of soft soils in this area that had proven to be challenging to characterize. For the test, a couple of sand embankments were constructed, which together with an extensive assortment of site investigation and monitoring equipment allowed for a faithful visualization of the consolidation progression of the underlying thick layer of organic material. Throughout the measuring campaign, special care was taken on the lateral displacements exerted on piles. These elements were conveniently located with an offset from the center line to better recognize the tri-dimensional deviatoric response of the soil layers below the embankment. This study proves to be a suitable case study to test the JMC model developed by Muraro (2019), as the loading conditions and the corresponding measurement equipment in the experiment allowed for the ample recognition of multiple stress pathways, in which deviatoric stress is preponderant.

Today, the state-of-the-art deals with such cases of soft soil by making use of variations of the Cam-Clay (CC) model (more specifically the Soft Soil (SS) and Soft Soil Creep (SSC) models) or the more generic Hardening model and HS SS. As previous research (Papadaki, 2013; Schadee, 2012; Siderius, 2011) on the Bloemendalerpolder case has shown, the available constitutive models, along with other simplified approaches have provided good approximations in terms of vertical displacement and pore pressure.

Contrastingly, they have proven to be inadequate when dealing with the behaviour of the material far from the geometric center (where deviatoric behaviour becomes preponderant). In this regard, the use of the JMC model could provide a more accurate replication of the case, as the distorsional properties of the formulation might better define this portion of the embankment.

1.1 Problem statement

Given the uncertainties when modeling organic soft soil materials, the need for a constitutive model that ponders the complex response of soil with high organic content becomes critical in improving the design procedures employed by the industry. Moreover, it is also relevant that the implementation of such a tool has to be done in commonly available software so that it can become accessible for companies dealing with this type of project.

The JMC model is presented as a promising option to better recognize the deviatoric behaviour of the peat, as it has successfully progressed from a mathematical formulation to a FEM framework. The implementation of the findings by Muraro (2019) in Abaqus FEA showed consistency and replicability of his results. Nonetheless, within the context of Geotechnical Engineering, the previous code is not widely used and its capacities in terms of soil mechanics are limited when compared with more specialized software. On this matter, Plaxis has become tightly integrated into common practice, and thus, it appears to be the most adequate choice looking for a practical platform for the JMC model. By effectively doing so, the model is not only made available in a more commercial tool, but it further proves its capabilities in a different modeling environment.

The specific selection of Plaxis 3D and the usage of the Bloemendalerpolder case arises as the best match to evaluate the JMC model. The case study conditions are characterized by the lack of symmetry in the domain and a geometry that requires a three-dimensional visualization to effectively model its general behaviour. Additionally, the presence of piles in the test embankments also introduces an additional degree of complexity to the model that supplements the evaluation of the model's resilience.

1.2 Objectives

As a result of the challenges hereby presented, the research on the implementation of the JMC model within the Plaxis 3D framework is defined by the following objectives:

- Assess the capabilities of the JMC model to replicate the monitoring data of the extensometers and piezometers during the construction of the Bloemendalerpolder embankments.
- Analyse the lateral deformation as described by the monitoring equipment installed during the test, both at the toe of the embankment and at the location of the piles.
- Compare the estimations made by the JMC model with those made by the SS and JMC model.

1.3 Research questions

Following the foregoing problem statement and the objectives proposed for its assessment, the principal research question is outlined as follows:

How does the constitutive model proposed by Muraro (2019) compares to current models in the prediction of lateral behaviour of peat?

Complementary to the principal directive of the present study, additional questions need to be introduced to discretize the problem into fundamental unknowns.

- *What are the limitations of the constitutive model in a 3D FEM environment?*

  Previous to this study the model has provided adequate results in elemental models and virtual testing of the material inside the Abaqus Unified FEA framework. The present endeavors lead to a more complex scenario that challenges the stability of the model in a novel framework.

- *What is the most significant effect of soil-structure interaction on the modeling of laterally loaded piles?*

  When evaluating pile behaviour in FEM, several conditions that limit the replicability of the field state due to the complexity of the mutually dependent relationship between the soil strata and the inserted piles. It is of relevance to identify the second-order constraints that condition the pile behaviour under lateral loading and which of these have a tangible impact on the pile response in the model.

1.4 Methodology

The foundation of this study relies on two main pillars, in one hand, the research previously executed regarding the Bloemendalerpolder case, where multiple authors (Papadaki, 2013; Schadee, 2012; Siderius, 2011) and independent companies (Fugro Geoservices B.V., 2016; Deltares, 2013; Plaxis, 2012) have tried to emulate the conditions of the site; and on the other, the research done by Muraro (2019) on the stress-strain response of peats. The initial portion of the research focuses on recovering and replicating their findings within Plaxis 3D so that the state of the art can be firmly defined in the framework. On this matter two research activities are initially executed: the verification of the constitutive model by using element-level testing and three-dimensional emulation with previous data; and the reconstruction of the Bloemendalerpolder models using the built-in tools of Plaxis.

Once the initial verification procedures are executed, the progression of the project is subdivided into stages of increasing complexity as new elements are progressively introduced into the model. The parameters of the model are calibrated with the laboratory tests from the Bloemendalerpolder case study. Later on, the model is built to the specifications of the case, at this point the results are validated by the field measurements dealing with the process of consolidation. Finally, once proven the effectiveness of the model to describe the soil material is, the study shifts its focus to the soil-structure interaction dynamics that occur when the piles are introduced.

The overall procedure for the study and the internal correlation between the information is presented in Figure 1.1, with the progression of the analysis moving from left to right.

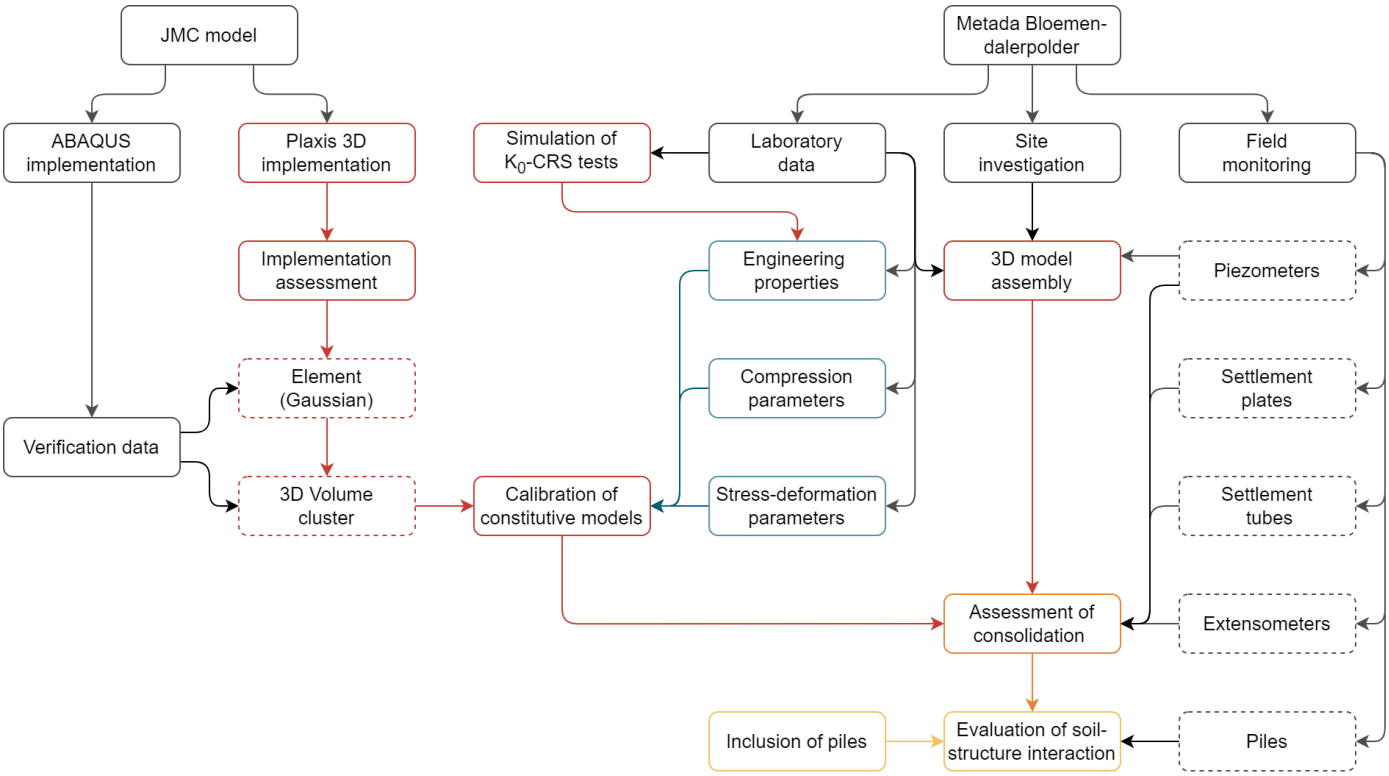

Figure 1.1: Visualization of research design

1.5 Limitations

– *Employing a user-defined soil model restraints the use of the more advanced formulations of Plaxis 3D*

  This is especially relevant in the use of *embedded piles* and the assessment of K_0 as a constant magnitude throughout the analysis. This latter constraint directly impacts the adequate initialization of the stress field.

– *The models cannot be fully characterized with the available information from the case study*

  Although the assortment of tests and monitoring data is extensive, they do not include all the necessary information to fully calibrate the JMC and NGI-ADP models (e.g., undrained triaxial test under extension, anisotropically consolidated triaxial test).

- *Plaxis 3D only includes Taylor's formulation to describe the void dependent permeability of peat*

  The high degree of deformability in peats implies that its state properties will vary greatly. Thus, the use of a semi-logarithmic rule to follow the evolution of hydraulic conductivity as a function of void ratio is not sufficient.

- *Creep, structuration, and gas development are not included in the used models*

  The influence of organic degradation, gas development, and creep are considered to properly describe peat (Edil and Dhowian, 1981; MacFarlane, 1969; Muraro, 2019). The JMC, SS, and NGI-ADP constitutive models do not account directly for these factors.

- *The input of depth-dependent variables in Plaxis 3D is not possible*

  When declaring variables for the materials, the software only allows for the declaration of a constant set of parameters. It is possible to utilize multiple soil layers to simulate this variability, but this remains only as a discrete approximation of said tendency, with higher computational demands.

- *Introducing a non-deformed volume cluster in a FEM field is not possible*

  The piles used to evaluate the deviatoric behaviour of the soil are introduced at stages where deformation has already taken place. Considering the need for a large-strain analysis to model this case, the elements composing the continuum are already warped, and introducing an undeformed geometry for the piles is not feasible.

2 | Site Conditions

The definition of the geotechnical context and the overall conditions of the Bloemendalerpolder project are hereby presented as a brief on the endeavors of the GeoImpuls program after five years of testing. Initially, the overview of the project is presented, followed by the implementation of the monitoring campaign and finally, a brief on the outstanding results of the case study.

2.1 Overview of the project

Within the efforts of the GeoImpuls Program, which focused on the assessment and mitigation of geotechnical failure in construction projects, the Bloemendalerpolder project came as an initiative by Fugro GeoServices B.V. and Deltares for the evaluation of long-term stability in the region between Muiden and Wesp (Figure 2.1). This multi-agency effort follows the need to better predict the settlement progress in the area, since the preceding experience showed significant deviation from the initial assessments (Hoefsloot, 2015; Schadee, 2012; Siderius, 2011). Moreover, it aimed to expand the knowledge on horizontal deformation of the ground and the interdependent interaction between the soil and pile response.

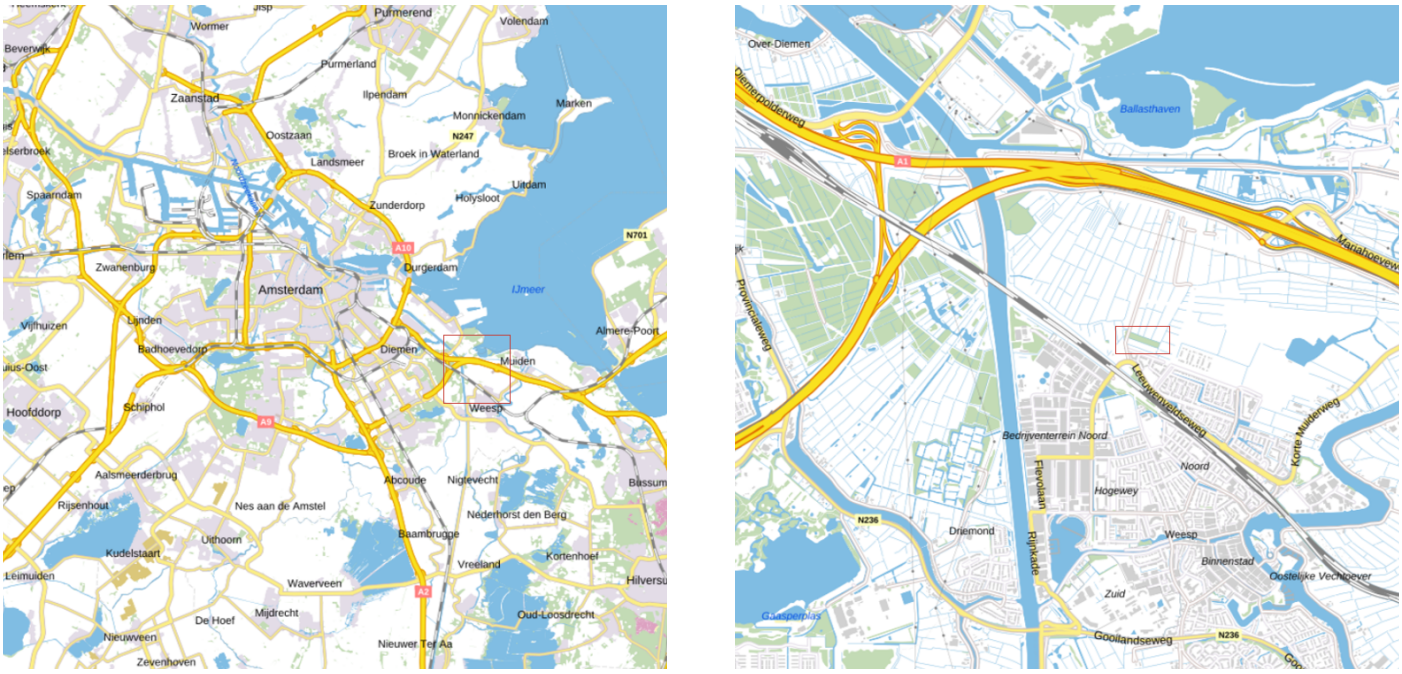

Figure 2.1: Location of the Bloemendalerpolder test-site

The experiment focused on the settlement of two test embankments constructed over a very soft clay layer during a 5-year lapse, with the distinction that each mound had a different drainage condition. Complementary to the soil structures, the installation of piles and an assortment of surveying equipment ensured the holistic evaluation of the relevant factors defining the consolidation behaviour. Besides the monitoring campaign, a characterization process of the site took place prior to and after the construction of the embankments. The chosen geometry and test conditions are shown in Figure 2.2.

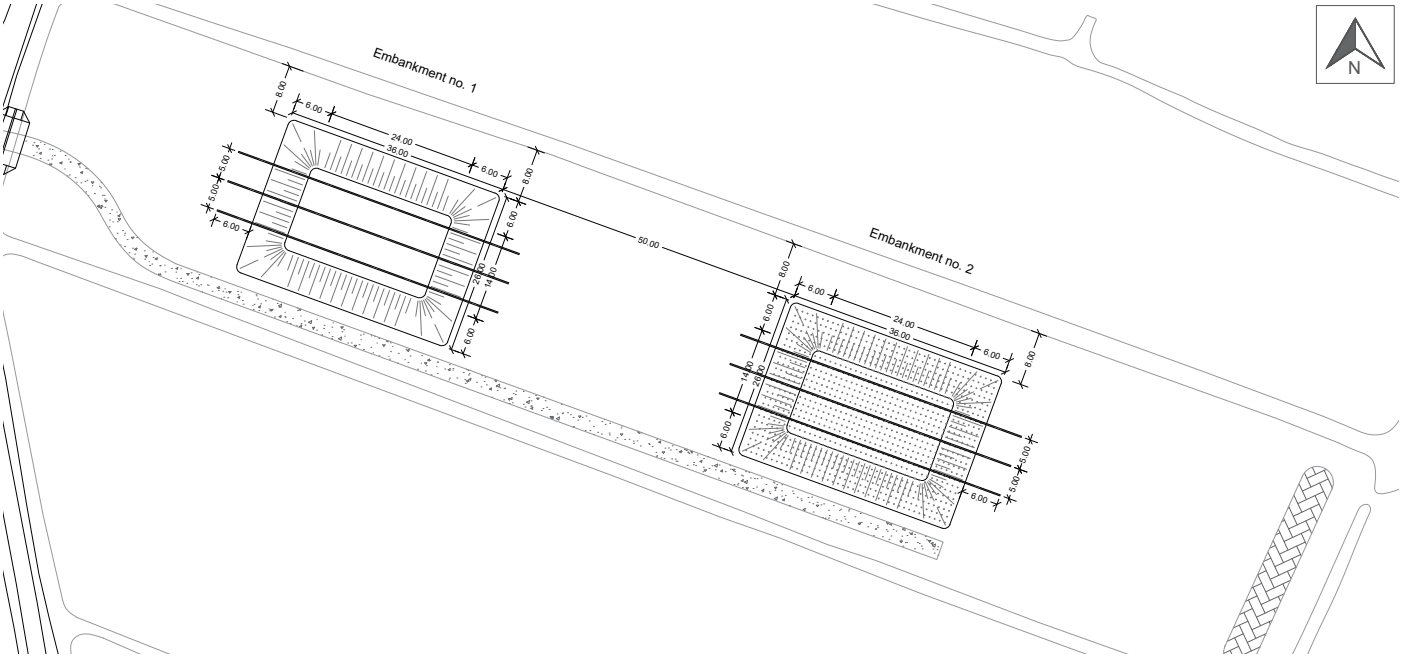

Figure 2.2: Site overview

A month previous to the construction (September 2010) a series of in-situ testing and site characterization procedures were performed around the site, focusing primarily on the construction areas, and complementing the measurements with reference locations next to the fills. The construction process started in October 2010 with the erection of a 1.0-meter layer, promptly followed by the installation of PDV (wick) drains in Embankment No. 2 (T2), which were arranged in a triangular pattern with 0.87 meters of separation in the long direction and 1.0 meter in the short span. Later on, the phasing of the of additional layers was 0.5 meters every three weeks. One month after the completion of the mound, a pair of HEA300 steel piles were installed in each embankment and, a year later, 0.5 meters were removed from the western half-section of both fills. The monitoring was finished in December 2015 as per design.

The general progression of the project follows the specification from the final report of Fugro GeoServices B.V. (Hoefsloot and Schadee, 2016) and is summarized in Table 2.1.

Table 2.1: Site interventions during the experiment's span

Activity	Date	Days	T1	T2
Site investigation	21/09/10	-	✓	✓
Installation of piezometers	24/09/10	-	✓	✓
Installation of extensometers	07/10/10	-	✓	✓
Installation of outer inclinometers	12/10/10	-	✓	✓
Raise mounds' height by 1.0 m	28/10/10	1	✓	✓
PDV drains placement	02/11/10	5	✓	
Raise mounds' height by 0.5 m	22/11/10	25	✓	✓
Raise mounds' height by 0.5 m	14/12/10	47	✓	✓
Raise mounds' height by 0.5 m	25/01/11	89	✓	✓
Raise mounds' height by 0.5 m	17/02/11	111	✓	✓
Installation of steel piles	10/03/11	132	✓	✓
Installation of inner inclinometers	16/03/11	138	✓	✓
Removal of half-mound by 0.5 m	19/12/11	416	✓	✓
End of test	10/12/15	1869	✓	✓

2.2 Site investigation

Following the historic data on the site up to 200 years ago, the area of the Bloemendalerpolder shows no relevant changes at surface (Kadaster, 2022). More specifically the site for the project did not show any apparent alterations (i.e. soil movement, construction) in the area of interest until the intervention of the GeoImpulse program in 2010. As such, in practical terms, the ground could be considered virgin ground.

The most relevant study performed on the area previous to the activities of this project was a CPT on the north-eastern portion of the test site (Siderius, 2011). The test was executed by Grontmij in 2006 at a depth of -15.2 mNAP and shows evidence of an upper cohesive layer with organic content (average R_f of 4.5%), followed by a silt until the end of the probing section. The latter, also shows a small inclusion of a clay lens between -12.0 mNAP and -13.0 mNAP.

The site is characterized by layered stratigraphy composed mainly of soft soil material with high organic content overlaying a Pleistocene sand layer. This condition is consistent with the expected soil structures in this geotechnical context. Moreover, a relative unvarying thickness of the soil layers was anticipated, however, although the exploration campaign showed no evidence of relevant macro structures, some variance was accounted for, both localized in Embankment No.1 (T1) and between mounds, with the second structure showing a thicker section of peat material.

As seen in Figure 2.3, T1 exhibits a consistent dip of the top level at the sand layer in the southwest direction, while the surface level shows an oscillatory variation just below -1.7 m NAP. This is not the case for T2 (Not depicted in this section), which appears to have a more consistent stratification. Previous studies have considered these changes in elevation as inconsequential and as such, have considered a completely parallel strata in their approach, regardless of the dimension in which the analysis is performed.

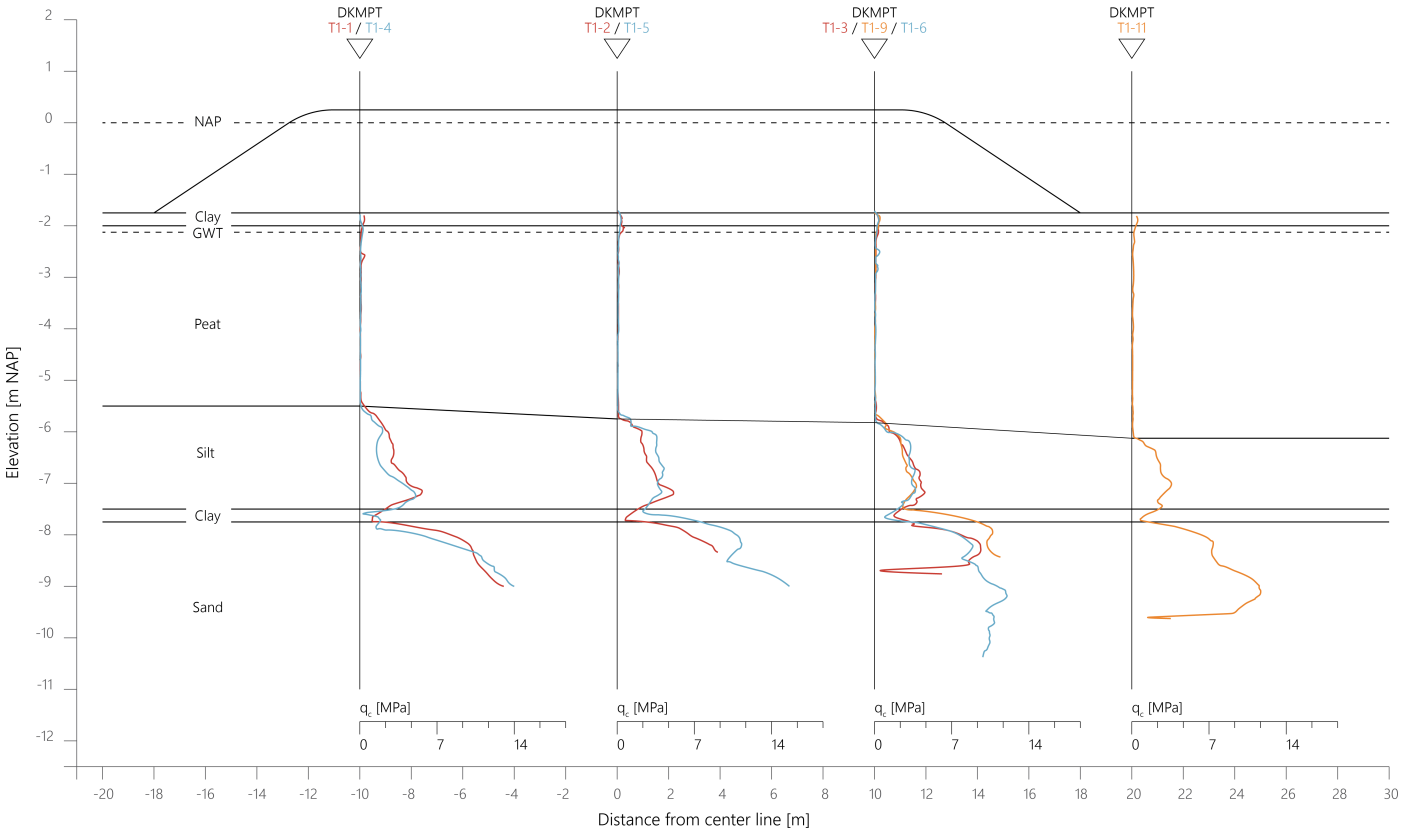

Figure 2.3: Cross section of the assumed stratigraphy at embankment no. 1

For the complete characterization of the site, multiple measurements of soil strength and sampling procedures (Table 2.2) were executed by Deltares and Fugro GeoServices B.V. Additional to the field measurements, laboratory testing of the volumetric weight, organic content, soil strength (Triaxial Test) and compressive parameters (Oedometer, K_0-CRS) complemented the procedure.

Table 2.2: Soil investigation procedures at the Bloemendalerpolder site

Code	Name	Description
DKMP-TX-X	Cone Penetration Test (CPT)	17 tests were performed at the site, with 8 measurements per embankment and another location outside of them as an additional reference. In the case of T1, the probing got on average a depth of -10.5 mNAP, while the tests in T2 reached -11.0 mNAP.
CPM-TX-X	Cone-pressuremeter Test (CPM)	Executed at four distinct depths at the north-western corner of each mound.
BPT-TX-X	Ball Penetration Test	Using a 78 mm ball penetrometer the tests were executed in 4 locations (2 per embankment).
VT-TX-X	Vane Test	Measured at three different depths in 4 locations (2 per embankment) using a 65/130 mm blade.
B-TX-X	Begemman borings	Two boreholes of approximately 8 meters (-7.65 mNAP at T1 & -8.69 mNAP at T2) were recovered below the geometric center of the mounds, along with a reference measurement outside the footprint of the embankments at the south-west area of the site.

2.3 Monitoring instrumentation

The monitoring campaign of the Bloemendalerpolder was composed of multiple assets that evaluated the behaviour response from the embankments and the underlying soil strata between October 2010 and July 2015. The specifics regarding the allocation of the instrumentation, along with the results from the procedure is reported by (Hoefsloot & Schadee, 2016).

The design of the measurement procedure provides redundancy for the sake of completeness, with the utilized instrumentation being displayed in Table 2.3. Moreover, the location of each device in embankment no. 2 is displayed in Figure 2.5, with embankment no. 1 having a homologous design. As previously mentioned, the distinction between both structures is the use of drainage. However, in terms of monitoring, the location of the instrumentation varies slightly as the layering on the second mount is thicker. Additionally, the first embankment also has a pore pressure gauge at the sand layer.

Table 2.3: Monitoring instrumentation used at the Bloemendalerpolder site

Code	Name	Description
ZB-TX-X	Settlement plate	Installed at ground level to measure the ground subsidence occurring below the embankments.
E-TX-X	Extensometer	"Double action" Borros type anchors were installed previous to the construction of the embankment to monitor the vertical displacement of the underlying soil material (Papadaki, 2013).
ZMS-TX-X	Hydrostatic profile gauge	Set of three HDPE settlement tubes of 100 mm diameter with even spacing of 5 meters and an offset of 6 meters for the evaluation of ground deformation.
HT-TX-X	Inclinometer	Intended for the measurement of horizontal displacement. A group of 4 devices is installed at 4-meter spans close to the toe of the embankment and parallel to the test piles.
PT-TX-X	Pile	A pair of HEA300 profiles installed by means of vibratory means with the weak axis perpendicular to the direction of the expected deformation.
WSM-TX-X	Piezometer	19 pore pressure gauges were installed across three locations at 3 different depths: one in the peat, one in the deep sand, and another at the toe of the slope.

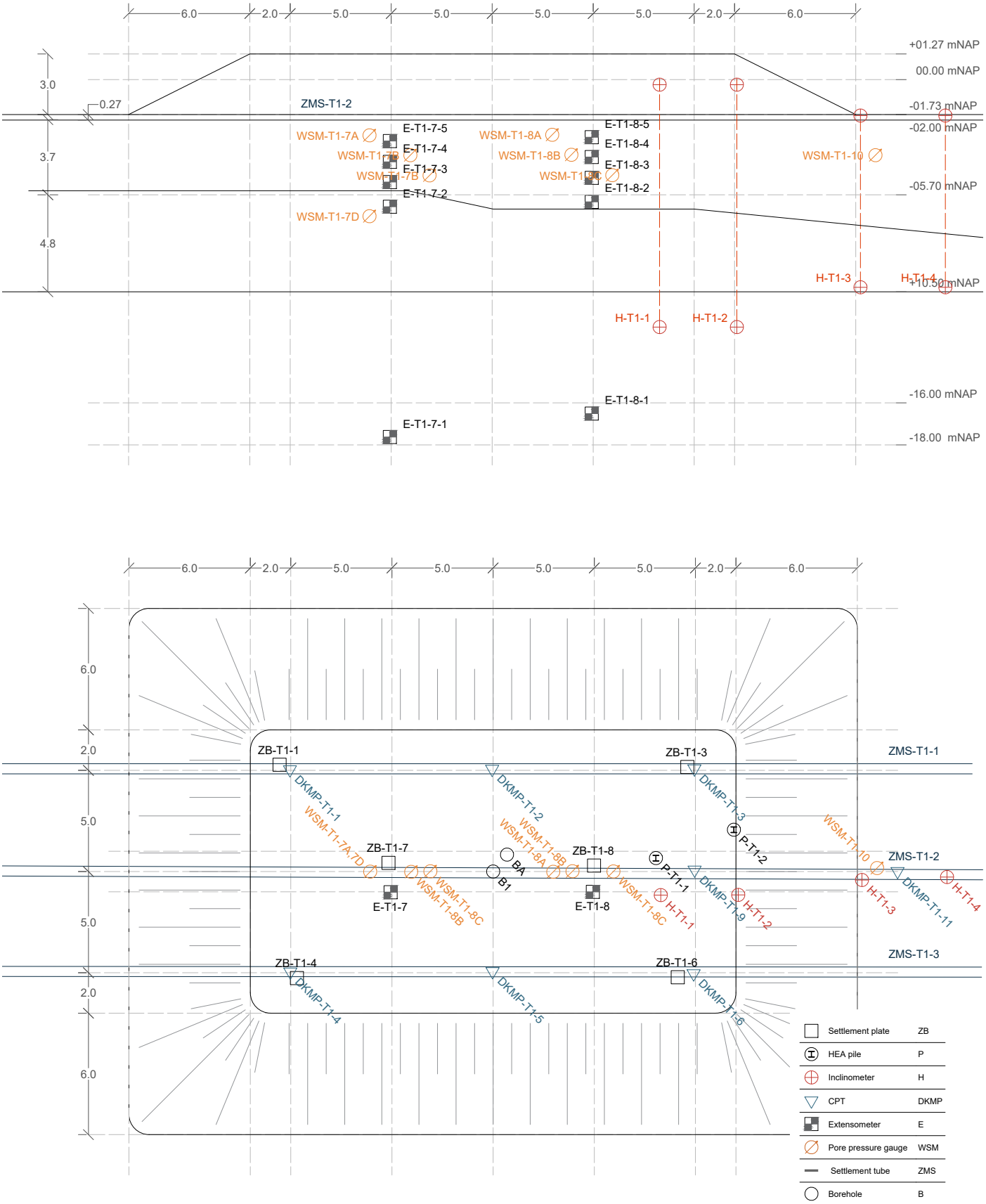

Figure 2.4: Layout of monitoring equipment at embankment no. 1

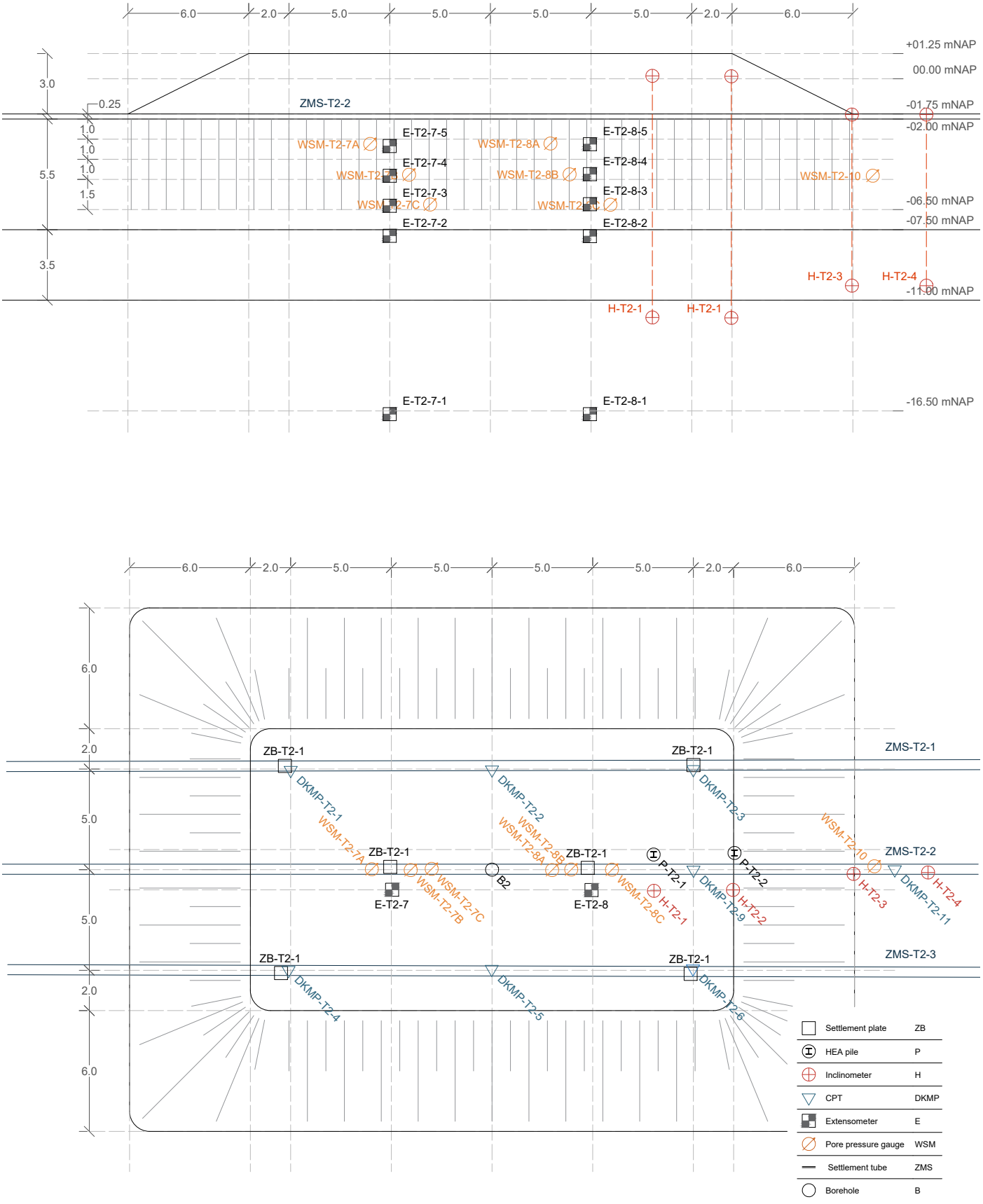

Figure 2.5: Layout of monitoring equipment at embankment no. 2

2.4 Measurement data

The assortment of results after 5 years of measurements of the trail embankments can be recovered from the *Meetresultaten Proefterpen Bloemendalerpolder te Weesp* (Hoefsloot & Schadee, 2016). This section presents the most relevant outcomes of said report.

2.4.1 Settlement

The vertical deformation of the trial mounds was measured in a redundant manner so that the overall behaviour could be visualized as the sum of all individual mechanisms. The data from settlement plates (Figure 2.6) and the extensometers showed the disparity between particular sections of the embankment; while the triad of hydrostatic profile gauges allowed for the recognition of the combined effect of the whole soil system. Moreover, the progression of these measurements complemented the results from the soil investigation to produce a rudimentary projection of the three-dimensional stratification.

Overall, the amount of settlement relative to the peat layer thickness is consistent between mounds, with the beacons located near the geometric center reaching higher values in the long term. There's an exception to this response regarding ZB-T1-7, as it was found that the western side of embankment no. 1 had a relevant difference in depth from the initial estimations. The presence of this variance in elevation is consistent with ZB-T1-4 and ZB-T1-1 and is further confirmed by the settlement tubes. It is assumed that no other macro structures are present due to the consistency of the other results.

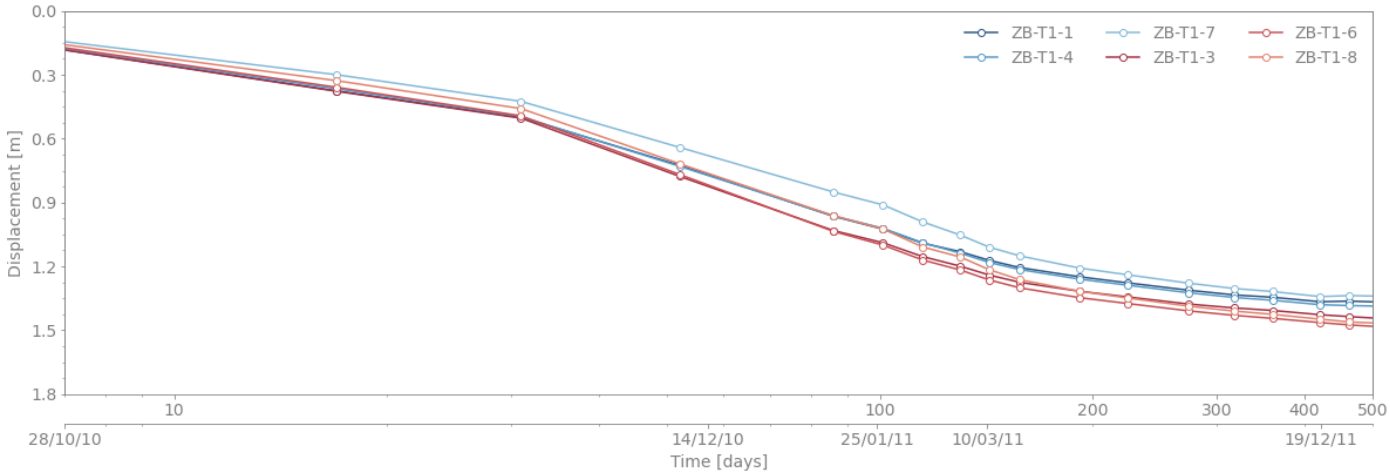

Figure 2.6: Measured displacements of settlement plates at T1 (Hoefsloot & Schadee, 2016)

From the settlement progression in the first mound, it can be seen that the total deformation of the layers is lower than in the second mound, as a consequence of the difference in thickness of the peat, which is 1.5 times larger in T2 than in T1. The apparent temporal similarity in the consolidation process from both embankments reflects the presence of drains in T2, as they enabled the thicker layer to simultaneously reach the same stage of consolidation as the T1.

The settlement plates positioned at the western side of both embankments have a clear rebound behaviour after the removal of the pre-consolidation load, as can be seen in Figure 2.6. ZB-T2,T1-1, ZB-T2,T1-4 and ZB-T2,T1-7, which are positioned directly below the removed half-portion of the embankments show an inflection point in their settlement progression as a result of the height removal, as this effectively introduced a new state of consolidation.

2.4.2 Horizontal displacement

Pure lateral deformation of the soil was recovered from the eastern sections of the embankments using inclinometers, which allowed for the decomposition of the effect along the X and Y direction. In comparison, the measurements from the piles do not reflect only the response of the ground, but the second-order interaction with the steel profiles.

The degree of lateral displacement rises with an increasing distance from the geometric center of the mound, ranging from 0.02 m to 0.15 m in T1; and 0.03 m to 0.30 m in T2. The behaviour of the deformation of all the tests exhibits a similar inflection close to the change in horizons and an outward curvature until the position of the measurement device is sufficiently far from the embankment (HT2-4 and HT1-4).

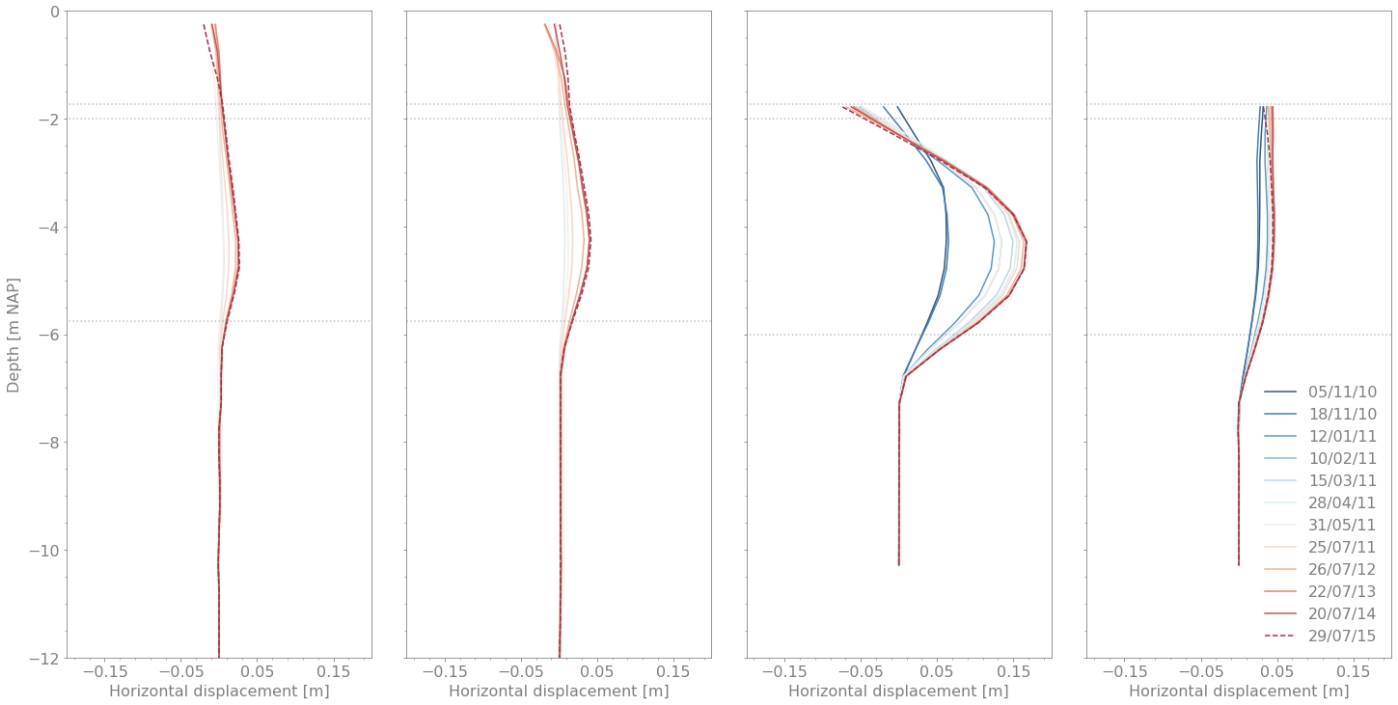

Figure 2.7: Progression of the horizontal displacements at T1 during testing (Hoefsloot & Schadee, 2016)

Looking at the upper section of the results, it can be appreciated that the closer to the center of the fill, the more the overlaying material limits the deformation of the element (similarly to the clamping effect of a pile cap). Conversely, the two inclinometers positioned far outside the footprint of the embankments (3 m) indicate no relevant constraint in movement at the top. The latter might be linked to the bulging of the material surrounding the sand fill, considering that not only does the direct restrain from the sand is absent in this section, but the bulging of the strata loosens the material and releases any possible clamping forces.

HT1-1 and HT1-2 as well as HT2-1 and HT2-2 (located within the mound) show a preferential deformation perpendicular to the long span. This effect could be attributed to the 1-meter offset from the fill's center line where the lateral movement starts to be relevant. The remaining inclinometers also exhibit deformation in this direction, but in an oscillating manner and without a relevant tendency.

2.4.3 Hydrostatic pressure

The pressure evolution is consistent with the progression of the test changes at the surface. In the initial stages, all devices show an overpressure following the construction of a new layer, with the devices in sand quickly dropping back to a steady state and the peat layers showing a slower decline. Further along, there's a relevant pressure drop in the devices situated at half mound that has the overload removed.

The expected distribution of the pressures in the soil strata would suggest that the further away from the center line of the embankment, the lower the perceived values of pressure. The lack of symmetry between devices preludes the divergence of measurements performed at the same depth in T1. This issue is further confirmed when analyzing WSM-T2-8C and WSM-T2-7C in T2, which despite having somewhat symmetric strata, their position is considerably different so that each device exhibits a different rate of pressure decline.

The maximum order of magnitude reached by the pressure measurements in each mound correlates with the position of the devices inside the peat layer, with the values at T2 reaching values around 5 ad 15 kPa, as they are located between 0.5 and 1.5 meters below their counterparts in T1.

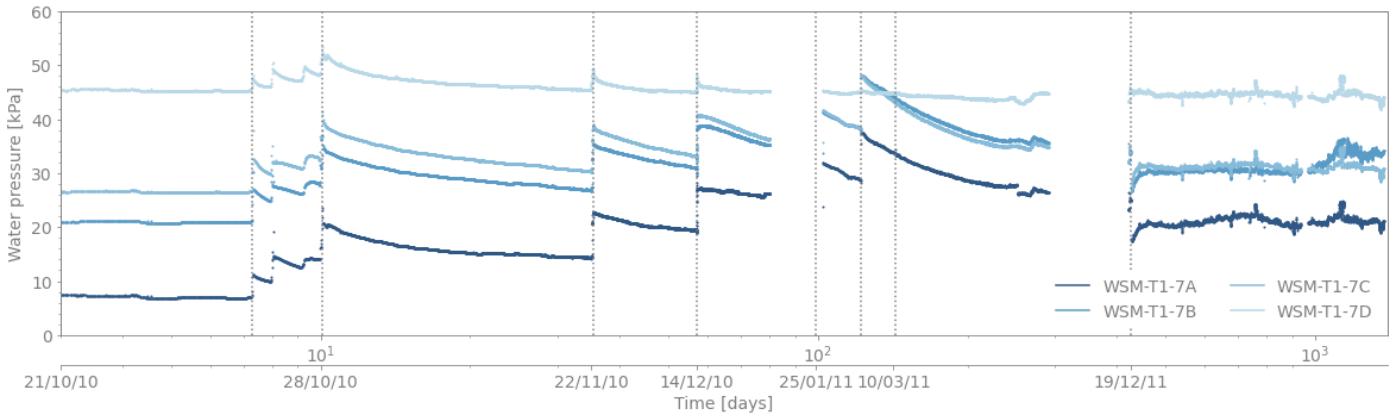

(a) West side

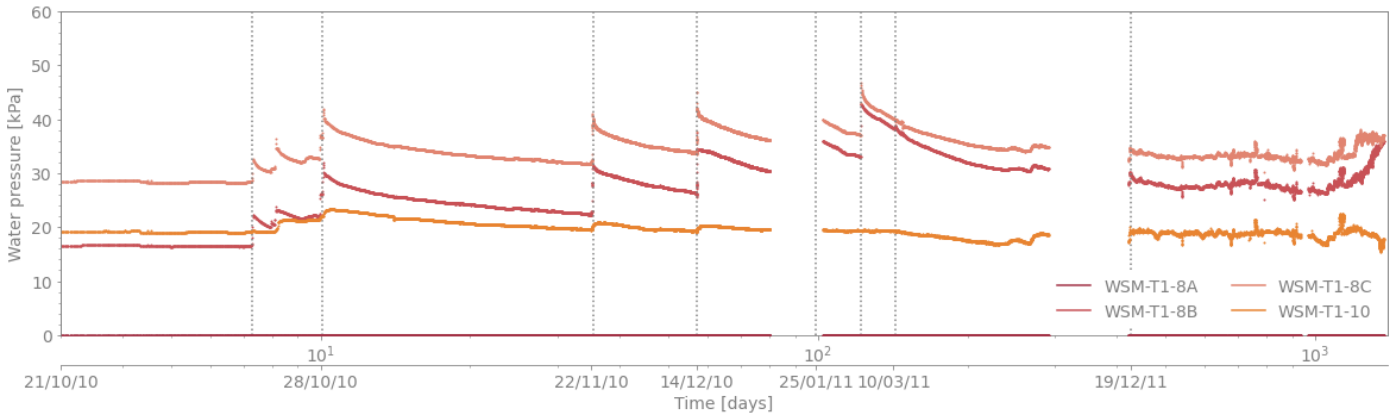

(b) East side

Figure 2.8: Evolution of water pressure in Embankment no. 1 (Hoefsloot & Schadee, 2016)

All devices in the WSM-T1-7 and WSM-T2-7 arrangements show a clear decline in pressure after the unloading of the half-mound on the 18/12/11 (Day 417). In all these cases, the considerable permeability and elastic rebound of the peat layer allowed for some re-absorption of water until reaching a new steady state inherent to the updated geometry of the fill. Contrastingly, the measurements below the unaltered section of the embankment still show a decreasing tendency, which could suggest that the consolidation process is not yet over at this time.

Both embankments perceived the installation of the pile on 10/03/2011, with the east side reaching higher values during this process. This effect is more relevant in the devices located closer to the surface. Nonetheless, it appears that the overall trend of pore pressure propagation does not change.

By comparing the water pressure data with the registry from the nearest raining gauge in Weesp (563) from the *Koninklijk Nederlands Meteorologisch Instituut*, the remaining relevant changes, consistent in all devices, can be correlated to rainfall phenomena. As major precipitation events align with the most preponderant inflections of the measured pressure.

The aftermath of the consolidation process also reflects on higher steady state pore pressure conditions, with an average increase of 10 kPa from the original respective baseline. Thus, suggesting the need for a time-dependent formulation based on the void ratio and consequentially, on the permeability.

3 | Literature Review

The evaluation of the capabilities of the constitutive models to simulate the lateral displacement of piles relies on the understating of their fundamental assumptions and formulations. Moreover, it requires a holistic grasp of the mechanisms that govern the deformation of both the soil and the structural elements. With this aim, this section of the project explores the theoretical concepts of peat behaviour, the constitutive models, the formulation of the consolidation process, and the dynamic of the soil-structure interaction in this context.

3.1 Peat

Whenever organic content is preponderant in the composition of soft soil, it can be defined as peat or turf. This material is characterized by a low volume weight, that could be lower than the density of the water whenever a gas fraction is present. Plant remains (fibers) and humus are the main constituents of this type of soil, which inherently introduces a heterogeneous composition with a preferential accumulation of a multi-level fibrous system in the horizontal direction. This arrangement facilities structuration within its matrix and enables a large degree of anisotropy in its mechanical properties.

The characterization process of this material is riddled with complexities due to the nature of its structure and the struggle of recovering representative samples from the site (Lefebvre et al., 1984). During testing, the response of peat is highly dependent on the stress path, with the fibrous constituents shifting their response as a function of the loading condition. Overall, fibers are expected to undergo "reorientation depending on the strain path" and perceive different degradation in their structure in each of them (Muraro & Jommi, 2020).

3.1.1 Compression behaviour

Considering that this material is the product of the accumulation of decayed vegetation (characterized by large hollow substructures of high permeability), the sensitivity to volume changes as a result of its interaction with water is critical in defining its mechanical behaviour. As the material is subjected to compression, the shrinkage potential enables considerable changes in volume as the water is easily expelled, just as the contrary, when relaxation takes place in an aqueous environment, it will rapidly absorb the surrounding fluid and rebound in size. Under confined conditions, this phenomenon becomes a cornerstone in defining the material strength as the degree of excess pore water pressure can lead to a lack of contact between the particulate phase of the soil and leave the fibers as the sole components sustaining load.

In compression stress paths, the mechanical behaviour of peat materials is similar to that of their inorganic counterparts, with two distinct rates of plastic strain during loading. In terms of the physical response, the change in the rate of plastic deformation is appreciated in the relationships of both strength and stiffness, as the material goes from stiff to soft when exceeding a stress threshold based on its loading history. This point is defined by the yield surface and thus, can be regarded as a generalized pre-consolidation pressure (Wood, 1991). Mechanically speaking, this yielding point defines the point where the soil undergoes structural rearrangement .

Further on, the natural decay of the material and its susceptibility to environmental agents reduce the confidence in its long-term assessment. Considering the difficulty of replicating the decomposition of the organic matter and the resulting bio-processes, the assessment of their contribution is hardly included in the laboratory testing. Therefore, the measured behaviour often disregards the influence of these components and yields non-characteristic parameters.

3.1.2 Shearing behaviour

Generally, soft soils are expected to suffer structural degradation over different stress paths (Cotecchia & Chandler, 1997). However, different straining modes are likely to occur depending on the loading path (Wood, 1991). The added intricacy of a fibrous network accentuates this variability as the structuration of the fabric activates differently in every stress path. As seen in Figure 3.1b, Muraro (2019) shows how the direction of the deformation has a distinct effect on the rearrangement of the fibers and produces different restraining effects on the soil matrix.

The presence of fibers not only represents structural anisotropy but also a reinforcing mechanism that provides additional bearing capacity in specific loading directions (e.g., deviatoric and tensile loading). Muraro (2019) describes the stress-strain response to be usually "dominated by strain hardening behaviour, with deviatoric stress increasing almost linearly with the deviatoric strain at high strain levels". Thus, peat is expected to be a highly competent material, with friction angles far superior to granular materials.

When measuring shear in triaxial tests, it is often found that the fibers' contribution produces a bi-modal deviatoric response. The path is characterized by a hook-like transition from the full response of the soil system to the reinforcing action of the fibers. Figure 3.1a depicts the range of influence of this phenomenon a low to a high degree of influence.

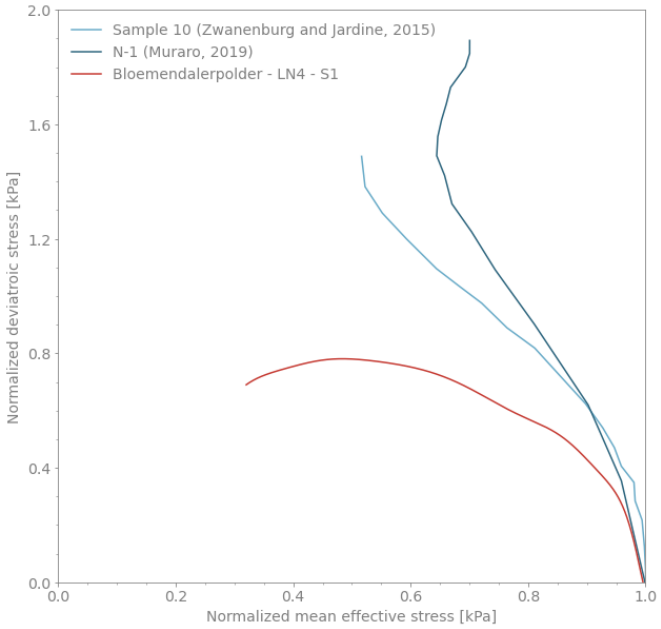

(a) Deviatoric behaviour relative to fiber content

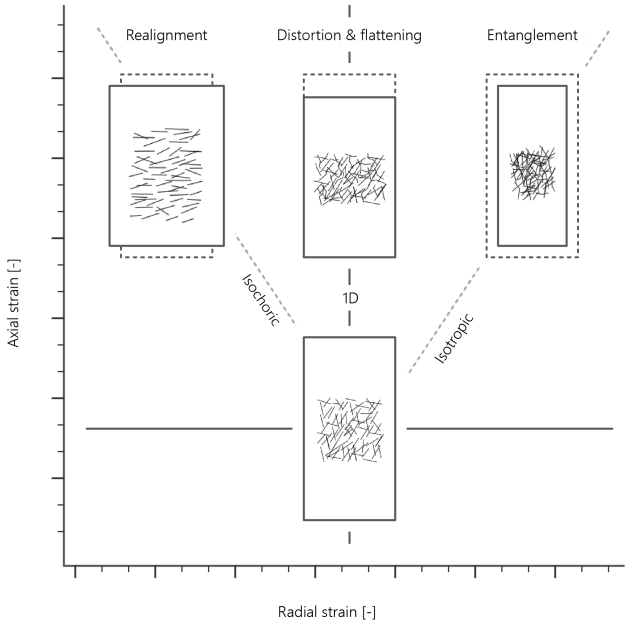

(b) Fiber network evolution (Muraro, 2019)

Figure 3.1: Influence of fibers in material behaviour

3.1.3 Hydraulic conductivity

There is an implicit uncertainty in the estimation of the hydraulic conductivity of natural soil deposits. Intrinsically, there is a considerable level of anisotropy in the material due to its genesis and composition, which further escalates by the effect of the stress history. Additionally, soil structuration and the presence of macro-pores enable preferential flow that can only be assessed at a large scale. Consequentially, it is expected that any parametric estimation different from a full field measurement (e.g., seepage tubes, auger hole tests) of this property is bound to fail in capturing a precise response of the soil (Tavenas et al., 1986).

The ever-changing conditions of groundwater surrounding soil structures of high organic content of the material also introduce another dimension to the complexity of the behaviour of peat in the long term, as the variance in water content also facilities the occurrence of secondary mechanisms by which the material incurs further degradation.

3.1.4 Field conditions

Due to the foregoing characteristics and their strict relation with the seasonal conditions, peat ground frequently shows a certain degree of over-consolidation (Hayashi et al., 2012; Lefebvre et al., 1984). Drainage conditions, material decay, creep, and the presence of vegetation have been linked to the divergence from a virgin state of the ground (Lefebvre et

al., 1984; Long, Grimstad, et al., 2022). Out of these agents, a preponderant factor is the fluctuation in the groundwater table, as the low volumetric weight and the state of submersion of the material cause the effective overburden pressure to be low (Hayashi et al., 2012). With the seasonal variation of the GWT, there is a cyclic wetting and desiccation process that alters the fabric. This OCR does not reflect a mechanical influence of artificial loading but a dynamic environment in which the boundary changes introduce variably in the stress conditions.

3.2 Constitutive models

The fundamental formulations used to describe soil materials are referred as constitutive models. This tools visualize the stress-strain relationship as a function of the stress state of the soil and complements its description with features that accentuate the relevant characteristics of the material.

3.2.1 Soft Soil

The general formulation of the Soft Soil model follows the findings of Brinkgreve (1994) regarding fine-grained soils with high compressive potential. It is meant as a tool to recognize the behaviour of soil before and after a pre-consolidation pressure (p_c) as either primary loading or unloading/reloading while having a consistent recollection of previously attained stress states. It was established as an associative model with a plastic realm defined by an elliptical threshold that evolves uniformly as a function of the maximum stress state. To define the dilatant and failure response of the soil, the model is aided by the Mohr-Coulomb criterion.

Within this framework, the parametric characterization of the material is based on logarithmic relation between the strain and stress conditions. Figure 3.2 exhibits two portions of the stress-strain curve, with the elastic progression rate defined by the modified swelling index (κ^*) and the plastic rate represented by the modified compression index (λ^*). These values are parallelly associated to the evolution of the yield surface with the reference magnitude of p_c.

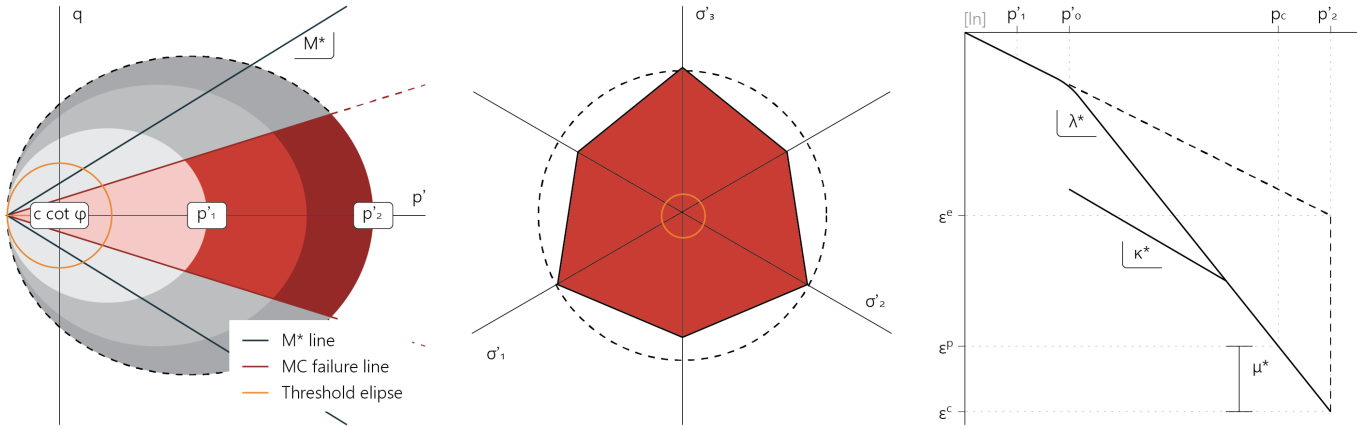

(a) $p' - q$ plane (b) Shape of the yield locus (c) Stress-strain relation

Figure 3.2: Graphical visualization of the SS and SSC models

To include the time-dependent deformation of soils, the modified creep index (μ^*) was proposed by Vermeer and Neher (1999) as an extension to the Soft Soil model. By using this parameter aging can be pondered into the plastic deformation of the soil in the form of time-dependent strain. The set of parameters needed for this model is shown in Table 3.1.

Table 3.1: Parameters of the Soft Soil Creep Model

Symbol	Parameter	Units
λ^*	Modified compression index	-
κ^*	Modified swelling index	-

μ^*	Modified creep index	-
ν_{ur}	Poisson's ratio	-
c'	Effective cohesion	kPa
ϕ	Friction angle	°
ψ	Diltancy angle	°
K_0^{NC}	Coefficient of lateral stress in normal consolidation	-
M	K_0^{NC} related parameter	-

As a critical state model, the hardening potential of the material is calculated as a function of the volumetric plastic strains. This formulation allows to distinguish the response of the strain as a function of the stress history. Although, this formulation is acceptable for fine-grained materials (Muraro & Jommi, 2020), the anisotropic response of peats calls for a loading direction-specific hardening.

$$\dot{\epsilon}_v^c = \left[\frac{\mu^*}{\tau}\right]\left[\frac{p_{eq}}{p_c}\right]^{(\lambda^*-\kappa^*)/\mu^*} \tag{3.2.1}$$

$$p_{eq} = p' + \frac{q^2}{M^{*2}\cdot(p'+c\cdot cot\,\phi}) \tag{3.2.2}$$

The model introduces a variable M to describe the aspect ratio of the ellipsoid bounding the elastic realm of the model. It is based on the K_0^{NC} value as it aims to improve the predictive behaviour at the normally consolidated range. It is worth noting that this magnitude is not related to the critical state line (often denoted M) and thus, henceforward this variable is referred as M^*. The magnitude of this property can be estimated based on the consolidation parameters used for the SS model as presented by Brinkgreve (1994) in equation 3.2.3.

$$M^* = 3\cdot\left[\frac{(1-K_0^{NC})^2}{(1-2\cdot K_0^{NC})^2} + \frac{(1-K_0^{NC})(1-2\cdot\nu_{ur})(\lambda^*/\kappa^*-1)}{(1+2\cdot K_0^{NC})(1-2\cdot\nu_{ur})(\lambda^*/\kappa^*)-(1-K_0^{NC})(1+\cdot\nu_{ur})}\right] \tag{3.2.3}$$

The yield function (Equation 3.2.4) is associative and describes an elliptical geometry as seen in Figure 3.2. It is complemented by a minimum threshold defined by $c'\cdot cot\,\phi$ to contain the values of the hardening cap in the compression side (Plaxis, 2022a).

$$f = \frac{q^2}{M^{*2}\cdot(p'+c'\cdot cot\,\phi)} + p' = 0 \tag{3.2.4}$$

The SS and SSC models are capable of evaluating soil with a non-linear behaviour in both compression and shear, as they ponder a stress-dependent stiffness. More importantly, they identify the stage of loading (i.e. primary loading, unloading, reloading) which allows to better understand pore pressure development and aging in soft soils. Conversely, they do not include more complex phenomena like the bonding effect or the anisotropy common in natural clays (Plaxis, 2022a) and disregards the effect of substructures and the presence of fibers.

3.2.2 NGI-ADP

The inclusion of the NGI-ADP model is a relevant change regarding the available tools in Plaxis since the previous efforts to model the Bloemendalerpolder case were made. This formulation, as proposed by Grimstad et al. (2012), is recommended by Plaxis (2022a) as the best fit to deal with peat in shearing conditions because of its capabilities to replicate anisotropic strength conditions and soil-structure interaction mechanisms.

Overall, the NGI-ADP model aims to describe the general stress state of soil by linking the undrained failure strength with the perceived strain in every loading direction (Grimstad et al., 2012; Plaxis, 2022a). In this manner, the tool is capable of identifying loading anisotropy and defining corresponding strength capabilities in said loading. Moreover, the implementation of the NGI-ADP model in Plaxis 3D also includes a depth-dependent variation, so that the well-known variation of the shear strength can be accounted for (Plaxis, 2022a). The definition of the necessary parameters are displayed in Table 3.2.

The shape of the yield locus is concomitantly defined by the Tresca approximation and a modified von Mises plastic potential function (Figure 3.3b), so that the simulations of the stress conditions of pure compression or pure extension are constrained (Plaxis, 2022a). As seen in Equation 3.2.5, the yield criterion of the NGI-ADP model in a plane strain

analysis displays this relation in a simplified manner. However, in the three-dimensional space, it is reassembled in terms of deviatoric invariants ($\hat{J}_2$,$\hat{J}_3$) and includes a Tresca criterion approximation ($H(\omega)$) to take the form of Equation 3.2.6.

$$f = \sqrt{\left[\frac{\sigma_{yy} - \sigma_{xx}}{2} - (1-k)\cdot\tau_o\cdot\frac{s_u^A - s_u^P}{2}\right]^2 + \left[\tau_{xy}\cdot\frac{s_u^A + s_u^P}{2\cdot s_u^{DSS}}\right]^2} - k\cdot\frac{s_u^A + s_u^P}{2} = 0 \tag{3.2.5}$$

$$f = \sqrt{H(\omega)\cdot\hat{J}_2} - k\cdot\frac{s_u^A + s_u^P}{2} = 0 \tag{3.2.6}$$

$$H(\omega) = cos^2\left[1/6\cdot cos^{-1}\left[1 - 2\cdot\frac{s_u^C}{s_u^A}\cdot\frac{27\cdot\hat{J}_2}{4\cdot\hat{J}_3}\right]\right] \tag{3.2.7}$$

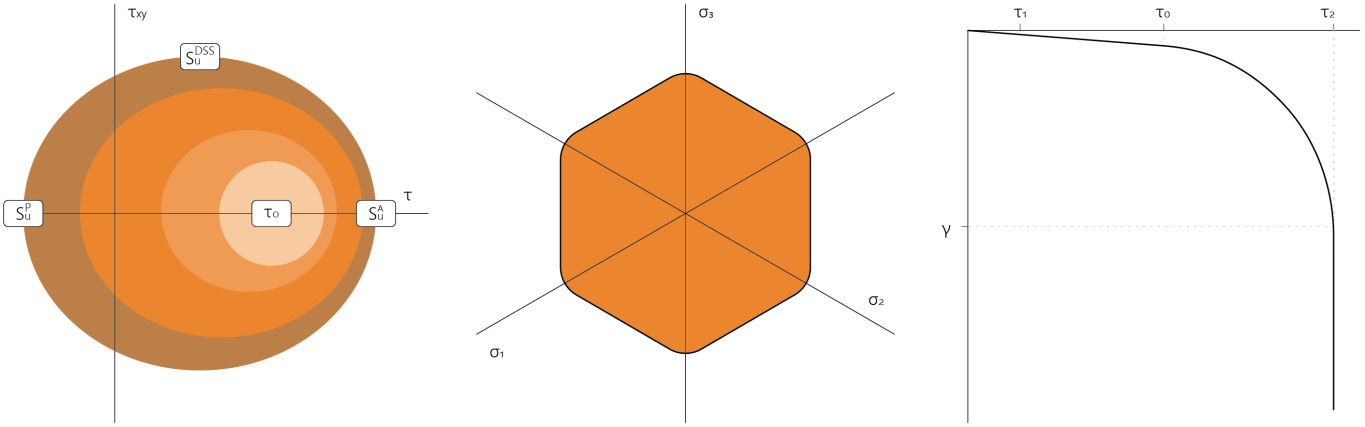

(a) $\tau - \tau_{xy}$ plane (b) Shape of the yield locus (c) Stress-strain relation

Figure 3.3: Graphical visualization of the NGI-ADP model

Table 3.2: Parameters of the NGI-ADP Model

Symbol	Parameter	Units
G_{ur}	Unloading/reloading shear modulus	kPa
γ_f^C	Shear strain in triaxial compression	%
γ_f^P	Plastic failure shear strain	%
γ_f^E	Shear strain in triaxial extension	%
γ_f^{DSS}	Shear strain in direct simple shear	%
$s_u^{A,ref}$	Reference active shear strength	kPa
z_{ref}	Reference level	m
$s_{u,inc}^A$	Increase of shear strength with depth	kN/m^2/m
s_u^P	Passive shear strength	kPa
s_u^{DSS}	Direct simple shear strength	kPa
τ_0/s_u^A	Initial mobilization	-

The hardening rule (Equation 3.2.8) is a stress path-dependent formulation that allows the differentiation between the plastic shear strain and the peak shear strain (Grimstad et al., 2012). Depending on the loading direction (i.e. extension and compression), the shear strain (γ^P) used as reference is varied as a function of it.

$$k = \begin{cases} 2 \cdot \sqrt{\gamma^P / \gamma_f^P} / [1 + \gamma^P / \gamma_f^P] & \text{if } \gamma^P < \gamma_f^P \\ 1 & \text{if } \gamma^P \geq \gamma_f^P \end{cases} \tag{3.2.8}$$

A potential source of uncertainty of the model in long-term conditions is the limited representation of the stress-strain relation. This is compensated to a certain extent by the use of the SHANSEP formulation, which works as an extension capable of including changes in the undrained shear strength ad better visualizing the stress history.

3.2.3 JMC model

The yield functions that are usually described in the critical state models bound the behaviour of the material in a volumetric hardening rule, which solely focuses on plastic volumetric strains and disregards the loading anisotropy usually present in organic soft soils (Muraro, 2019). Because of this, Muraro and Jommi (2020) proposed the conjunction of a volumetric and a deviatoric hardening rule to indirectly account for the contribution of the fibers in the response of the material.

In the JMC model, the soil response is not only able to distinguish between loading stages as a function of the maximum pre-consolidation stress, but it can also differentiate the response base on the loading direction (Figure 3.4), where the evolution of the yield locus and plastic potential show an independent transformation in both size and shape.

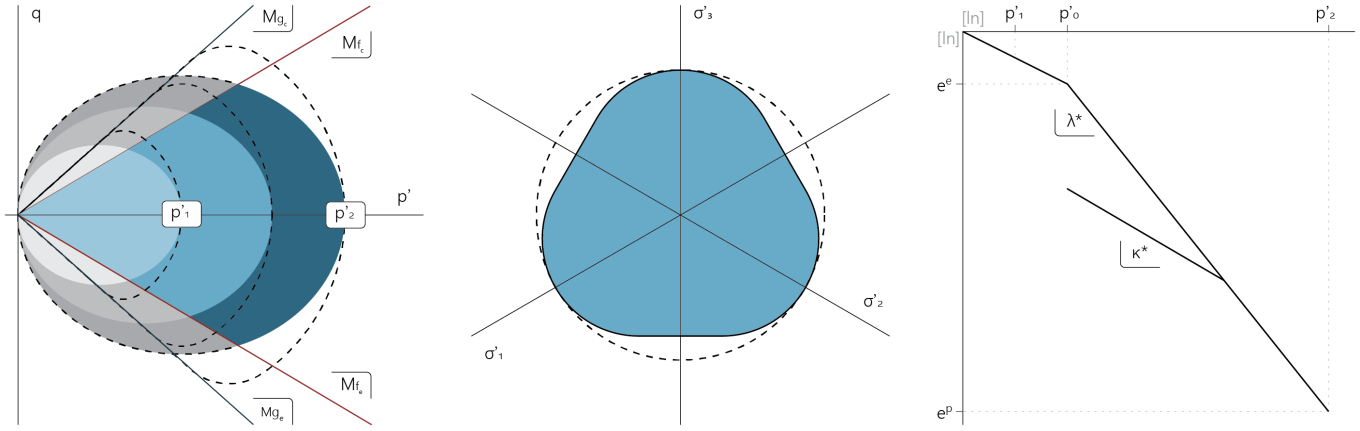

(a) $p' - q$ plane (b) Shape of the yield locus (c) Stress-void ratio relation

Figure 3.4: Graphical visualization of the JMC model

Table 3.3: Parameters of the JMC model (Muraro & Jommi, 2020)

Symbol	Parameter	Units
c_M	Ratio of M_e over M_c	-
e_0	Initial void ratio	-
D_0	Magnitude of deviatoric hardening	-
D_1	Rate of evolution of deviatoric hardening	-
p_0	Pre-consolidation pressure	kPa
$M_{g,c}$	Stress ratio at critical state	-
$M_{f,c}$	Stress ratio linked to the horizontal tangent of the yield locus	-
κ	Slope of the isotropic unloading–reloading line	-
λ	Slope of the isotropic normal compression line	-

ν	Poisson's ratio	-
χ_f	Shape coefficient of the yield locus	-
χ_g	Shape coefficient of the plastic potential	-

By means of drained and undrained triaxial tests, Muraro and Jommi (2020) demonstrated that the evolution of the pre-consolidation mean effective stress strongly correlates with both volumetric and deviatoric strains along distinct stress paths. The elastoplastic model, by means of a mixed hardening rule, linearly relates the occurrence of volumetric and deviatoric plasticity.

$$\frac{\delta p'_c}{p'_c} = \left[\frac{\nu}{\lambda - \kappa}\right] \cdot (\delta\epsilon_p^P + D \cdot \delta\epsilon_q^P) \tag{3.2.9}$$

The distortional hardening coefficient (D) is pivotal in defining the degree of influence of the deviatoric-plastic strain. Further on, it allows for the occurrence of dilation in the hardening realm, which has been associated to fibrous peats (Muraro & Jommi, 2020).

$$D = D_0 \cdot e^{-D_1 \cdot \epsilon_q^p} \tag{3.2.10}$$

The yield formulation of the JMC model is presented in terms of p' and q. Equation 3.2.11 Two major components dictate the progression of the yield surface of the elastic realm, the χ_f coefficient that describes its shape and the M_f that limits the upper boundary of the yield points.

$$f = q^2 + \left[\frac{{M_f}^2}{1 - \chi_f}\right] \left[\frac{p'}{p'_c}\right]^{2/\chi_f} \cdot {p'_c}^2 - \frac{{M_f}^2 \cdot {p'_c}^2}{1 - \chi_f} = 0 \tag{3.2.11}$$

Despite the fact that the generalized expression for the plastic potential (Equation 3.2.12) is of the same form as the yield locus, these equations are non-associative and as such requires additional homologous parameters (χ_g and M_g) that track and bound the shape of the elliptical geometry.

$$g = q^2 + \left[\frac{{M_g}^2}{1 - \chi_g}\right] \left[\frac{p'}{p'_g}\right]^{2/\chi_g} \cdot {p'_g}^2 - \frac{{M_g}^2 \cdot {p'}^2}{1 - \chi_g} = 0 \tag{3.2.12}$$

The present formulation is able to deal with the two basic assumptions of concern in the three-dimensional system of equations of Biot (1941); the reversibility of stress-strain relations under final equilibrium conditions (1) and the linearity of the stress-strain relations (2). The definition of the compression behaviour is comparable to that of the SS model, while the flexibility of the yield function and plastic potential allows a homologous capability to that of the NGI-ADP model to deal with anisotropic loading.

3.3 Consolidation

The estimation of the gradual adaptation of granular material to varying stress conditions is bound by the simultaneous change of the solid particles and the fluid entrapped within the porous space. To visualize this behaviour there's a need to establish a link between the mechanical equilibrium and the groundwater flow, as the displacements and the stress state of the soil system are mutually dependent (Zeitoun & Wakshal, 2013). Thus, a coupled formulation has to be employed to define the mechanical response of the soil, while also defining the competence of the material to allow the migration of fluids through its matrix.

Two basic principles inherently described the aforementioned dynamic, Darcy's law for flow propagation in a porous medium and Terzaghi's effective stress principle for saturated soils. The latter is extended by including the non-reversible behaviour of the soil skeleton in an incremental form so that as the stress-strain relationship varies, the stiffness of the ground also evolves. In this matter, time-dependent parameters allow to simulate the progression by evaluating the current state of the soil as an effect of the previous stress history.

The implementation of the consolidation framework for any arbitrary load in the three-dimensional space was first proposed by Biot (1941). In his work, the definition of consolidation includes the interdependent variation of stress, strain,

and pore pressure in the three directions so that general equations of deformation can be formulated in the form of equations 3.3.1 - 3.3.3. Based on this, the transient process is assumed to be the balance between the deformation gradient and the change in effective stress, with the physical properties of hydraulic conductivity and stiffness governing the rate at which this phenomenon occurs.

$$G \cdot \nabla^2 s_x + \frac{G}{1-2\nu} \cdot \frac{\partial \epsilon}{\partial x} - \alpha \cdot \frac{\partial \sigma_x}{\partial x} = 0 \tag{3.3.1}$$

$$G \cdot \nabla^2 s_y + \frac{G}{1-2\nu} \cdot \frac{\partial \epsilon}{\partial y} - \alpha \cdot \frac{\partial \sigma_y}{\partial y} = 0 \tag{3.3.2}$$

$$G \cdot \nabla^2 s_z + \frac{G}{1-2\nu} \cdot \frac{\partial \epsilon}{\partial z} - \alpha \cdot \frac{\partial \sigma_z}{\partial z} = 0 \tag{3.3.3}$$

By assuming that hydraulic conductivity is isotropic and that water is incompressible, the magnitude of the pore pressure can be calculated by equation 3.3.4. With this inclusion, the time-dependent component of the consolidation can be clearly appreciated.

$$k\nabla^2 \underline{u} = \alpha \cdot \frac{\partial \epsilon}{\partial t} + \frac{1}{Q} \cdot \frac{\partial \underline{u}}{\partial t} \tag{3.3.4}$$

Within a FEM environment, the conjunction of the process and the material response is analyzed in individual elements that discretize the field of interest. Each of these components is solved relative to the neighboring conditions and their independent contribution results in the response of the continuum. Because of this, the foregoing differential equations are assembled in matrix form (Equation 3.3.5) to relate the coupled response of all the otherwise independent constituents (Plaxis, 2022c).

$$\begin{bmatrix} \underline{K} & \underline{C} \\ \underline{C}^T & -\underline{S} \end{bmatrix} \cdot \begin{bmatrix} \Delta \underline{s} \\ \Delta \underline{u} \end{bmatrix} = \begin{bmatrix} 0 & 0 \\ 0 & \Delta t \cdot \underline{H} \end{bmatrix} \cdot \begin{bmatrix} \underline{s}_0 \\ \underline{u}_0 \end{bmatrix} + \begin{bmatrix} \underline{K} \cdot \Delta \underline{s} + \underline{C} \cdot \Delta \underline{u} \\ \Delta t \cdot \underline{q} \end{bmatrix} \tag{3.3.5}$$

A guiding component in the calculation of consolidation is the stiffness of the material, which in its simplest form, follows the definitions of Young's module and Poisson's ratio as seen in the abovementioned equations. However, it is possible to estimate these conditions by means of parameters that visualize the degree of settlement in terms of its stress history (e.g., compression and swelling indexes). Considering that regardless form the compression stress paths that the soil elements perceive, a similar pattern can be observed in the evolution of stiffness (Wood, 1991). Overall, within the realm of previously attained stress levels, the response will be rigid, then, after exceeding the previous maximum stress the resistance to deformation varies more steeply.

Although all these formulations are formulated in terms of small-strain behaviour, solving for non-linear problems with larger deformations requires a change in the definition of the strain. Nonetheless, the added complexity of incorporating a logarithmic strain can be circumvented by employing an Updated Lagrangian formulation (Plaxis, 2022b). This approach allows the calculation of the strain tensor with virtual displacements that progressively converge to the large-strain result. The use of this tool is paramount in the analysis hereby presented.

3.4 Lateral load-deflection behaviour

The structural response of laterally loaded piles is primarily defined by two mutually dependent non-linear factors: the evolution of the bending stiffness as a function of the bending moment (1) and; the stress-stiffness relation of the surrounding medium (2), which can become further convoluted by depth-dependent soil properties or the presence of a multilayered stratum. Because of this, even if one element of the soil-pile system simulates a linear behaviour (usually the pile), the overall conditions of the dynamic will remain non-linear (Duncan et al., 1994).

The application of a novel vertical force on a soil body will result not only in vertical stress and displacement but in the dissipation of energy to the adjacent medium within an influence area. This transferring mechanism results in concordant effects in the horizontal direction defined by a vertical-to-lateral ratio coefficient (k_a, k_p, k_o), which depends on the confinement conditions. Because the extent of this effect in the underlying stratum is limited, the need for the soil to undergo consolidation due to the applied load decays with increasing distance from the geometrical center of the source. As previously mentioned, the consolidation phenomenon constitutes a rearrangement of the soil particles that will further increase the stiffness of the material.

As a general principle of statics in soil mechanics, the equilibrium between a pile and the adjoining granular mass is inherently subject to the balance of forces occurring in the plane of interaction of the elements. As stated by Rankine

(1857), the resistance to displacement of this surface is only controlled by forces acting above the angle of repose (ϕ) of the soil, considering that the stability of the soil is independent of the pressures that make an angle exceeding this angle. The translation of this concept into the three-dimensional space yields a volume of influence with wedge geometry in which all the components contained within become relevant to its static balance. These elements are to be discerned into those that prompt the surroundings to deform and those that prevent the ground from spreading.

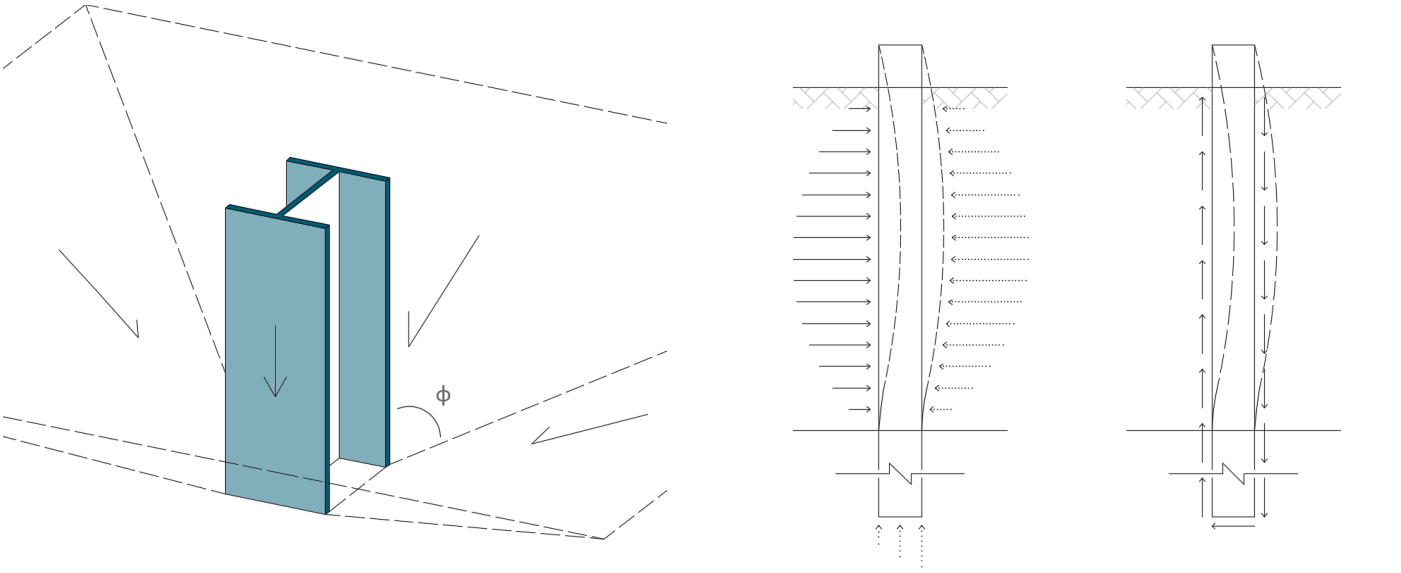

(a) Soil volume acting on the pile

(b) Active and passive forces acting on the pile

Figure 3.5: Distribution of stress during lateral-load deflection

With the pile progressively deforming by the effect of the soil movement in the major loading direction, there is a corresponding soil resistance of the material behind it, which is initially preponderant at the far side of the supports (i.e. pile cap, base layer). The soil strength in this section of the system becomes mobilized and in turn, favors the distribution of the additional loads to portions of the soil that have not been mobilized (Duncan et al., 1994). Then, given the time-dependent behaviour of the soil, the load transferring occurs differently throughout the lifetime of the pile.

4 | Characterization

A macro-scale evaluation of the JMC model relies on a comprehensive characterization of the constitutive material from the soil structure and the underlying stratification. Following this directive, the present section begins with the recovery of the state and index properties, both to define the initial conditions of the material and to visualize the expected values of the mechanical properties. Later on, using the laboratory and *in situ* testing results, a general definition of the engineering parameters is proposed. Lastly, the selection of the relevant variables for each of the models (i.e., SS, JMC, and NGI-ADP) is made.

The general mechanical properties are defined with the assortment of oedometer, triaxial compression, and K_0-CRS tests as reported by Alink (2010). Relative to the compression properties and state variables, they are retrieved from the FEM simulation of the K_0-CRS tests. In the case of the shearing parameters, their evaluation is also complemented with the cone pressuremeter (CPM) and vane *in situ* tests' results; while the proposed magnitudes referring to tensile behaviour follow results found in the literature.

The estimations from these procedures are mainly compared with the work from Fugro (2010 - 2016), Siderius (2011) and Schadee (2012), who focused predominantly on the mechanical behaviour of the peat. On the other hand, the most relevant efforts on the composition of the material were performed by Deltares (2011) and Papadaki (2013). As such, the recovery of the properties intrinsic to the peat is based on the work of the latter.

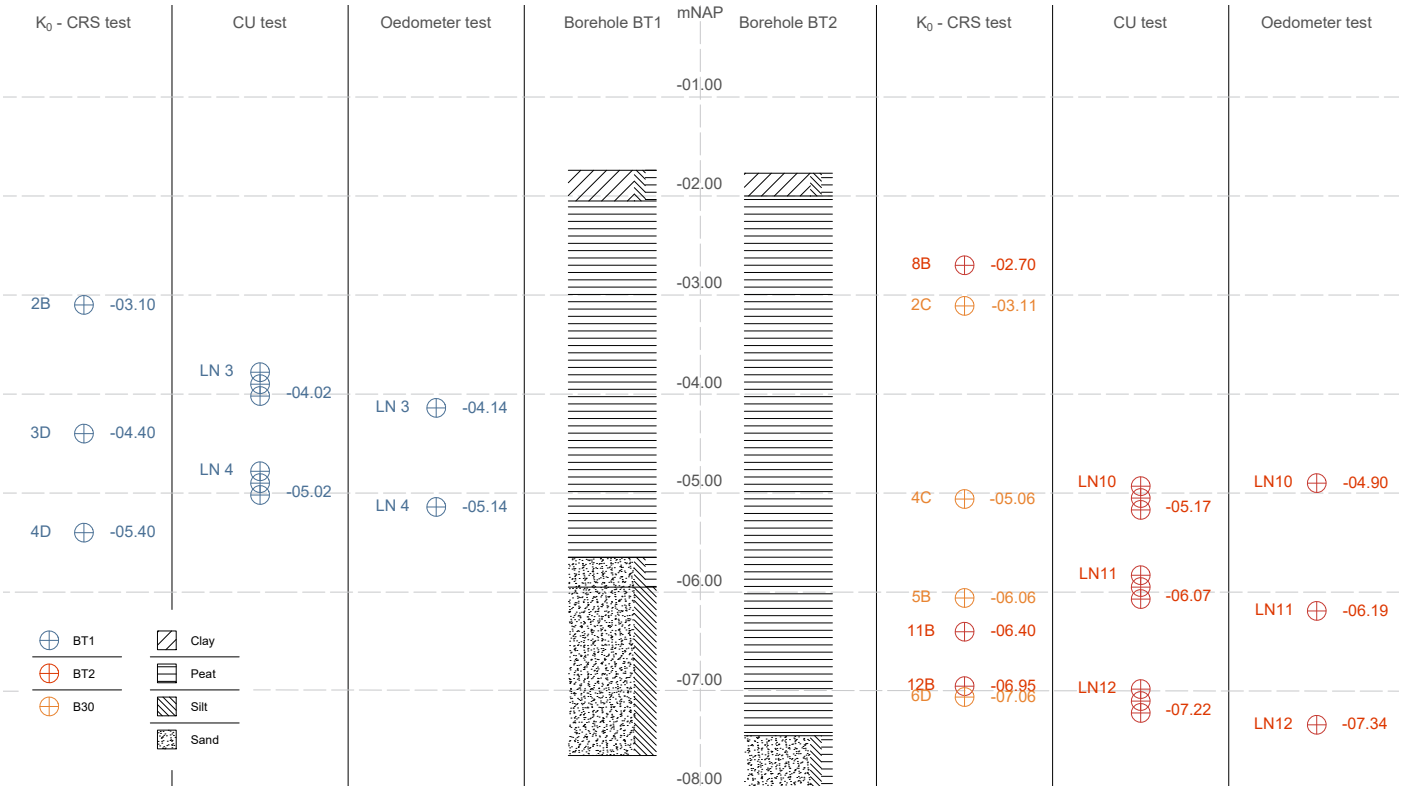

Figure 4.1: Locations of laboratory samples

The samples used in the foregoing laboratory tests, along with their location relative to the nearest borehole, are shown in Figure 4.1. The procedure hereby presented takes them all into consideration, so that an arithmetical average of

each parameter can be presented as an overall representation of the behaviour of the original data set. Nonetheless, for the proposed model parameters, an additional value referred as "estimation" is employed in each case. The distinction between both values is made with the intention of dissociating the effects of incongruous samples.

4.1 Engineering properties

4.1.1 Intrinsic properties

The material of interest is designated as a Reed peat by previous authors, considering the presence of this type of fibers and large pieces of wood (Papadaki, 2013). Through the use of CT-scan and ESEM imaging, the composition of the material was identified as "sub-horizontal plant tissue" embedded in a matrix of finer material. The coarse fibrous sub-structure is composed by rootlets which are primarily responsible for the presence of large voids and the characteristic anisotropy of peat (Den Haan & Kruse, 2007).

The geotechnical classification of the material, in accordance to the NEN-5104:1989 code, is peat with low mineral matter (*Vm*). It is represented by an average initial water content (w_0) of 855.1 % and an initial void ratio (e_0) of 14.4, which is consistent with the empirical correlation of such variables in the Dutch context (Den Haan & Kruse, 2007). Moreover, said magnitudes lay within the expected range for superficial deposits with no relevant coverage or pre-loading. The literature reports that peat with similar stress history can display an initial water content as high as 2 000.0 % and a void ratio up to a magnitude of 30 (Hanrahan, 1954; Mesri and Ajlouni, 2007).

The index properties of the material are shown in Table 4.1 following the results from Papadaki (2013) and Alink (2010). In the case of specific gravity (ρ_s) the reported values fall below the empirical prediction by Den Haan and Kruse (2007) based on the loss of ignition. Considering that the organic material alone is likely to have a ρ_s value between 1.4 and 1.6 (Mesri & Ajlouni, 2007) and that the loss of ignition (L_i) is relatively low, it would be expected that the samples would yield a magnitude closer to 1.66. Despite the fact that these values fall in the lower bound of fibrous peat with large *in situ* water content (MacFarlane, 1969), it is considered that defining the peat as fibrous peat might not be accurate.

Table 4.1: Intrinsic properties of peat (Alink, 2010; Papadaki, 2013)

Sample	Depth	Specific gravity (G_s)	Loss of ignition (L_i)	Organic content
	m NAP	-	%	%
BA-5A-1	-3.97	1.536	69.98	68.78
BA-5A-2	-3.97	1.534	67.09	65.77
BT1-3	-4.14	1.580	79.90	79.19
BA-5B	-4.22	1.452	73.08	72.00
BA-5C	-4.70	1.484	68.56	67.30
BT2-10	-4.90	1.622	77.30	76.39
BT1-4	-5.14	1.640	73.00	71.92
BA-6A	-5.25	1.479	65.95	64.58
BT2-11	-6.19	1.718	64.80	63.39
BT2-12	-7.34	2.242	24.50	21.48

4.1.2 State properties

When visualizing the state properties of the peat, the main reference is the K_0-CRS tests performed by Deltares (2011) and reported by Alink (2010). These reports provide the initial properties of each sample (e.g., void ratio, water content); and asses the evolution of the hydraulic and stress conditions based on the measured excess pore pressure and deformation response. Nevertheless, the anisotropic composition and the non-uniform response of the soil, as well as the operational limits of the testing apparatus, introduce inconsistencies in these trials that decrease the confidence level of the reported estimations.

Despite the constraints of the K_0-CRS tests (explained in detail in Appendix C), their prescribed deformation and the measured water pressure at the later stages remain as indisputable indicators of the soil behaviour, which in turn allow for an inverse problem analysis. By means of a FEM formulation, the consolidation process from each K_0-CRS test is

replicated and compared to the pore pressure generation to discern the representative values that yield the measured response. Considering the vital role of the water pressure response in the coupled process and the soil behaviour, its adequate simulation can be correlated to a satisfactory declaration of the state parameters.

Following the reports by Alink (2010), the tests simulations are composed of three loading phases; along with a re-loading and a relaxation stage. However, the full extent of them cannot be used to define the state properties, as the measurements previous to the reloading phase show inconsistencies proper of unsaturated samples. As described in Appendix C, by simulating the second and third loading ramps it is assumed that the actual magnitude of the hydraulic conductivity (k_v) can be recovered. In Figure 4.2a two cases of these simulations (Figure C.12) are presented; exemplifying the two types of results during the procedure. With some samples (e.g., 2C, 6D, 12B) being effectively replicated and others displaying divergence at the later stages of the test.

Based on literature correlations and data sets, the range of k_v coefficients shown in Figure 4.2b is consistent both in terms of the type of material and with respect of the stress state. Following the overview on the permeability coefficient by Mesri and Ajlouni (2007) a magnitude between 1.0 E^{-8} and 1.0 E^{-6} m/s is to be expected for a peat with a void ratio of 15. Relative to the stress conditions, MacFarlane (1969) indicates that an equivalent load of only a few feet, such as the present condition, would have a vertical permeability in the range of 1.0 E^{-8} m/s.

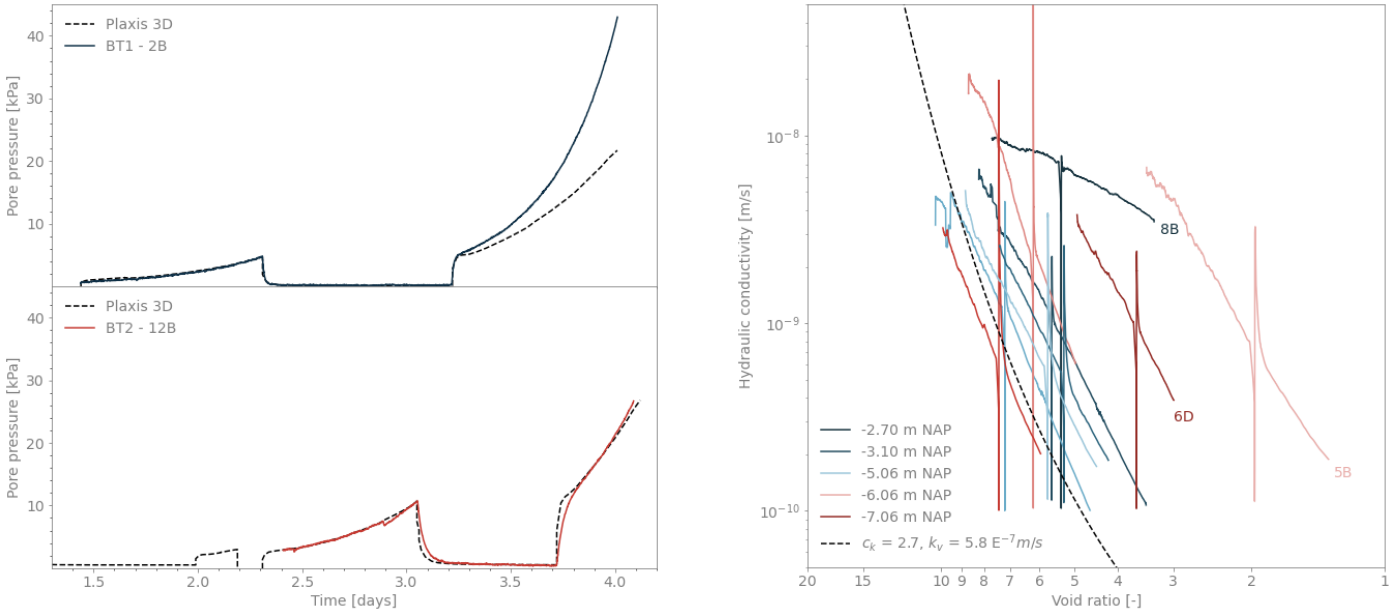

(a) Representative simulations of K_0-CRS tests

(b) Evolution in logarithmic space

Figure 4.2: Progression of hydraulic conductivity based on void ratio dependency

The average coefficient of permeability (c_k) is calculated as 3.05, which is low compared to the empirical formulation based on the void ratio by Mesri and Ajlouni (2007) (c_k = 3.75), as well as the values used by Ammerlaan (2011) and Siderius (2011) (c_k = 4.00). However, sample 4D, which greatly affects the average value, shows the highest divergence during the K_0-CRS simulations and is considered an outlier in this analysis. Thus, by removing these values an estimation of 2.75 can be recovered.

Table 4.2: Comparison of drainage parameters

		Ammerlaan (2011)	Siderius (2011)	Schadee (2012)	Papadaki (2013)	Hoefsloot (2014)	Estimation
e_0	-	15.0	15.0	15.0	16.0	15.0	15.0
k_v	m/s	5.00 E^{-8}	2.31 E^{-7}	2.31 E^{-7}	1.85 E^{-7}	1.00 E^{-6}	5.79 E^{-7}
c_k	-	4.00	4.00	4.00	0.53	1.75	2.75

Relative to the hydraulic conductivity (k_v), although the average value of 2.68 E^{-7} m/s can be calculated based on the analysis. A magnitude of 5.8 E^{-7} m/s is found to be representative of the case during the migration to the Bloemendalerpolder field simulation, as this variable can be further modified on the basis of the possible differences in the field

and laboratory tests. On this matter, Hayashi et al. (2012) cites from his previous work that the measurements from field tests can be between 10 and 30 times larger than those recovered from an odometer test.

4.2 Stress-deformation parameters

4.2.1 Compression Parameters

The compression behavior of the Bloemendalerpolder soil can be estimated based on the linearization of compression and unloading response, which can be recovered from the oedometer and K_0-CRS tests. When these measurements are formulated in a logarithmic space, it is possible to recover a set of compression and swelling indices for the constitutive models of interest. Further on, the abovementioned K_0-CRS FEM simulations are used to corroborate the mechanical response.

From the oedometer results it can be said that the change in void ratio displays a bi-linear behaviour during virgin consolidation (Figure 4.3a). This phenomenon is consistent with the testing of fibrous peats as previously described by Edil and Dhowian (1981). Nonetheless, by visualizing this evolution during the K_0-CRS tests (Figure 4.3b), which were measured with a higher frequency, it is evident that said dichotomy is, in reality, a discrete stepping of a logarithmic response. When comparing both, it is clear that a semi-logarithmic relation $log\,\sigma'_v - v$ (used to compute the normalized parameters) is not sufficient to emulate the large degree of deformation displayed by peat. On this matter, the soft soil and the JMC models instead make use of modified compression parameters based on fully logarithmic planes (Figure 4.3b).

The testing of the peat in the K_0-CRS apparatus exhibits behaviour consistent with the expected response of reed peat, with a high deformation potential and a reduced swelling response ($\lambda^*/\kappa^* \geq 7$). Although the small degree of creep during the relaxation portion of the tests could be linked to an amorphous designation (O'Kelly & Pichan, 2013), the strain evolution presented in these tests is not frequently found in this type of peat. Given the intrinsic properties and more specifically the large content of inorganic material (Table 4.1), this compression behaviour is considered atypical.

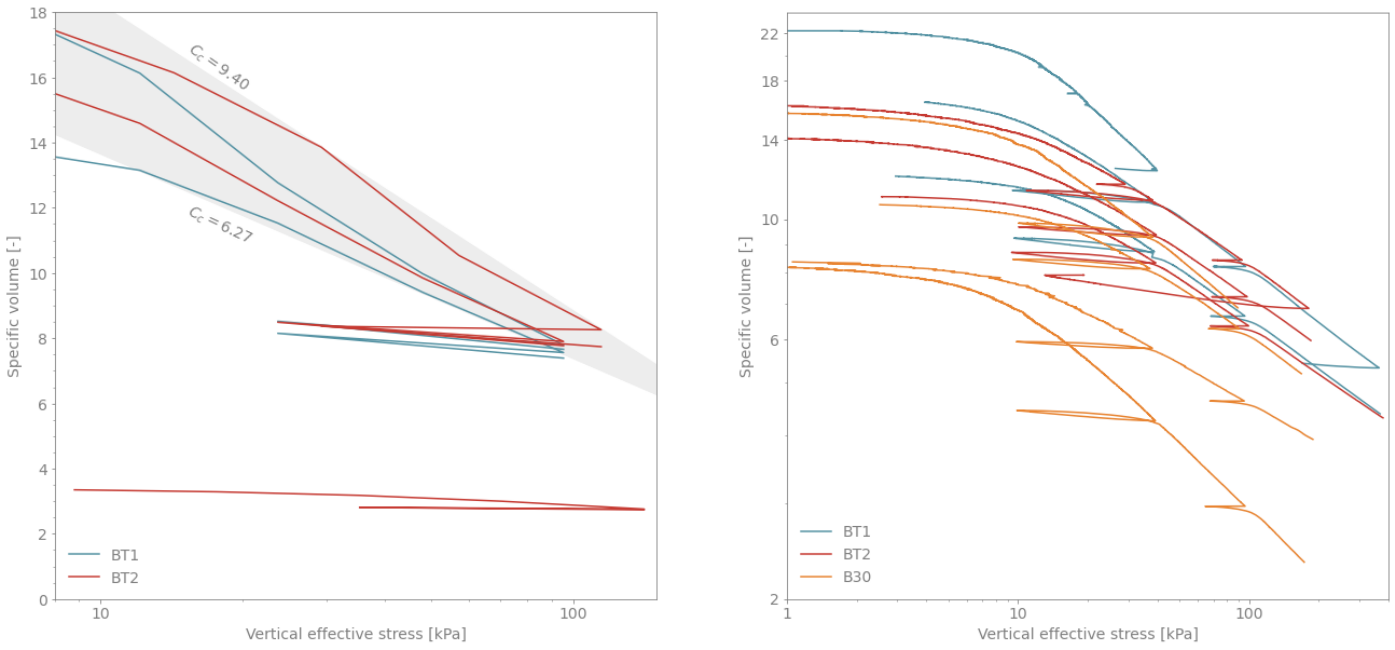

(a) Odometer tests

(b) K_0-CRS tests

Figure 4.3: Estimation of volumetric stress-strain relationship

Although the analysis focused on the modified compression (λ^*) and swelling indices (κ^*) by prioritizing the information provided by the constant displacement tests, the lack of certainty from these tests is also present in terms of the mechanical behaviour. Theoretically, it is assumed that this test enables the calculation of the mean effective stress (p') by means of the measured value of σ_h. Nonetheless, as displayed in Figure 4.4a and discussed in Appendix C, the evolution of said factor is erratic. As a result, the adequate projection of the consolidation process in the $ln\,p' - ln\,V$ and $ln\,p' - ln\,\epsilon_v$ spaces (needed for each model respectively) is hindered and the calibration is based on the FEM simulations of the K_0-CRS tests.

Edil and Dhowian (1981), Hayashi et al. (2012) and Muraro (2019) describe that typical behaviour of this test would appear as a gentle decrease until the consolidation yield stress, at which point this value should become relatively constant. In this case, possibly due to a troublesome contact between the peat samples and the walls of the testing equipment, that cannot be clearly appreciated. In turn, the values keep decreasing even during the normal consolidation stage and no clear convergence can be identified. This progression is consistent with the findings presented by MacFarlane (1969) for peat, where it is stated that the K_0 starts in a range of 0.5 and decreases with increasing consolidation pressure.

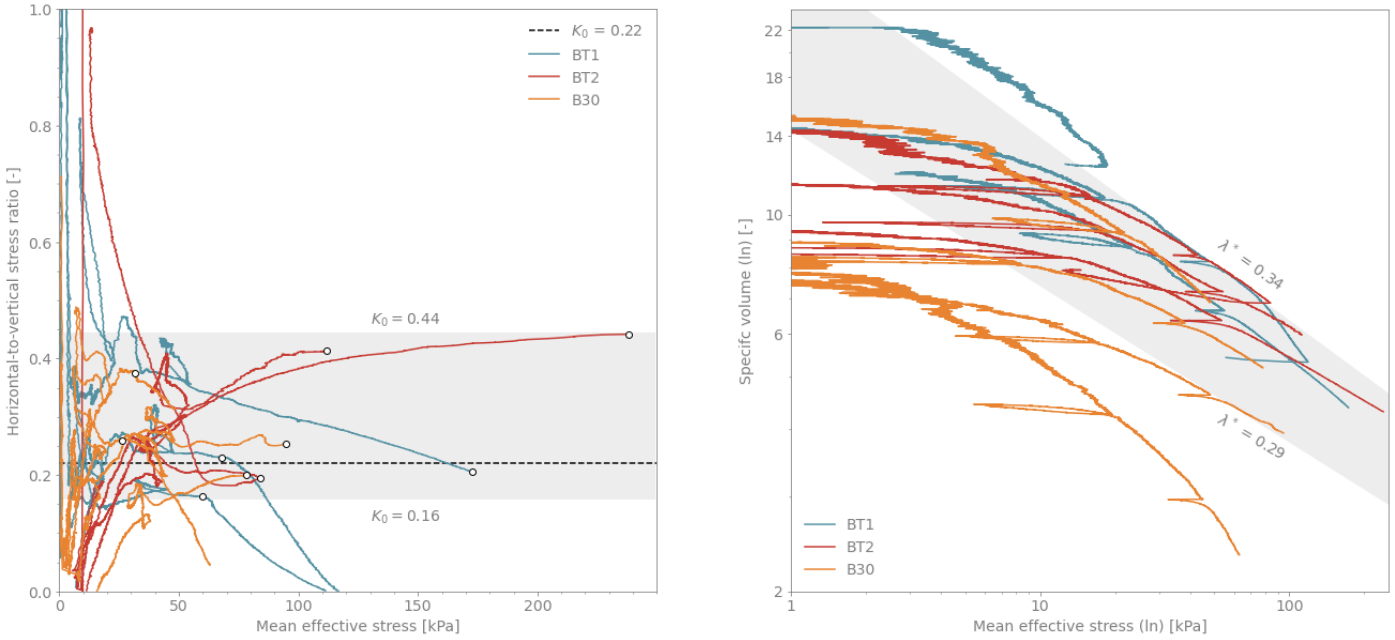

(a) Vertical-to-horizontal stress relation

(b) Evolution of specific volume

Figure 4.4: Estimation of modified compression parameters during K_0-CRS tests

Despite a low degree of confidence of the data recovered using this methodology, the process is executed by identifying the portions of the trail where the K_0 is somewhat constant. As it can be appreciated in Figure 4.4b, the visualization of the mean effective stress cannot be considered representative since the drop in the value of K_0 has an effect in the tendency of the deformation slope, which fictitiously forces a steeper magnitude of the consolidation coefficients. However, λ^* can be approximated in the span where the value of K_0, as the magnitude of the mean effective stress can be defined with higher fidelity.

The modified compression parameters had not been directly estimated by previous authors and were instead derived from abc Isotache parameters. In the case of the models employed by Siderius (2011) and Schadee (2012), the employed values for the soft soil model were based on the predictive estimations by Ammerlaan (2011), while the values for λ^* and κ^* used by Papadaki (2013) are based on his own estimations of a and b and the use of Plaxis Test Facilities. Finally, Hoefsloot and Schadee (2014) recalculated the initial estimations by Fugro based on the progression of the settlement upon that stage of the test. All these efforts are compared with the present endeavor in Table 4.3.

Table 4.3: Comparison of modified compression parameters for the SS model

		Ammerlaan (2011)	Papadaki (2013)	Hoefsloot (2014)	Calculated	Estimated
λ^*	-	0.407	0.215	0.300	0.330	0.360
κ^*	-	0.080	0.029	0.080	0.053	0.050

There is a clear distinction between the representative values for each embankment, with the average magnitude of λ^* for T1 at 0.36, while for T2 it is found at a constant value of 0.31. The selected values for the modified parameters are 0.36 for λ^* and 0.05 for κ^* in the case of the SS model, while for JMC, the value of λ^* is modified to 0.34.

4.2.2 Shear Strength

Conventional practice correlates the shear strength of peat by means of frictional (ϕ) and cohesion (c') components (MacFarlane, 1969), but the constitutive models of interest also require the inclusion of critical state parameters to effectively formulate the behaviour of the material. In the Bloemendalerpolder peat, it appears that the effect of the fibers is not preponderant to define the response of the material, considering that their tensile capacity does not provide additional resistance to the matrix as seen in fibrous peats (Den Haan and Kruse, 2007; Mesri and Ajlouni, 2007; Muraro, 2019). With the goal of identifying the shearing properties, the present section links the results of the consolidated-isotropically undrained triaxial and the K_0-CRS tests to calculate these values.

Different from these samples, the work of Muraro (2019), Zwanenburg and Jardine (2015) show that when fibrous peat is tested, the deviatoric stress displays a transitioning behaviour between the soil matrix and the reinforcing action of the fibers. This effect appears in the form of a convex inflection towards the critical state line, which causes the stress path to exhibit a 'hook' trajectory as the material perceives higher resistance with increasing load. In the present case, the undrained triaxial tests do not display this distinctive mechanical response and as a consequence, the peat can be designated as amorphous and the mixed hardening rule included in the JMC model may be disregarded.

To define the critical state line in compression (M_g), the effective cohesion intercept is considered negligible, as seen in the work of Yamaguchi et al. (1985) and Muraro and Jommi (2020). The projection of this line is done within two frameworks to ensure consistency in terms of stress and strain (Figure 4.5). In both approaches, M_g aims to better represent the behaviour of the samples tested at higher stress (42 kPa - 62 kPa), as this order of magnitude is closer to that of the final state of the trial embankments.

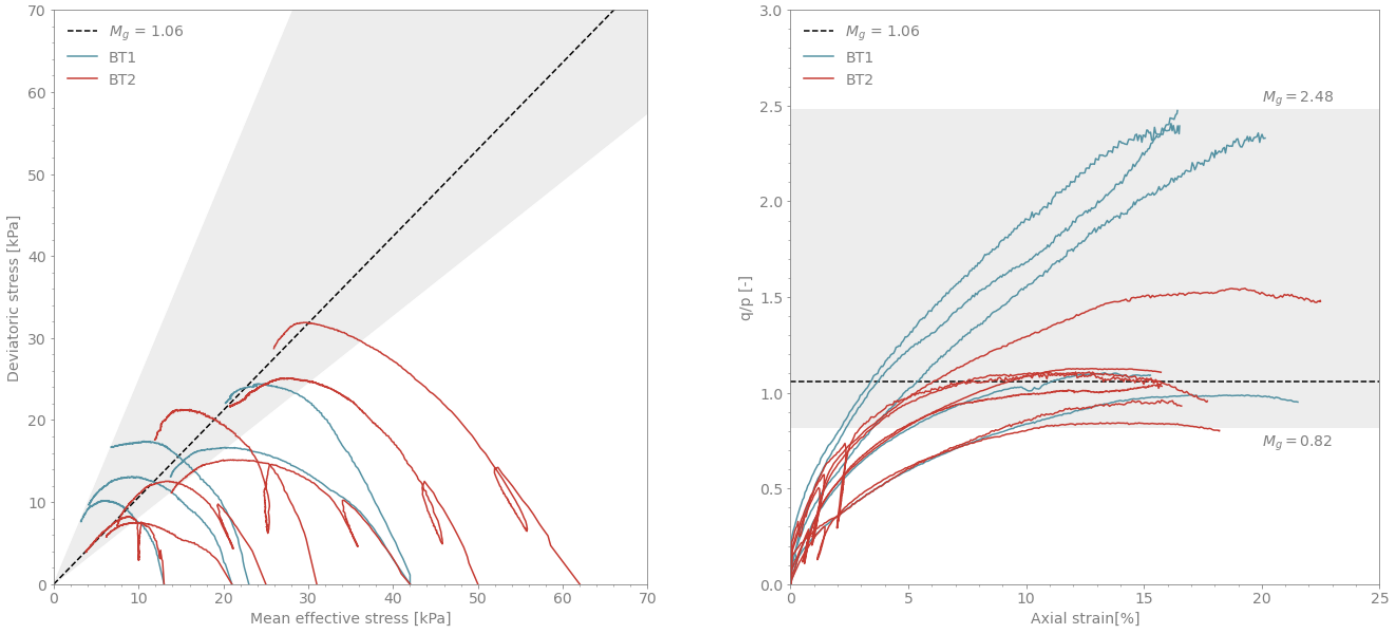

(a) Progression of stress conditions

(b) Evolution of deformation

Figure 4.5: Visualization of critical state line

Based on the magnitude of M_g a corresponding effective friction angle (ϕ') can be recovered from the Mohr-Coulomb failure envelope formulation (Equation 4.2.1), as it describes their interdependence. Furthermore, the analysis can be further extended using Equation 4.2.2 after Jaky (1948), so that a theoretical K_0 value can be estimated based on the critical state. Parallely, the values from Figure 4.4a can be equally related to a theoretical magnitude of M_g. Redundancy is needed as the use of empirical expressions for K_0 has shown unacceptable values (Edil & Dhowian, 1981).

$$M_c = \frac{6\,sin\,\phi'}{3 - sin\,\phi'} \tag{4.2.1}$$

$$K_0{}^{NC} \simeq 1 - sin\,\phi' \tag{4.2.2}$$

Table 4.4 indicates that despite the considerable disparity in both tests, the spread of results overlaps in a wide range, with all the possible estimations from the K_0-CRS tests falling in the range of the triaxial undrained compression. On the basis of favoring the reliability of the triaxial tests and to persevere the consistency of the formulation value, the estimated values of ϕ' and K_0 are based on a M_g magnitude of 1.06.

Table 4.4: Comparison of critical state line (M_c)

	Undrained Compression (CU)			K_0-CRS		
	M_g	ϕ'	K_0	K_0	ϕ'	M_g
	-	°	-	-	°	-
Minimum	0.85	21.9	0.63	0.44	34.1	1.38
Maximum	2.48	61.3	0.12	0.16	57.1	2.33
Average	1.38	34.2	0.44	0.28	46.1	1.89
Estimated	1.06	26.8	0.55	0.22	51.3	2.11

The estimation of the angle of friction is set at 27°, a low value compared with average values for fibrous peat as presented by Mesri and Ajlouni, 2007, Edil and Dhowian (1981) and Hayashi et al. (2012). Additionally, the magnitudes for ϕ' and K_0 are also lower than those calculated by the empirical relations based on the of loss of ignition by Hayashi et al. (2012). Relative to previous authors (Papadaki, 2013; Schadee, 2012; Siderius, 2011), their characterization led to friction angles in the same order of magnitude (Table 4.5).

In the case of the K_0 value, fibrous peats often show a value around 0.30, which tends to increase to around 0.53 if the nature of the material is more amorphous, as the fibers are considered to provide lateral reinforcement (Edil and Dhowian, 1981; Mesri and Ajlouni, 2007). Consequentially, it can be said that the organic matter present in the peat from the Bloemendalerpolder has no reinforcing effects on the material, further confirming the amorphous designation.

Table 4.5: Comparison of shear strength parameters

		Alink (2010)	Siderius (2011)	Papadaki (2013)	Hayashi (2012)	Estimated
ϕ'	°	20.6	25.0	25.0	45.1	27.0
${K_0}^{NC}$	-	0.26	0.50	0.31	0.30	0.55

For the implementation of the NGI-ADP model, the base strength parameters are the undrained shear strength (s_u) and the unloading/reloading shear modulus (G_{ur}), which can also be recovered from the undrained triaxial tests (Figure 4.6).

Figure 4.6: Shear parameters in CU tests

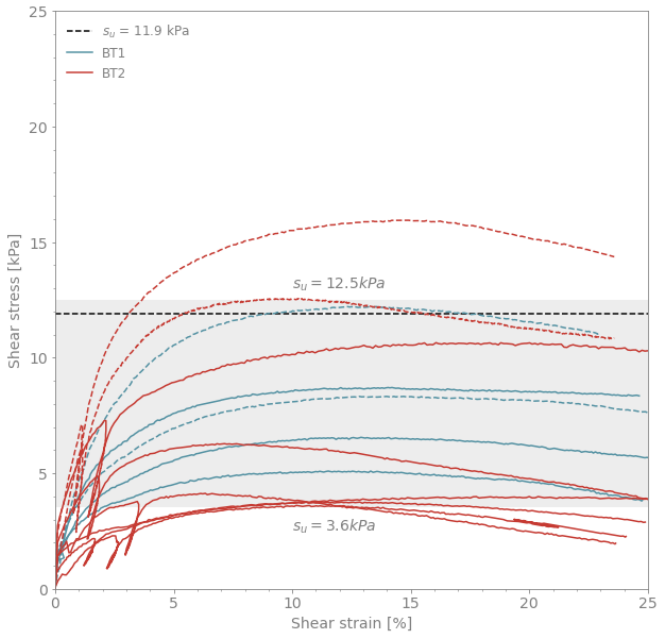

(a) Progression of shear stress

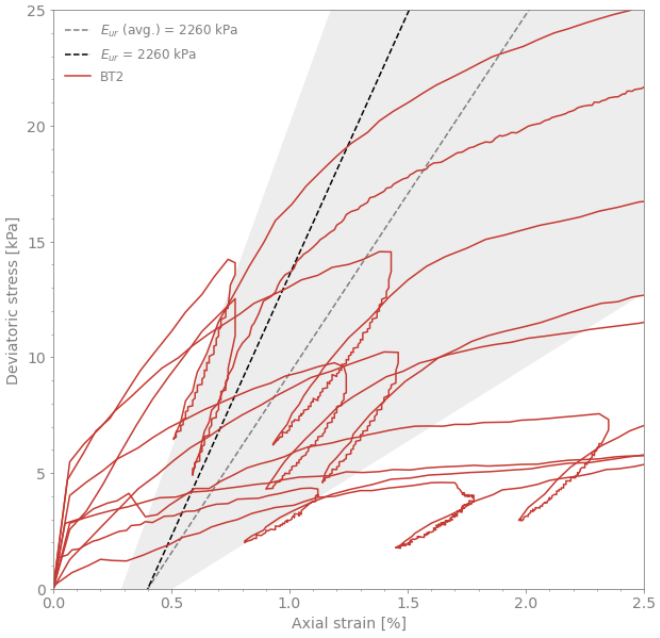

(b) Unloading/reloading portion of CU tests

The selection of a single representative value for the abovementioned strength properties can be further confirmed based on the *in situ* measurements of the shear strength, which also make possible the estimation of the depth-dependent behaviour. In the case of G_{ur}, the calculation is based on its linear stiffness counterpart, the unloading/reloading Young's modulus (E_{ur}), by means of equation 4.2.3. This procedure yields an average magnitude of 574 kPa and an estimation of 837 kPa. In comparison, the cone pressuremeter results provide a lower directly measured 433 kPa (Figure 4.7c).

$$G_{ur} = \frac{E_{ur}}{2 \cdot (1 + \nu)} \tag{4.2.3}$$

From the figures below, it can be appreciated that the strength of the soil has a tendency to decrease with increasing depth. This effect was also perceived by Landva (1980), who attributed the behaviour to the shortcomings of the test. However, the work from MacFarlane (1969) and the consistency of the s_u values with the triaxial results illustrate their engineering relevance.

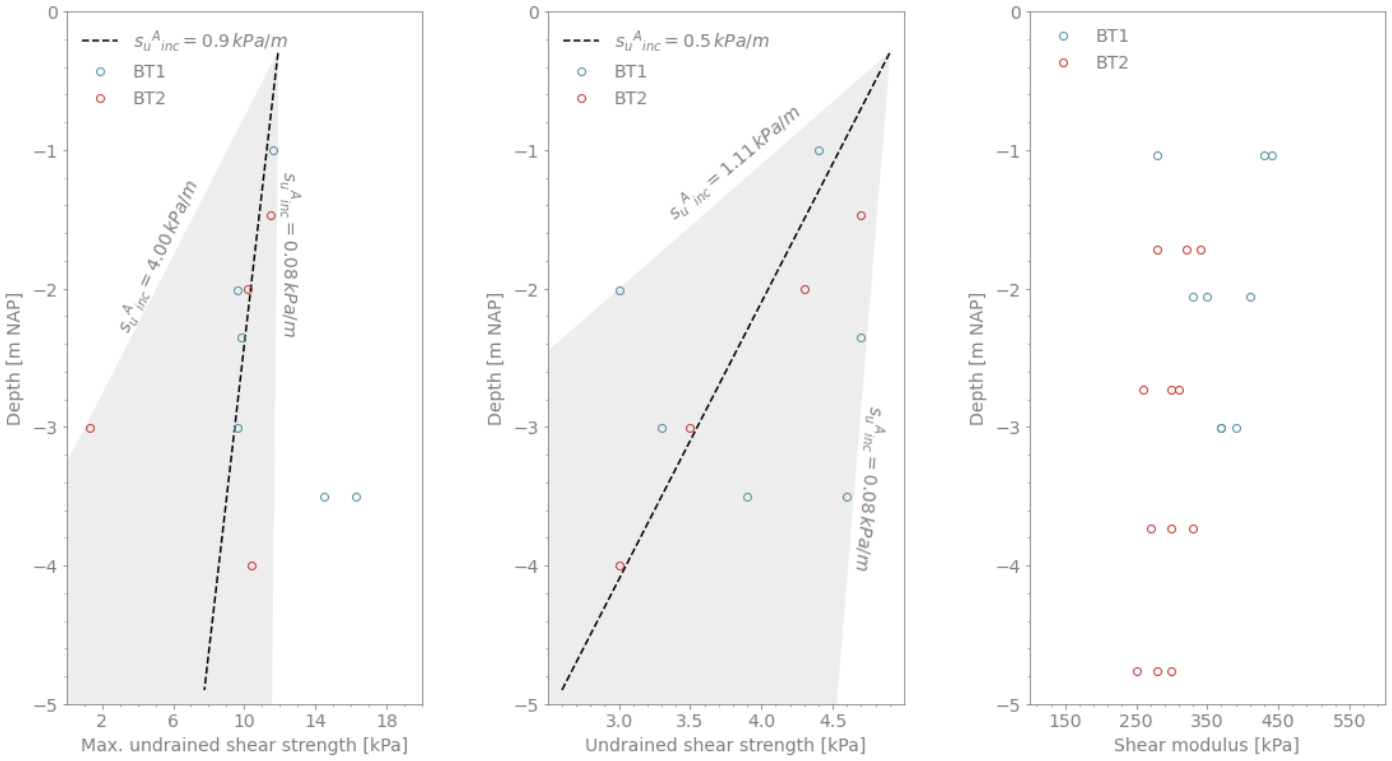

(a) Maximum undrained shear strength (b) Remoulded undrined shear strength (c) Shear modulus

Figure 4.7: *In situ* measurements of shear strength

4.2.3 Tensile Strength

Considering the absence of case-specific extension testing and the inherent complexity in its execution and interpretation, the recovery of tensile parameters in the present work relies on the research from Yamaguchi et al. (1985) and Muraro (2019). Both experimental procedures used peat with index and state properties similar to the peat in the Bloemendalerpolder case (Table 4.6). However, the samples of Yamaguchi et al. (1985) were tested parallel to the preferential alignment of the fibers, while the peat of Muraro (2019) is highly fibrous.

	e_0	w_0	L_i	OC	ρ_p	γ	ϕ'	M_c	M_e	c_M
	-	%	%	%	-	kN/m^3	°	-	-	-
Yamaguchi (1985)	5.84	918.7	71.67	-	1.66	10.8	35	1.43	2.97	2.077
Muraro (2019)	9.90	855.0	-	90.14	1.50	-	43	1.75	1.11	0.632
Estimation	14.70	880.7	69.03	67.79	1.49	10.3	27	1.06	-	-

Table 4.6: Engineering properties of peat from similar cases

Despite the similarities, when comparing the engineering properties it could be assumed that the peat used by Yamaguchi et al. (1985) is closer to the present case. This idea is reinforced when comparing the order of magnitude of the stress-strain relation during compression from both cases, as the results from Muraro and Jommi (2020) attain considerably higher stress levels. On the other hand, Muraro and Jommi (2020) illustrates consistency with the Mohr-Coulomb failure envelope (Equation 4.2.4) when calculating the value of M_e, which the former fails to do.

$$M_e = \frac{6\,sin\,\phi'}{3 + sin\,\phi'} \tag{4.2.4}$$

MacFarlane (1969) cites the work of Helenelund on the correlation between shear and tensile strength, where it is established that the former is usually twice the magnitude of the latter. Following the results of Section 4.2.2, it is then considered that the tensile strength would range in the order of 5.0 kPa. This value is relatively high for submerged tensile strength that usually sits between 0.0 and 2.0 kPa (Den Haan & Kruse, 2007).

Den Haan and Kruse (2007) shows that in the Dutch context, strains during tensile strength tests have reached up to 6.0 %, which would suggest that the extension results of Yamaguchi et al. (1985) are too high. Nonetheless, the analysis done by Iereidis (2019) shows that even an amorphous peat could provide a strain as high as 55.0 % depending on the test. This is possibly due to the close relationship between the strength of the peat and the orientation of the fibers.

Comparatively, the high content of large pieces of organic matter (i.e., wood, rootlets) in the Bloemendalerpolder peat is also relevant, as it could be assumed that their presence hinders the contribution of the pull-out resistance from any diffused smaller fibers favoring particle interlocking within the sample (Den Haan and Kruse, 2007; Mesri and Ajlouni, 2007).

Given the amorphous nature of the peat and the already minimal contribution of fibers in the undrained triaxial tests, the use of formulation 4.2.4 is considered as representative. This assumption minimizes any effects from the fibers and yields a M_e value of 0.79 (c_M ratio of 0.73).

4.3 Calibration

Given the unknowns that still remain due to the lack of additional experimental data (i.e., DSS shear, stress probe triaxial tests, extension tests), some of the parameters have to be defined with a sensitivity analysis. The procedure hereby presented formulates and calibrates the remaining variables of interest from the corresponding models.

4.3.1 JMC model

The still evasive variables for the JMC model are those pertinent to the shape of the plastic potential and the yield locus. Relative to the former, Muraro and Jommi (2020) propose a relationship between the χ_g parameter and some of the foregoing properties (Equation 4.3.1). However, a homologous formulation for the yield locus does not exist and thus, its definition requires the assembly of said limit by identifying the yielding point in multiple stress paths. Given that this procedure is not possible in the present case, a sensitivity analysis of the slope and shape of the yield locus is made.

$$\chi_g = \frac{2}{9} \cdot \frac{\lambda}{\lambda - \kappa} \cdot \frac{M_{g,c} \cdot [(6 - M_{g,c})^2 - 9]}{6 - M_{g,c}} \tag{4.3.1}$$

Having all other parameters for the model defined in the previous sections, M_{f_c} and χ_f are varied systematically starting from a value equal to their counterpart in the plastic potential (Figure 4.8). Considering that the M_{g_c} value intrinsically bounds the extent of deviatoric behaviour, any changes to the yield locus reflect mainly on how that limit is reached.

Broadly speaking, the slope of the yield locus (M_{f_c}) will dictate the type of plasticity shown by the soil as it approaches the critical state. Consequentially, if the magnitude M_{f_c} is lower than M_{g_c}, a softening behaviour will be displayed as the stress combination reaches the CSL; on the contrary, a higher value will yield a hardening response. Figure 4.8a exemplifies the softening phenomenon by illustrating the progressive degradation of the deviatoric stress as M_{f_c} is reached at an earlier stage.

As to what concerns the shape of the yield locus (χ_f), alternating its working range influences the admissible stress states within the elastic realm. Figure 4.8b depicts the effects of an elastic response of the soil as a function of the value of χ_f, given an increasingly linear approximation to the critical state and a larger inclusion of extension points.

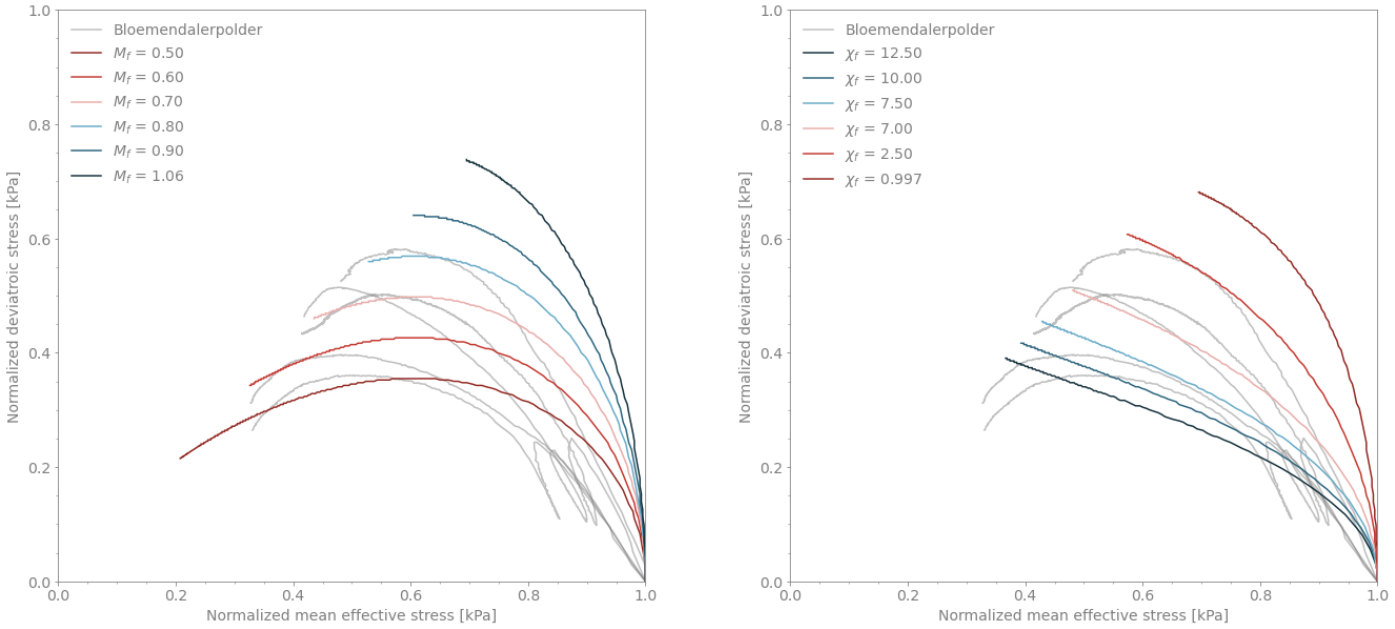

(a) Variation of M_f with χ_f = 0.997

(b) Variation of χ_f with M_f= 1.06

Figure 4.8: Sensitivity of the JMC model to variations in the yield locus

It can be appreciated that the behaviour of the Bloemendalerpolder peat can be approximated by either allowing more softening to occur or introducing more elasticity and extension in the soil response. Favoring the latter would be consistent with the overall response of the samples in the CU tests, given that regardless of their pre-consolidation state the evolution of the deviatoric behaviour is fairly linear. Contrastingly, most of the tested samples show a clear inflection prior to reaching the M_{g_c} slope (Figure 4.5a), which would suggest a milder M_{f_c} slope (consistent with a softening response). Therefore, the most favorable condition of both parameters is chosen (χ_f = 7.5 and M_f= 0.7), and using the unit as starting point, the complementary variable is varied towards the upper and lower bounds of their operational range (Figure 4.9).

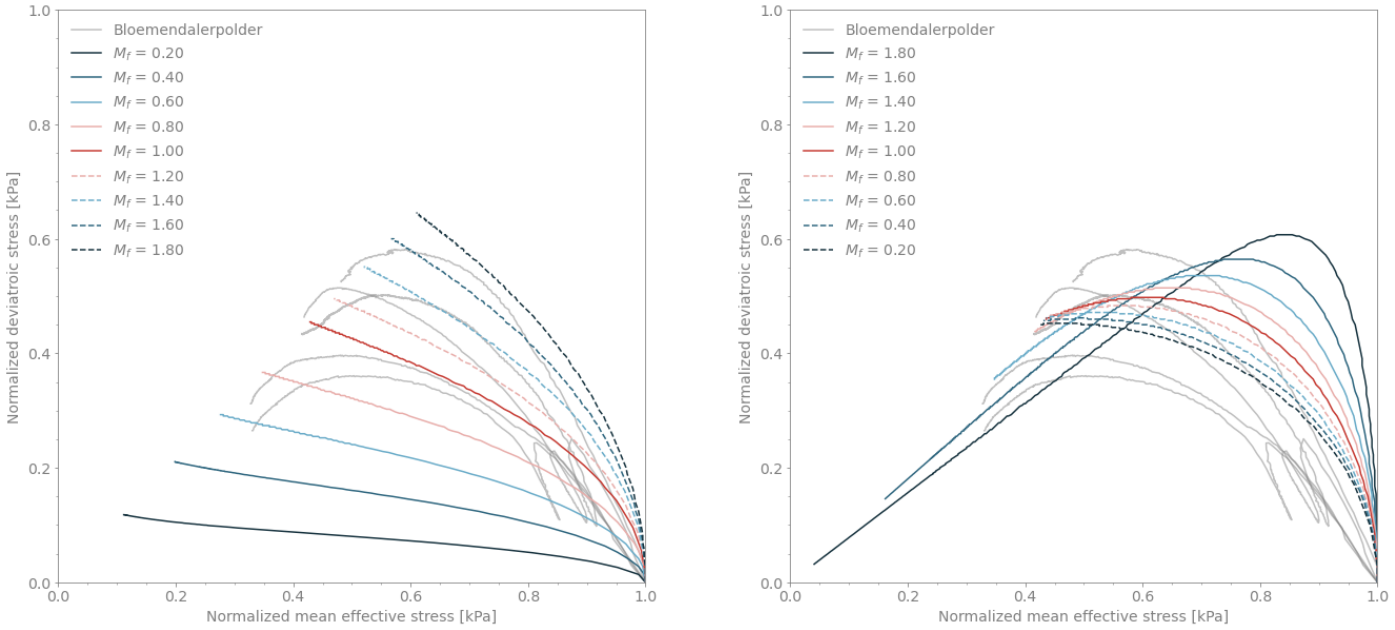

(a) Variation of M_f with χ_f = 7.5

(b) Variation of χ_f with M_f= 0.7

Figure 4.9: Refined sensitivity of the yield locus parameters

The variation of the parameters of interest in Figure 4.9a shows that a model iteration using a predominantly linear response will not be able to faithfully replicate the initial stress progression. This can be attributed to the overlapping elliptical geometries of the yield and plastic potential surfaces, which invariably dictates a curved response regardless

of the stress state. Comparatively, replicating softening inflection at the apogee in the original data set is not realistic, considering that the reproduction of such response with the model is also accompanied by a stiffer response in lower stress states (Figure4.9b). From both figures, it is concluded that a suitable combination of parameters needs to have a M_f value slightly lower than M_g = 1.06, and a mild curve that can average the behaviour of the set.

Once the effects of the model have been visualized, the whole set of CU tests is compared to their best fit using the JMC model, so that the working range of the M_f and χ_f can be identified (Appendix B). For the final selection of the model parameters, the analysis considers the five CU tests representative of the final stress state condition on the field. Each of these samples is considered independently and a set of values is selected based on the best fit in terms of excess pore pressure, axial strain, and deviatoric response.

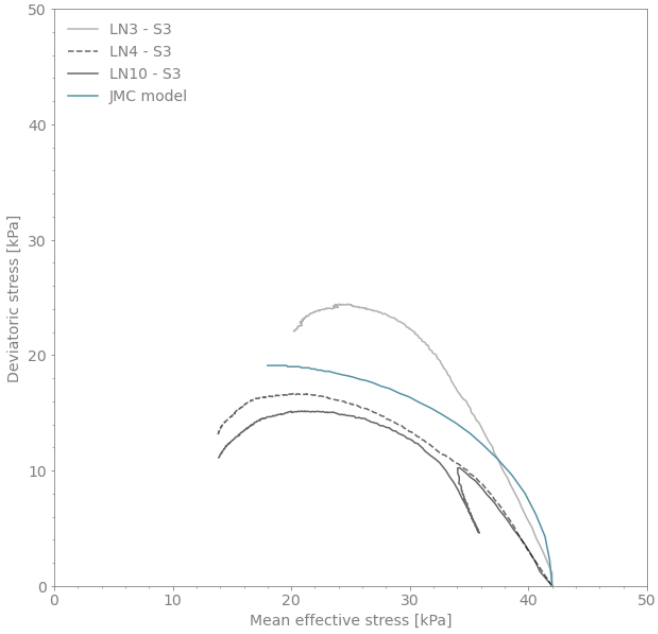

(a) Stress path - p_c = 42 kPa

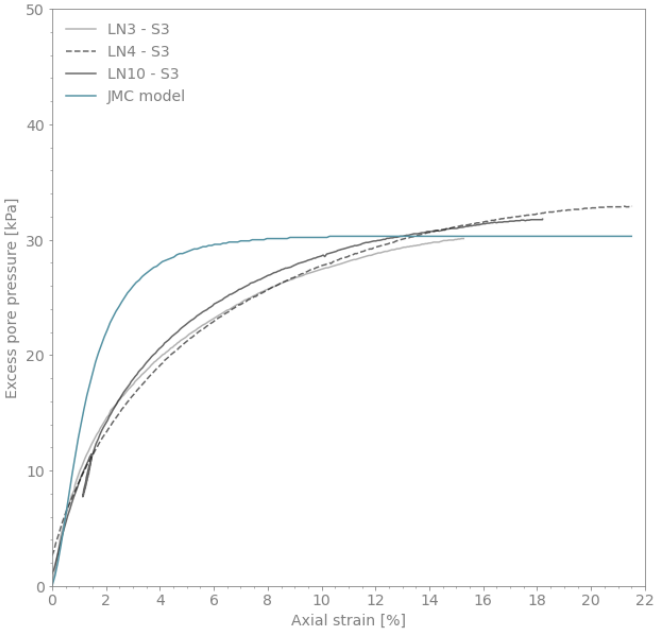

(b) Excess pore pressure-axial strain relation - p_c = 42 kPa

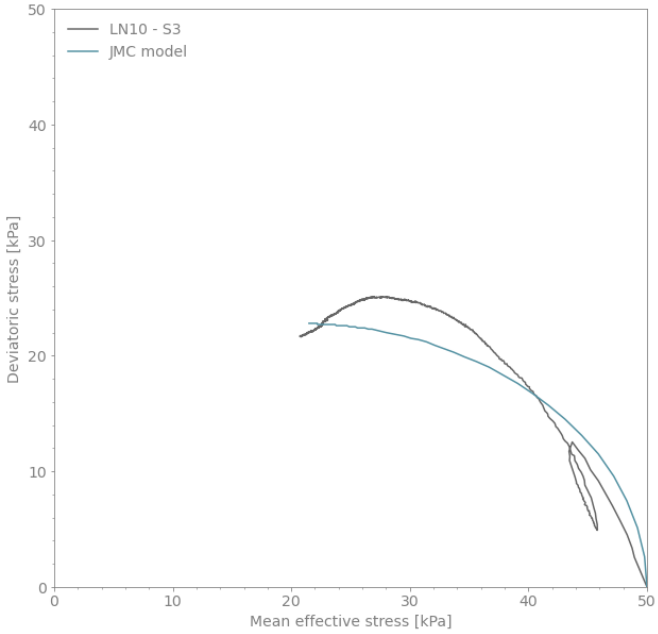

(c) Stress path - p_c = 50 kPa

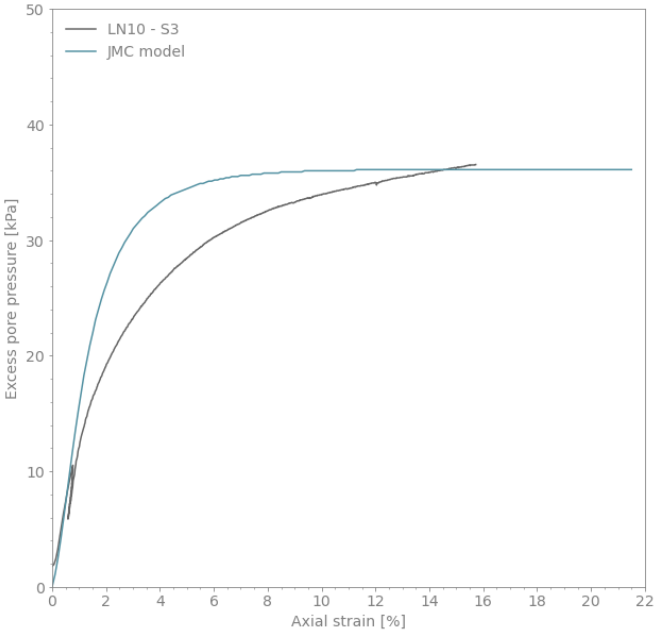

(d) Excess pore pressure-axial strain relation - p_c = 50 kPa

Figure 4.10: Comparison of JMC model with experimental results

As seen in Appendix B only the behaviour of samples LN-03 and LN-04 (BT1) is accurately replicated by the model. The tests from BT2 display a linear stress path at the initial portions of the shearing phase, which cannot be adequately emulated by the model. The overall best fit is chosen and displayed in Figure 4.10, while the summary for the selected

properties can be seen in Table 4.7.

Table 4.7: Reference parameters for the advanced testing with the JMC model

c_M	e_0	D_0	D_1	p_0	$M_{g,c}$	$M_{f,c}$	κ^*	λ^*	ν	χ_g	χ_f
-	-	-	-	kPa	-	-	-	-	-	-	-
0.73	15	0.0	0.0	-	1.06	0.85	0.060	0.340	0.18	0.816	2.5

4.3.2 Soft Soil model

All the parameters required for the SS model were recovered from the aforementioned tests in Section 4.2.1. However, for the SS and SSC, the slope of the critical state line cannot be used as an input and it is in turn implicitly defined in the superposition of the MC failure criterion. Table 4.8 displays the input values used in the model during the field simulations.

Table 4.8: Reference parameters for the advanced testing with the SS and SSC models

c_{ref}	ϕ'	ψ	ν	K_0^{NC}	κ^*	λ^*
kPa	°	°	-	-	-	-
1.75	27.0	0.0	0.18	0.55	0.360	0.060

4.3.3 NGI-ADP model

The primary directive of NGI-ADP is the definition of the strain and stress levels based on three loading directions so that a deviatoric field can be estimated using these values as limits. Nonetheless, other than the triaxial compression test, no specific tests were performed in the original testing campaign to define the values relevant to direct shearing and extension. Despite the absence of these measurements, some of the values can be estimated based on correlations with field testing, while the reaming are proposed based on the literature review.

The definition of shear strength in extension was calculated using the relation of the undrained shear strength in the Mohr-Coulomb space using the estimated value of ϕ' = 27.0 degrees (Equation 4.3.2). For the shear value during DSS, Plaxis (2022a) and Grimstad et al. (2012) illustrate a possible correlation between the strength boundaries provided in compression and extension using equation 4.3.3. Finally, the initial mobilization (T_0) is expressed as a function of K_0 in equation 4.3.4 as proposed by Plaxis (2022a).

$$ {S_u}^P / {S_u}^A = \frac{3 - sin\,\phi'}{3 + sin\,\phi'} \tag{4.3.2} $$

$$ {s_u}^{DSS} / {s_u}^A = \frac{1 + {s_u}^P / {s_u}^A}{2} \tag{4.3.3} $$

$$ T_0 = -0.5 \cdot (1 - K_0) \cdot \sigma'_{yy_0} \tag{4.3.4} $$

A shear strain value in compression can be recovered from the CU tests as a function of the axial strain relation $3/2 \cdot \epsilon_a$, which can be used as the frame of reference to infer the extension that can be expected in the other directions. Based on the measurements by Muraro (2019) and Yamaguchi et al. (1985) it is possible to recover attained magnitudes between 10.0 and 15.0 % in terms of extension, but, they would prove to be insufficient to preserve the relation ${\gamma_f}^E > {\gamma_f}^{DSS} > {\gamma_f}^C$ required by the model. Hence, based on the comments from Section 4.2.3 and the review of the model by Iereidis (2019), it is assumed that the shear strain in extension could reach a magnitude of 30.0 %, while the value for shear can be expected as halfway point between both values.

The undrained shear strength can be recovered from the results in Section 4.2.2, as they show consistency between the undrained triaxial tests and the field measurements at a magnitude of 11.9 kPa. On the contrary, considering the large spread of results of the unloading/reloading shear modulus (G_{ur}) and the K_0 values presented in Section 4.2.1, the values for G_{ur} and T_0 are varied between the range of measured values to find the best fit.

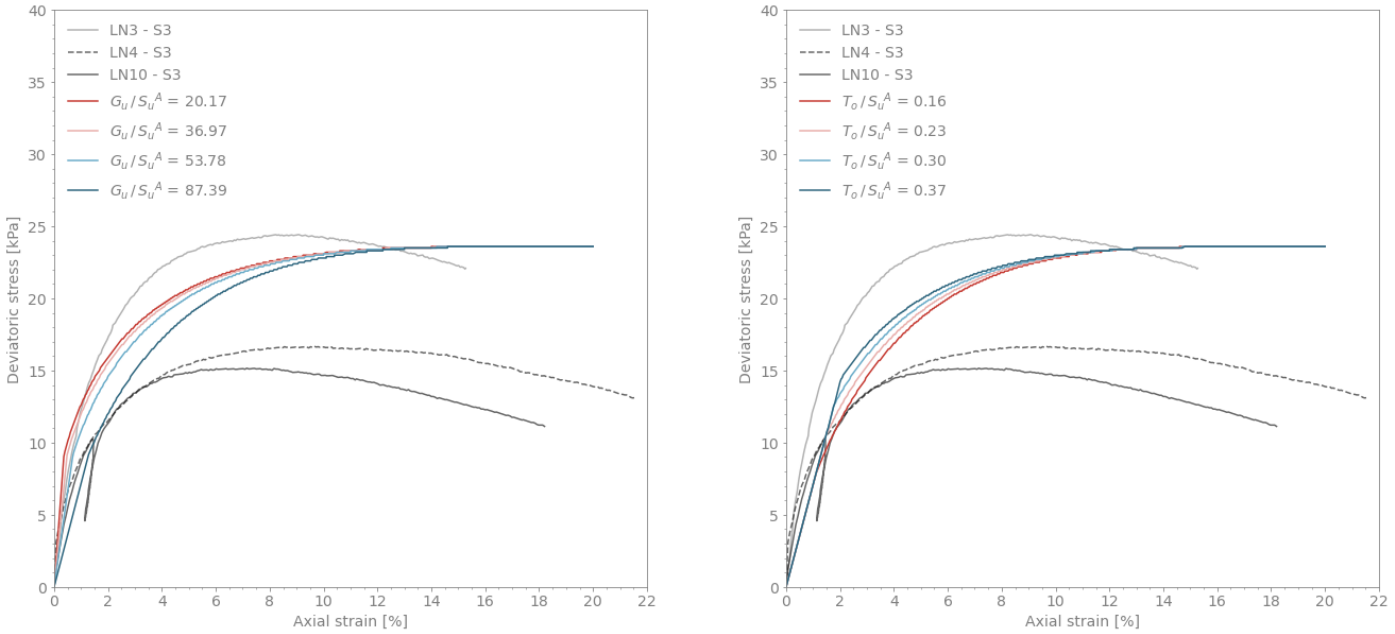

(a) Variation of $G_{ur}/{S_u}^A$

(b) Variation of $T_0/{S_u}^A$

Figure 4.11: Sensitivity of the NGI-ADP model to variations in the shear response

The final selection of the values of interest was based on the average field measurement of G_{ur} (433 kPa), while the initial mobilization was based on the estimated magnitude of K_0. The summary of the selected parameters for the model is shown in Table 4.9.

Table 4.9: Reference parameters for the advanced testing with the NGI-ADP model

${G_{ur}}/{S_u}^A$	${\gamma_f}^C$	${\gamma_f}^E$	${\gamma_f}^{DSS}$	${S_u}^A{}_{ref}$	${S_u}^A{}_{inc}$	${S_u}^P/{S_u}^A$	${T_0}/{S_u}^A$	${S_u}^{DSS}/{S_u}^A$
-	%	%	%	kPa	kPa/m	-	-	-
20.17	22.5	30.0	27.3	11.9	-0.9	0.73	0.189	0.87

4.4 Discussion

- The material was described by previous authors as reed peat, which is consistent with the preponderant content of large wooden pieces and the high water content. However, this procedure suggests that the intrinsic properties and the mechanical response are more fitting of amorphous peat. The lack of fiber reinforcement is evident in the triaxial testing results (Figure 4.5a), as the hook commonly shown by fibrous peats when approaching critical state is completely absent. Moreover, based on the findings by Mesri and Ajlouni (2007) and MacFarlane (1969), a low friction angle ($\phi = 27°$) and a K_0 coefficient of 0.55 are not characteristic of a fibrous material. These considerations limit the usage of the JMC model features, as the relevance of the mixed hardening rule is deemed unnecessary.
- The resulting calibration of the JMC and SS models shows a high fidelity in replicating the overall behaviour of the Bloemendalerpolder data set, while the NGI-ADP appears to disregard the effects of excess water pressure and thus is limited in recreating the stress path (Figure 4.12). On one side, JMC provides a better estimation of the stress-strain relations when compared with SS and NGI-ADP, but SS shows a more desirable pathway in the excess pore pressure generation.
- The SS and JMC approximations are considered equally adequate with respect to the consolidation progress. Although the NGI-ADP reaches an adequate end-of-consolidation state, it fails to estimate the transition between the initial and final stages, since the generation of strains appears to follow a linear behaviour.
- NGI-ASP better fits the data in the deviatoric stress-axial strain relation with a progressive evolution that falls in between the samples.

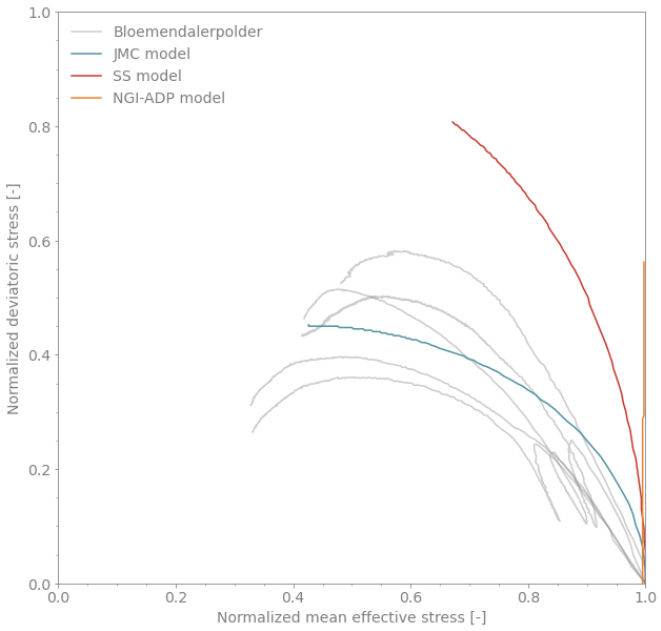

(a) Stress path

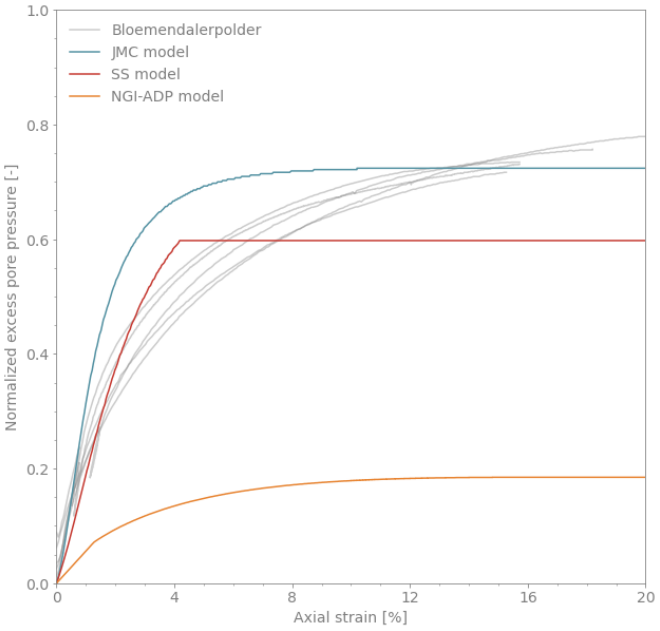

(b) Excess pore pressure-axial strain relation

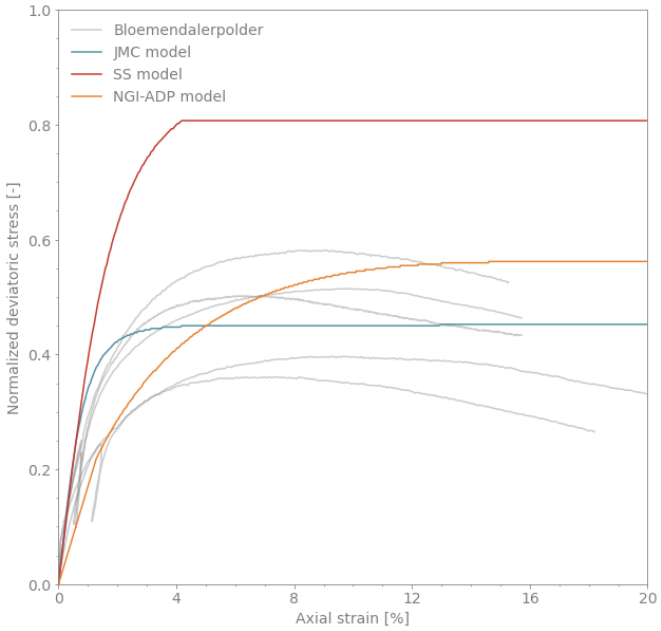

(c) Deviatoric stress - axial strain relation

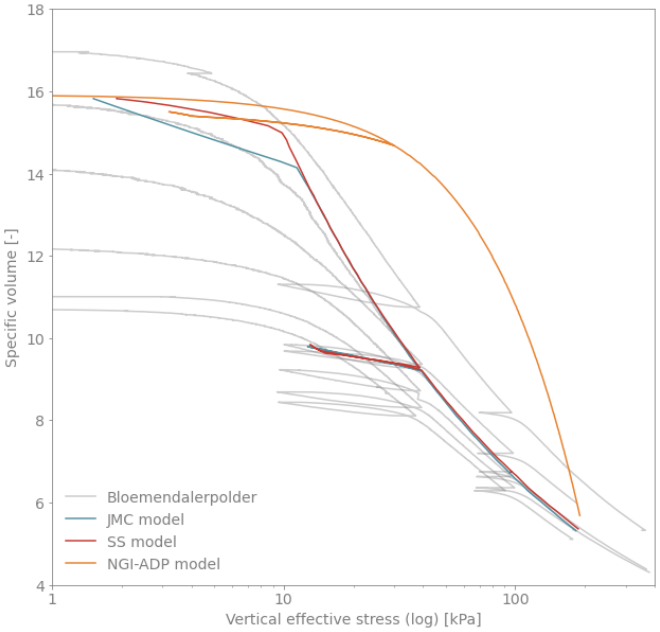

(d) Volumetric stress-strain response

Figure 4.12: Comparison of JMC model with experimental results

- As stated by Muraro (2019) and Iereidis (2019), the standard testing of peat should be complemented with additional tests such as the K_0-controlled triaxial testing, triaxial extension the direct shear to better identify the response of peat in multiple directions. Given the absence of these additional tests, it is possible that more complex mechanisms could not be identified with the available information.
- Concerning the original data, some of the samples showed a certain degree of inconsistency that would cause a relevant divergence from a representative behaviour. Although most of the abnormal samples can be linked to a location close to a change in horizon, the reasoning behind their removal is supported by the following statistical or qualitative considerations:
  - In the case of samples 4D and LN12, a box plot analysis deemed them as statistical outliers in terms of their compressive properties. This condition can be attributed to their state parameters, which already fall at the extremes of the spread.
  - For sample LN12, it can be seen that its fundamental properties differ from those expected from a *Vm* peat

as reported by Den Haan and Kruse (2007). The bulk modulus exceeds considerably the typical range (9.32 - 11.08 kN/m^3) with 13.2 kN/m^3 and the void ratio and water content fall out of the expected parameters.

  - Sample 4D was also singled out from the data set due to the comparatively high linear strains during the K_0-CRS tests, which is consistent with the appraisal of Papadaki (2013). Furthermore, when visualizing the behaviour of the sample as a function of time, the response is considerably more erratic than other samples, with the ranges varying for several orders of magnitudes in
  - Sample 5B shows an inconsistent behaviour when compared with a somewhat similar sample (11B). When looking at the metadata from this particular test, its problematic nature is further confirmed when comparing the expected compressible from such a large water content (Mesri & Ajlouni, 2007) and the result.
  - Sample 6D also exhibits contrastingly low state values that drop substantially from the average of the data set.
  - There is a relevant discrepancy between the results shown for sample 5B in the report by Alink (2010) and the original data. Neither JMC nor SS can accurately replicate the later stages of this test.

- The information provided by K_0-CRS tests on the earth pressure coefficient (K_0) displays inconsistencies at the initial portion of the test. This might be attributed to the non-perfect contact between the sample and the lateral ring.

5 | Model

Embankment no. 1 from the Bloemendalerpolder project is modeled in FEM using Plaxis 3D and following the specifications regarding geometry and loading conditions presented in Chapter 2. The objective of the present section is to exhibit the preliminary steps in the model implementation and the systematic assembly of the model (i.e. geometry and phasing). With this objective, the reasoning for the parameter selection is initially described; later on, the geometric considerations and their corresponding assumptions are defined, followed by the initialization of the stress field and hydraulic conditions. Lastly, the relevant considerations for the subdivision of the continuum and its evolution through the analysis are presented.

The relevance of using a 3D FEM methodology lies in the flexibility to incorporate a complex geometry and multiple distinct non-parallel strata, which result in considerable deviation from the idealized conditions of arithmetic formulations. The use of FEM also provides an advantage to other procedures by accounting for buoyancy, time factors, and the update of porosity-dependent parameters (Long, Grimstad, et al., 2022). On the contrary, the tool is not without flaws, as the general assumptions of the FEM formulation and how it is built into the modeling software limit the implementation of any case.

A three-dimensional approach was selected over a 2D plane strain FEM model given the limits of the latter to adequately visualize the out-of-plane effects of the non-infinite embankment. As it has been described, the embankment covers a rectangular area over a non-parallel stratigraphy in which piles are positioned in a non-symmetric way. Therefore, no point in the domain perceives an identical stress change, which deems the three-dimensional approach as the most adequate option. However, given the computational advantage of further simplifying the implantation of the model into a half mound, the present case explores the use of the northern section for the iteration procedure, while a full model of the soil body is employed for the final results.

5.1 Materials

The preliminary estimation of the peat properties of the previous chapter is now extended with the estimation of the auxiliary materials, both in the case of the remaining soil horizons and the additional components describing the embankment intervention. In the case of the silty sand and the clay, the use of correlations based on the volumetric weight and the CPT measurements provides an acceptable approximation. While the properties of the embankment and the cement-bentonite surrounding the inclinometers are based on the reported values of Fugro (2011,2014,2015), although they remain predominately ambiguous. Finally, the well-known specifications of the HEA300 steel profile and the concrete used during their installation, are modified into a single composite material.

The characteristics of the peat material were defined following the procedure described in Chapter 4, where the combination of laboratory data, FEM modeling, and empirical correlations ensure a holistic parametrization of the material. During the characterization process, sufficient information was recovered to define the working range of the characteristic values for the usage of the SSC, SS, NGI-ADP, and JMC models. Hence, based on these values, the model is varied to further understand the case. Figure 5.1 summarizes the known information of this horizon in both test mounds.

As it can be appreciated, the overall variation of the geotechnical profile in T1 suggests a linear distribution as a function of depth in the material properties, which can be correlated with a change in water content, and thus with a variance in void ratio. Regardless, it is worth noting that the mechanical response close to the surface deviates from what would be expected if this distribution was employed. In turn, as it is evident from samples 8B and 2B, the most shallow material has a higher stiffness, which can be explained by a state of mild over-consolidation and perhaps restructuration in this area.

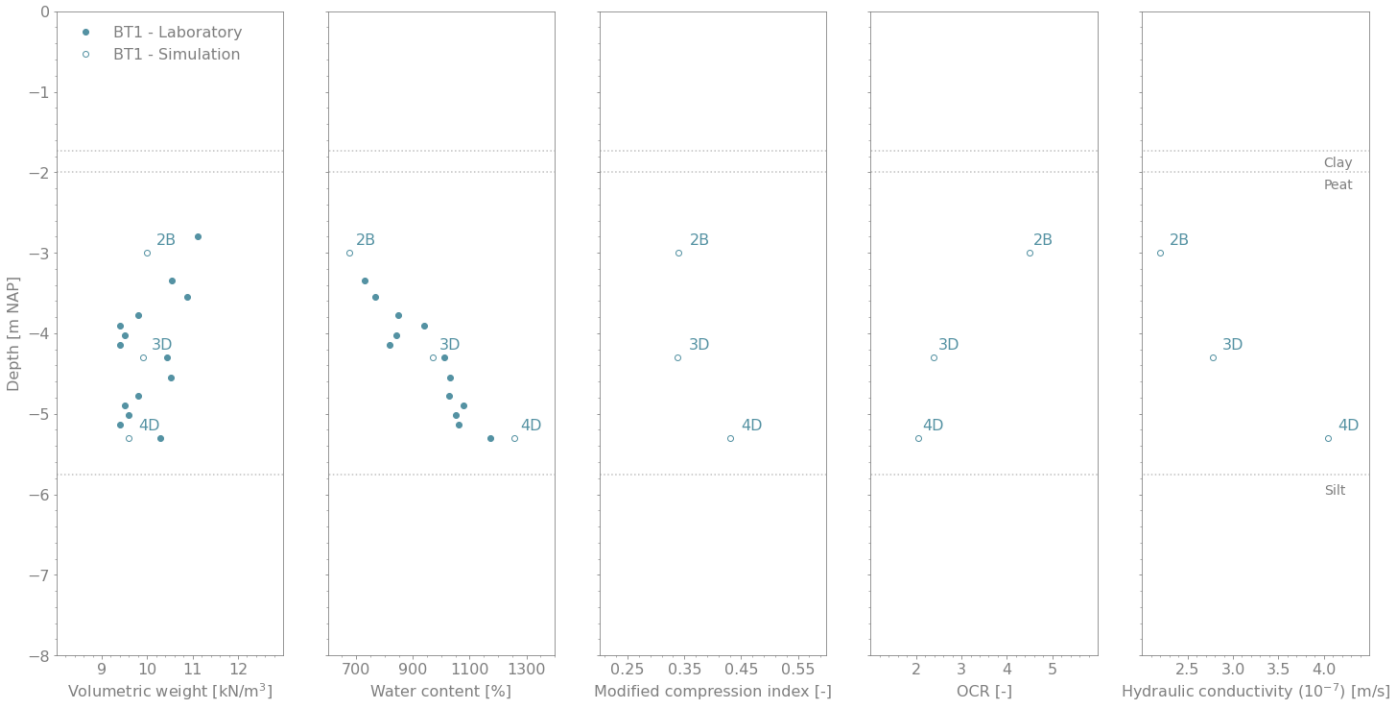

(a) Embankment no. 1

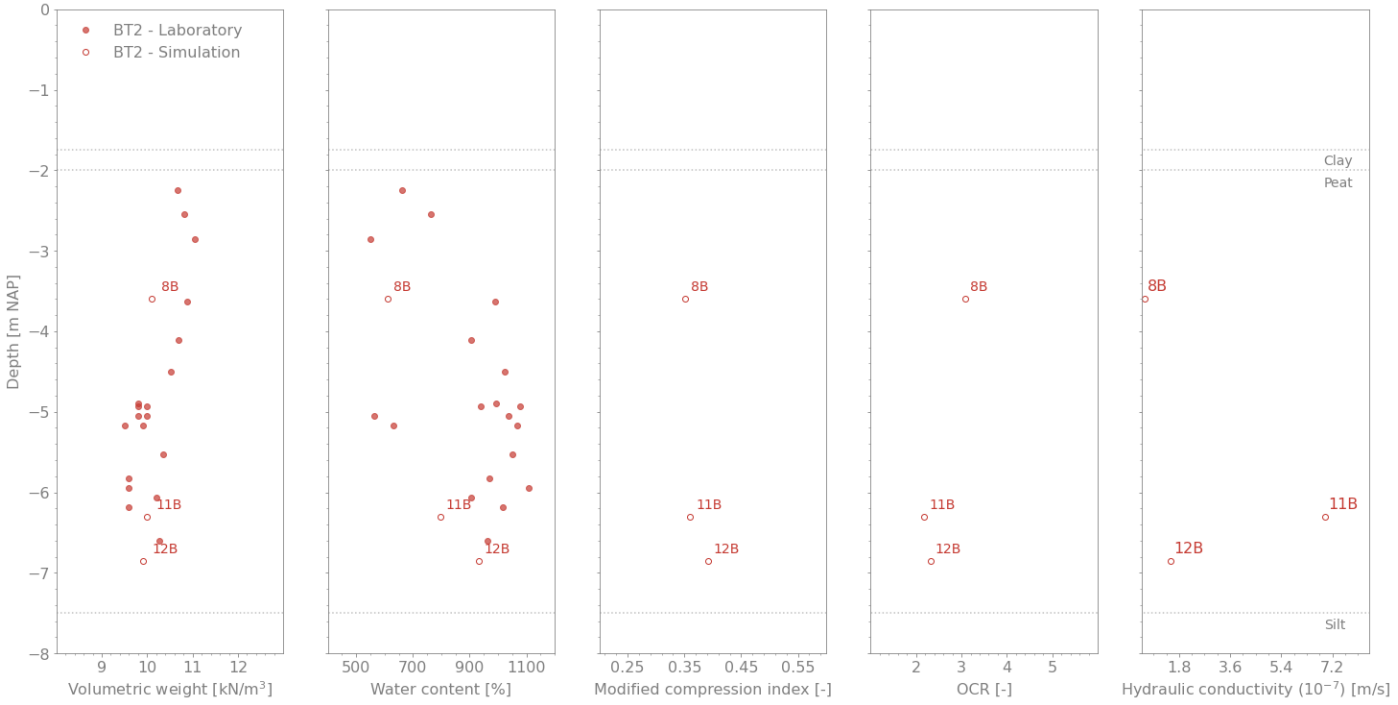

(b) Embankment no. 2

Figure 5.1: Geotechnical profile of the Bloemendalerpolder site[1] [2]

The absence of testing of the clay and silt layers made relevant the use of empirical correlations based on the CPT and the measured volumetric weight. Moreover, given the uncertainty of these materials, their characteristics are also modified to improve the fitting of the curves in terms of deformation and to ensure a hydraulic system that yields an adequate response of the excess pore pressure.

The underlying sandy silt can be modeled as a bi-linear elastic model (i.e. Mohr-Coulomb) as this layer mostly partakes in the embankment's behaviour as a boundary condition. In terms of geometry, it aids in providing the peat layer

[1] The *BT1 - Laboratory* set includes the results from the volumetric weight estimations, Oedometer, and CUSS tests of Borehole BH1.
[2] The *BT1 - Simulation* set displays the estimated parameters from the FEM emulation of the K_0 - CRS tests.

with a variable horizon and thus, with limiting the variable thickness of said layer (Figure 5.2). With respect to the hydraulic conditions, the layer is required to allow drainage without any relevant overpressures, hence a relatively higher conductivity is necessary. Finally, due to the considerably higher stiffness when compared to the clay and peat layers, it also plays a major role in limiting the overall settlement of the strata.

Complementary to the aforementioned roles, this layer implicitly ensures the stiffness of the end condition of the piles/inclinometers installed. Within the scope of Schadee (2012) for the adequate modeling of the piles in this case, the author demonstrated that the MC model fulfills the necessary requirements without introducing a higher level of uncertainty in the behaviour. Furthermore, Hayashi et al. (2012) took a similar approach and effectively model his case.

Relative to the overtopping clay layer, the Mohr-Coulomb model is assumed to also be sufficiently representative for the material. Based on the relatively low thickness of the layer, it is assumed that the contributions of this horizon are minimal in terms of mechanical response (Papadaki, 2013; Schadee, 2012). On the other hand, special care is taken with the imposed hydraulic conditions, as they are vital in providing an adequate drainage path.

Table 5.1: Mechanical properties of the complementary soil materials

Parameter	Units	Fill	Clay	Silt
Unit weight ($\gamma_{sat}/\gamma_{nat}$)	kN/m^3	19/17	14/14	20/16
Friction angle (ϕ'_k)	°	28.0	20.0	32.5
Cohesion (c'_k)	kPa	0.0	2.0	0.0
Diltancy angle (ψ')	deg	0.00	0.00	2.00
Young's Modulus (E_{ref})	kPa	5 000	4 000	20 000
Possion's ratio (ν_{ur})	-	0.300	0.200	0.300
K_0	-	0.500	0.500	0.500
Permeability (k_y)	m/d	10.0	5.0 e^{-3}	0.5
Initial void ratio (e_o)	-	0.5	0.5	0.5

Two structural materials are required for the modeling of the case, the steel piles and the cement-bentonite slurry used to install the inclinometers. Different from the well-known properties of the former, the cement-bentonite mixture has more uncertainty in its definition and requires further analysis. As reported by Alink (2010), the mixture contains a 5:6 ratio of cement to bentonite, based on this, it is expected that with the considerable volume expansion from the mineral particles, the strength potential and density from the mixture would reduce further (Zhang et al., 2013). Because of the assumed softer nature of the, it is considered that an elastic behaviour of the mixture disregards the brittle nature of the cement fraction, which in reality introduces discontinues and thus, strength softening around the fracture points (Flessati et al., 2021). The findings of Flessati et al. (2021) on the simulation of the material using the Modified Cam-Clay model are used as the basis to extrapolate the properties in this case (based on the cement-to-bentonite ratio).

Table 5.2: Reference parameters for the modeling of the piles

Element	E	γ	ν	k_v	λ	κ	M
	MPa	kN/m^3	-	m/s			
HEA300	2.1 E^8	78.5	0.20	0.0	-	-	-
Cement-bentonite	-	11.0	0.25	0.0	1.97	0.06	2

5.2 Model assembly

The geometric implementation of the present case in the FEM space makes use of volume clusters to which the above-mentioned materials are assigned. These elements are primarily subdivided in the domain layers and the auxiliary components. The aim of this segment of the procedure is to describe these elements and the relevant assumptions made for their definition.

5.2.1 Stratigraphy

A preponderant advantage of the postdiction of a case is the holistic overview of where the settlement actually took place. As it was mentioned in Chapter 2, the Bloemendalerpolder case included a large assortment of devices at various spatial coordinates, from which the deformation response can be visualized. Of these measurements, the settlement profile gauges (ZMS) were of special interest when building of the model, as the implicit relation between the measured vertical deformation at a given point and the thickness of the soil layer, allows for a refinement of the assumptions made during the site investigation.

From the ZMS measurements, it was possible to translate their settlement trends to define the sections of the field that perceived higher movement. By coupling these findings with the CPT information, the areas of the field prone to settlement can be better identified and thus defining the lower boundary of the incompressible layers. In principle, this process relays on the consideration that the CPT measurements of embankment no. 1 (DKMP-T1-1 to DKMP-T1-11) provide known depths of an underlying silt layer (as seen in Figure 2.3), while the settlement profiles provided by ZMS-T1-1,2,3 are used to connect this points (Figure 5.2).

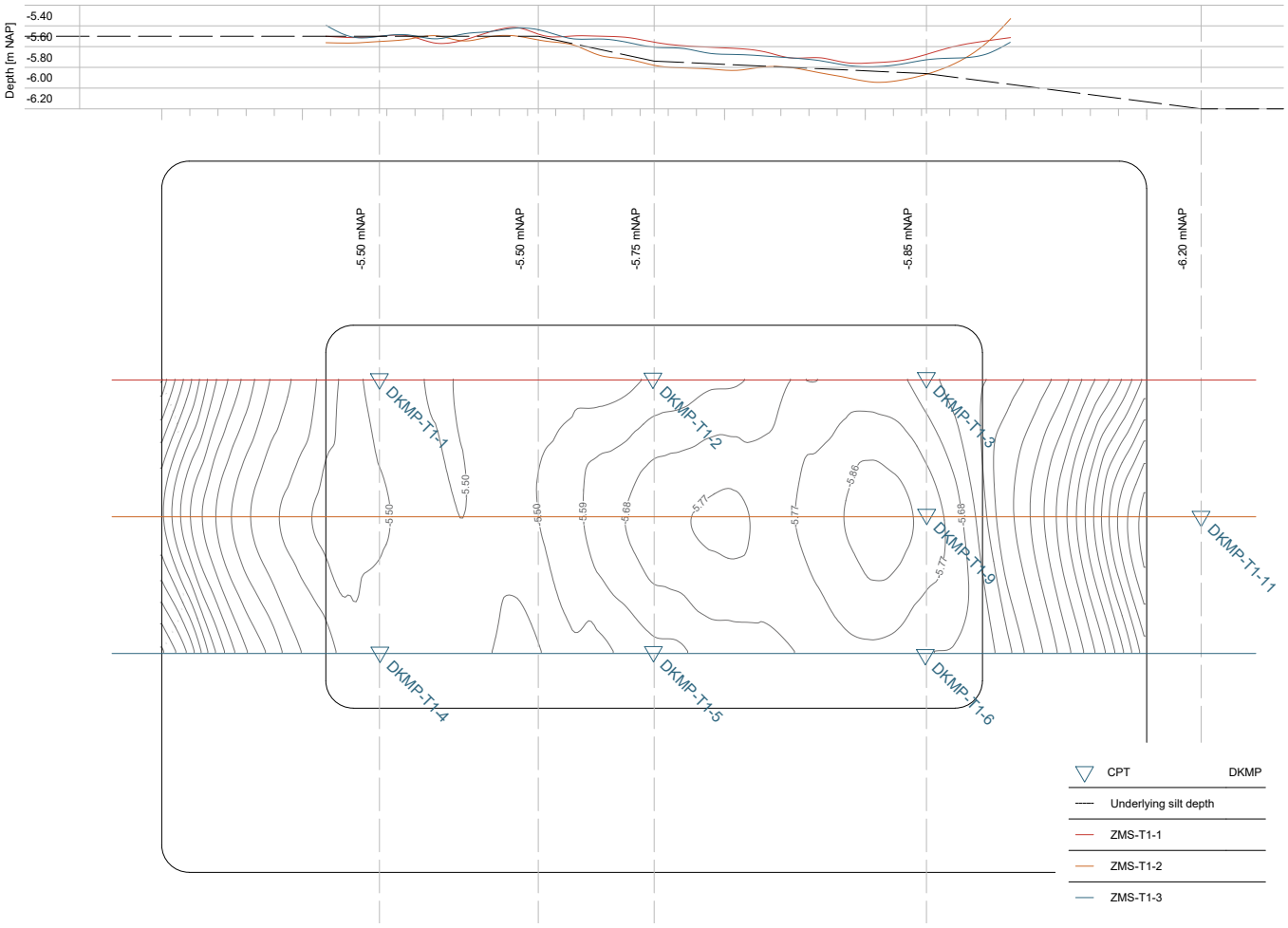

Figure 5.2: Simplification of silt layer for the T1 model

By superimposing their effects on the embankment geometry a variable trend can be identified, with a plateau at the western side of the mound and a semi-continuous increase in depth in the eastern direction. Despite the fact that assuming a constant stratification would still be valid for engineering purposes, the measured results are evidence that within the footprint of the embankment, a differential settlement is present, with differences in vertical deformation up to 80 cm. In virtue of this differentiation, the present project deems relevant to consider a variable thickness in the lower bound of the peat layer as the one presented above.

For the clay layer, a simple approach was followed to define this thickness, given its contrastingly narrow thickness. From the CPT data, it can be seen that the clay layer varies around -1.73 m NAP with a variability of ± 2 cm; this estimation is further confirmed by the reports of Ammerlaan (2011), Hoefsloot and Schadee (2016). Just like previous authors, based on these considerations the surface level is settled at the average value of -1.73 m NAP. Relative to the lower

boundary of the material, a depth of -2.00 m NAP can be defined as the overall trend, nonetheless, the western side (DKMP-T1-1 and DKMP-T1-3) shows a deeper level of around 10 cm, which is initially disregarded. The inclusion of the layer is regarded paramount because of its high state of over-consolidation and the highly contrasting properties to those of the peat, especially in terms of hydraulic conductivity.

Regardless of the recognition of additional layers further below, and more importantly the component sand below; they are assumed inconsequential given the considerable difference in stiffness between the overlaying peat material and the already included components. It is believed that the contrast with the silty-sand horizon already provides sufficient contrast to perform the role of lower boundary. Moreover, for what concerns the 10 20 cm clay layer, located between the sand and the silt, its presence is ignored based on its dimensions.

5.2.2 Embankment

The embankment is assembled as a group of volume elements that replicate the truncated pyramid geometry, by subdividing the total height of the mound by the reported height of each step (Figure 5.3a). The model includes no other elements to emulate the mound besides the volume cluster, which is solely described by a single elastic material as reported in Table X.X. Nonetheless, volume elements representing the piles and inclinometers do intersect the mound on the western side of the soil body. This soil structure has a footprint of 24 by 36 meters and rises 3 meters above the ground level.

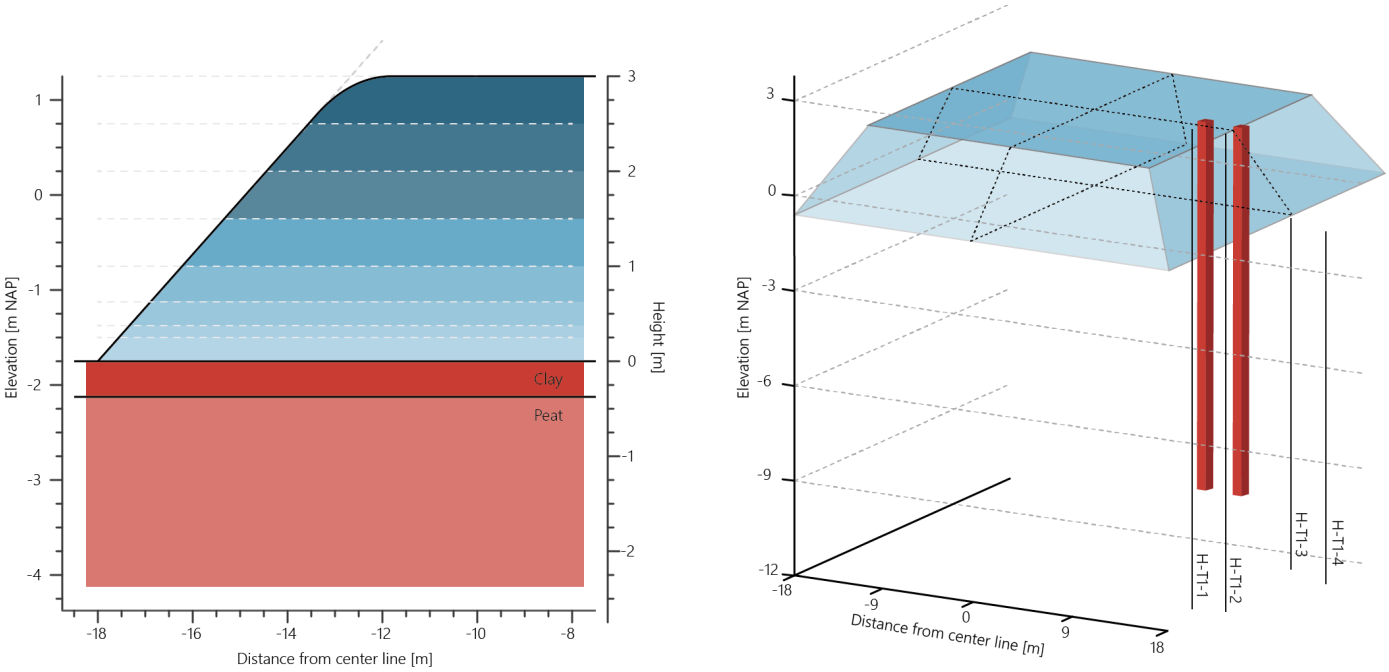

(a) Subdivision of embankment

(b) Position of volume elements

Figure 5.3: Dimensions and geometry of volume elements

A special consideration was made in the case of the first rise of the mound, instead of a single increase of 1 meter as reported by Alink (2010), it is modeled and implemented as four non-equal loading steps. The basis for this decision follows the response shown by the water pressure measurements as they are evidence of the construction process that spans 3 days to be completed. In consequence, a part of the consolidation process already takes place before the step is even completed, as it is displayed in Figure 5.4. Based on this image, it is clear that the four steps have distinct loading and relaxation times, and thus, different magnitudes of dissipated pressure. Based on these differences, the known increase in height of 1 meter is split based on a weighted average of the total amount of excess pore pressure attained in this period.

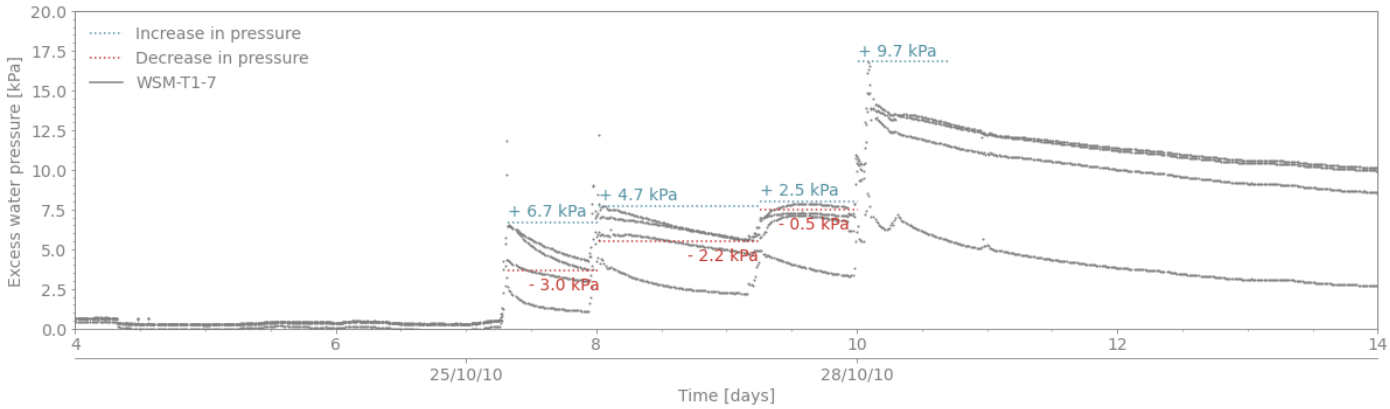

Figure 5.4: Excess pore pressure during first construction step

5.2.3 Complementary elements

As described in Section2.4.2, the soil response is evaluated with a set of six independent inclinometers of which two were attached to HEA300 steel beams. This renders the analysis as a soil-structure interaction problem, given that the evaluation of the deviatoric behaviour of the peat is strictly linked to the simultaneous response of the material and the devices that measure it. The pile elements are modeled as prismatic volume clusters with a square profile. Considering the implicit complexities of modeling the pile with its characteristic geometry, the model makes use of an equivalent composition that provides an equal behaviour to that of a HEA300 beam. Since both elements are of equal length the column stiffness formulation would imply that the formulation of an analogous square pile has to provide an equal bending stiffness ($E \cdot I_z$). Hence, by equating this property to a simplified geometry, a theoretical equivalent pile can be calculated. On this matter Siderius (2011) and Schadee (2012) proved the relativity of the pile presented in Table 5.3.

Table 5.3: Mechanical properties for the modeling of the piles

Element	Width	Depth	E	I_y	I_z	$E \cdot I_z$
	m	m	MPa	m^4	m^4	kg m^2
HEA300	0.29	0.30	2.1 E^8	1.8 E^{-4}	6.3 E^{-5}	1.3 E^4
Equivalent square	0.26	0.26	3.5 E^7	3.8 E^{-4}	3.8 E^{-4}	1.3 E^4

Different from the rest of the measuring devices utilized for the evaluation of the embankments, the inclinometers are also modeled as volumetric elements due to their position and installation process. The most preponderant consideration of this decision follows the construction process of the tubes where the inclinometer devices can travel. They required a boring of a 6 in spanning three meters after the change of the silty-sand horizon, the replacement of said volume with a cement-bentonite mixture, and the subsequent insertion of the inclinometers' conducts with a diameter of 20 mm (Alink, 2010).

The geometry produced by this intervention is an annular shaft, which brings out a series of problematic constraints in the meshing process. Mainly, the size of the element relative to the domain and the cylindrical volume against a predominately rectangular element arrangement. Thus, it is necessary to approximate the behaviour with a volume that possesses equivalent inertial characteristics. With this aim and following the fundamental formulation of pile stiffness, it is possible to define a regular square prism that opposes deformation equally to the real annular area.

Table 5.4: Mechanical properties for the modeling of the cement-bentonite column

Element	Width	Diameter	E	I_y	I_z	$E \cdot I_z$
	m	m	MPa	m^4	m^4	kg m^2
Cement-bentonite	-	0.17	3.4 E^4	3.9 E^{-5}	3.9 E^{-5}	1.32
Equivalent square	0.13	-	5.6 E^4	2.4 E^{-5}	2.4 E^{-5}	1.32

The use of the less computationally intensive *embedded piles* is not employed in the present project since the interaction with the highly deformed field, when the piles are introduced, remains unstable. Moreover, as the research by Dao (2011) suggests, although the usage of these elements allows for more efficient running of the model and the recovery of the data, the results do not vary significantly from a volume element. This consideration was further confirmed in the Bloemendalerpolder case with the results presented by Schadee (2012) for Plaxis 2D, as they also showed a limited variation when compared to the modeling with a volume cluster approach.

5.2.4 Domain

To ensure the adequate simulation of all relevant mechanisms of the embankment and the underlying stratigraphy in FEM, it is necessary to establish a sufficiently large model for them to occur. Considering that imposing a restrictive boundary disposition would simulate the presence of unrealistic discontinuities of the failure planes, it can be said that the level of accuracy of the analysis is linked to a suitable extension of the model. Therefore, to ensure compliance, the size of the domain is defined based on the analytical evaluation of the spatial influence of the embankment's construction.

As a semi-infinite space employing a FEM formulation to describe the hydro-mechanical coupling (Equation 3.3.4), it is considered that such a model obeys the principles of homogeneity, isotropy, and elasticity assumed by the Boussinesq formulation for stress distribution. Additionally, as the results from the profile gauges (ZMS-T1 and ZMS-T2) show, the embankment behaves as a flexible strip. These considerations would suggest that the use of equation 5.2.1 can provide an apt estimation of the construction's footprint. Using this fundamental formulation for a semi-infinite domain and assuming a uniform distribution of stress equivalent to the load of the embankment at the surface, the change in effective stress throughout the field is calculated (Figure 5.5b).

$$\sigma_v = \frac{q}{\pi} \cdot [\alpha + sin\,\alpha \cdot cos(\alpha + 2 \cdot \beta)] \tag{5.2.1}$$

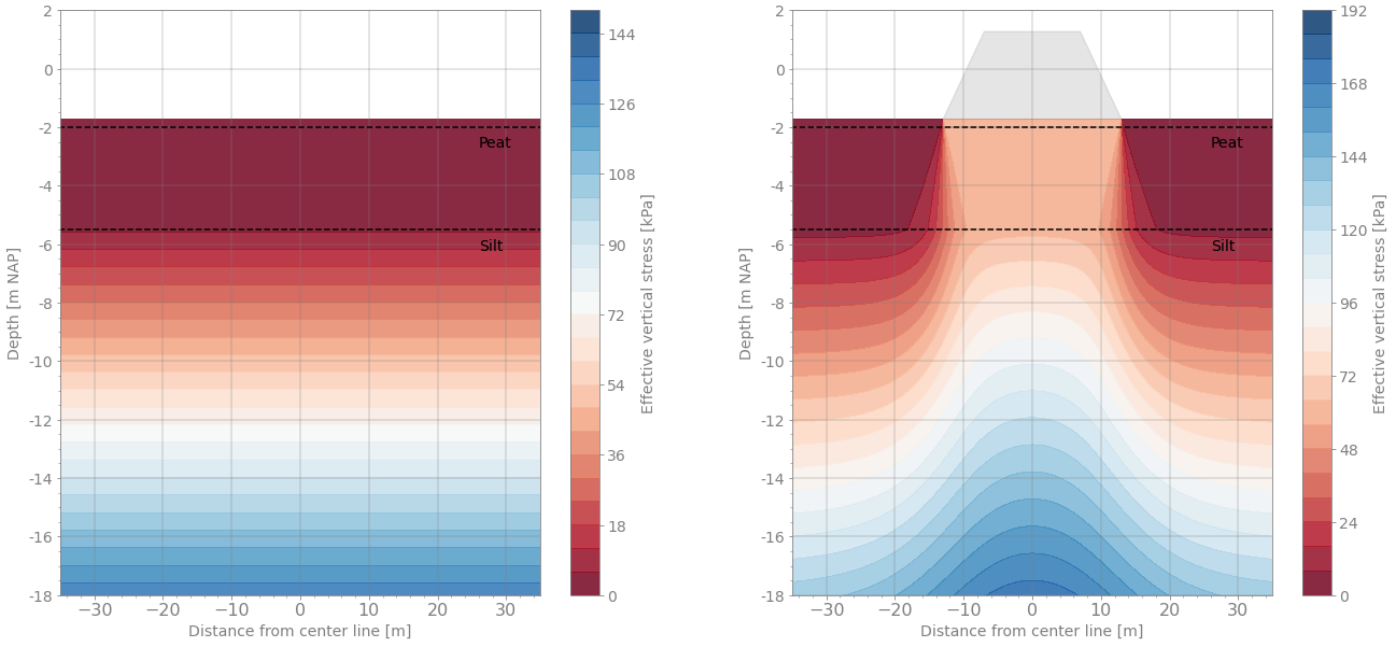

(a) Initial state

(b) After construction

Figure 5.5: Stress distribution of T1 at -5.5 mNAP axis

When evaluating the embankment in both directions at - 18 m NAP, it can be seen that the loading influence is null at 36 meters from the center line of the soil body along the weak axis, while the homologous analysis of the long axis yields a magnitude of 54 meters. Both magnitudes equate to a domain-to-embankment ratio of 3. It is understood these results provide an overestimation, mostly because the plastic deformations that characterize this type of case further constrain the influence extension.

Within a FEM model, it is implicit that the potential deformation of the continuum space is bound to the morphing freedom of the assortment of individual elements. As such, the lack of spatial extension for the mobilization of the furthest elements has a constraining effect on those closer to the embankment. Therefore, an assumed normally fixed

boundary of the domain in which a portion of the mechanism should still occur effectively provides additional competence to the soil body and prevents the full extension of the deformation.

5.3 Stress field

A critical step in the model formulation is the adequate initialization of the stress field previous to the application of any load (Hayashi et al., 2012; Lefebvre et al., 1984; Long, Grimstad, et al., 2022; Long, Paniagua, et al., 2022). Failing to emulate the stress history in the model inherently disregards the actual stiffness of the ground, which arises from the previously attained densification level of the soil. In other words, attaining the same level of settlement between a well-defined stress field and virgin soil would require considerably lower compressibility indices in the latter and would in turn signify that the material is stiffer. Additionally, complementary parameters such as the creep rates, the hydraulic conductivity, and the K_0 have a direct correlation with the over-consolidation.

Biot (1941) remarks on the influence of the stress distribution upon the settlement potential, especially when dealing with materials with a low-grade elastic modulus. The need for this procedure is further aggravated by the fact that using a *gravity loading* initialization in Plaxis 3D disregards any declared value of OCR/POP (Plaxis, 2022b). Therefore, without additional intervention, the over-consolidation magnitude of the field would be 1.0 and the material would be inherently softer.

In the present case, the initial state of the stress field calls for a high level of pre-consolidation at the surface with an exponential decrease with increasing depth (Figure 5.1). Despite the absence of artificial loading throughout the field's history, the laboratory tests displayed a mild over-consolidation across the peat layer, starting from an OCR of 4.5 close to the surface and sharply decreasing towards a value of 2. As previously described in Section 3.1, this can be attributed to the variability in the GWT, aging of the material, and other environmental agents. This phenomenon, regardless of the type of difference in peat material, can also be appreciated in the fields studied by Hayashi et al. (2012) and Long, Grimstad, et al. (2022).

A faithful simulation of this over-consolidation profile requires complex modeling of the environmental interactions with the site and its natural processes. As a consequence, a precise knowledge of said dynamics and considerable computational power is required, which renders this type of approach as unrealistic given the objectives of this study. Hence, to approximate the stress history, the model relies on a series of hydro-mechanical stages that provide a simplified scheme of the OCR distribution (Table 5.5).

In principle, this process relays on the application of a surface load after the initialization of the field based on the volumetric weight of its components. Therefore, before the load is applied the only stress history recorded by the software is that of the overburden. Once the load surface is applied, the stress is distributed following the fundamental formulation for an elastic medium, which describes a progressive decrease of the influence of this load at higher depths. Having incorporated this novel stress distribution using a consolidation analysis, Plaxis 3D needs to re-balance the equilibrium of the field in an elastoplastic analysis. Because of the coupled nature of the intervention, excess pore pressure is generated and hence a final dissipation phase is needed to arrive to a new initial state for the rest of the analysis.

To define the implementation of the above-mentioned procedure an analytical approximation is performed to define the necessary load that best prescribes the field conditions. Once more, by using equation 5.2.1 it is possible to calculate the effect of the surface loading in the domain to reflect the change in effective stress at the varying depth and thus, the over-consolidation ratio at which the model is allowed to start. The use of this formulation implies that the most influential factors are the surface load, the position of the GWT, and the volumetric weight of the strata. However, a fundamental limitation within Plaxis 3D is that a change of material of the volume elements between phases signifies a reset of the state parameters (Plaxis, 2022b). The estimation of the arrangement to initialize the OCR field mainly focused on varying the uniform load, which produced the distribution presented in Figure 5.6.

Table 5.5: Initialization of OCR field in Plaxis model

Phase	Description	Elements	Comments
Initial Time: 1000	Calculation of the initial stresses using an elastoplastic analysis based on the volumetric weight of the soil.	- Total soil volume	- Ignore undrained behaviour
Loading Time: 0.04	Application of a fictitious surface load to the whole extension of the model using a consolidation procedure.	- Uniform load of 9.5 kPa	- Updated mesh - Reset displacements - Reset time - Tolerance: 0.001
Consolidation Time: -	To suppress the effect of the previous loading in terms of excess pore pressure, the model is allowed to undergo a consolidation procedure until a minimum threshold is reached.	- Removal of 9.5 kPa surface load	- Updated mesh - Reset displacements - Reset time - Tolerance: 0.001
Plastic nil-phase Time: 7.28	Elasto-plastic analysis to resolve out-of-balance forces and ensure equilibrium.	-	- Updated mesh - Reset displacements - Reset time - Tolerance: 0.001

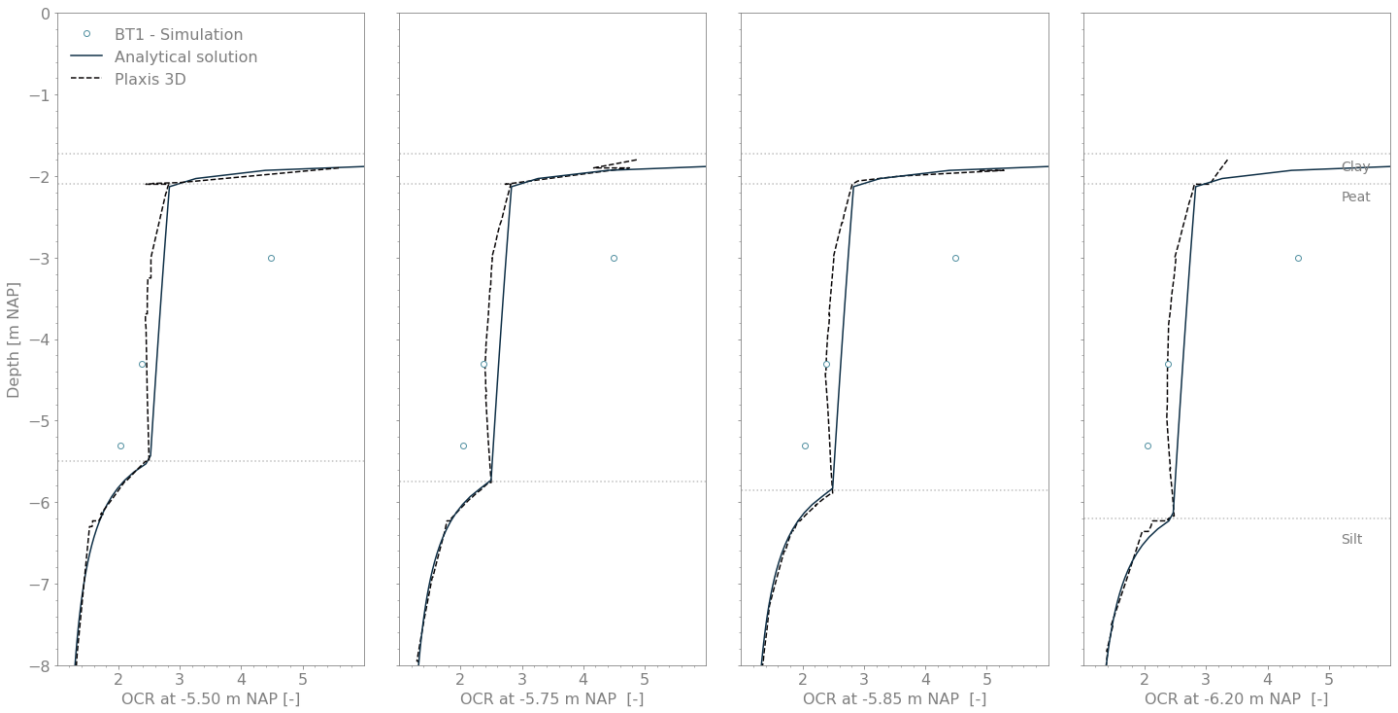

Figure 5.6: Replication of OCR field for T1

The procedure yields an adequate approximation of the bottom half of the peat layer and effectively replicates the mild over-consolidation of the clay layer. Nonetheless, the OCR at the most superficial portion of the peat is underestimated as much as 72 % closer to the clay horizon. Although the resulting monotonic emulation of the OCR field is fundamentally flawed, it already provides an improvement to declaring a constant magnitude of pre-consolidation.

5.4 Pore pressure distribution

To establish the depth of the piezometric surface, the analysis utilized the initial measurement of the water pressure to define a baseline. Because these recorded magnitudes vary in time, a basic statistical analysis was executed to identify a water level of - 1.99 m NAP that would better describe all devices. Nonetheless, to better fit the results of embankment no. 1 a value of - 2.10 m NAP was selected as this value fit had a better fit to points on the west and east side of the embankment, with only two measurements (WSM-T1-7B and WSM-T1-8C) not being confidently described by it.

The recorded measurements of the hydrostatic conditions of the field started approximately 1 week previous to the first intervention of the field. This lapse previous to construction is relatively short to define a representative value. Considering no relevant data from the national registry for water levels in the surrounding 100 meters, these measurements are the only valid reference.

From the measurements displayed in the picture below it is clear that a linear hydrostatic distribution assuming a volumetric weight of water 10 kN/m^3 and starting at - 2.10 m NAP is a representative fit for all, as no abrupt changes can be perceived in base level. However, the values providing the largest increase in the working range of this function (WSM-T1-7B and WSM-T1-10) are found at the center of the peat layer. This could suggest a curved tendency influenced by the variability in water content and subsequent decrease as it approaches the more permeable silt.

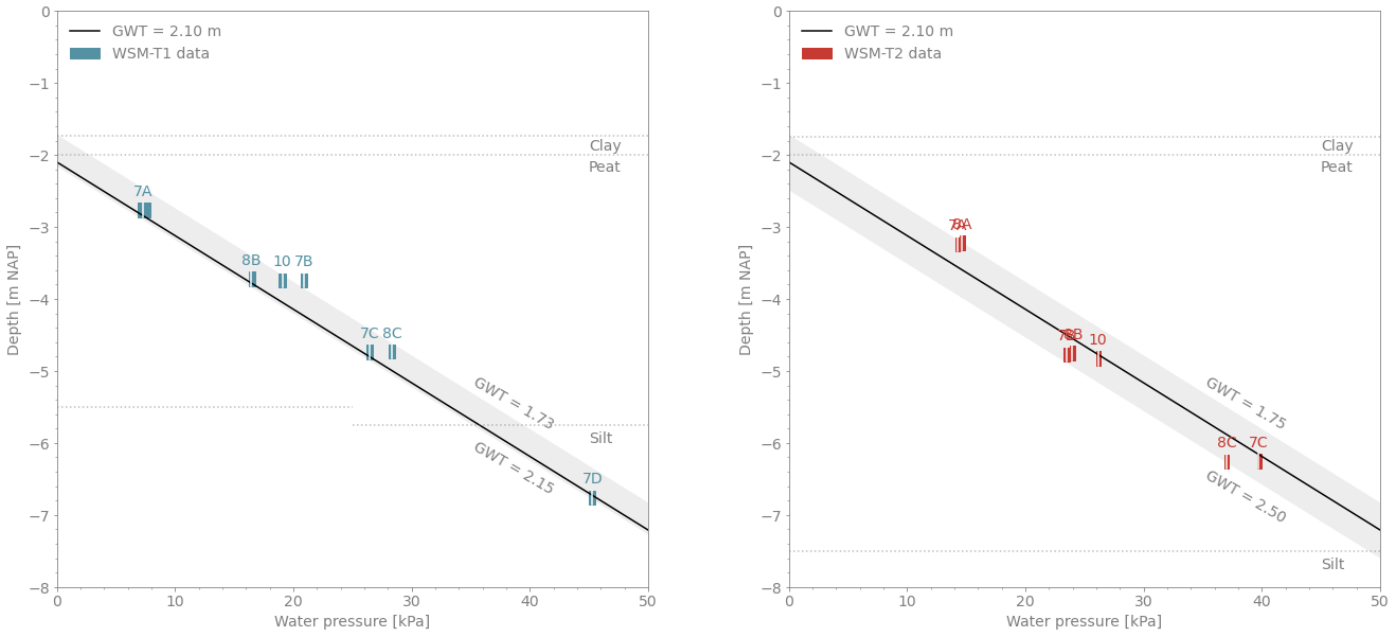

(a) Embankment No.1

(b) Embankment No.2

Figure 5.7: Hydrostatic conditions previous to embankment construction

For the present analysis, a single hydrostatic level is considered at the foregoing depth of - 2.10 m NAP, which remains constant throughout the analysis. The evident interactions in the long-term with the rainfall events are completely disregarded despite their influence in the water pressures.

5.5 Mesh

The mesh generation procedure favored an increased precision at 1.5 times the embankment footprint, with even further precision at the elements surrounding the piles and inclinometers. With this objective, auxiliary line and volume elements were introduced to the model to favor an adequate distribution. Although some geometric variations to the FEM model were introduced, the procedure hereby presented was employed indistinctively.

The process followed the automatic distribution of coarse elements, with a minimum element size factor of 5.0 E^{-3}. This was done to ensure a well-balanced element size throughout the mesh and compensate for the large ratio between the thickness of the volume elements (e.g. embankment's loading steps) and the size of the domain.

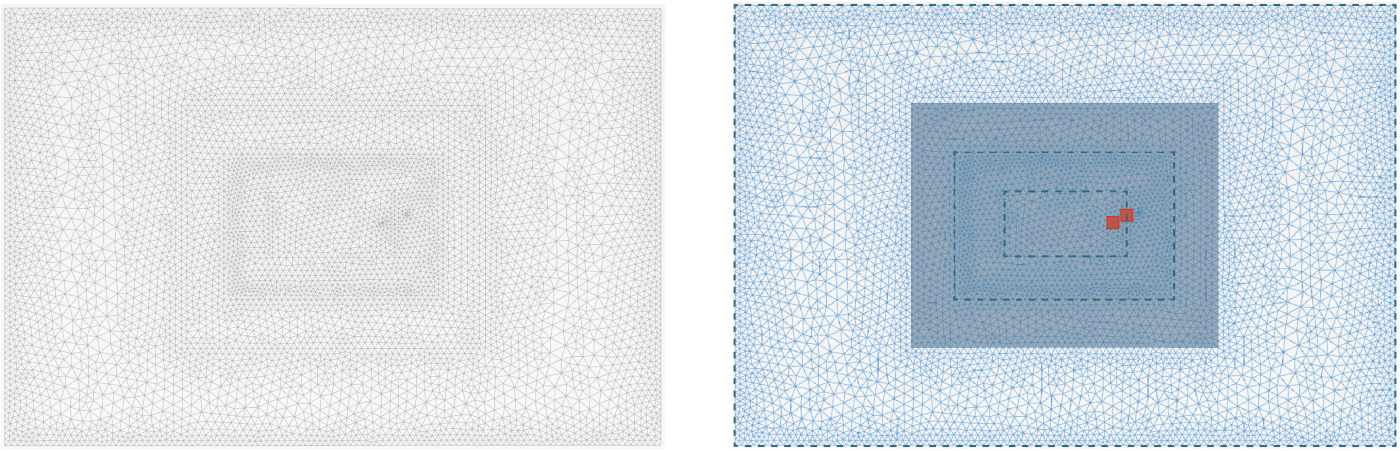

(a) Mesh arrangement

(b) Volume elements guiding meshing procedure

Figure 5.8: Plane view of the meshing arrangement

The refinement of the mesh can be further improved by means of volume elements, which provide localized geometric guidelines to the meshing process. They are created within the medium to provide a higher level of control in the portion of the model that can become coarser than the average mesh element. These elements are auxiliary to the model components and do not possess foreign properties that could introduce inconsistencies to the overall behaviour. It is of relevance in improving the precision of the mesh without inquiring into a drastic increase in computational time.

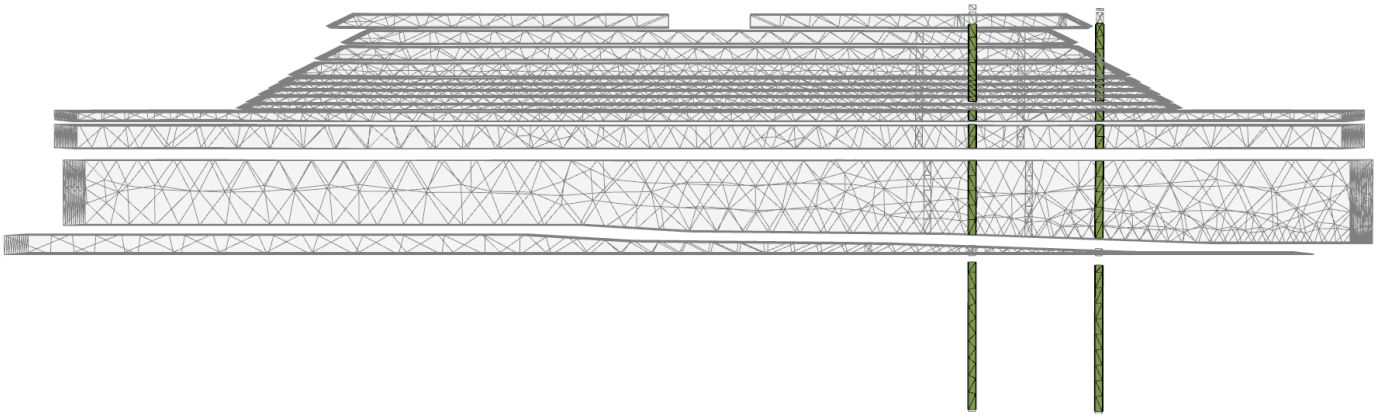

Figure 5.9: Mesh distribution of volume elements

It is relevant to mention that for the FEM model to replicate an equivalent response to that of a large-strain analysis, the previously described mesh has to be restarted between phases by means of an updated Lagrangian analysis. Considering that a small strain approach is not able to match the large deformations perceived in this case, the definition of the engineering strain (based on an original unaltered geometry) is no longer valid, and thus, the strain has to be reformulated as a function of the newly attained deformation of the volume it represents. Due to the increased complexity to account for this effect, the FEM model is instead calculated with a small-strain formulation, in a mesh that updates to a new "initial state" in every phase (Brinkgreve, 1994).

The use of an updated Lagrangian analysis appears to be indispensable for the correct estimation of the settlement. The work of Schadee, 2012; Siderius, 2011 and Papadaki (2013) on the Bloemendalerpolder, as well as similar studies such as Long, Paniagua, et al. (2022) and Long, Grimstad, et al. (2022), stress the advantage of this tool to correctly estimate the high degree of compressibility.

5.6 Phasing

The construction details of the site relative to the temporal and spatial changes at the site are replicated in the model following the reported information of Ammerlaan (2011) and Hoefsloot (2015). However, the specific input of days is corroborated by the response of the most superficial measurements of the excess pore pressure. There is leeway for

criticism in this assumption, as it has been reported that the water pressure can present delays in their response after loading (Long, Paniagua, et al., 2022). This is not considered relevant in this case as the recorded dates were congruent with the measured responses and therefore, they are allowed to be employed as further insight into the embankment's interventions.

Table 5.6: Phasing of Plaxis model

Phase		Time [days]		Embankment height [m]	
		Interval	Cumulative	Step	Total
1.1.1	Loading	0.04	7.32	0.20	0.20
1.1.2	Relaxation	0.61	7.93	-	0.20
1.2.1	Loading	0.09	8.02	0.25	0.45
1.2.2	Relaxation	1.13	9.15	-	0.45
1.3.1	Loading	0.11	9.26	0.08	0.53
1.3.2	Relaxation	0.69	9.95	-	0.53
1.4.1	Loading	0.06	10.01	0.47	1.00
1.4.2	Relaxation	0.04	10.05	-	1.00
1.5.1	Loading	0.04	10.09	0.47	1.00
1.5.2	Relaxation	25.04	35.13	-	1.00
2.1.1	Loading	0.16	35.29	0.50	1.50
2.1.2	Relaxation	21.74	57.00	-	1.50
3.1.1	Loading	0.19	57.19	0.50	2.00
3.1.2	Relaxation	41.81	99.00	-	2.00
4.1.1	Loading	0.25	99.25	0.50	2.50
4.1.2	Relaxation	22.70	121.95	-	2.50
5.1.1	Loading	0.31	122.26	0.50	3.00
5.1.2	Relaxation	20.80	143.06	-	3.00
6.1.1	Pile installation	0.20	143.26	-	3.00
6.1.2	Relaxation	278.00	421.26	-	3.00
7.1.1	Unloading	6.00	327.26	-0.50	2.50
7.1.2	Relaxation	122.74	550.00	-	2.50

6 | Behavioural aspects of the embankment

Previous to the analysis of the deviatoric behaviour and the soil-structure interaction of the mound no. 1 of the Bloemendalerpolder case, the overall response of the soil body has to be emulated. As a hydro-mechanical process, ensuring a proper representation of the embankment requires a faithful usage of hydraulic and mechanical variables that can simultaneously reproduce the deformation and excess pore pressure recorded during the test. The present chapter deals with this objective in a systematic progression, by increasing the complexity of a three-dimensional FEM model to account for all the factors related to the embankment in a somewhat individual manner.

The first approach of this endeavor is the simulation of a simplified geometry, where only the stratigraphy is replicated. In this level of complexity, the model migrates to a more intricate layer arrangement than that of the K_0-CRS test, while still preserving the unidirectional response of the deformation and flow perceived in these experiments. Later on, a half-mound is assembled to incorporate the horizontal component of flow and the reduced stiffness of the field as the stress distribution is no longer constrained by a normally fixed boundary to guide the settlement. It's in this stage, where no additional components (i.e. inclinometers and piles) are implemented, that the first indication of the deviatoric behaviour can be analyzed. Finally, as the full model is built to integrate the non-symmetric auxiliary components, the extent of the model capabilities can be assessed.

The procedure mainly follows the response of the SS model, which is later compared to the estimations made by the JMC model. This decision follows the practical need of employing a model that can run fast and without instabilities so that implementation constraints can be more easily identified. Considering the soft soil model as the premier model in Plaxis 3D, it can be assumed that the coding efficiency has been thoroughly tested and is not bound by the coding limitation of a user-defined model such as JMC. Therefore, following the solution of these errors, a realistic comparison with JMC can be performed. The NGI-ADP model, on the other hand, was not incorporated in the progressive build of the FEM model, as the advantages of its usage are only preponderant in the soil structure interaction.

The results on settlement and excess pore pressure hereby presented are color-coded based on their position relative to the surface and to the weak axis of the embankment. The WSM-T1-7 (West side) measurements are displayed in blue, while their eastern counterparts are shown in red. Additionally, the depth variation is shown based on the monochromatic transition of these two colors from dark to lighter, with the most superficial measurements in darker colors.

6.1 Simplified geometry

Having proved that a volume cluster using the JMC model can consistently provide adequate results of strain and stress in an elastoplastic analysis (Appendix A), the analysis now follows a basic implementation of the Bloemendalerpolder field. The aim of the simplified geometry is to corroborate the stability of the JMC model when dealing with a multi-layered system and intersecting volumes, while also comparing the possible divergence from the estimation of the SS model during one-dimensional loading.

The response of this model is comparable to the inner sections of the embankment (e.g. locations T1-7 and T1-8), as their behaviour could be approximated by this one-dimensional approach. Therefore, the only results compared at this stage are the settlements measured by the extensometers (*E-T1-7* and *E-T1-8*) and the piezometers (*WSM-T1-7* and *WSM-T1-8*) at their corresponding depth. Regarding the latter, instead of the real scattered location of the WSM devices in the embankment, their positioning is made concentric to the domain, which limits the comparison with the recorded data.

To construct this model, the stratigraphy and geometry of the western (T1-7) and eastern (T1-8) sections of the embankment are simplified to an equidistant layering over-topped by volume elements of sand material representing the construction steps of the embankment (Figure 6.1). These elements are also intersected at their geometric center by a rectangular prism simulating the piles. The model is complemented by the inclusion of interface surfaces at the sides of

the pile, as they enable a differential response between volume clusters. Although the introduction of these additional elements is not comparable to the measurements of the inclinometers, it provides an indication of the stability of the model to work with more advanced Plaxis tools.

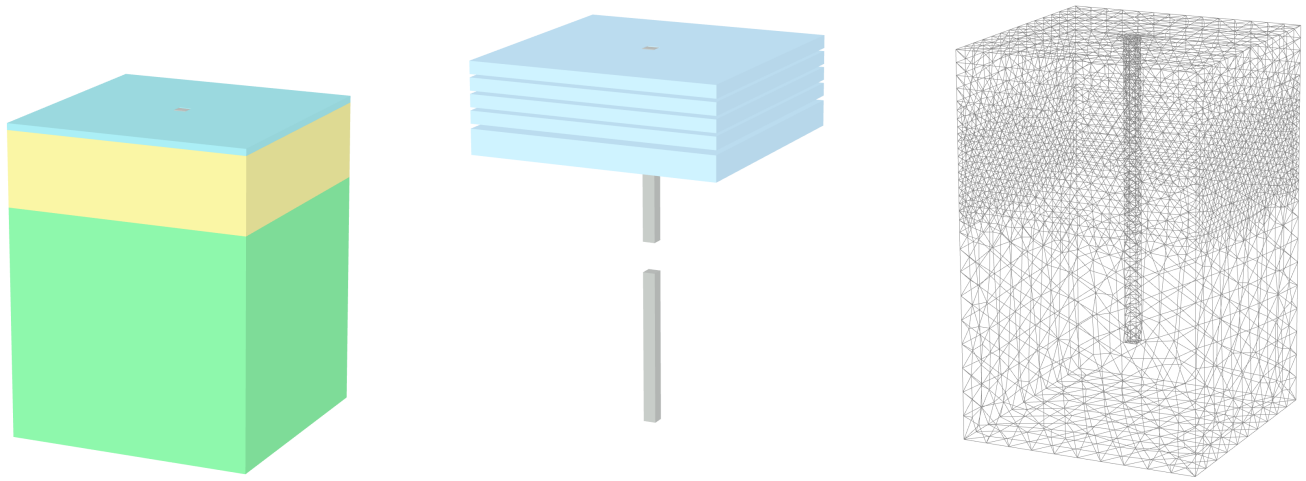

(a) Model stratification (b) Complementary elements (c) Mesh arrangement

Figure 6.1: Assembly of simplified geometry in the three-dimensional space

6.1.1 Settlement

In one-directional compression the models do not differ from each other. This response was consistent with the laboratory simulations of the K_0-CRS, where it was concluded that the preponderant distinction between these models in one-dimensional loading was the initial response. In the Bloemendalerpolder experiment, the change in stress state from the first loading step was close to that of the highest value of POP, thus it appears that the effects of the foregoing difference are suppressed when simulating the loading process. As a consequence, the nearly identical virgin compression line from both models is given protagonism and yields an equal settlement response.

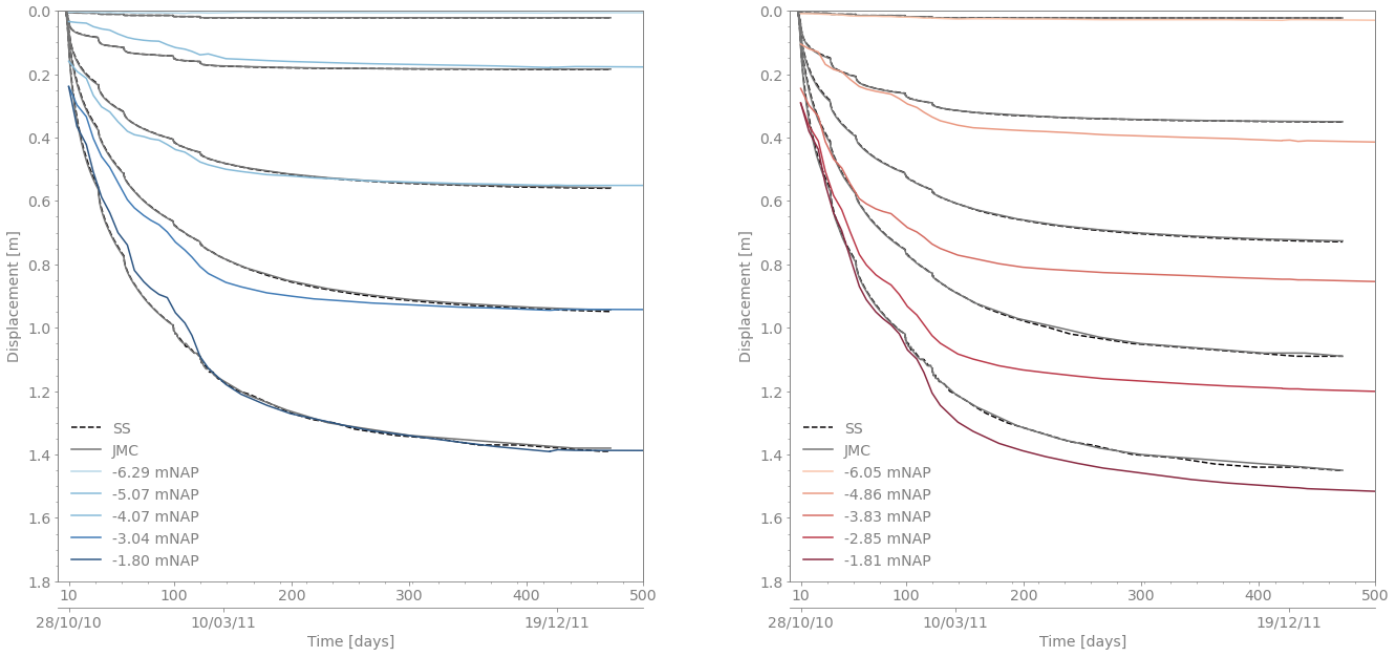

(a) E-T1-7 (West side) (b) E-T1-8 (East side)

Figure 6.2: Estimation of settlement with simplified geometry

The calibrated value of the modified compression index for the SS and JMC model uniformly overestimated the settle-

ments. Therefore, an independent curve-fitting procedure led to the reduction of this magnitude by 20 %. Such variation was also evident in the one-dimensional evaluation of the field by Fugro, as their forecast with the compressive parameters (i.e. CR, b) from the laboratory under-predicted the site response (Hoefsloot and Schadee, 2014). This tendency is to be expected when translating from a controlled setting to the field, as it is common for the site to show higher stiffness and hydraulic conductivity (C. Jommi, personal communication).

It can be appreciated that the deepest measurement of the extensometers is located either in the silty-sand horizon or completely embedded in it as the extent of the vertical displacement is almost null, which is evidence of the stiffer nature of the deeper layers. On the western side, *E-T1-7-2* (-6.29 m NAP) has a negligible difference throughout the test, while the eastern side *E-T1-8-2* (-6.09 m NAP) is able to visualize a bit of the compressible peat layer. This suggests that the only material compressing is the peat and the clay close to the surface, and the deeper horizons can be disregarded. Moreover, given these results, it is evident that the positioning of the soil horizon is relatively adequate, and thus, upholds the consideration that the underlying material is solely a stiff boundary that allows drainage.

Considering that the west and east simplified models employed the same material set with an increased thickness of the peat as the only distinction, it is considered that at this stage the estimated geometry is not representative of the real case. However, as stated by Hayashi et al. (2012), the practical estimates in peat ground have a tendency to vary by 0.1 meters from the actual deformation, which would account for the difference between sides of the embankment. It is expected that with a higher degree of complexity in the model, and more importantly the varying depth of the silt layer, this difference might be diluted.

6.1.2 Hydraulic conditions

In this step, the hydraulic properties of the field system were further adjusted based on the embankment's settlement, as per the recommendation of Tavenas et al. (1986), Chai and Miura (1999). The authors mention that when no permeability field tests are executed the most suitable approach to define the hydraulic conductivity is the back analysis of this property. With this aim, the following graphs show the result of an iterative procedure to define a representative conductivity of the compound system.

The refining procedure of the hydraulic conductivity focused on the magnitudes required by the silt and clay layers, as the vertical permeability of the peat had been defined based on the values of the K_0-CRS (Appendix A). The first step was the definition of the silt layer, given its role as a drainage mechanism and the possibility of comparing its response to *WSM-T1-7D*. This decision follows the preconception that the device is completely embedded into this layer. By defining the over-pressure magnitudes at this output and having defined the distribution of the c_k and k_v parameters for the peat (Figure 5.1), the clay layer was then adjusted so that the intermediate measurements of peat were not skewed.

The calculated pore pressure response was recovered at the corresponding position of the piezometers, but two devices were manually modified to fit the measurements. As it was previously described in Section 5.4, the initial hydrostatic pressure of three devices within the peat layer does not fit the assumed hydrostatic distribution based on the piezometric level at -2.1 m NAP. Therefore, the estimations of the model have an inherent divergence of 1.5 kPa in the case of *WSM-T1-8C* and 4.5 kPa for *WSM-T1-7B*. By assuming that the deviation shown by these piezometers can be disregarded, the present project compensates for the foregoing difference by manually increasing the base level of the estimations. The only advantage of this modification is the better visualization of the excess pore pressure at varying depths.

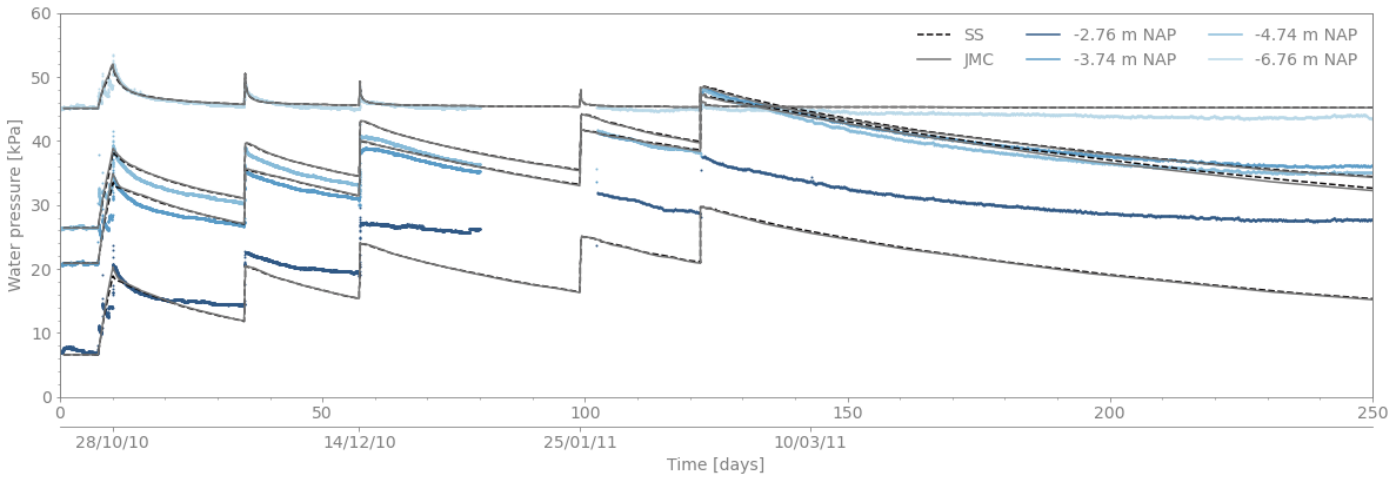

(a) WSM-T1-7 (West side)

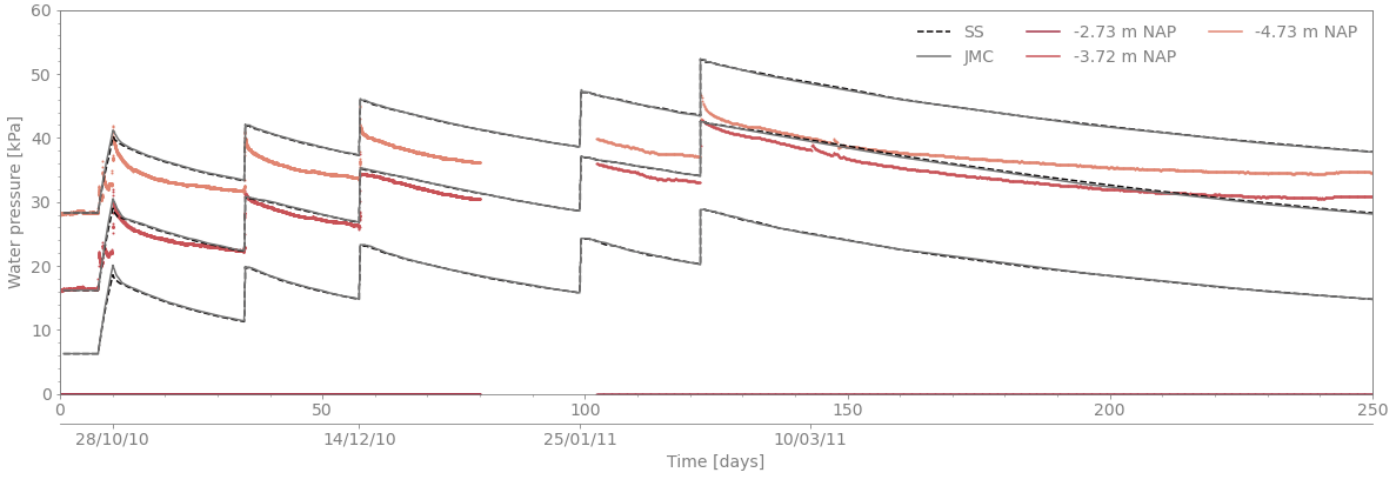

(b) WSM-T1-8 (East side)

Figure 6.3: Estimation of pore pressure with simplified geometry

From this procedure, it was proved that the average estimation for c_k of 2.7 and the isotropic hydraulic conductivity of 0.065 m/d (7.5 E^{-7} m/s) of peat is valid even as the model goes into a more complex arrangement. Nonetheless, it was clear that this unique set cannot faithfully represent the field with the proposed initial stress distribution and semi-logarithmic law. The first indication is the higher dissipation rate throughout the field, which produces inconsistencies in the long term. Moreover, based on the results shown by *WSM-T1-7A*, the proposed magnitudes of permeability are insufficient to attain the same excess pore pressure closer to the surface, which is believed to be affected by the mild over-consolidation at this depth.

This section also sheds some light on the actual silty nature of the underlying horizon, which had been originally considered as a sand material by previous authors (Hoefsloot, 2015; Schadee, 2012; Siderius, 2011). The relatively low q_c values (roughly 4 MPa) and proposed magnitudes of stiffness at the theoretical lower bound of the sand, where now complemented by an estimated hydraulic conductivity of 0.5 m/d (5.8 E^{-6} m/s), to suggest that the sand designation was not representative. It is believed that the sandy character of the soil is minimal and the silt portion defines the material's behaviour.

In terms of the variation in the models, the distinction between them is practically absent in the excess pore pressure, with only the immediate dissipation after loading slightly varying. This can already be attributed to a similar behaviour displayed by the K_0-CRS simulations, which showed that under the same conditions, the numerical approximation of the JMC model will drop at a slightly higher rate.

6.2 Half-mound model

As a higher degree of complexity, this model is extended to include the field characteristics, by replicating its geometry and extending the domain as described in Section 5.2. The objective of this model is to recognize the influence of the lateral effects that the embankment placement has solely on the ground. Nevertheless, as the piles are unnecessary at this stage and the implementation of the full extent of the case is computationally intensive special considerations are made: the geometry is divided along the weak axis and no auxiliary elements are installed. To ensure that this model is representative, a closed hydraulic boundary is included at the point of division so that the geometry can be assumed as mirrored. This consideration reduces the number of elements in the FEM model by half and the computational time by one-third.

The model employed in this section introduces the necessary extent of the domain along with the vertical variability of the peat layer as described in Section 5.2. The geometry of the embankment is divided as depicted in Figure 6.4. Additionally, to the comparison made with the excess pore pressure and the settlement measured by the extensometers in the previous model, the results can now be also compared with the inclinometers. Because of the three-dimensional variation, it is expected that some of the limitations shown by the simplified geometry in terms of attained deformations and pore pressures will be faced out.

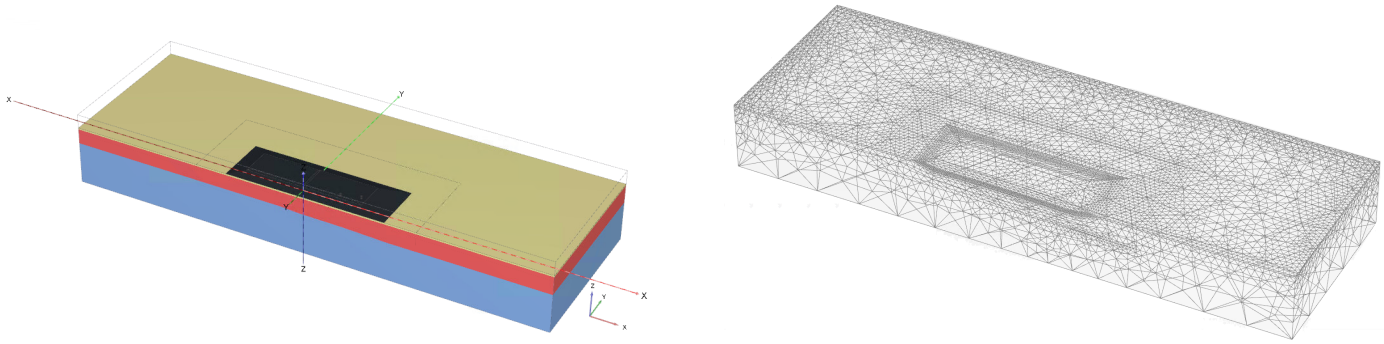

(a) Model stratification (b) Mesh arrangement

Figure 6.4: Assembly of the half-mound model in the three-dimensional space

6.2.1 Settlement

When visualizing the resultant displacement of the embankment at the weak axis (Figure 6.5), it can be appreciated that the high compressibility of the peat material localizes the settlement below the footprint of the embankment. The western side displays higher deformations as a result of the deeper level where the silt horizon is located and forces the soil body to tilt in this direction.

Different from the simplified geometry, curve fitting was not necessary to improve on the initial laboratory estimation of the modified compressive index (λ^*), neither for the SS nor the JMC model. Although some adjustments can be made to find an average value that improves the description of the excess pore pressure, the variables provided by the independent simulation of the K_0-CRS tests yield an acceptable result. Considering this fact, it can be assumed that the need of pruning the stiffness variables is predominately linked to the lack of representation of a 1D calculation.

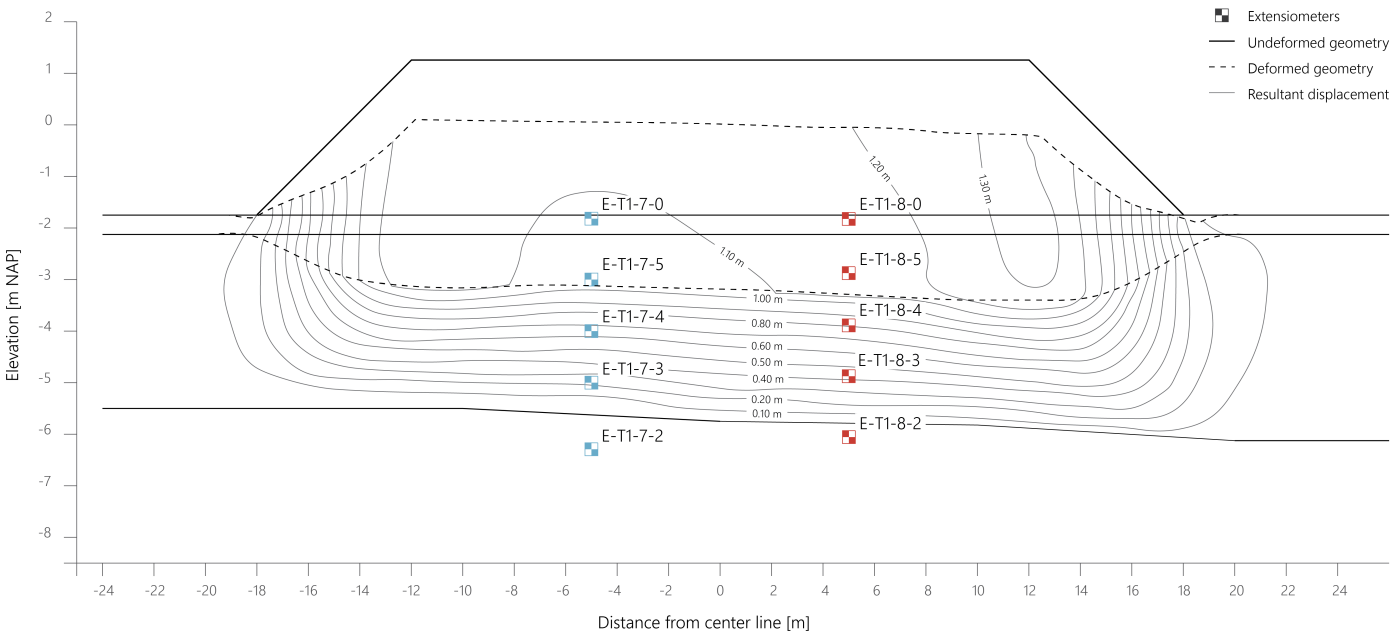

Figure 6.5: Resultant displacements of T1 after final rise of embankment (phase 5.1.1)[1]

When comparing the abovementioned behaviour with the measured deformation of the extensometers in Figure 6.6, it can be said that the divergence displayed by the simplified geometry at the eastern side is partially reduced. However, with good replicability of *E-T1-7* and the deeper levels of *E-T1-8*, the lack of representation of the eastern side remains.

Given that the geometry is built with conditionants from the pre-and postdiction (i.e., CPT and ZMS measurements), it is assumed that altering this proposed geometry would cause inconsistencies in the representation of the field. Thus, if the stratigraphy is considered to be correct, the discrepancy between the eastern and western sections of the mound can be attributed to variations in the characteristic material of each side.

[1]The deformed geometry is based on the simulation of the half-mound geometry with the SS model. The scaling vertical-to-horizontal ratio is 2:1.

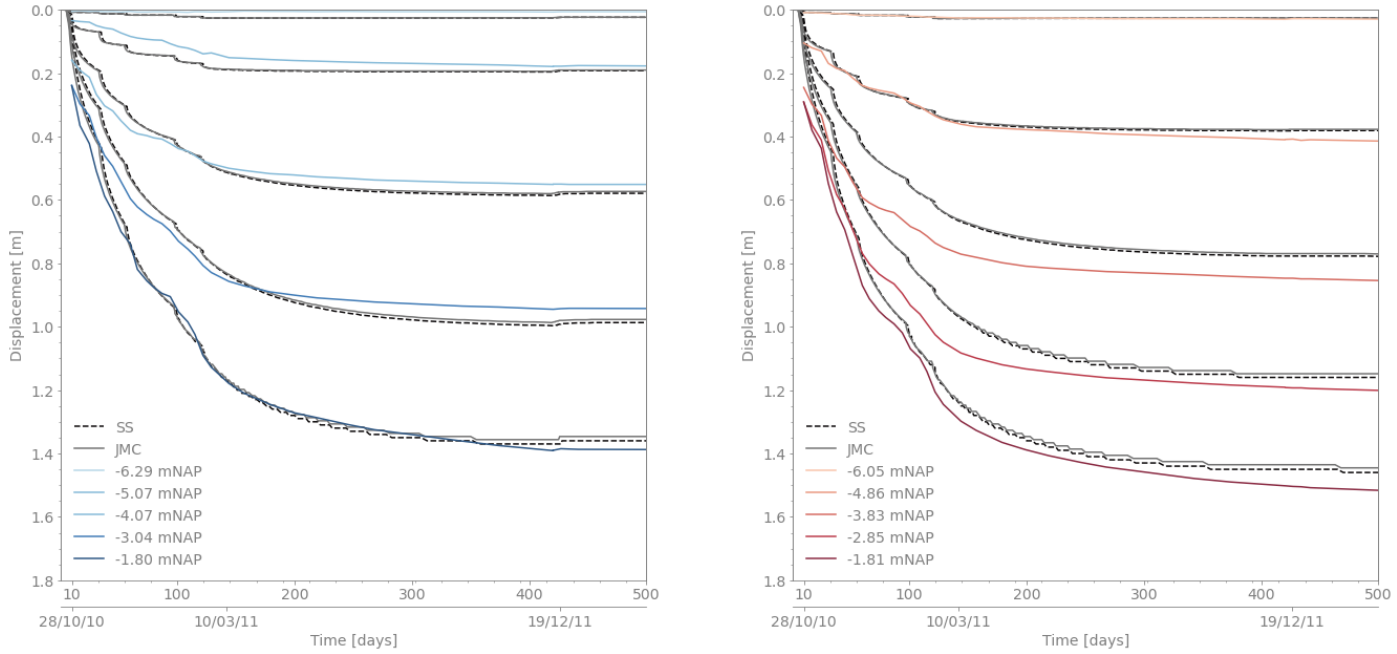

(a) E-T1-7 (West side)

(b) E-T1-8 (East side)

Figure 6.6: Estimation of settlement at various depths of the half-mound model

Despite the perceived improvement shown in Figure 6.6 in the final deformation at the various layers, the occurrence of the settlement still shows a temporal deficiency, which is especially evident in the inner portion of the peat layer. However, more than a shortcoming of the mechanical behaviour, is a critique of the pore pressure dissipation. It is assumed that the compression at these depths was not accompanied by the characteristic evolution in void ratio, which in turn allowed for a faster dissipation rate.

6.2.2 Hydraulic conditions

As depicted in Figure 6.7, the excess pore pressures generated during the simulation are characteristic of a double drainage field, with the highest values concentrated at the center of the embankment. This behaviour is consistent with the response of the intermediate measurements (*WAT-T1-7B* and *WAT-T1-8B*), which show the lowest dissipation rate.

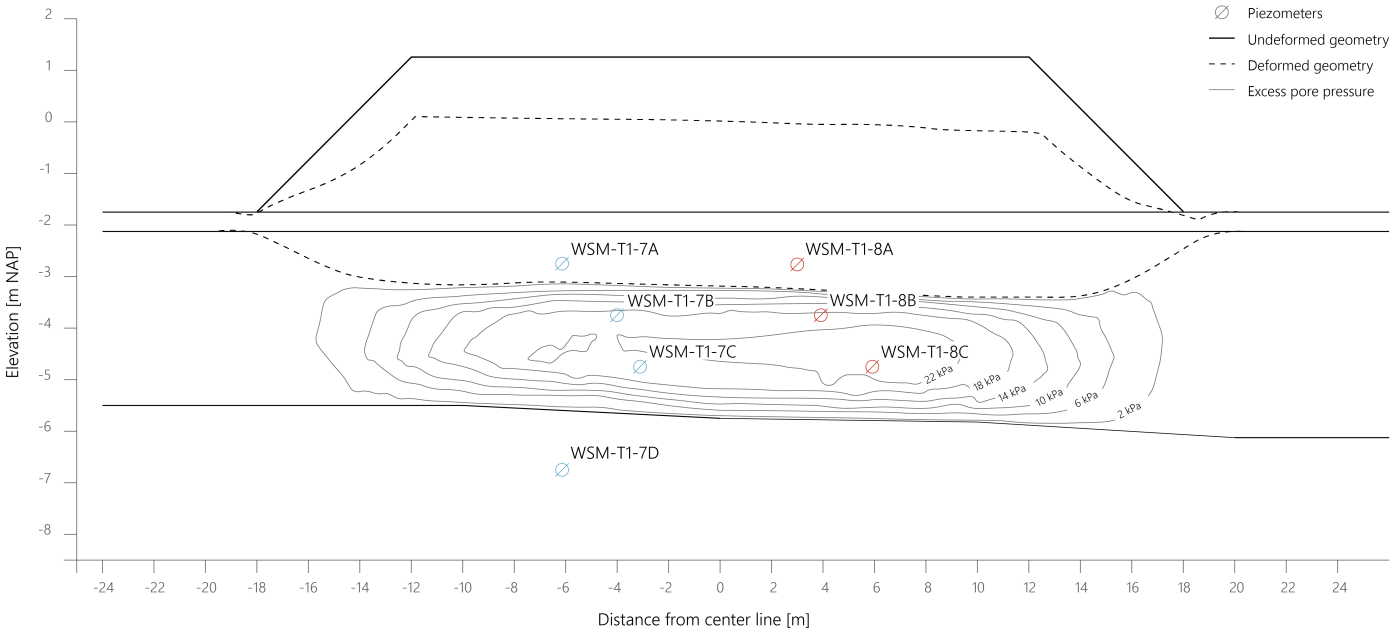

Figure 6.7: Visualization of excess pore pressure after raising the last level of the embankment (Phase 5.1.1)

The comparison of the excess pore pressure as a function of time between the recorded data (*WAT-T1-7* and *WAT-T1-8*) and the simulation of the JMC and SS models are displayed in Figure 6.8. Additional to the three-dimensional variation from the simplified geometry, this model also incorporates the segmented construction of the first raise of the embankment (described in Section 5.2.2) and the removal of the half-mound after a year after construction. Moreover, the conditions for the visualization of the excess pore pressure described in the simplified geometry hold true in this case as well.

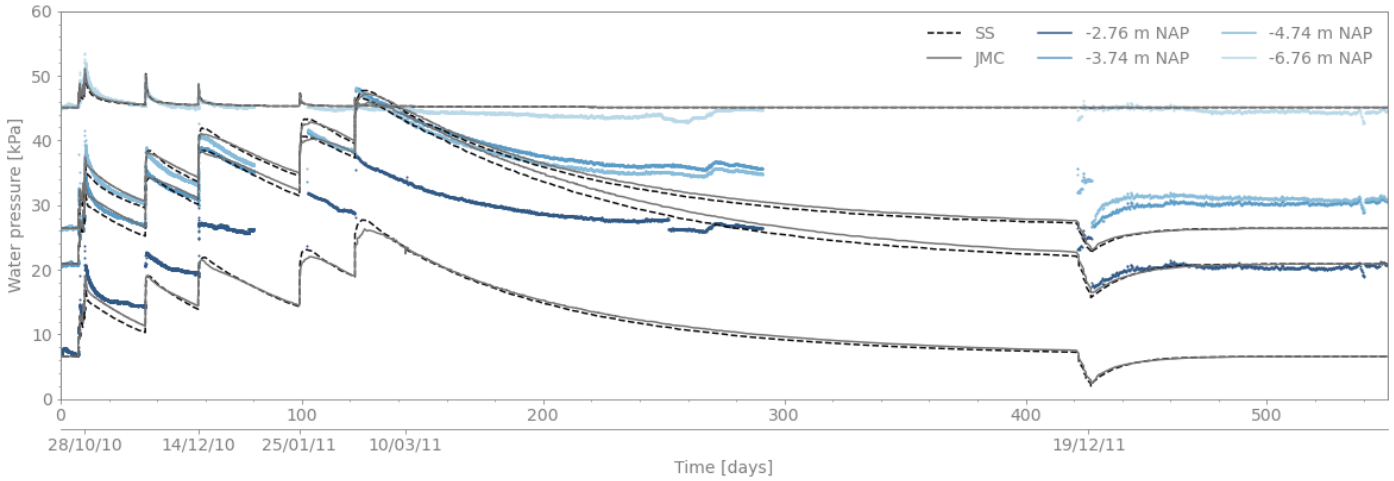

(a) WSM-T1-7 (West side)

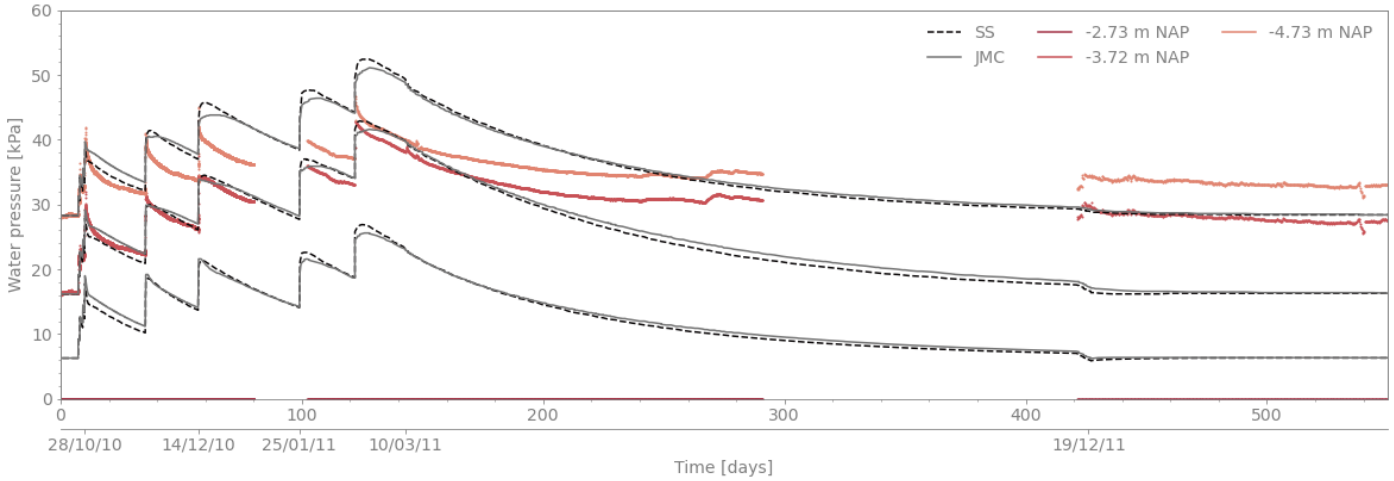

(b) WSM-T1-8 (East side)

Figure 6.8: Estimation of pore pressure with the half-mound model of embankment no. 1

Once again, the intermediate and lower levels of the embankment are faithfully replicated, while the most superficial measurement is underestimated. This behaviour is consistent with the parameter distribution shown in Figure (5.1), where these portions of the peat layer clearly displayed a similar composition, while the upper, more highly consolidated peat diverges. Consequentially, it is considered that a better estimation of the hydraulic conductivity profile would improve this response.

From the abovementioned results, it can also be appreciated that although the first 150 days of the test are replicated effectively, there is a more abrupt drop in the pore pressures in the long term. This behaviour can be linked to the limitations of Taylor's formulation to emulate the evolution of hydraulic conductivity in peat. As it was seen in the K_0-CRS simulations, this tool was insufficient to replicate the pressure after considerable deformation, which now is translated into an inadequate estimation of the change in the void ratio of the field. Therefore, it can be concluded that a logarithmic rule is fundamental for the assessment of the permeability of the peat.

6.2.3 Lateral displacement

Figure 6.9 shows the resulting deformation of the field along a 0.5-meter offset from the weak axis, while also comparing it with the measured values of the inclinometers (HT-T1-1 to HT-T1-4). A strong correlation can be seen between the portions of higher deformation and the inflection points of the measuring apparatus As it can be appreciated, the further away a device is located from the center line, the higher the lateral deformation of the field and the inclinometers. It is not until the HT-T1-4 measurement that this behaviour changes, given that this element does not perceive an imposition from the embankment. Additionally, the field shows a consistent increased deformation on the eastern side and the previously seen tilt in this same direction.

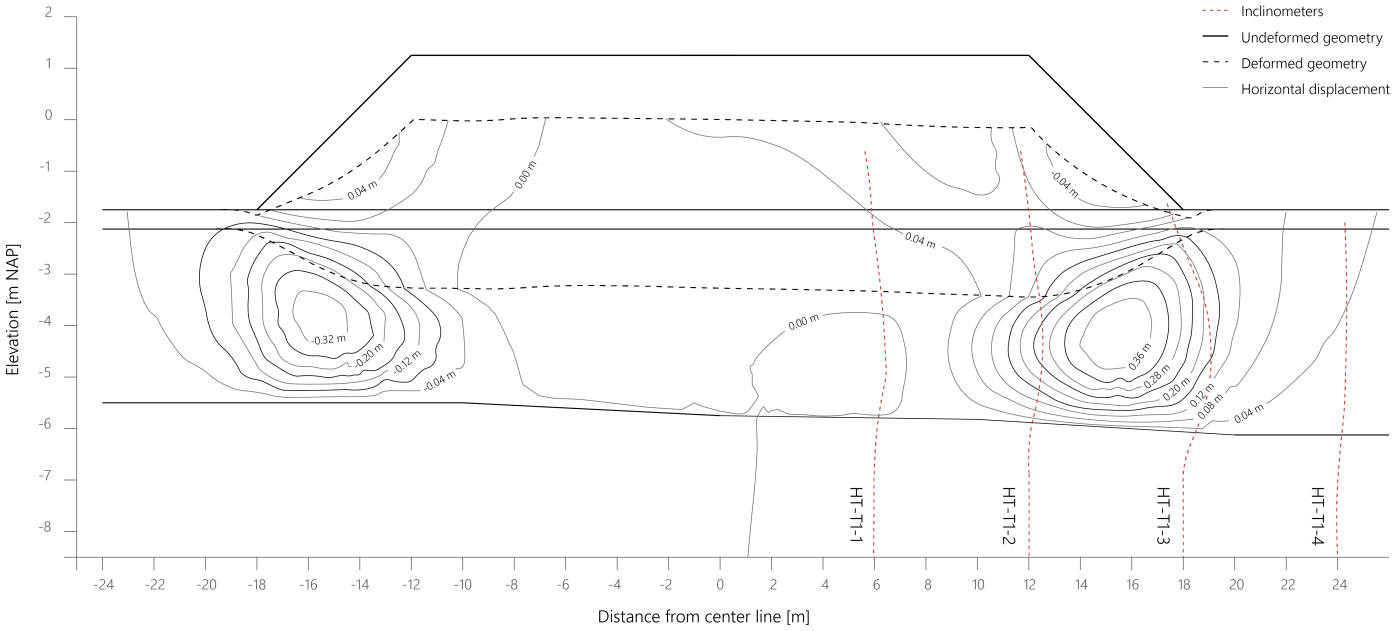

Figure 6.9: Horizontal displacements of T1 after embankment construction[2]

When comparing these values with the individual measurements through time in Figure 6.10, it can be appreciated that although both the JMC and the SS model approximate the behaviour of the lateral displacements, both overestimate the deformation. This effect is specifically located outside the embankment, where the estimations made by the JMC model are up 3 times larger than the measured ones, while the soft soil model is closer in magnitude. Contrastingly, a better fit can be perceived at the inside of the mound's footprint, where the deviatoric behaviour is not as relevant.

The pseudo advantage of the SS model over the JMC in terms of lateral deformation appears to be a reflection of the shortcomings of the model when evaluating the deviatoric stress. This is assumed based on the perceived response during the characterization process, where the SS consistently provided an underestimation of the attained stress level (Section 4.4). Thus, when the case is evaluated with the SS model, the highly conservative yield surface appears to produce lower lateral stresses for the same change in vertical stress, and thus the required stress level is decreased.

Although the geometry of deformation is relatively similar, there is a clear discrepancy at the upper and lower boundaries of the peat layer, which is considered to be linked to the influence of the measuring device. As reported by Alink (2010), the measurement of the inclinometers occurs in a PVC tube that was fixed to the ground by means of a cement-bentonite slurry, which in turn filled a 6 in borehole. It is evident, that despite having a relatively low difference in mechanical properties to that of the surrounding soil, the presence of these foreign agents also guided the measured response. Evidence of these inconsistencies can be found in the experiments by Chai and Miura (1999), where the inclinometers' casings also skewed the measured lateral response close to the surface.

Evidence of this can be appreciated at the silt horizon, where the measurement still shows horizontal displacements even a meter below the peat layer. This should not be the case as it has been confirmed that the silt material is considerably more stiff and no deformation should be appreciated. It is considered that said response is proper of a pile element, as the stiffer cement-bentonite forces the silty layer to also deform as a secondary effect from the deformation above. The effects of the installation system can also be seen at the highest segments of the inclinometers, where considerable negative displacement suggests that the continuous PVC element also deformed in the opposite direction.

[2]The deformed geometry is based on the simulation using the half-mound geometry and the SS model, with a scaling vertical-to-horizontal ratio of 2:1. The superimposed deformation of the inclinometers is that of the final measured values of HT-T1-1,2,3,4 recovered during the experiment.

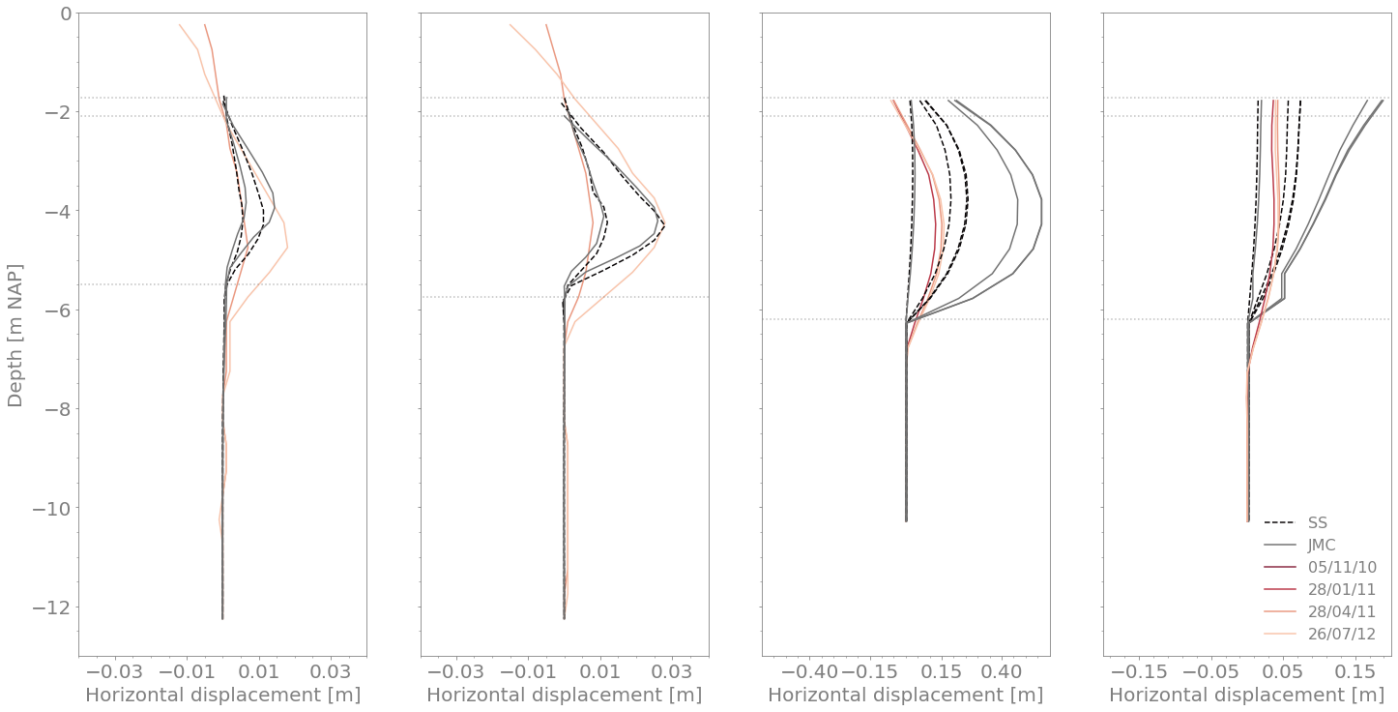

Figure 6.10: Progression of the horizontal displacements at T1

6.3 Full model

After independently defining the behaviour of the embankment, the aim of this full integration is to produce a stable model in which the evaluation of the deviatoric behaviour can be reliably executed. The proven parameters shown in the half-mound model are preserved, but now the full field is included and the stratigraphy is slightly changed. Additionally, the model also introduces the pile elements to represent the steel piles and the cement-bentonite-PVC column. As shown in the figure below, this variation can be seen in the extension of the domain and the pile elements which are now displayed in the mesh arrangement.

The need for this model extension is found in the non-symmetric location of the steel piles and inclinometers, and to reduce any uncertainty coming from implementing only half of the embankment. A complete geometry also allows to compare the settlement to the records of the settlement plates (ZB) and the settlement profilers (ZMS).

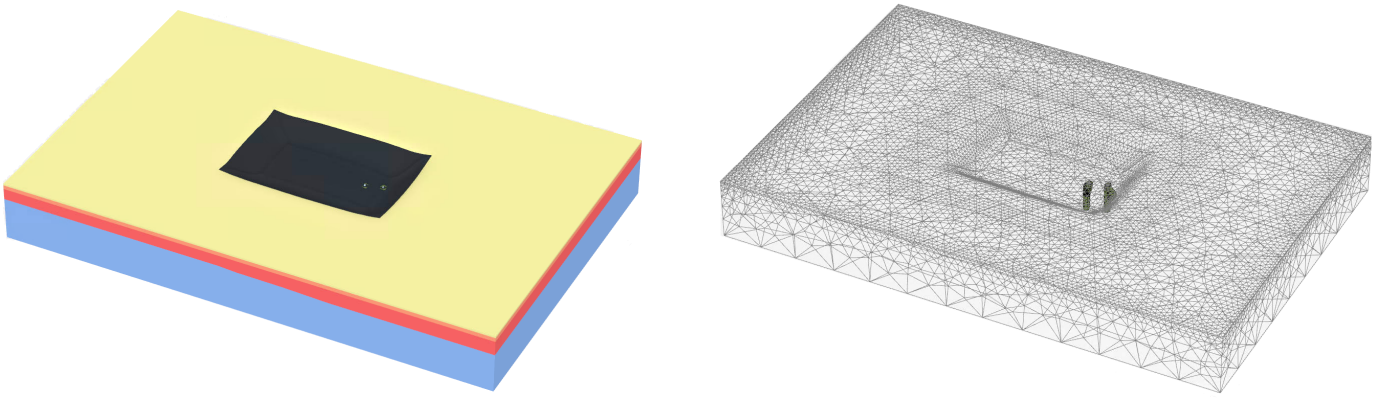

(a) Model stratification

(b) Mesh arrangement

Figure 6.11: Assembly of full model in the three-dimensional space

Based on the BT1 boring and the CPT information (displayed in Figure 2.3), the present work considered the clay layer horizon at -2.0 m NAP. This decision was in accordance with the estimations of Ammerlaan (2011), Siderius (2011), and Hoefsloot and Schadee (2014). However, two relevant factors suggest that the lower limit of the clay strata could actually be located at a lower depth.

The first indicator of this condition was recognized in the behaviour of the inclinometers HT-T1-3,4, where the measurements show evidence of an additional inflection point in the upper layers. This phenomenon could be attributed to the relatively higher stiffness of a highly consolidated clay covering the peat. This is consistent with the work of Lefebvre et al. (1984), who showed that this stiff crust is common in a lacustrine environment. In this case, utilizing the magnitude of -2.0 m NAP, even with an overestimation of the material's stiffness does not provide the same level of restriction, which would suggest that such a layer has to be thicker. In the pile behaviour analysis of Schadee (2012), the thickness of the clay was considered to be 20 cm thicker (-2.2 m NAP) and yielded a better estimation of the lateral displacements at this section.

On the other hand, it is known that peat is not usually found above the position of the GWT (C. Jommi, personal communication). It is assumed that the large hydraulic sensitivity of the material allows it to follow the water level, effectively providing an upper limit for said layer. Hence, based on the definition of the piezometric level, which follows the discussion on the hydraulic conditions of the field (Section 5.4), and it's further confirmed by the excess pore pressure results in Sections 6.1.2 and 6.2.2, the clay layer horizon is moved 10 centimeters below at -2.1 m NAP.

6.3.1 Settlement

When comparing both models in terms of resultant displacement as shown in Figure 6.12, the calculations made with the JMC model result in a higher magnitude, despite the similar geometry of the deformation itself. The half-mound model proved that the settlement calculation in terms of extensometers is equal for both constitutive models, however, the introduction of the considerable difference in lateral direction brings about a greater change in geometry when the JMC model is employed.

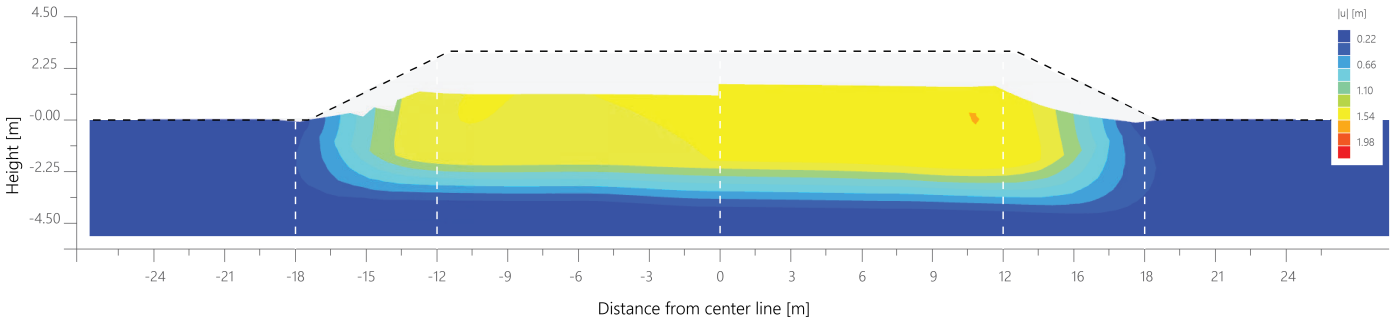

(a) Soft Soil model

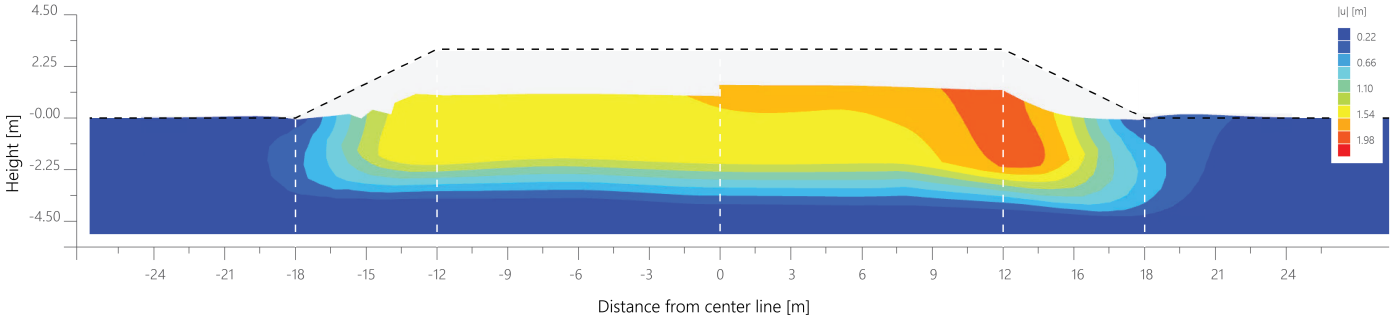

(b) JMC model

Figure 6.12: Resultant displacement of weak axis of T1 at 550 days

The foregoing result is also confirmed when quantitatively comparing the deformation at surface (-1.73 m NAP) with the measurements of the settlement plates. Different from the assessment made by the extensometers, the deformation magnitudes shown by the settlement plates are also dependent on the later behaviour, as they fully replicate the changes on the material overtopping their base plates. Given this distinction and knowing that both models overestimate the lateral deformation (with JMC at a higher degree), it is to be expected that both will display higher values as well.

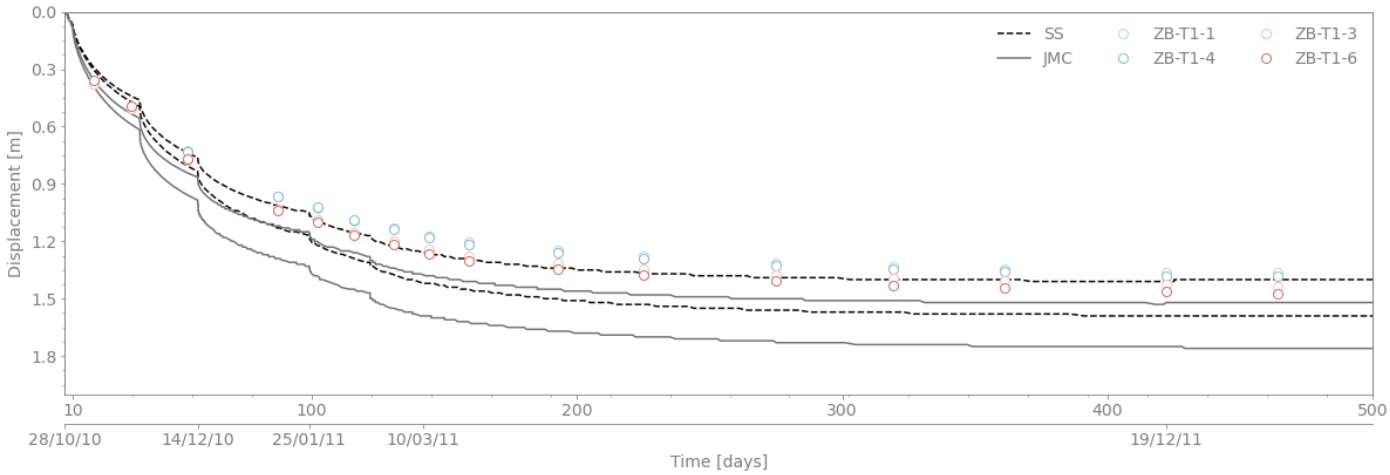

Figure 6.13: Estimation of superficial settlement of embankment no. 1

6.3.2 Hydraulic conditions

In the specific case of peat, the nature of the soil aggravates the degree of anisotropy, especially in terms of the hydraulic conductivity in the vertical and horizontal direction (Hanrahan, 1954; MacFarlane, 1969; Mesri and Ajlouni, 2007). Despite the fact that for amorphous peat this variability is not expected to be preponderant (Edil & Dhowian, 1981), the influence of this factor is still assessed. This is done by introducing a variation of $k_h = 5 \cdot k_v$ to the peat, as it is often found that the relation of k_h/k_v lays between 3 and 5 in the Dutch context (Mesri & Ajlouni, 2007). Then, it is compared to the estimation made by the SS model as its shown below.

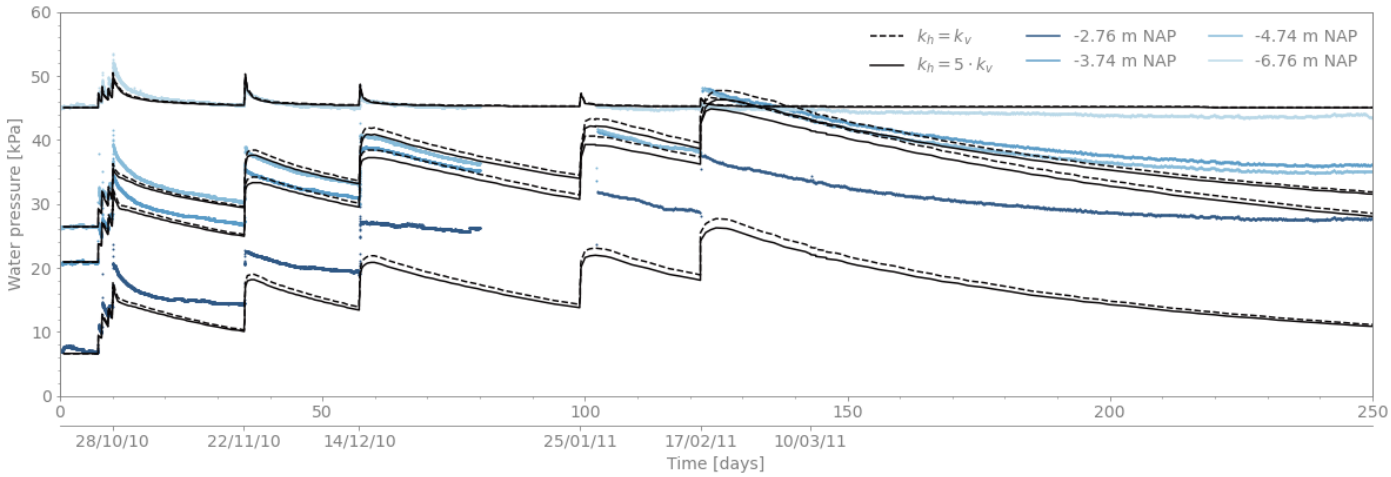

Figure 6.14: Variation of hydraulic conductivity in the horizontal direction

The increment of the horizontal hydraulic conductivity has an average reduction of 5.0% in the magnitude of the excess pore pressures with respect to a homologous isotropic parameter, while the effect in the measured settlement is null. Hence, it is considered that employing this variation in the material adds unnecessary complexity to the model without providing a relevant advantage.

If non-isotropic permeability is disregarded, no additional changes are implemented in the model, other than the removal of the closed boundary mid-embankment from the half-mound model. As expected this assumption is valid at the lower level of complexity and the hydraulic conditions remain equal when visualizing the Bloemendalerpolder case as a full model. Knowing the long-term limitations of the employed tools, Figure is 6.15 displays the efficiency at which the models replicate the pore pressure response, with virtually no distinction in terms of water pressure at the center of the embankment.

The previously mentioned constraints remain, with the most preponderant being the inadequacy of employing a single distribution of hydraulic parameters in the vertical and horizontal direction. Additionally, the high dissipation rate of excess

pore pressure after day 150 still persists when migrating from the half-mound model to this version. This consistency reaffirms the insufficient capabilities of the semi-logarithmic rule to describe void-dependent hydraulic conductivity.

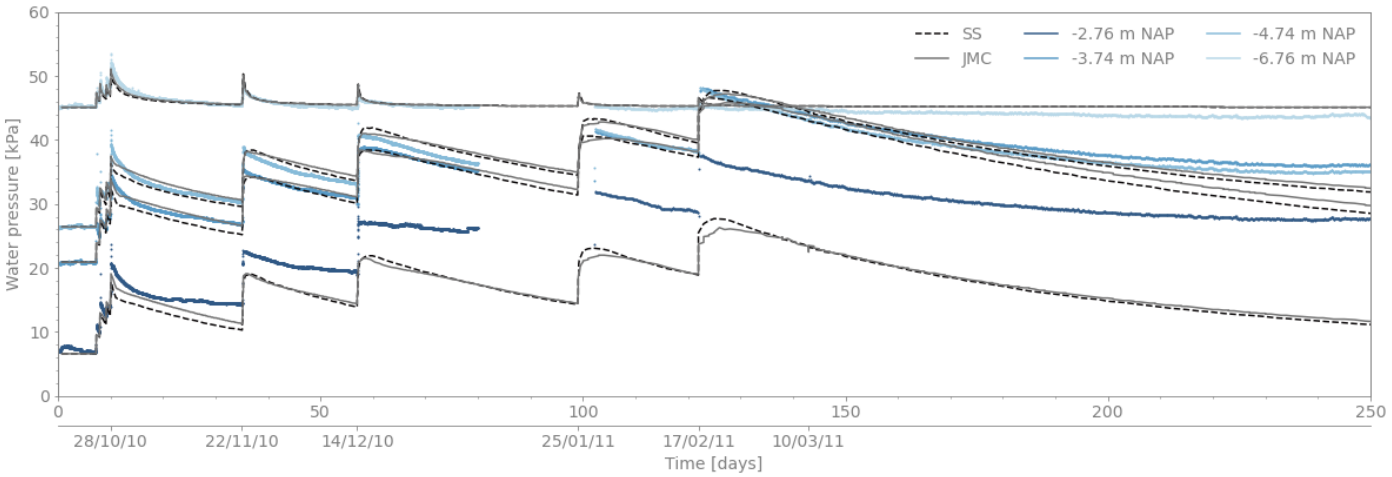

(a) WSM-T1-7 (West side)

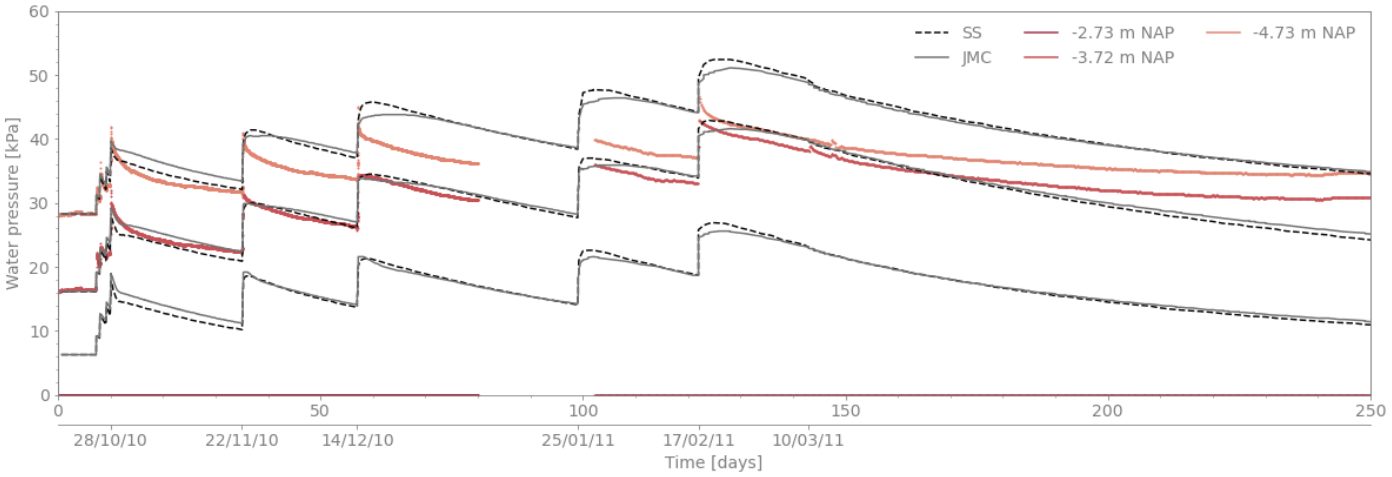

(b) WSM-T1-8 (East side)

Figure 6.15: Estimation of pore pressure with full model of embankment no. 1

6.3.3 Lateral displacement

As was mentioned in Section 6.2.3, despite of the close replication of the soil deformation by both constitutive models, there are fundamental inconsistencies that call for further scrutiny of the analysis. Considering that the whole set of inclinometers consistently showed an inflection in the deformation inside the silt layer and a negative deflection at the head of the device, it is suggested that these inconsistencies can be attributed to the bending of a column element.

Following the procedure described in Section 5.2.3, an equivalent square element is employed to simulate the compound system of cement-bentonite and PVC. It is relevant to remark that these elements are not active throughout the process, as there is a temporal difference in the installation of the inner and outer inclinometers. As a consequence, the outer devices (*HT-T1-1,2*) can be compared against results from the complete span of the experiment, while *HT-T1-3,4* only refer to results after the embankment was completed. This anachronism signifies that the response of the piles (inclinometers) corresponds to different stages of the consolidation process. Thus, this variance implies that the initial conditions of the surrounding soil differ between the equivalent volume clusters.

As can be seen the less stiff silt warped at the point of insertion of the cement-bentonite body, which allowed for a more faithful deformation of the soil. In consequence, the deformation of the soil appears to extend to the silt, influenced by its support function to the pile. Relative to the magnitude of the response, it can be seen that lateral deformation decreased, which is congruent with the fact that soil now has to oppose a higher stiffens and an additional support condition.

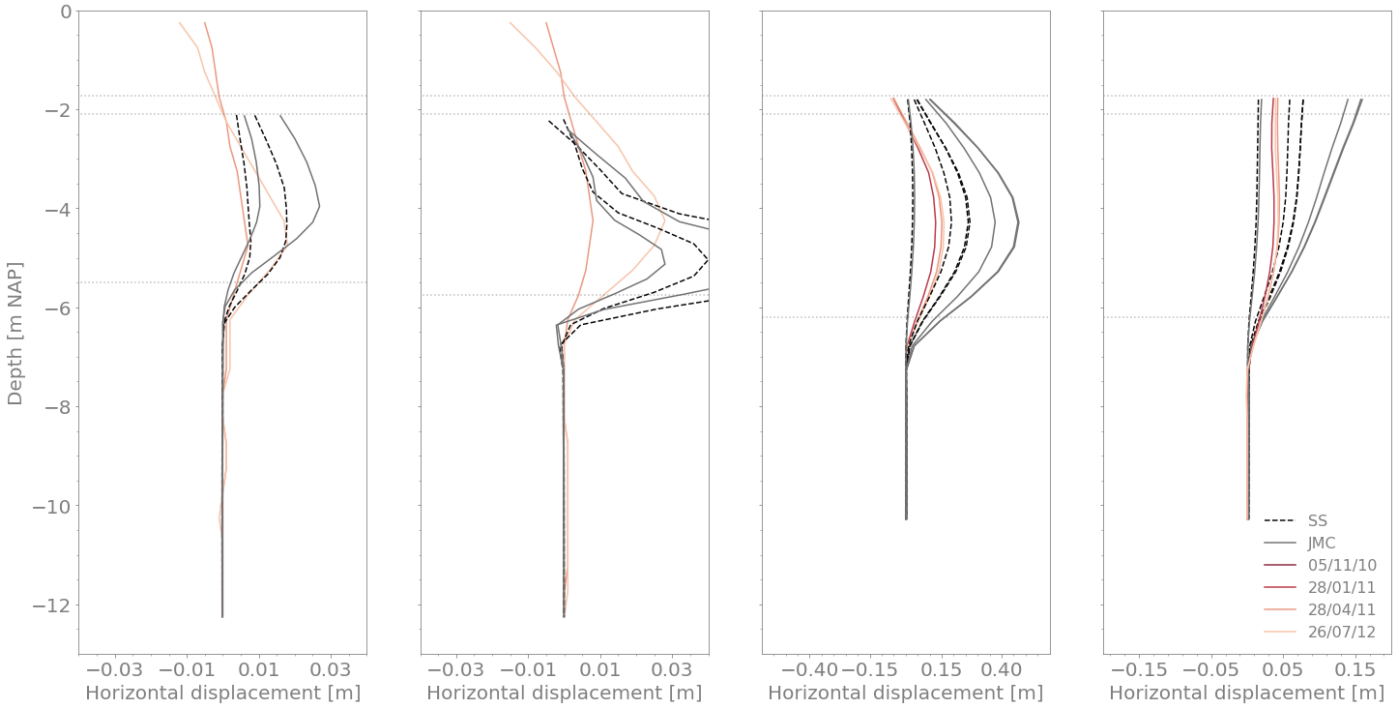

Figure 6.16: Progression of the horizontal displacements at T1

Relative to the distinction between models, the difference in the calculated response by the JMC and SS formulation did not differ greatly from the estimation without a cement-bentonite column. The JMC still provides an overestimation of the lateral response at *HT-T1-1,2*. Contrastingly, the results of *HT-T1-3,4* became less representative, with an increased displacement and the loss of the deformation geometry [3].

6.4 Discussion

The response of the Bloemendalerpolder field to the construction of Embankment no. 1 was closely emulated using the SS and JMC models. The successful execution of this procedure relied on the adequate calibration of the material based on the laboratory information. Additionally, to prevent severe divergence in the results, additional sensitivity procedures on two partial models were executed to define the operational limits of the tools, while also reducing the extent of the model's variability. From the procedure hereby reported, the following outcomes can be highlighted:

- A vital preceding step in this analysis was the replication of the K_0-CRS simulations as shown in Appendix C. Based on this process, calibration of the models is done in a controlled environment, which also helped in identifying a clear distribution of the parameters throughout the field. Additionally, it aids in reducing a relevant portion of the implicit uncertainty when transferring from laboratory testing to a FEM model.
- It is known that laboratory testing underestimates the value of the property due to sample disturbance and sample size effect (Chai & Miura, 1999). Hayashi et al. (2012) remarks from his previous work that this effect is also present in peats, with the hydraulic conductivity obtained through laboratory testing (i.e., oedometer test) varying from the field tests in at least one order of magnitude ($k_{field} = 10 \sim 30 \cdot k_{lab}$). Evidence of this variability was also found in the *Selva Agdenes* study in Norway, where the required permeability values for the model varied in several orders of magnitude from the measured values (Long, Paniagua, et al., 2022).

  Although this effect was not perceived between the results of the characterization and the FEM models, the K_0-CRS testing simulations showed a variation of that order between the calibrated values and the estimations made by Deltares (2012). The aforementioned variation might be linked to more fundamental assumptions of testing or modeling and not so much to the variation between the sample and the field.
- The need for stiffer compression parameters when translating the Bloemendalerpolder case to the FEM environment was only appreciated in the simplified geometry (Section 6.1). The simulation in three-dimensional space did not perceive this recurrent effect of FEM analysis.

[3] A possible explanation for this matter is further discussed in Section 7.2

- The proposed initial stress conditions (Section 5.3) are a good approximation for the average state of the field but fail to provide representative conditions closer to the surface. This limitation was evident in the excess pore pressure results, where the piezometer located around this depth shows a distinct behaviour.

  Manually providing a c_k or k_v to emulate the response of this device would require the use of fictitious values. On the other hand, if the stress field is improved and void dependent permeability rule is employed, these portions would inherently become less porous and the hydraulic conductivity would better fit these results.

- The lack of replicability of the *E-T1-8* seen in the models hereby presented was also evident in the work of Papadaki (2013), who explored the simulation of the extensometers in both one and two-dimensional models. It is assumed that the parameters describing the western side may diverge from the ones employed at the eastern portion of the field. Thus, to ensure the conciliation between the field and the FEM model, two distinct materials could be assigned or the thickness of the peat could be increased. Nevertheless, relative to the latter, further changing the geometry would present inconsistencies with the site investigation and the measurements of the inclinometers.

- Anisotropy of the hydraulic conductive is disregarded based on the low influence it has on the field. This is congruent with the usually low permeability ratio found in amorphous peats (Edil & Dhowian, 1981).

- The measured deformation of the inclinometers cannot be replicated without the introduction of the cement-bentonite and PVC column. This means, that the measurements of these devices are not a direct evaluation of the peat layer, but the result of soil-structure interaction.

- The apparent better estimation of the lateral deformation produced by the SS model is considered a reflection of the less flexible yield and plastic surfaces, which do not allow the reproduction of a comparable stress level to that present in the field. The more conservative calculation of stress is accompanied by a reduced effect on the perceived strains in those locations.

- The imposed condition of the embankment on the head of the *HT-T1-3* simulates the effect of a completely fixed support. Regardless, the present model failed to identify the right combination of parameters that provided such conditions. A lot of flexibility can be found on this matter, as no information regarding the properties of the fill material was found, other than the volumetric weight reported in the assortment of Fugro reports (2011,2012,2014,2016).

7 | Soil-structure interaction

The instrumentation campaign of the Bloemendalerpolder case allowed for the measurement of excess water pressure dissipation and the evolution of deformation during the construction of the test mounds. For the present section, the lateral response measured by the inclinometers is of special interest, as it provides an indication of the deviatoric behaviour of the material underlying the embankments. Nonetheless, different from the previously emulated measurements of settlement and pore pressure; these devices are not only a reflection of the soil behaviour, but of a more complex soil-structure interaction.

Using the aforementioned measurements, the capabilities of the JMC, SS, and NGI-ADP models to replicate the deviatoric behaviour of the Bloemendalerpolder peat are hence presented. This is done by means of intersecting the verified full model (Section 6.3) with volume clusters simulating the presence of the steel piles and the cement-bentonite columns used during the installation of inclinometers. Furthermore, this assessment is extended by utilizing the advanced features of the models and comparing them to the estimations made by the calibrated JMC model.

7.1 Driving mechanisms

The displacement patterns shown by the settlement tubes (ZMS) and the extent of the lateral displacement provided by the inclinometers (HT) are evidence of a multi-directional deformation of the ground as a response to the construction of the embankment. As more sand is added at the surface, the collapsible peat layer translates this load into vertical compression, while a portion of the plastic deformation displaces material outwards. The influence on the surroundings of this mechanism is relatively small due to the high porosity of the peat, which provides considerable slack within its matrix to rearrange its components. The deformation is only impeded below, where a varying silt horizon dictates the collapsible portion of the field.

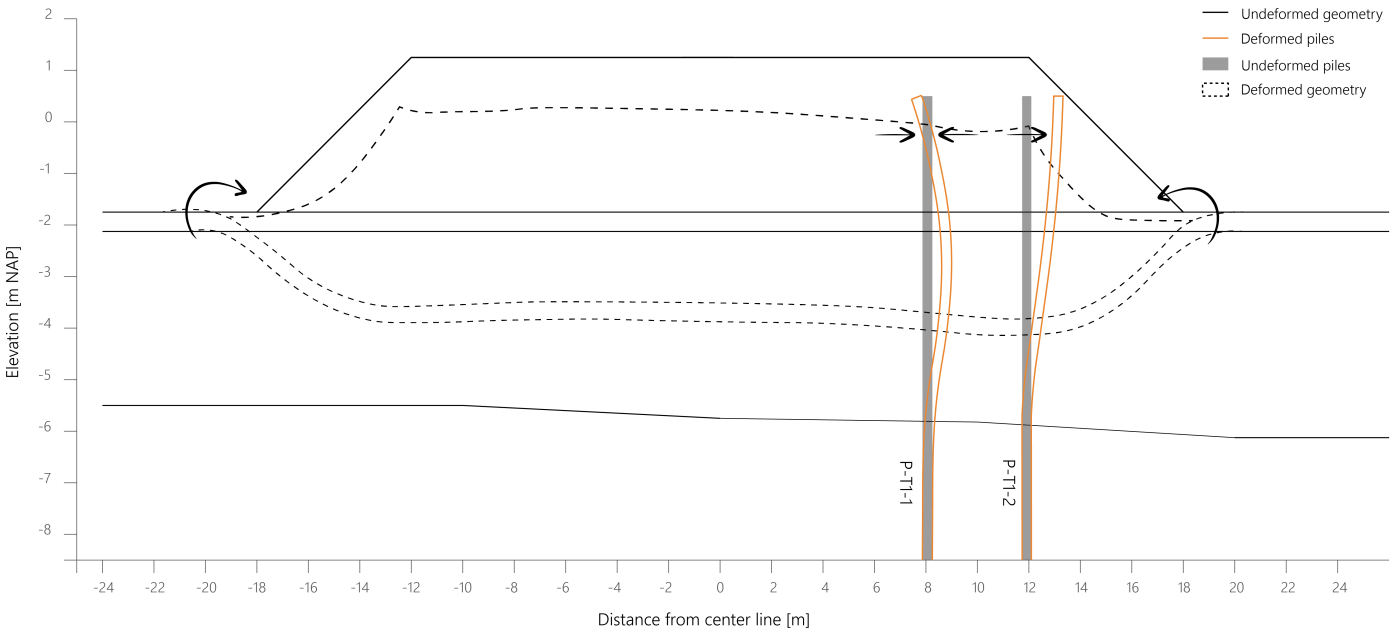

Figure 7.1: Conceptual visualization of embankment behaviour

Following the evaluation of the measurements of the site and further visualizing the response of the embankment in Chapter 6, it is evident that the mound behaves as a non-rigid body. As a consequence, an uneven deformation occurs below the embankment's footprint, which is further aggravated by the variable thickness of the peat layer. The resulting differential settlements in the vertical direction are complemented by a complex distortion in the horizontal direction, with the highest magnitudes of deformation occurring below the foot of the embankment.

The lateral component of this settlement process is the primal mechanism by which the deviatoric behaviour occurs in the peat layer. However, as this deformation reaches the position of the HEA300 steel piles, the outward deformation of the peat becomes a driving force that causes these structures to bend, while the soil behind them provides a resisting force that prevents said deformation, effectively introducing a soil-structure interaction. At the surface, the variable distortion of the compressible layer forces an inward inflection of the slopes of the embankment, as the internal part causes the highest degree of settlement. As displayed by the deformed geometry in Figure 7.1, the external deformation of the soil body closes in and constrains the movement of the piles. This effect was paramount in defining the support conditions of each pile, which further influenced their response to the soil deformation.

When comparing the measurements made by *P-T1-1* and *P-T1-2*, it can be said that more than the lateral effects of the peat layer, the deformation geometry produced by each pile is dependent on their position relative to the embankment. As described by Schadee (2012), the upper section of *P-T1-1* rotated in the opposite direction of the loading, as the restriction of movement provided by the embankment produced a normally fixed support condition. On the other hand, given the location of PT1-2, the crown of the embankment offered a softer clamping effect and thus, a relative absence of the negative clamping moment (Schadee, 2012; Siderius, 2011).

7.2 Pile simulations

The effects of the deviatoric behaviour of the ground are visualized in terms of the lateral displacement displayed by the *P-T1-1* and *P-T1-2* devices. For this endeavor, the estimations of the embankment made by the SS and JMC models are extended by the inclusion of these structural elements. Their comparison against the pile measurements is made at 40 days (28/04/11) and 410 days (26/07/12) after installation.

The approach to visualize the deformation of the piles was the summation of the deformation solely occurring after installation, which was successful for the evaluation of *H-T1-1,2* before the cement-bentonite modification. This way, all previous deformations are manually disregarded and only the phase-specific translations remain.

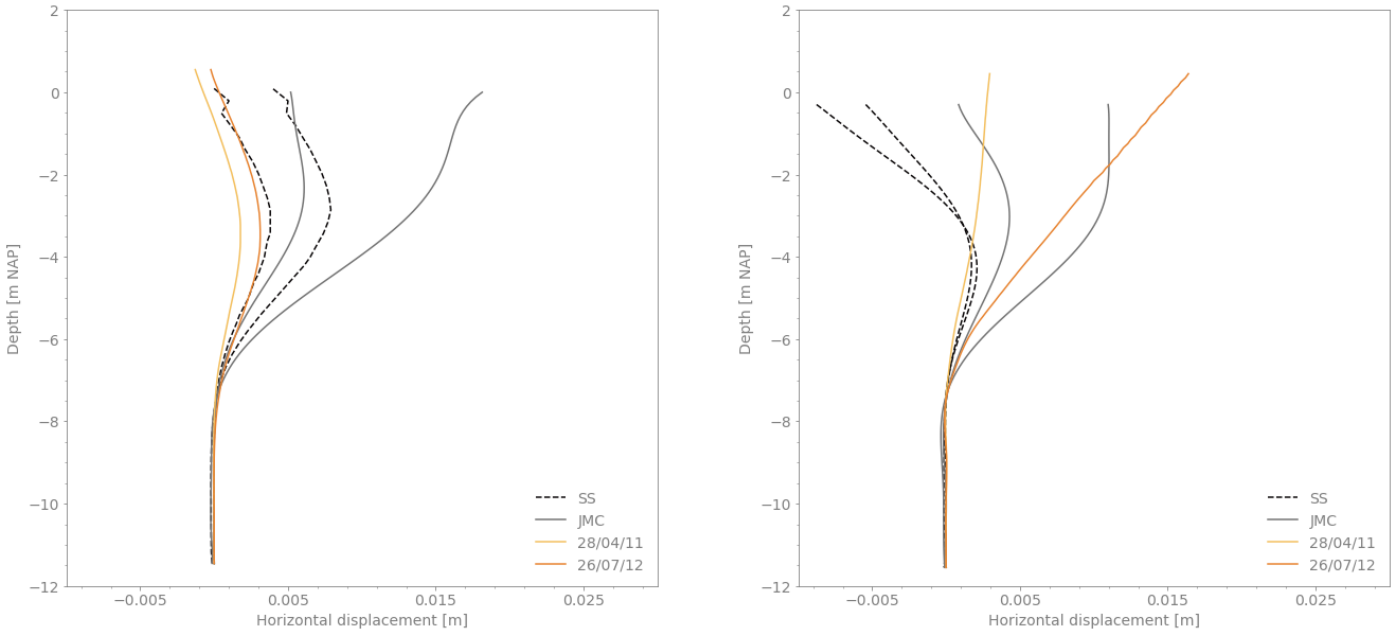

(a) P-T1-1

(b) P-T1-2

Figure 7.2: Estimation of soil-structure interaction occurring at the piles

From Figure 7.2 it can be concluded that the level of deformation estimated by the SS model better approximates the measurements of *P-T1-1*, while the JMC model more accurately describes *P-T1-2*. However, based on the comparison

of the undrained triaxial simulations (Figure 4.12), it is known that the SS model fails to fully develop the same level of deviatoric stress as the Bloemendalerpolder peat. That being the case, it is concluded that the lower deformations shown by the piles are not linked to a better match of the strain, but a poor estimation of the deviatoric stress. Conversely, the overestimation of deformation calculated with the JMC model during the evaluation of the inclinometers (Section 6.3.3) can also be appreciated in this case.

Although the calculation of the inflection and lower curvature of the piles is somewhat faithfully recovered by both models, a poor estimation at the upper section is equally consistent. The genesis of this phenomenon can be better appreciated in Figure 7.3, where the comparison between the models also shows the divergence in the embankment's geometry. With the higher horizontal displacements generated by the SS and JMC models at the peat layer, the embankment is allowed to deform further and thus, provides less opposition to the pile movement. This fact is accentuated by the poor replication of the stress state close to the surface, as it was already reported when analyzing *HT-T1-3* and *HT-T1-4* in Section 6.3.3.

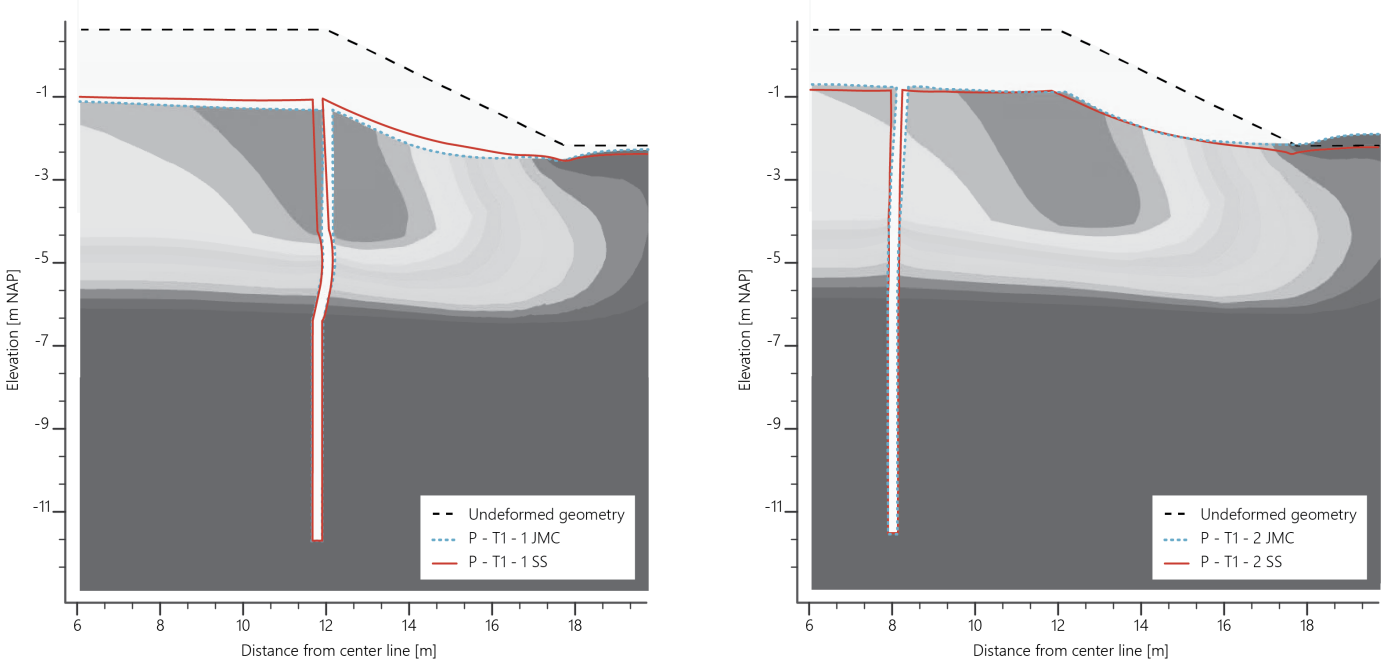

(a) P-T1-1 (b) P-T1-2

Figure 7.3: Comparison of embankment geometry at the end of test[1]

The foregoing deficiencies are also bound to limitations of the FEM formulation, which forced an inadequate initial condition for the piles. Given that the introduction of a different element into a field occurs in the form of a material replacement, inserting a pile means that a volume cluster characterized by a soil material is now assigned a set of parameters representing steel. Because this volume has already been deformed, when it's replaced by the equivalent column, the pile no longer represents a straight column but a deformed one.

Evidence of this limitation in the FEM model is displayed in Figure 7.4, as it depicts how the deformed pattern of the elements is preserved between the pile installation and the end of the test. From Figure 7.4a, it is clear that the elements representing the column attain a geometry after the construction of the mound, reaching a maximum deflection of 15 centimeters in the case of *P-T1-1*. Once the equivalent piles are introduced, there is a change in the mechanical properties of these deformed elements, however, there is no realignment of the column. Therefore, from this stage onward, the volume keeps deforming following the same pattern.

By further comparing this location with the estimations made for *HT-T1-1* and *HT-T1-2* without the introduction of a new material (Figure 6.10), a large inconsistency can be appreciated in the order of magnitude of the deformation. The large values estimated with the piles can therefore be linked to this prescribed deflection, which is not representative of the real case.

When the cement-bentonite columns are used to better estimate the inclinometers (Section 6.3.3), it can be seen that this effect is also present even when the stiffness of the "pile" material is close to the soil. As the estimation of the inner inclinometers perceive the same effect, as they are also introduced after the consolidation process has progressed.

[1] Each pile element is plotted in a distinct axis, as their location relative to the embankment varies in both horizontal directions.

This would prove that the occurrence of this geometric discrepancy is unavoidable without resetting the FEM field, which would no longer be representative.

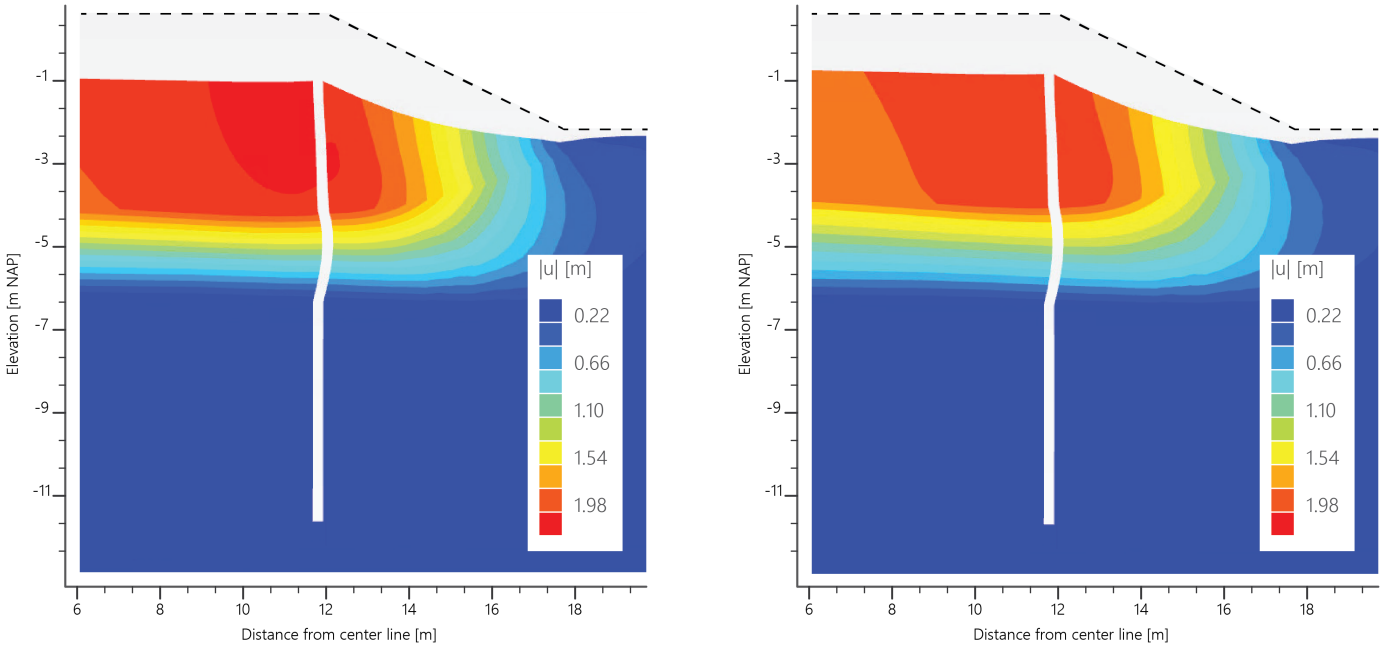

(a) Before installation (Phase 6.1.1)

(b) At the end of the test (Phase 7.1.2)

Figure 7.4: Visualization of the deformation perceived by the volume cluster representing the piles

This phenomenon had already been reported by Siderius (2011), who also followed the approach of considering the phase displacements of interest independently and calculate the deformation as the sum of these translations. Employing this consideration, Schadee (2012) built upon his analysis and intervened in the pile elements with artificial support conditions and imposed a clamped response at the head of the piles. However, neither of these options addressed the pre-deformed volume cluster, and thus, the deformation of the piles was still based on the response of a non-vertical column.

7.3 Lateral behaviour

Because the FEM simulation of the pile could not be conciliated with the measurements, the comparison between models is made using the inclinometers *H-T1-3* and *H-T1-4*. This is made possible, given the fact that these elements were installed before the construction of the embankment and thus, are not impacted by the deformation inconsistencies that bound the equivalent volume cluster of the steel piles.

The results display in this section replicate the set of results from the JMC and SS models shown in Figure 6.16 and include the results of the NGI-ADP model. Three specific dates are used as reference: the 5/11/10 represents the immediate response at the beginning of the consolidation process; the 28/04/11, occurs approximately at the transition of the secondary compression; while 26/07/12 provides an outlook 1 year into the secondary compression for *H-T1-3*.

The lateral deformation is further complemented by a comparison of the accompanying bending moment. To estimate this structural condition of the inclinometer, a polynomial equation based on the deformation curve is derived and then, a double differentiation (Equation 7.3.1) provides the resulting bending moment. Relative to the estimations made with the constitutive models, the bending moment is recovered by integrating the stress distribution. In this approach, it is relevant to remark on the uncertainty of the stiffness from the cement-bentonite PVC column, which affects all calculations equally.

$$M(y) = E \cdot I \cdot \frac{d^2v}{dy^2} \tag{7.3.1}$$

An extensive iteration procedure was performed to refine the unknown properties of the sand embankment. However, it was only a combination of extreme values that yield an adequate replication of the support condition at the head of

HT-T1-3. This phenomenon is also evident when comparing the results of *HT-T1-4*, with all constitutive models following a somewhat adequate trend in the lower midsection, but overestimating the displacements as they approach the surface.

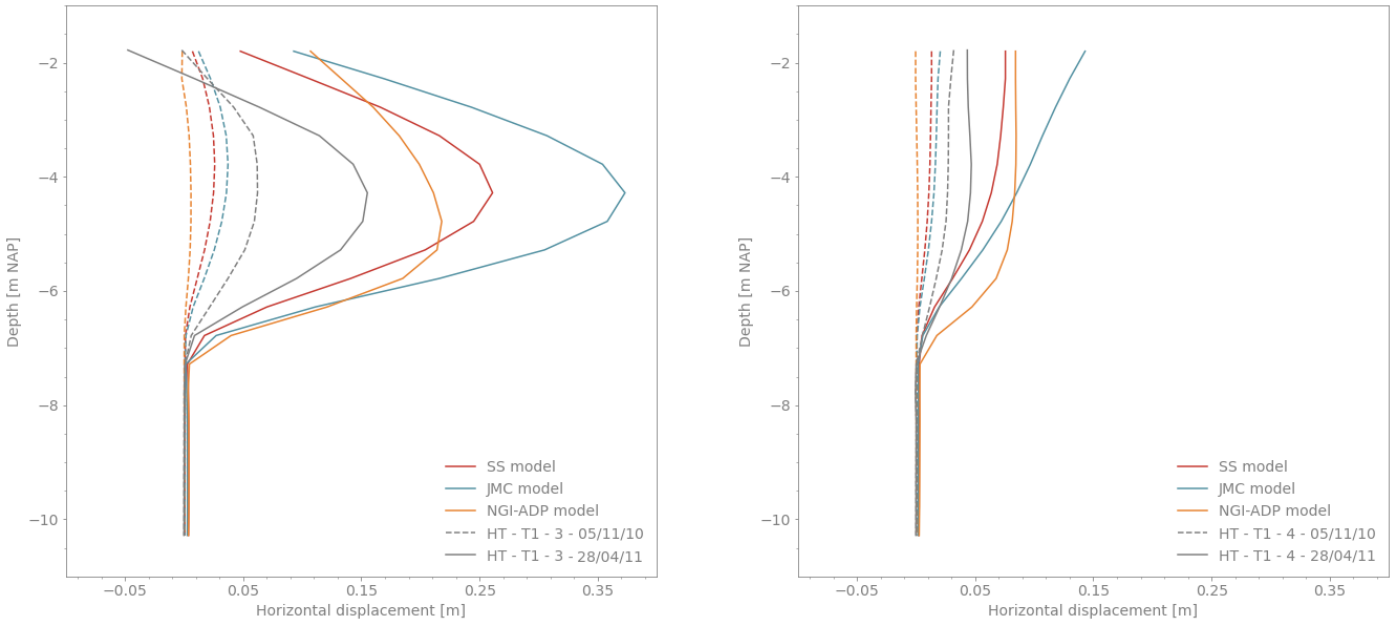

(a) HT-T1-3

(b) HT-T1-4

Figure 7.5: Estimation of soil-structure interaction occurring at the inclinometers

Both the JMC and SS model closely follow the deformation pattern of the inclinometers, with a consistent overestimation of the mid and final conditions, and an underestimation of the initial response. The most faithful estimation of the initial response is given by the JMC model, while for the long-term, the NGI-ADP provides the closest approximation to the measurements. In the case of the latter, there is a considerable distinction in the deformation, which can be attributed to the built-in capabilities of the model to estimate the variation of its parameters with depth.

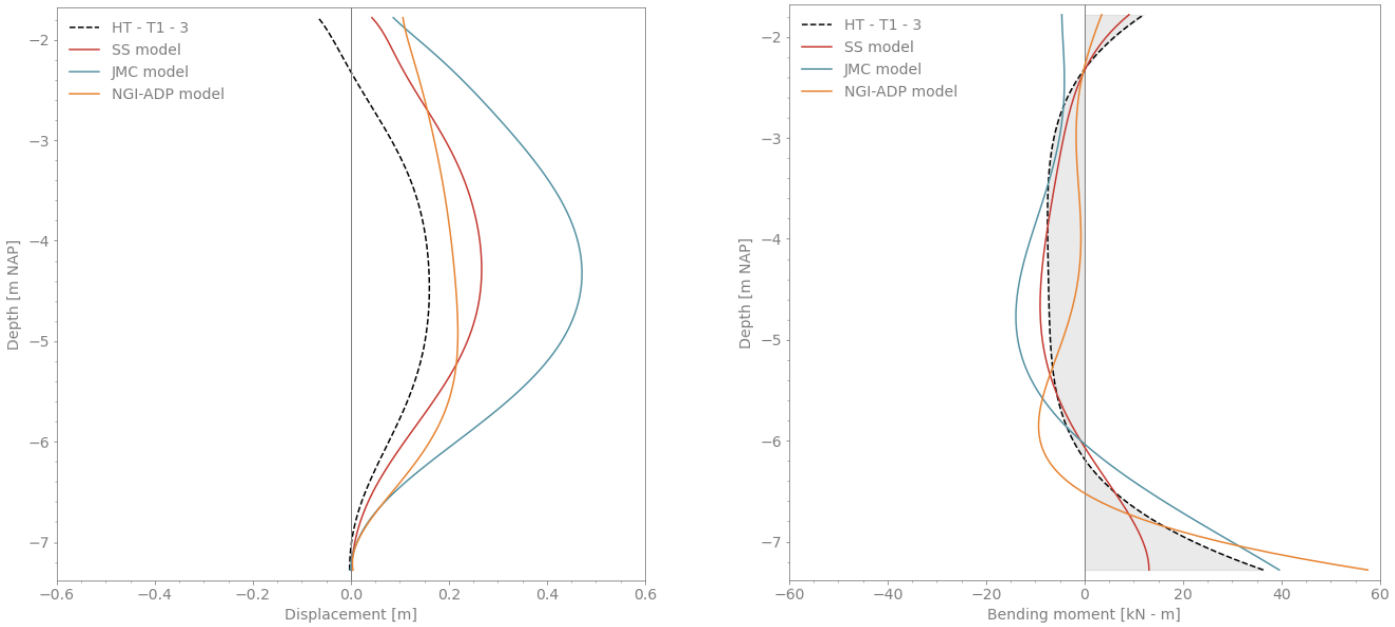

(a) Lateral displacement

(b) Bending moment

Figure 7.6: Measured and calculated conditions of HT-T1-3 at 26/07/12

By comparing the structural conditions, it is confirmed that the consistent lack of replicability by all models is linked to the poor representation of stress at the upper layers. The JMC and SS model provides a similar distribution in the lower section of the inclinometer, but as the pile approximates the surface, it is clear that stress initialization does not provide

an adequate platform to generate a representative stress state as the consolidation progresses. Additionally, based on the calculation of the excess pore pressures (Figure 6.15), it is considered that the inadequacy of the void-dependent permeability of the peat also failed to provide the temporal consistency in the deformation.

7.4 Advanced properties

The calibration of the models, as it has been presented up to this section of the project, emulated the field test based on the available laboratory data. However, during this project, the inclusion of the distinct features of each model is not used. That is the addition of the hardening rule built into the JMC model and the creep parameter in the Soft Soil model. Therefore, the comparison of the models was reduced to a contrast of the behaviour of the yield surface and the non-associativeness of the constitutive model.

With the objective of further comparing the capabilities of the models, this section displays the effects of employing the advanced properties of each model and how they compare to the deviatoric estimation made by the proposed calibration of the JMC model.

7.4.1 Mixed hardening rule

The only reference of the deviatoric response of the peat was a collection of consolidated-isotropically undrained triaxial compression tests, of which none displayed a strengthening behaviour and thus, would suggest that the use of the mixed hardening rule is unnecessary. However, when comparing the results with a similar geomorphological profile in Uitdam (Zwanenburg & Jardine, 2015), it can be seen that as much as some peat samples display a mild hardening, others display a response close to that of the Bloemendalerpolder peat. Therefore, assuming that the laboratory data does not provide a full picture of the peat as mentioned in Section 4.4, it is considered relevant to discuss the (perhaps unnoticed) presence of deviatoric hardening.

Following the abovementioned, the more advanced mixed hardening rule is included in the JMC model. This feature of the model includes not only the volumetric hardening (also included in the SS and SSC models), but also integrates the deviatoric plastic strains which are preponderant in describing peat behaviour. Thus, the previously described parameters of the JMC model (Table 4.7) are now complemented by a magnitude of deviatoric loading (D_0) of 1.0 and a rate of evolution (D_1) of 10.0.

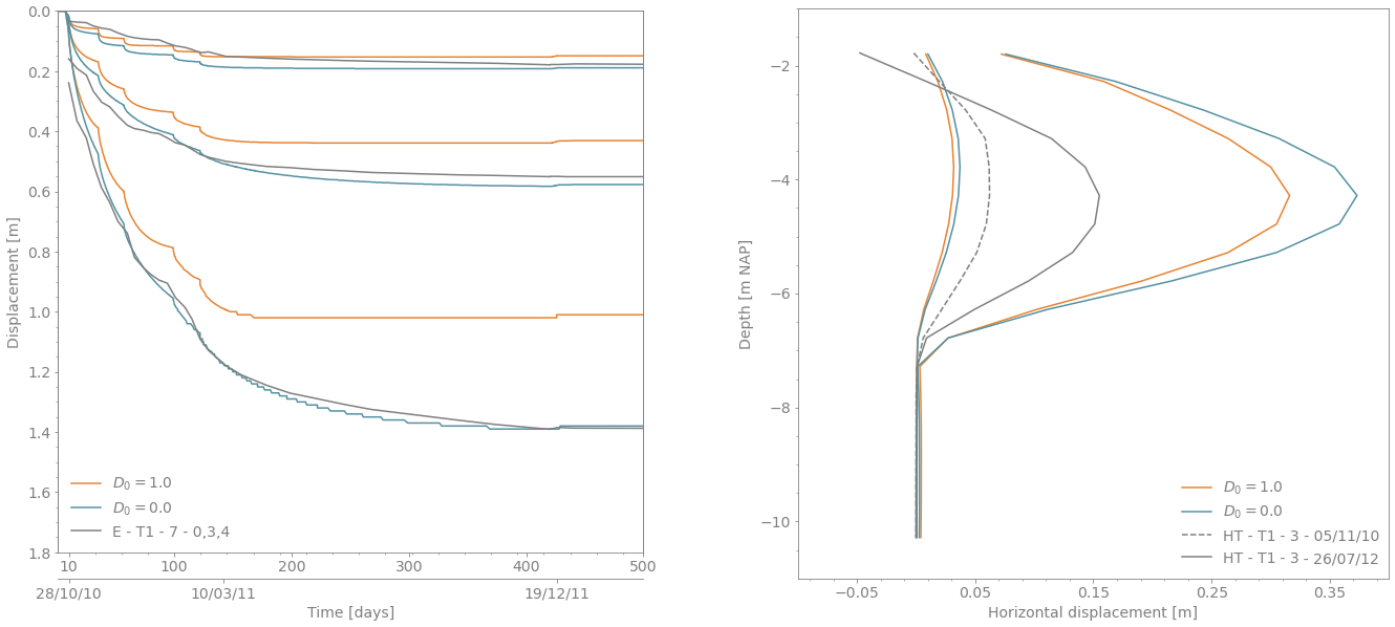

(a) Vertical displacement

(b) Horizontal displacement

Figure 7.7: Effect of the deviatoric hardening rule on deformation

7.4.2 Creep

As previously mentioned, the present project disregards the influence of creep to provide a consistent framework for the comparison of the models. This is done on the basis that in contrast to fibrous peat, the influence of creep is not as relevant on amorphous peat (O'Kelly & Pichan, 2013) and the absence of this parameter in the JMC and NGI-ADP models. In this section, the influence of the soft soil model is visualized to understand its potential for the present case.

The property is included in the form of the modified creep index (μ^*). It was not calculated in the present and in turn, the estimation of 0.014 made from the laboratory tests was used. This magnitude has been consistent in all cases, with the only exception being the postdiction results by Hoefsloot and Schadee (2014). The introduced parameter also requires an adjustment in the hydraulic conductivity (within the working range), as the mechanical response differs.

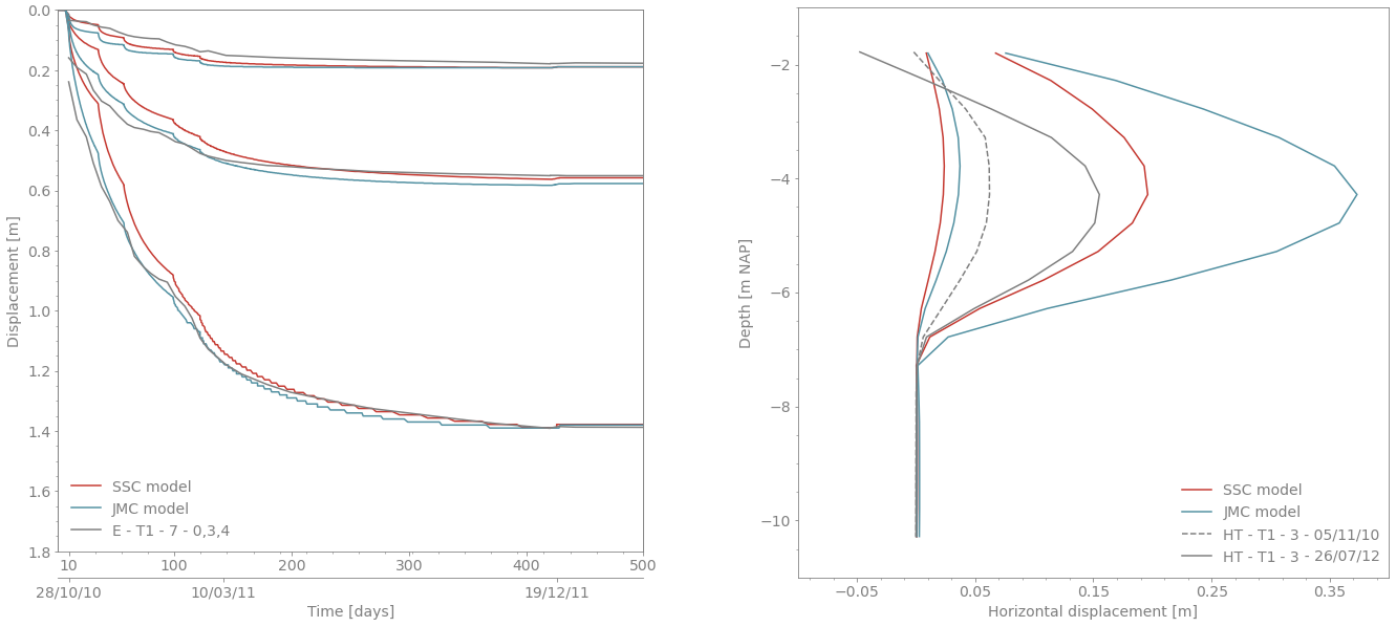

(a) Vertical displacement

(b) Horizontal displacement

Figure 7.8: Effect of creep on deformation

A strong case is made on the relevance of creep in peats (Den Haan and Kruse, 2007; Long, Grimstad, et al., 2022; Muraro, 2019), and more specifically in the present case due to the additional time-dependent settling seen in the settlement profiles and plates (Hoefsloot & Schadee, 2014). When visualizing the effects on the SS model of the relatively low value of μ^*, the difference is limited to a lower pace in the settlement but no change in the magnitude. While a higher lateral deformation is also seen in the upper sections of the inclinometer. Both are assumed to be a reflection of the deficient initialization procedure, which yields unrealistic creep rates.

7.5 Discussion

- The inclusion of an undeformed element in an already deformed field is not feasible in the current state of Plaxis 3D. Given the formulation of this calculation method, the introduction of an element only signifies the replacement of the characteristic material defining the volume cluster. Nonetheless, this change has no effect on the attained geometric conditions previous to the swap of materials. In large-strain conditions, this effect is aggravated by the extent to which the ground has deformed before the change.

  Based on the fundamental constraints of using pile elements, the only practical alternative to compare the lateral deformation and stress conditions of the Bloemendalerpolder case is the use of inclinometers *HT-T1-3* and *HT-T1-4*. This is plausible due to the temporal difference between these and the steel piles or the inner inclinometers, as they were present before the embankment was built.

- The JMC model provided the closest estimation of the initial response of both inclinometers. Nonetheless, despite efficiently preserving the deformation pattern of *HT-T1-3* it also displays the highest divergence in the long term. When evaluated in terms of bending moment, the structural forces ungainly follows the real behaviour of the pile.

– Without any additional changes to the JMC model, by utilizing the rate of evolution (D_1) a reduction of 5 cm was shown in the lateral deformation of *HT-T1-3*. The inclusion of the deviatoric hardening component is evidence of the potential of the model to better approach the measurements.

  On the contrary, this reduction in lateral deformation also has an inconsistent impact on vertical deformation, as a higher degree of hardening is attained. It appears that due to the implicit inclusion of the vertical strain in the definition of the deviatoric strain, the contribution of this component is being accounted for twice. Once, as part of the volumetric deformation and partially ($2/3 \cdot \epsilon_v$) in the deviatoric.

– The NGI-ADP produces the closest level of long-term lateral displacement to that attained by *HT-T1-3*, as well as the most akin emulation of the deformed geometry of *HT-T1-4*. Contrastingly, this response can be associated with the failure to replicate the extent of the consolidation process in terms of vertical deformation. The limited capabilities to reproduce the volume-strain relation, as seen in the laboratory conditions (Figure 4.12d), were crucial in producing a low degree of settlement at the field, which reflected in lower lateral deformations.

  The forgoing consideration, accentuated by the restrictions of the FEM implementation, produced a deficient simulation of the deformation pattern of *HT-T1-3* and an overestimation of the lateral displacement of *HT-T1-4*. It is therefore assumed, that regardless of the capacity to efficiently replicate shear behaviour (Figure 4.12c), its meager ability to produce a better estimation of the driving mechanisms (i.e., vertical displacement) renders the use of NGI-ADP as a sub-optimal option in this case.

– The soft soil model produces the best average estimation of all measured factors of the Bloemendalerpolder field. The geometry of the deformation is consistently followed in all accounts, although it still results in an overestimation of the deformation and an underestimation of the bending moment.

– Different from the work of Schadee (2012) and Fugro (2014, 2015), the need for a creep index is not considered to be preponderant in the analysis, although it is still relevant in the long-term of the ZMS and ZB results. This assumption would be consistent in amorphous peat, as the creep potential is lower than that of their fibrous counterparts (MacFarlane, 1969; O'Kelly and Pichan, 2013). On the other hand, it is possible that the effects of creep were partially compensated during the procedure.

– The lack of representation of the stress field closer to the surface, previously mentioned in Chapter 6, became crucial during the analysis of the lateral displacements. Being that regardless of the implicit differences between the models, all estimations showed the highest divergence from the measurements at the upper sections of *HT-T1-3* and *HT-T1-4*. It is considered that a relevant source of incompatibility, in this case, was the stress field, as it can be seen in Figure 5.6, that the same locations displayed the highest difference in OCR.

– During the iterative procedure it was found that the sensitivity of the JMC model to a change in Poisson's ratio was considerably lower than the soft soil model.

8 | Conclusions and Recommendations

The final section of this project explores the most relevant impressions from the field test results, the characterization of the material, and the usage of the constitutive models in the Plaxis 3D environment. Moreover, recommendations are made on possible improvements to this work and future research.

8.1 Conclusions

Based on the specifications of the Bloemendalerpolder experiment described in Chapter 2 and on the characterization process shown in Chapter 4, the measured response of Embankment no. 1 was closely replicated (Chapter 6). This procedure allowed to independently evaluate the overall response of the soil body and proceed to the assessment of the steel pile elements, with an already proven emulation of the geotechnical aspects of the experiment.

The analysis of the field measurements allowed for the holistic visualization of the hydro-mechanical response of the soil body. The parallel assessment of water pressure, settlement, and horizontal deformations showed distinct faces of the consolidation process, which together provided a complete picture of the experiment. However, as the modeling progressed and deeper scrutiny went into the records, the following considerations were made.

8.1.1 Field measurements

- *The response of the western and eastern sides of the embankment is not alike*

  The conciliation between the estimation and measurements of the hydro-mechanical response was not consistent throughout the field. Both for the excess pore pressure and the vertical displacements, the data shows a distinct behaviour on each side of the field. Further modifying the geometry to enable congruent deformation on both sides of the embankment is not feasible, since it would introduce a discrepancy with the ball penetration tests, the CPTs, and the data from the inclinometers.

  Therefore, it is concluded that the state parameters might also vary in the horizontal direction, which could suggest that the stress field might be more complex than initially considered.

- *The installation process of the inclinometers restricted the evaluation of the lateral deformation of the soil*

  None of the provided measurements of lateral displacement of the Bloemendalerpolder solely reflect the behaviour of the ground. Both the piles and the inclinometers display the response of soil-structure interaction. This in turn adds an additional level of complexity, which prevented the comparison of the models' capabilities relative only to the soil material.

- *The horizon below the peat layer is better described by silt parameters*

  Previous modeling endeavors had considered the incompressible layer below the peat as sand and had provided properties as such, however, based on the site investigation data and the modeling it is considered that this layer behaves more so like silt. Through the analysis of the drainage conditions of the peat, the material utilized a hydraulic conductivity of 0.5 m/d, which can be often linked to the permeability of silty soil. Additionally, when executing the evaluation of the pile elements (both cement-bentonite and steel), the stiffness required at the supports had to be considerably lower than that of sand material.

8.1.2 Characterization

- *The peat present in the Bloemendalerpolder is amorphous*

During the characterization process, the state and engineering properties displayed conflicting values between a Reed peat and an amorphous peat designation. On one hand, the high water content and compressibility shown by the material could be linked to a material with a relevant presence of organic material. However, these values were inconsistent with the high inorganic content, high K_0 value.

A relevant indication of the amorphous nature of the Bloemendalerpolder peat was the TxCU laboratory tests, which displayed a low friction angle and no indication of the typical hook response shown by fibrous peats.

– *The FEM simulations of the K_0-CRS tests were paramount in defining the engineering properties of the peat*

The definition of a representative magnitude for the coefficient of earth pressure at rest (K_0) and the hydraulic conductivity (k_v) from the K_0-CRS tests required an in-depth analysis of each sample to reduce the uncertainty from the laboratory testing and the migration to a FEM environment.

From these simulations, it was possible to recover a combination of representative properties yielding an equal response to that measured in the tests. The magnitude of these values varied from the estimations made by previous authors by one order of magnitude.

– *The difference between the SS and JMC models in 1D compression is not significantly different*

Considering the results of the K_0-CRS simulations and Chapter 6 on the embankment response, both models produce similar results when evaluated in one-directional loading. However, the contrast between them is evident in the development of the deviatoric stress, as seen in the TxCU simulations (Section 4.4) and later confirmed during the evaluation of the lateral response.

– *The effects of creep were disregarded in this comparison*

The creep component was not included in this analysis so a uniform framework of comparison between the tested models could be provided. Still, it is known that a low degree of creep was displayed in the K_0-CRS tests, and Hoefsloot and Schadee (2016) remark on the high relevance of this factor. Moreover, the settlement profilers, as well as the settlement plates in the eastern section show a low degree of deformation after the secondary stage of consolidation.

The analysis made in Section 7.4.2 does not asses the full extent of its influence, as it is feasible that some of its effects were compensated during the calibration procedure. The influence of this component should be explored in detail.

8.1.3 FEM analysis

– *The substandard replication of the OCR field hindered the analysis*

The stress field initialization was assumed to be sufficiently good, as it confidently described the lower-mid region of the field. Nonetheless, based on the comparison with the excess pore pressure and later to the lateral displacement, it is concluded that the proposed description of the field is insufficient. Considerable over-consolidation has to be introduced in the first meter, with a softer decrease towards unity with depth. This in turn would improve the estimation of the restrain at the surface from the piles and would better replicate the pore pressures.

The use of a discretized layer arrangement, which is the recommended approach in the literature for such a complex distribution, was not possible. Two independent factors contribute to this fact: the disregard by Plaxis 3D of the OCR/POP during the "gravity loading" stress initialization (1) and the need to assemble a dense mesh (2) to compensate for the high ratio between the thickness of these layers and the large extent of the domain.

– *A logarithmic law to evaluate the relationship between void ratio and hydraulic conductivity is indispensable for the Bloemendalerpolder case*

The simulation of the K_0-CRS tests provided an inkling of the limited capacity of Taylor's formulation to describe the full evolution of the excess pore pressure in the laboratory. Because the tools provided an adequate estimate of the hydraulic conditions in the assumed range of the field, no additional considerations were made. Nonetheless, the attained level of porosity was insufficient to provide a representative dissipation rate in the long term.

The work of Schadee (2012) with Plaxis 2D, showed better results in terms of excess pore pressure, as the software has the capabilities to update water pressures as it does the mesh. Based on this and the limitations of the model hereby employed, it is evident that a fully logarithmic law would provide a representative progression of this property.

– *No relevant advantages were perceived by introducing anisotropy in the hydraulic conductivity*

There are no field measurements of hydraulic conductivity and thus, no real information on the hydraulic conductivity over depth. This allows a certain degree of flexibility when defining the characteristic values, which led to a calibration procedure to define the anisotropy of this parameter. Although the dissipation was slightly accelerated with the variation of the hydraulic conductivity in the horizontal direction, the deformation was not substantially altered and thus, no practical differences were perceived in the response of the field.

– *The HT-T1-3 and HT-T1-4 measurements are the only viable option to evaluate the lateral behaviour of the field*

The introduction of unaltered geometries in a deformed field is not possible. Thus, it can be said that the only frame of reference to adequately compared the models are the inclinometer measurements from *HT-T1-3* and *HT-T1-4*, as they are the only elements that were installed before the deformation occurred. Additionally, since they are the only elements installed before the intervention, they are also able to describe the effect of the initial response.

8.1.4 JMC model

– *The JMC model provides, on average, the best emulation of the peat in laboratory conditions*

The SS and JMC models provide a comparably adequate approximation of the one-dimensional deformation, while the NGI-ADP better replicates the shearing behaviour. However, the JMC model shows a faithful response in all accounts (i.e., TxCU, odometer and K_0-CRS) and simulates the most accurate stress path in the *p' - q* space.

– *The efficient emulation of the initial response by the JMC model is consistent across the field*

The deformation pattern and the order of magnitude calculated using the JMC model nearly followed that of the *HT-T1-3* and *HT-T1-4* inclinometers at the beginning of construction. However, in the long term, it was also the highest overestimation of the parameters.

– *The contribution of the vertical strain is accounted in the mixed hardening rule twice*

One of the most advantageous properties of the JMC model is the mixed volumetric and distortional hardening rule, which allows for a better description of the realignment of the fibers and the reinforcing effect it has on the material (Muraro, 2019). Given the amorphous nature of the peat in the Bloemendalerpolder case, the analysis did not require the introduction of such a rule, and the model was calibrated without considering it.

In Section 7.4, when this feature is introduced, it can be appreciated that the deviatoric component of the hardening rule is also influencing the vertical deformation. Thus, it can be said that the contribution of the vertical plastic strains is accounted for by both the volumetric and deviatoric components of the rule.

8.2 Recommendations

– *Utilize the SS and SSC when designing with amorphous peats*

When dealing with amorphous peats or organic clays with little to no fiber influence, the JMC model provides no significant practical difference to the estimations made by the SS model. Considering the more complex characterization process required to calibrate the JMC model, it is deemed unpractical to employ such a model.

– *Develop a reliable stress field initialization procedure for virgin peat fields*

A major limitation of the FEM implementation was the replication of the stress state before the embankment's construction. The present project failed to simulate the over-consolidation condition of the peat with the available tools in Plaxis 3D. This stress distribution is typical in virgin peat fields (Hayashi et al., 2012; Lefebvre et al., 1984; MacFarlane, 1969; Zwanenburg and Jardine, 2015) and the development of a consistent methodology could provide a valuable tool for the inexperienced user.

– *Further research regarding the hardening rule in the JMC model*

Additional research can be dedicated to the mixed volumetric and distortional hardening rule, by evaluating its influence in stress-strain paths different from the axisymmetric.

– *Design a small-scale field experiment to evaluate deviatoric behaviour of peat*

The analysis hereby presented relied on the complex and intricate framework of the Bloemendalerpolder to compare the capabilities of the models. The inconsistencies and multiple assumptions made throughout the process

suggest that the results are riddled with uncertainty. It is considered that a smaller-scale experiment with reconstituted material could provide an intermediate step to further understand the capacity of the model.

– *Develop a comprehensive characterization campaign of the extension properties of peat in the Dutch context*

Given the absence of testing in extension of the Bloemendalerpolder peat, a major source of uncertainty was the definition of tensile parameters for the JMC and NGI-ADP models. Going through the literature, it was evident that only a handful of papers have explored these properties and let alone, produce a comprehensive regional study of the working range of those parameters. To adequately define the anisotropic strain–strength behaviour, it is important to subject the material of interest to an extension stress path (Grimstad et al., 2012), this becomes critical in the case of fibrous peat, where the reinforcement provided by the organic material influences the strength of the material (Muraro, 2019; Yamaguchi et al., 1985). Nonetheless, these tests are uncommon and expensive and thus provide a major limitation in the usage of the model.

To facilitate the use of JMC model in engineering practice and to provide a base reference of the mechanical capabilities of peat in extension, it could be of relevance to develop a country-wide campaign for the characterization of its properties. This process could provide a framework for the correlation of properties to the engineering response or produce a comprehensive reference data set.

9 | References

Alink, E. (2010). *Grondonderzoek, laboratoriumderzoek en plaatsing van instrumentatie*. Fugro GeoServices B.V.

Ammerlaan, P. (2011). *Zettingspredicties betreffende proefterpen Project Boemendalerpolder te Weesp*. Fugro GeoServices B.V.

Biot, M. A. (1941). General theory of three-dimensional consolidation. *Journal of applied physics*, *12*(2), 155–164.

Brinkgreve, R. (1994). *Geomaterial models and numerical analysis of softening* (PhD dissertation). Delft University of Technology. Mekelweg 5, 2628 CD Delft.

Chai, J.-C., & Miura, N. (1999). Investigation of factors affecting vertical drain behavior. *Journal of Geotechnical and Geoenvironmental Engineering*, *125*(3), 216–226.

Cotecchia, F., & Chandler, R. J. (1997). The influence of structure on the pre-failure behaviour of a natural clay. *Géotechnique*, *47*(3), 523–544.

Cotecchia, F., & Chandler, R. (2000). A general framework for the mechanical behaviour of clays. *Géotechnique*, *50*(4), 431–447.

Dao, T. (2011). *Validation of PLAXIS embedded piles for lateral loading* (Master's thesis). Delft University of Technology. Mekelweg 5, 2628 CD Delft.

Den Arend, E. (2010). *Schelpfactoren bij door grond horizontaal belaste palen* (Master's thesis). Delft University of Technology. Mekelweg 5, 2628 CD Delft.

Den Haan, E., & Kruse, G. (2007). Characterisation and engineering properties of Dutch peats. *Proceedings of the Second International Workshop of Characterisation and Engineering Properties of natural soils*, *29*, 2101–2133.

Duncan, J. M., Evans Jr, L. T., & Ooi, P. S. (1994). Lateral load analysis of single piles and drilled shafts. *Journal of geotechnical engineering*, *120*(6), 1018–1033.

Edil, T. B., & Dhowian, A. W. (1981). At-rest lateral pressure of peat soils. *Journal of the Geotechnical Engineering Division*, *107*(2), 201–217.

Flessati, L., Della Vecchia, G., & Musso, G. (2021). Mechanical behavior and constitutive modeling of cement–bentonite mixtures for cutoff walls. *Journal of Materials in Civil Engineering*, *33*(3), 04020483.

Grimstad, G., Andresen, L., & Jostad, H. P. (2012). NGI-ADP: Anisotropic shear strength model for clay. *International Journal for Numerical and Analytical Methods in Geomechanics*, *36*(4), 483–497.

Hanrahan, E. T. (1954). An investigation of some physical properties of peat. *Géotechnique*, *4*(3), 108–123.

Hayashi, H., Yamazoe, N., Mitachi, T., Tanaka, H., & Nishimoto, S. (2012). Coefficient of earth pressure at rest for normally and overconsolidated peat ground in Hokkaido area. *Soils and Foundations*, *52*(2), 299–311.

Hoefsloot, F., & Schadee, L. (2014). *Eindevaluatie zettingsmodellen Project Boemendalerpolder te Weesp*. Fugro GeoServices B.V.

Hoefsloot, F., & Schadee, L. (2016). *Meetresultaten Proefterpen Boemendalerpolder te Weesp*. Fugro GeoServices B.V.

Hoefsloot, F. (2015). Long term monitoring test embankments Bloemendalerpolder-Geo-Impuls program. In *Geotechnical safety and risk v* (pp. 621–627). IOS Press.

Iereidis, C. (2019). *Implementation of the new dutch guidelines on the macrostability assessment of dikes using different constitutive models* (Master's thesis). Delft University of Technology. Mekelweg 5, 2628 CD Delft.

Jaky, J. (1948). Pressure in silos. *Proceedings of the 2nd International Conference on SMGE*, *1*, 103–109.

Kadaster. (2022). *Topotijdreis: 200 jaar topografische kaarten*. Retrieved September 29, 2022, from https://www.topotijdreis.nl/satelliet/2011/@130800,481465,13.56

Landva, A. (1980). Vane testing in peat. *Canadian Geotechnical Journal*, *17*(1), 1–19.

Lefebvre, G., Langlois, P., Lupien, C., & Lavallée, J.-G. (1984). Laboratory testing and in situ behaviour of peat as embankment foundation. *Canadian Geotechnical Journal*, *21*(2), 322–337.

Long, M., Grimstad, G., & Trafford, A. (2022). Prediction of embankment settlement on swedish peat using the soft soil creep model. *Proceedings of the Institution of Civil Engineers-Geotechnical Engineering*, *175*(5), 507–522.

Long, M., Paniagua, P., Grimstad, G., Trafford, A., Degago, S., & L'heureux, J.-S. (2022). Engineering properties of norwegian peat for calculation of settlements. *Engineering Geology*, *308*, 106799.

MacFarlane, I. C. (1969). *Muskeg Engineering Handbook* (tech. rep.). Univeristy of Toronto Press.

Matlock, H. (1970). Correlation for design of laterally loaded piles in soft clay. *Offshore technology conference*.

Mesri, G., & Ajlouni, M. (2007). Engineering properties of fibrous peats. *Journal of Geotechnical and Geoenvironmental Engineering*, *133*(7), 850–866.

Muraro, S., & Jommi, C. (2020). Pre-failure behaviour of reconstituted peats in triaxial compression. *Acta Geotechnica*, *16*(3), 789–805.

Muraro, S. (2019). *The deviatoric behaviour of peat: A route between past empiricism and future perspectives* (PhD dissertation). Delft University of Technology. Mekelweg 5, 2628 CD Delft.

O'Kelly, B. C., & Pichan, S. P. (2013). Effects of decomposition on the compressibility of fibrous peat—a review. *Geomechanics and Geoengineering*, *8*(4), 286–296.

Papadaki, E. (2013). *Modelling of peat compressed under sand bodies: Experimental and numerical approach* (Master's thesis). Delft University of Technology. Mekelweg 5, 2628 CD Delft.

Plaxis. (2022a). *Material models manual*. Version 22.01. Bentley Systems, Incorporated.

Plaxis. (2022b). *Plaxis 3D-reference manual*. Version 22.01. Bentley Systems, Incorporated.

Plaxis. (2022c). *Scientific manual*. Version 22.01. Bentley Systems, Incorporated.

Rankine, W. J. M. (1857). II. On the stability of loose earth. *Philosophical transactions of the Royal Society of London*, (147), 9–27.

Schadee, L. (2012). *Paalfundaties onderworpen aan tijdsafhankelijke horizontale belastingen door zachte bodems* (Master's thesis). Delft University of Technology. Mekelweg 5, 2628 CD Delft.

Siderius, K. (2011). *Tijdsafhankelijke effecten bij door grond horizontaal belaste palen* (Master's thesis). Delft University of Technology. Mekelweg 5, 2628 CD Delft.

Skemption, A., & Northey, R. (1952). The sensitivity of clays. *Geotechnique*, *3*(1), 30–53.

Tavenas, F., Tremblay, M., Larouche, G., & Leroueil, S. (1986). In situ measurement of permeability in soft clays. *Use of In Situ Tests in Geotechnical Engineering*, 1034–1048.

Taylor, D. W. (1984). *Fundamentals of soil mechanics*. John Wiley; Sons.

Vermeer, P., & Neher, H. (1999). A soft soil model that accounts for creep. In *Beyond 2000 in computational geotechnics* (pp. 249–261). Routledge.

Wood, D. M. (1991). *Soil behaviour and critical state soil mechanics*. Cambridge University Press. https://doi.org/10.1017/CBO9781139878272

Yamaguchi, H., Ohira, Y., Kogure, K., & Mori, S. (1985). Undrained shear characteristics of normally consolidated peat under triaxial compression and extension conditions. *Soils and Foundations*, *25*(3), 1–18.

Zeitoun, D. G., & Wakshal, E. (2013). Biot's theory of consolidation. In *Land subsidence analysis in urban areas: The bangkok metropolitan area case study* (pp. 119–174). Springer Netherlands.

Zhang, P., Guan, Q., & Li, Q. (2013). Mechanical properties of plastic concrete containing bentonite. *Research Journal of Applied Sciences, Engineering and Technology*, *5*(4), 1317–1322.

Zwanenburg, C., & Jardine, R. (2015). Laboratory, in situ and full-scale load tests to assess flood embankment stability on peat. *Géotechnique*, *65*(4), 309–326.

Appendix

A Verification of the JMC model implementation in Plaxis 3D

The aim of this phase of the procedure is to ensure that the implementation of the code within the Plaxis 3D environment is consistent with that of ABAQUS Unified FEA. As previously mentioned, the competence of the JMC model in the latter was demonstrated by Muraro (2019) using the parameters shown in Table A.1 and as such, these results are used as a frame of reference during verification. Consequentially, the assembly of analogous conditions to the ABAQUS Unified FEA model is required despite the fact that the available tools and boundary conditions differ between software, which implicitly limits an exact replica of the reference model.

Table A.1: Reference parameters for the elemental testing of the JMC model

c_M	e_0	D_0	D_1	p_0	p_{atm}	p_{ref}	p_{tmult}	$M_{g,c}$	$M_{f,c}$	κ^*	λ^*	ν	χ_f	χ_g
-	-	-	-	kPa	kPa	kPa	-	-	-	-	-	-	-	-
0.632	10	0.0	0.0	15	100	1.0	0.0	1.75	1.50	0.03	0.20	0.3	2.0	0.98

The assessment is subdivided in three stages of dynamic testing: the assurance of the code stability of a single integration point (1), the reliability of nodal relations within a volume cluster (2), and the consistent interaction with other materials and FEM elements in the domain (3). For the evaluation of the first two, a comparison between the elastoplastic analysis from each software is performed. This quantitative analysis has to ensure that behaviour of the stress-strain response (*log p' - ϵ_v*) and the effective mean-to-deviatoric stress relation (*p' - q space*) is equal. Following these phases, the usage feasibility of the built-in components of Plaxis 3D along with the JMC model is tested, by varying the analysis methodology to a coupled process and including additional layers and structural elements into a fictitious consolidation case.

A.1 Integration Point

The adequate implementation of a constitutive model within a FEM environment has to be initially evaluated by means of a single-point algorithm, where the response of an individual stress point to stress and strain changes is studied. In this isolated state, the fundamental nodal equations model is solved along with the constitutive by preserving the equilibrium with prescribed external forces. Boundary and domain constraints of the material's behaviour, such as pore pressure or self-weight are excluded from the analysis.

Two sets of stress conditions are evaluated, so that together may allow for a holistic assessment of the stability of the model. In the first case the sample is subjected to isotropic consolidation from a starting mean effective stress of 5.0 kPa up to 100.0 kPa, from that point onward a deviatoric behaviour is simulated by either loading or unloading in the vertical direction until the node has bear 10.0 % of strain. Similarly, the second case also starts from an initial isotropic state of 5.0 kPa, but the stress path follows k_0 consolidation up to 100.0 kPa; once more the sample perceives loading or unloading up to a prescribed stain of 10.0 %.

This portion of the validation procedure is executed in the *Soil Test* complementary testing module of Plaxis 3D. This extension comes with some inherent limitations, namely the unviable initiation of an undrained stress path emulating that of an undrained triaxial test from an inhomogeneous stress state (Plaxis, 2022a). Moreover, the more generic tool to simulate more complex stress conditions is bound by a binary selection of either drained or undrained, which makes the recreation of the combination of k_0 path with undrained compression/extension impossible.

Considering the aforementioned limits, the isotropic consolidation case is reduced to a theoretical consolidation of 100.0 kPa, from which undrained loading and unloading can start. Figure A.1a depicts the stress evolution starting from this magnitude, as it faithfully follows the results from ABAQUS Unified FEA. The isotropic and k_0 consolidation paths are tested independently, with the remaining assortment of sub-figures proving the fidelity of the results under these conditions.

Figure A.1: Validation of the JMC model for a single integration point

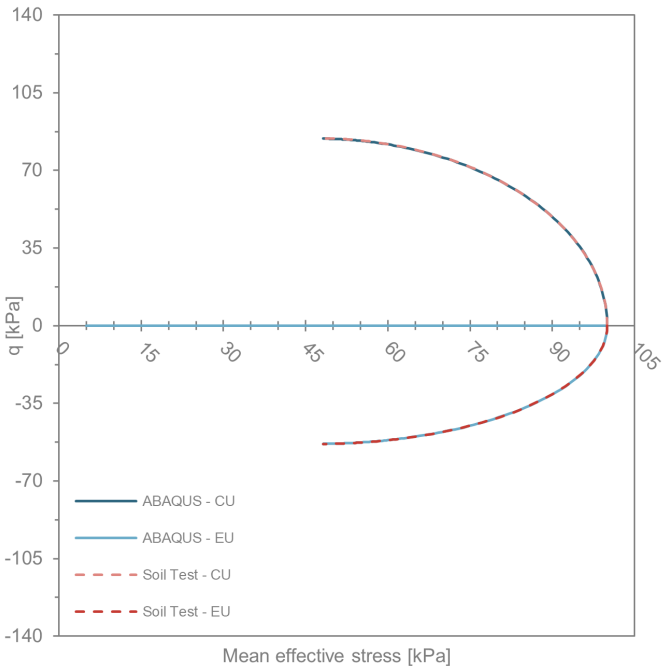

(a) Stress conditions during undrained compression

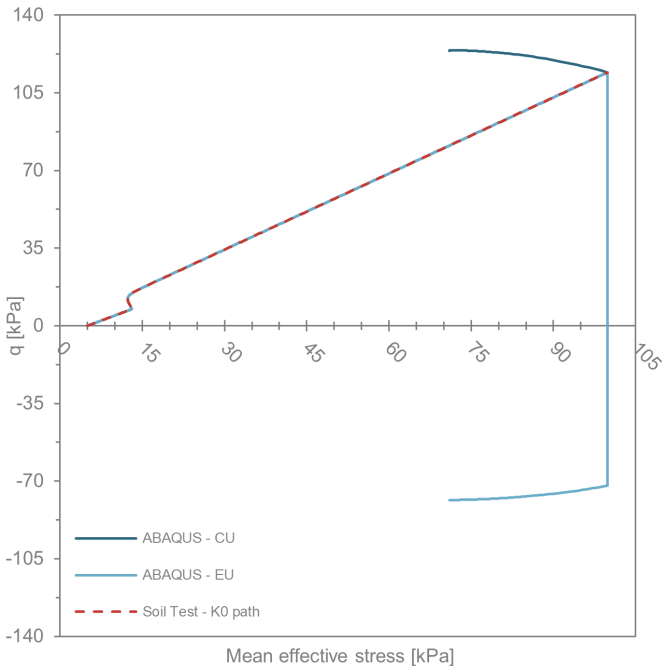

(b) Stress conditions during K_0 consolidation

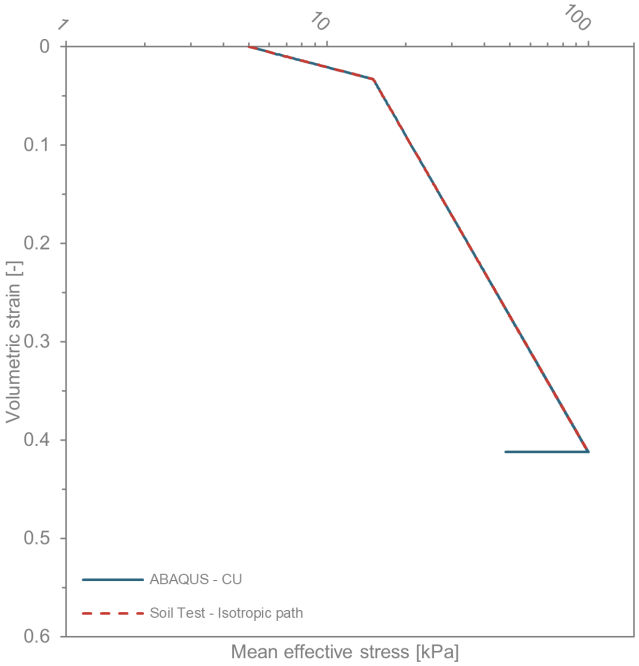

(c) Strain evolution in isotropic consolidation

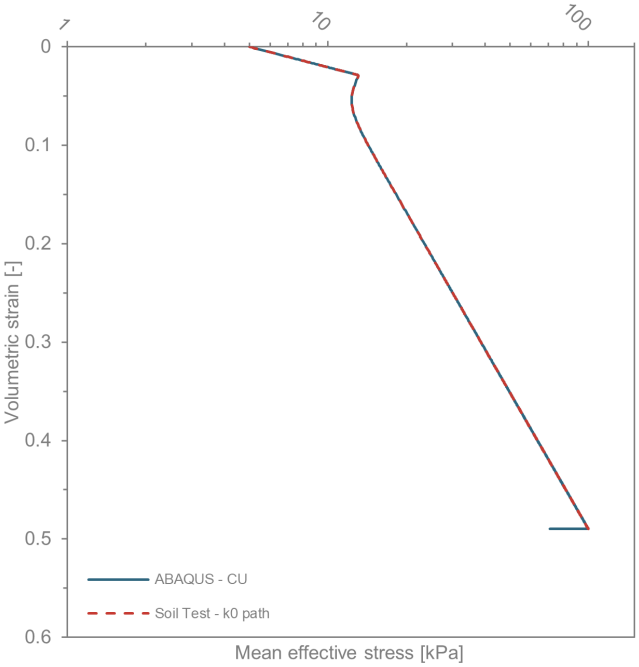

(d) Strain evolution in K_0 consolidation

A.2 Volume cluster

The testing of the constitutive model builds upon the stability of a single integration point by expanding the verification into the three-dimensional space. The effective execution of this step requires the translation of the established conditions from Section A.1 to a volumetric domain. Once again, a successful result is bound to how closely the output relates

to that of ABAQUS Unified FEA. Considerable advantage over the single integration point algorithm is the absence of practical limits to the stress path simulation.

The testing of a three-dimensional element is done by means of an elastoplastic deformation analysis following the small-strain theory. Hence, all the perceived changes in the volume are calculated with respect to the original meshing arrangement. The model is composed solely of a 1.0 m^3 cube, to which the JMC model is assigned, along with the material properties described in Table A.1. The volume is further subdivided in 10-noded tetrahedrons with a *relative element size factor* of 10 (Figure A.2).

At the boundaries of the domain, the deformation conditions vary as a function of the calculation phase as shown in Table A.2. The drainage conditions are declared as *open* throughout the calculations in the elastoplastic analysis, as it does not account for a coupled formulation and therefore, renders a change in the water flow bounds as inconsequential. Additionally, to ensure that the influence of groundwater remains idle, the pressure head is positioned at the base of the geometry.

During the parametric declaration of the material, it is possible to state the drainage type as an *Undrained (A)*, in this fashion, the software makes use of effective parameters for stiffens and strength (Plaxis, 2022b). Nonetheless, for the emulation of the loading setup of the original tests, a change in material behaviour is needed between a drained state during consolidation and an undrained state at the deviatoric phases. The distinction between either behaviour is done by the binary declaration at each loading phase of either using the declared behaviour or *ignore undrained behaviour* of the material.

Figure A.2: Element distribution in meshing procedure

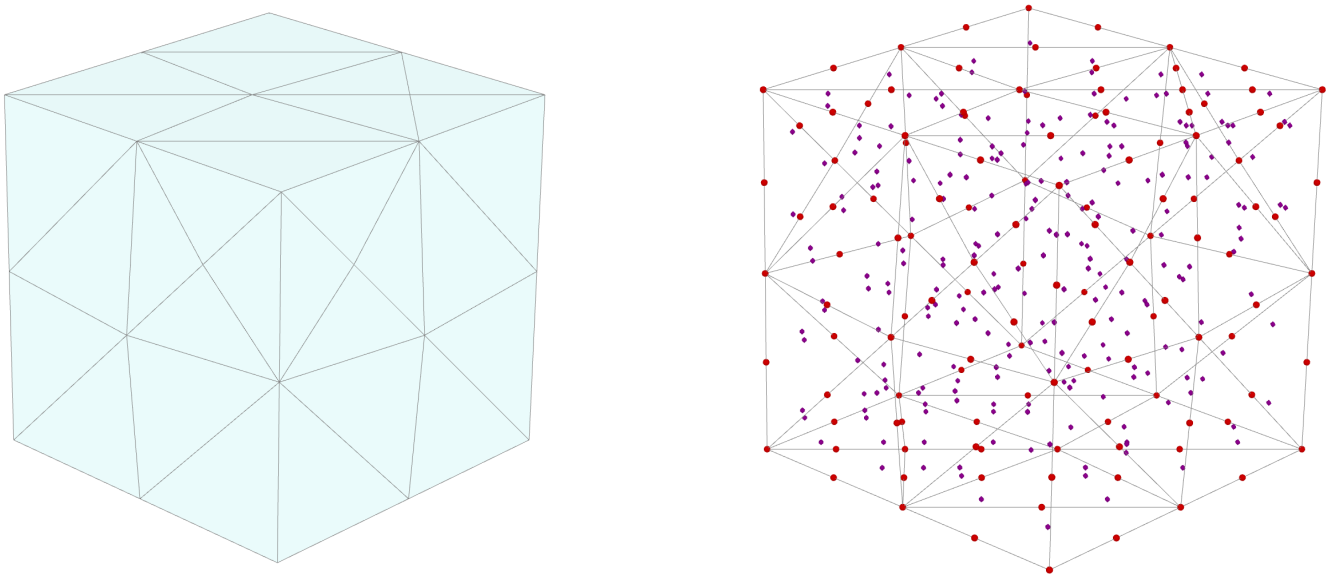

(a) Element contours

(b) Stress points and nodes

Complementary to the volume element, the stress conditions can be introduced by a uniform load or a prescribed displacement. The characterization of such forces is done by creating surface elements at the sides of the cube perpendicular to each major direction. These elements can be defined as:

- *Surface load*. A static load with a uniform perpendicular distribution ($\sigma_{n,ref}$) is assigned to the full extent of the surface geometry. The magnitude of this component is defined as the maximum total stress to be attained.
- *Surface prescribed displacement*. A uniform distribution of a static displacement is applied to the entire surface geometry. The value of the deformation is defined in terms of a distance that can be positive or negative simulating the necessary translation. Depending on the direction of interest, the displacement of the complementary axes is set to be free.

The foregoing boundary considerations and elements converge in the model in the form of loading phases. That is, they influence the volumetric cluster as a combination of components that is instantaneously applied in a sequencing manner (Table A.2). In general, the four cases of interest start from an initial phase where the three surface loads exert 5.0 kPa isotropically; at this point, the displacements and state variables are reset and thus become the basis for the actual loading of the sample. Then, while ignoring the designation of undrained behaviour, the sample can follow either an isotropic or a k_0 consolidation until an effective mean stress of 100.0 kPa; the selection of one or the other implies a

change in boundary conditions and the usage of surface loads. Lastly, a deviatoric phase follows with a simultaneous change in the stress conditions in the vertical direction and the release of all constraints in the horizontal directions. The vertical adjustment can come either from a surface-prescribed displacement or a surface load.

Table A.2: Phasing conditions for volume cluster testing

Plane	XY_{min}	XY_{max}	XZ_{min}	XZ_{max}	YZ_{min}	YZ_{max}
	Phase 1.0: Raise to initial condition					
Boundary	N.F.	Free	N.F.	Free	N.F.	Free
Loading	-	5.0 kPa	-	-5.0 kPa	-	5.0 kPa
Displacement	-	-	-	-	-	-
	Phase 2.1: Isotropic consolidation					
Boundary	N.F.	Free	N.F.	Free	N.F.	Free
Loading	-	100.0 kPa	-	-100.0 kPa	-	100.0 kPa
Displacement	-	-	-	-	-	-
	Phase 2.2: k_0 consolidation					
Boundary	N.F.	Free	N.F.	N.F.	N.F.	N.F.
Loading	-	176.0 kPa	-	-	-	-
Displacement	-	-	-	-	-	-
	Phase 3.1: Deviatoric loading					
Boundary	N.F.	Free	N.F.	Free	N.F.	Free
Loading	-	-	-	-	-	-
Displacement	-	-0.1 m	-	-	-	-
	Phase 3.1: Deviatoric unloading					
Boundary	N.F.	Free	N.F.	Free	N.F.	Free
Loading	-	-	-	-	-	-
Displacement	-	0.1 m	-	-	-	-

[1] N.F. - Normally fixed

The numerical control parameters are paramount in the faithful reproduction of the stress-strain evolution under the effect of the foregoing components. Considering that the default iteration parameters favor computational time, the precision of the output is compromised, especially in terms of the automatic load stepping. Despite the adequate formulation of the boundary conditions, the *tolerated error* between iterations had to be set to 1.0 E^{-3}, while the *load fraction per step* was minimized to a magnitude of 5.0 E^{-3}.

The usage of two relevant tools from Plaxis 3D was necessary for the successful outcome of the volume cluster analysis. Firstly, the *arc-length control* procedure was kept active as per recommendation from Plaxis (2022b), as this case is a load-controlled analysis with considerable plastic behaviour, which otherwise would not be allowed to converge. In comparison, the *over-relaxation factor*, which is employed as an optimization procedure based on the "deliberate over-estimation of the equilibrium error", had to be reduced to a value of 0.8. In essence, this value allows for an oscillatory approximation around the exact solution that relays on the extrapolation from the previous iteration (instead of the usual initial stress method) so that the numerical unbalance is resolved in fewer steps. However, in the case of the JMC model, using a higher value of *over-relaxation factor* introduced instabilities when reaching the pre-consolidation stress (p_0) during k_0 consolidation. Another approach to resolve the convergence complication could be to allow a higher number of unloading steps, which alters considerably the stress evolution of the sample.

The resulting stress paths in the *log p'* - ϵ_v and *p'* - *q* spaces are depicted in the following figure .

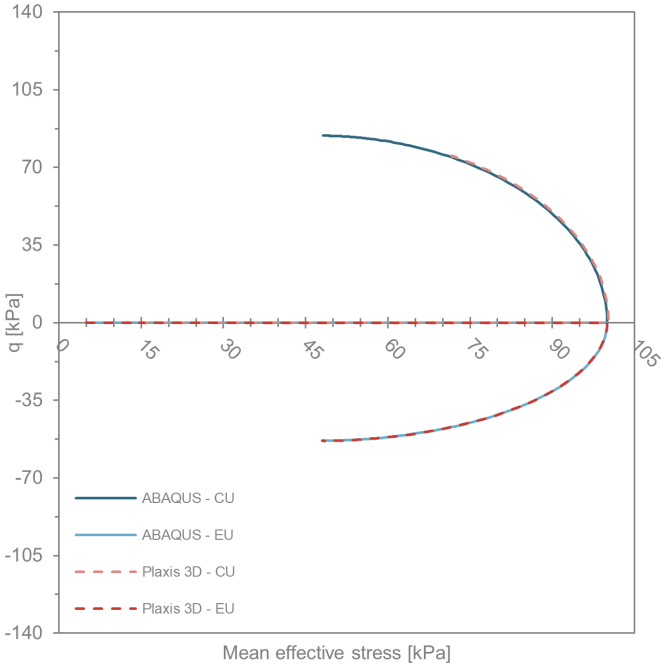

(a) Stress conditions during undrained compression

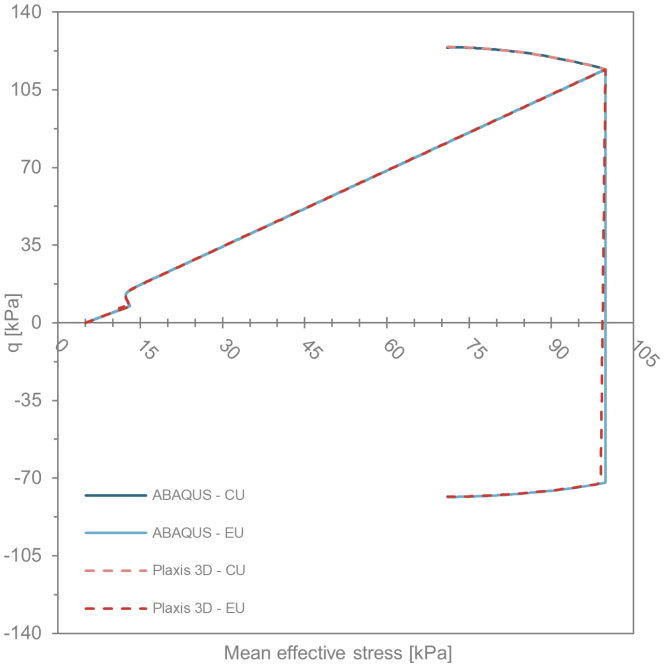

(b) Stress conditions during K_0 consolidation

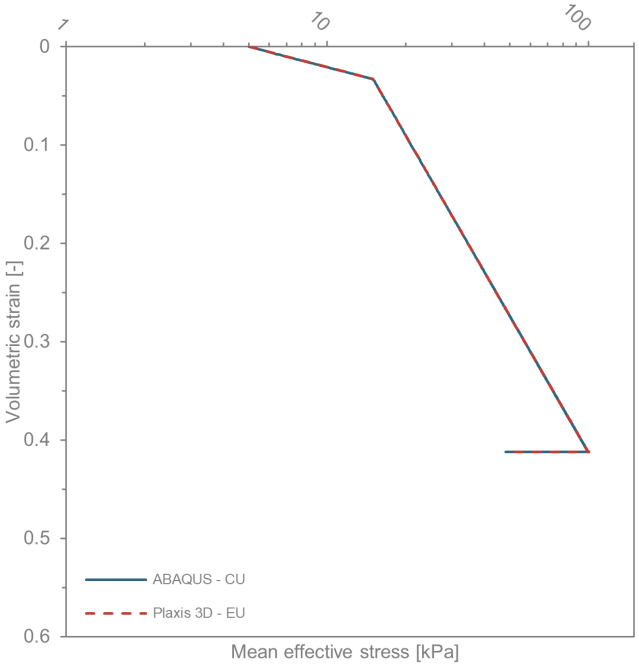

(c) Strain evolution in isotropic consolidation

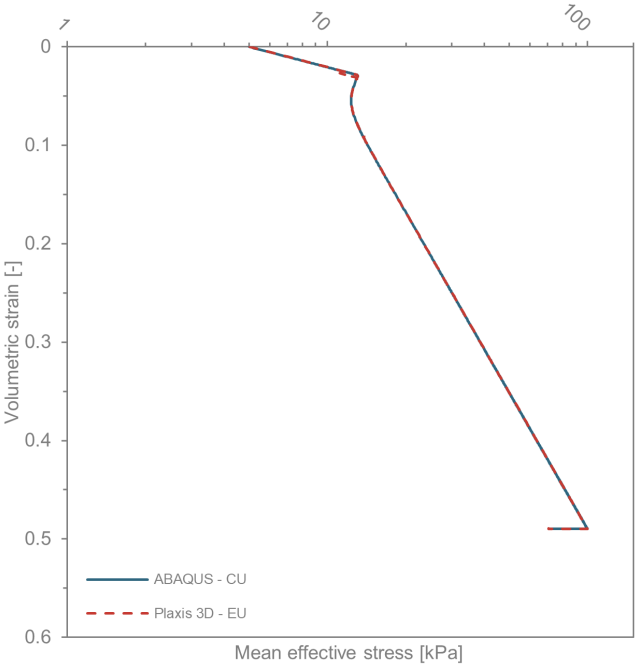

(d) Strain evolution in K_0 consolidation

Figure A.3: Validation of the JMC model for a volume cluster

B Simulation of CU triaxial tests

The present section aims to understand the extent of the capability of the JMC model to describe the response of the peat at the Bloemendalerpolder field. Given this directive, each individual CU triaxial test is simulated using the best-fit parameters of the model so that a working range for the calibration of the model can be defined. The summary of the procedure is displayed in Table B.1, followed by the results of each individual test and their estimation using the constitutive model.

The procedure is executed in the *Soil Test* module from Plaxis, by employing the single Gaussian point simulation of a triaxial test. The type of test is an isotropically consolidated undrained test. To each test, there is a corresponding initial cell pressure (referred in Table B.1 as σ_0) and a measured axial strain (ϵ_a), which are used as input conditions.

Table B.1: CU Triaxial Parameters

Sample	σ_0	ϵ_a	M_g	χ_g	M_f	χ_f
	kPa	%	-	-	-	-
LN3 - 1[1]	11.0	15.89	1.05	0.812	1.28	1.800
LN3 - 2	23.0	16.42	2.48	0.590	1.59	3.000
LN3 - 3	42.0	15.27	1.09	0.828	0.98	1.400
LN4 - 1	13.0	16.51	2.36	0.680	1.50	2.300
LN4 - 2	21.0	20.14	2.32	0.707	1.20	2.300
LN4 - 3	42.0	21.53	0.98	0.781	0.72	1.900
LN10 - 1[1]	11.0	18.94	2.50	0.573	1.58	3.700
LN10 - 2	23.0	16.59	0.95	0.767	0.61	1.200
LN10 - 3	42.0	18.20	0.84	0.708	0.63	1.600
LN11 - 1	13.0	15.76	1.08	0.824	1.10	1.300
LN11 - 2	25.0	17.69	1.10	0.832	0.76	1.100
LN11 - 3	50.0	15.72	1.01	0.795	0.85	1.400
LN12 - 1[1]	15.4	16.05	-	-	-	-
LN12 - 2	31.0	22.49	1.52	0.927	1.18	2.000
LN12 - 3	62.0	15.72	1.12	0.840	1.08	3.000
Average	-	-	1.40	0.773	1.08	2.000
Estimation	-	-	1.06	0.816	0.85	2.500

[1] Disregarded due to erratic behaviour during testing

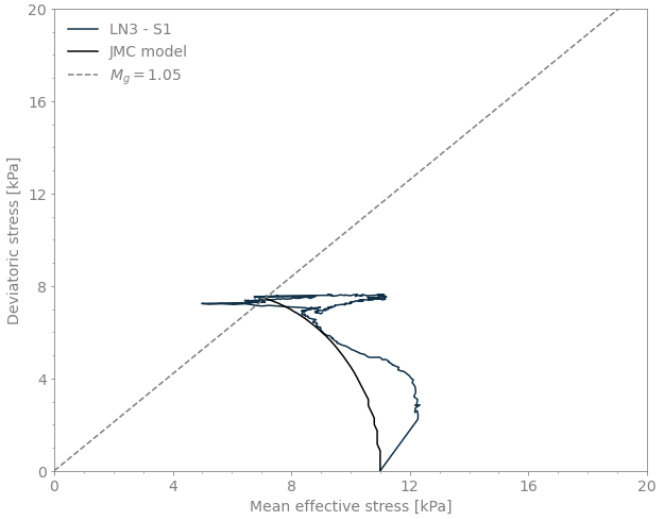

(a) S1 - Stress path

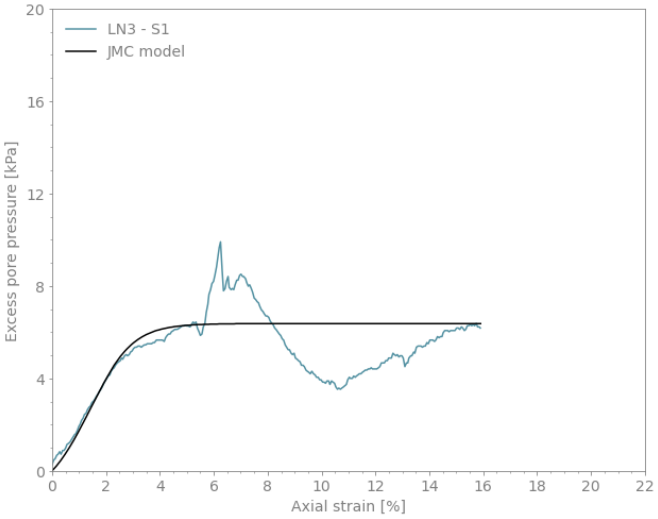

(b) S1 - Excess pore pressure - axial strain relation

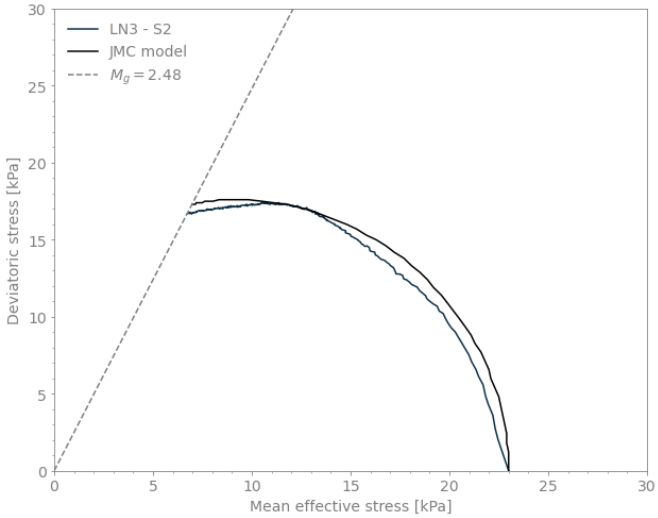

(c) S2 - Stress path

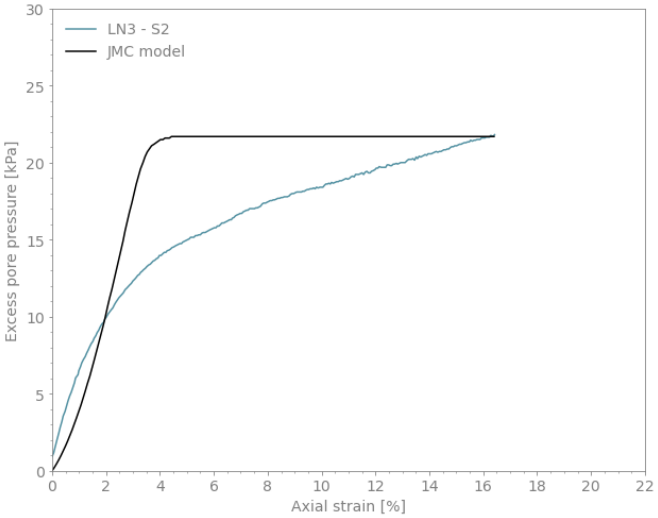

(d) S2 - Excess pore pressure - axial strain relation

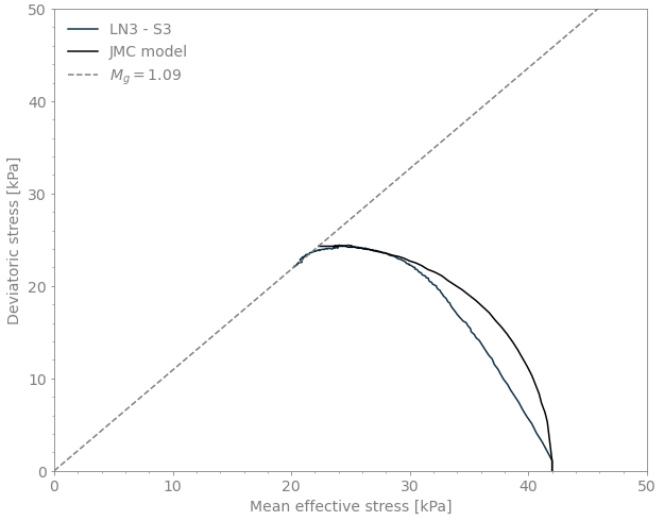

(e) S3 - Stress path

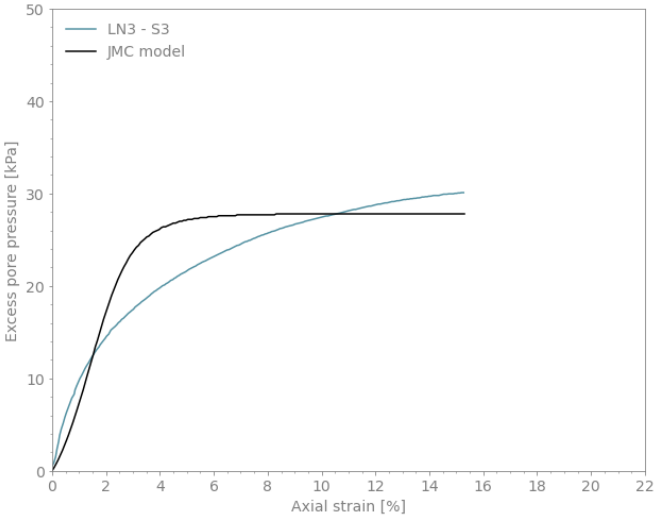

(f) S3 - Excess pore pressure - axial strain relation

Figure B.1: Simulation of CU triaxial tests of sample LN3

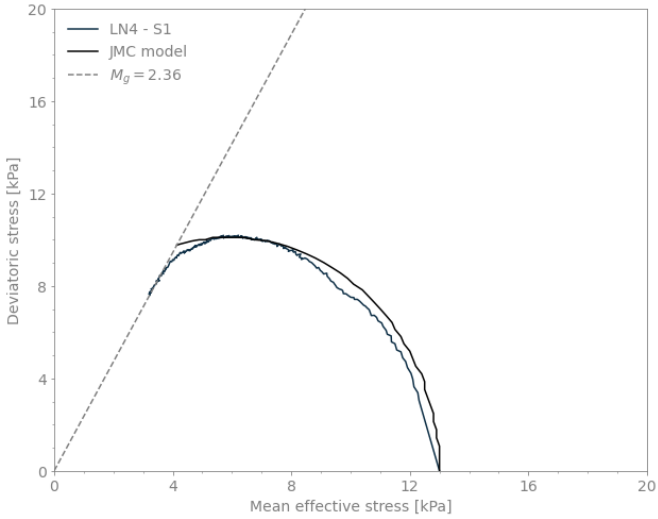

(a) S1 - Stress path

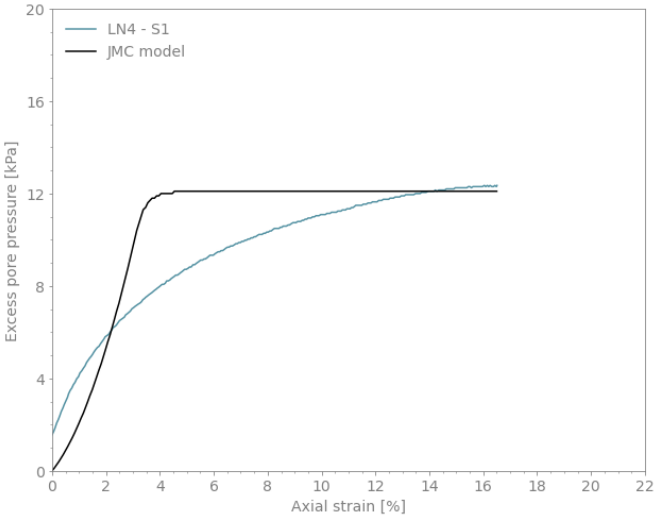

(b) S1 - Excess pore pressure - axial strain relation

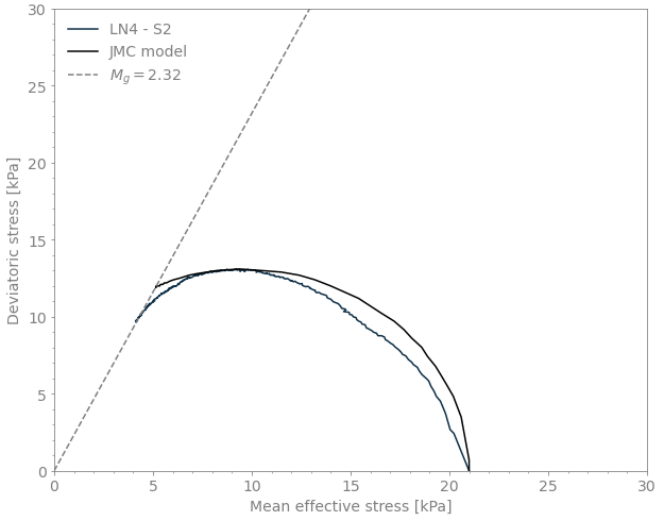

(c) S2 - Stress path

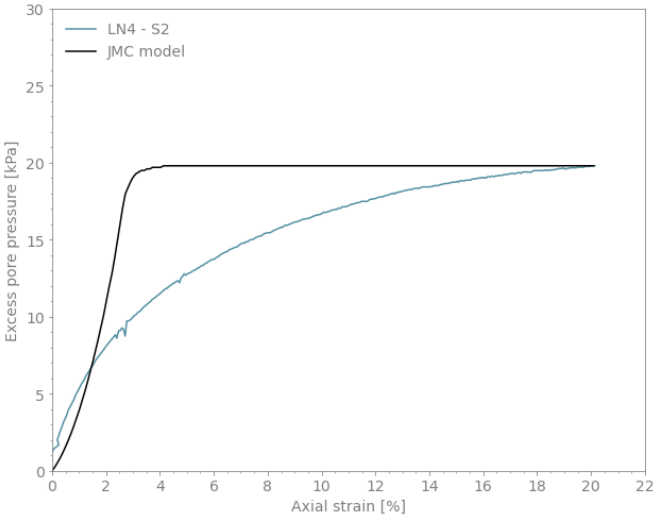

(d) S2 - Excess pore pressure - axial strain relation

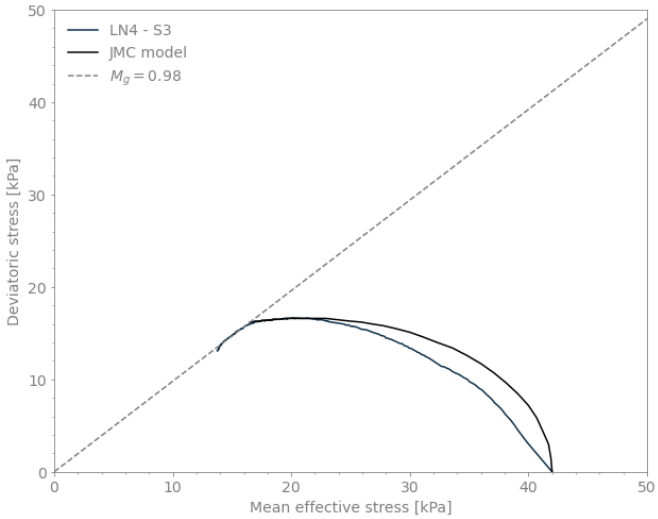

(e) S3 - Stress path

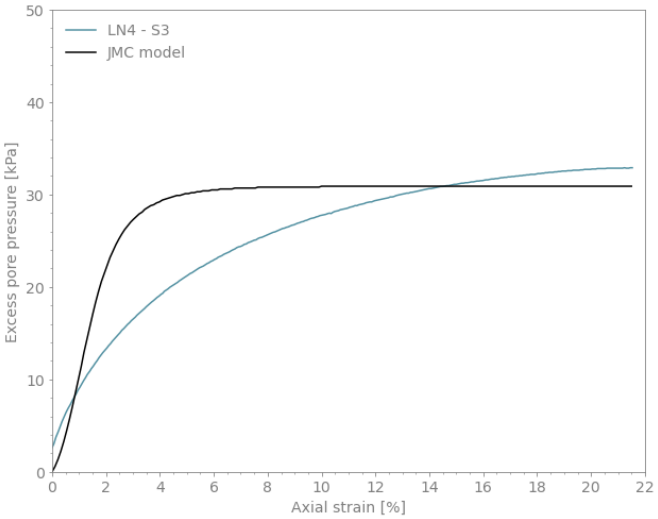

(f) S3 - Excess pore pressure - axial strain relation

Figure B.2: Simulation of CU triaxial tests of sample LN4

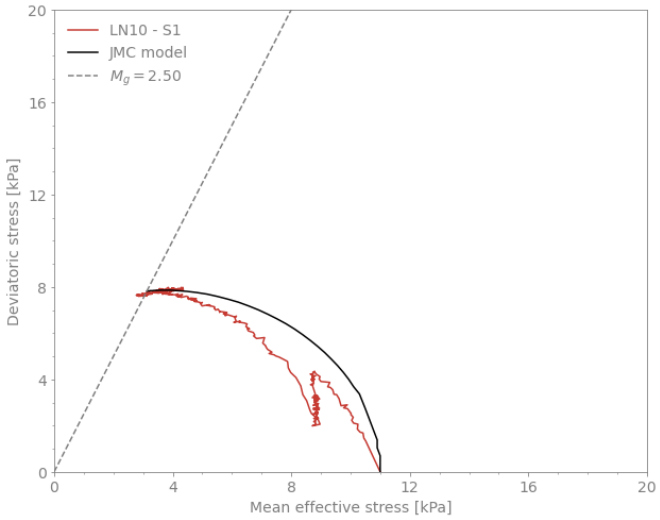

(a) S1 - Stress path

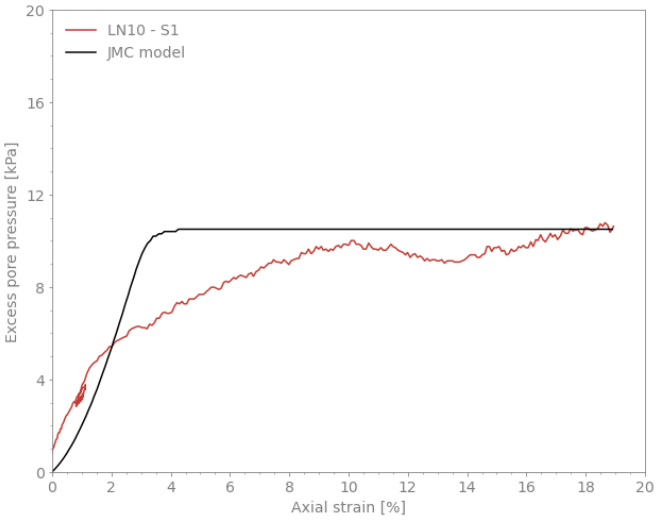

(b) S1 - Excess pore pressure - axial strain relation

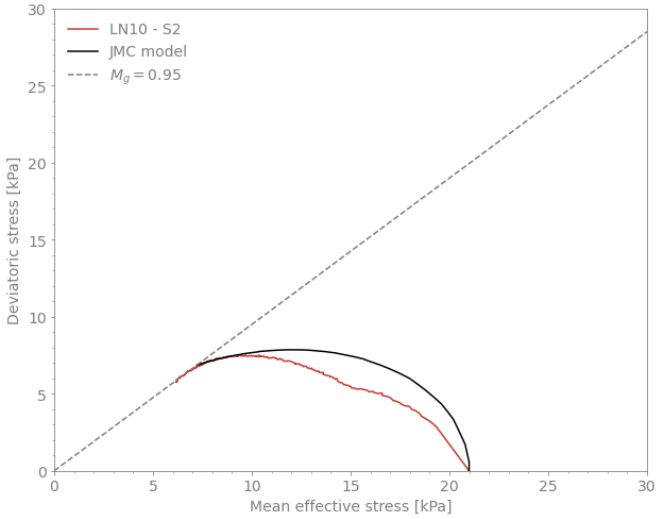

(c) S2 - Stress path

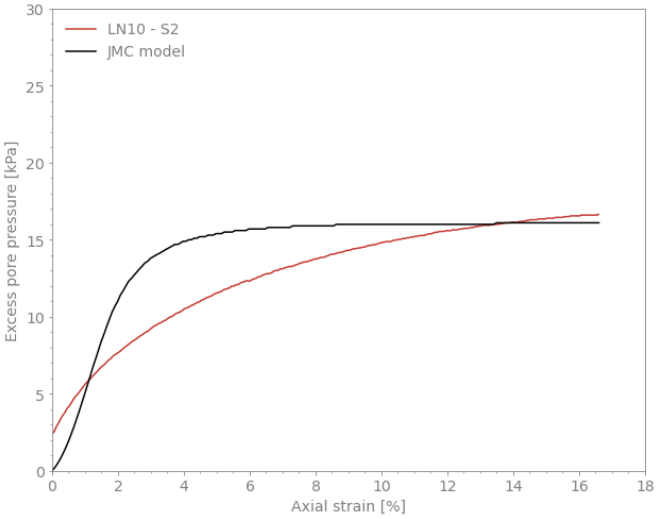

(d) S2 - Excess pore pressure - axial strain relation

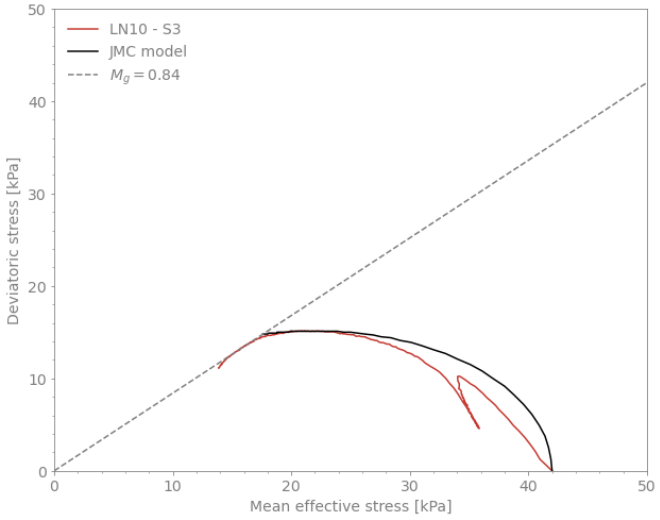

(e) S3 - Stress path

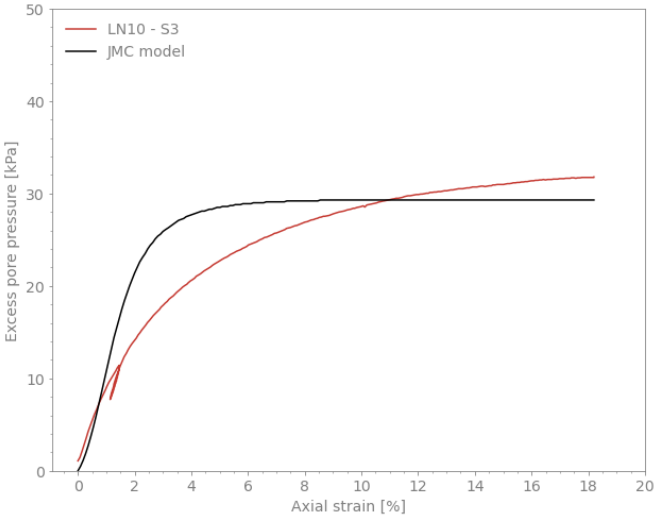

(f) S3 -Excess pore pressure - axial strain relation

Figure B.3: Simulation of CU triaxial test of sample LN10

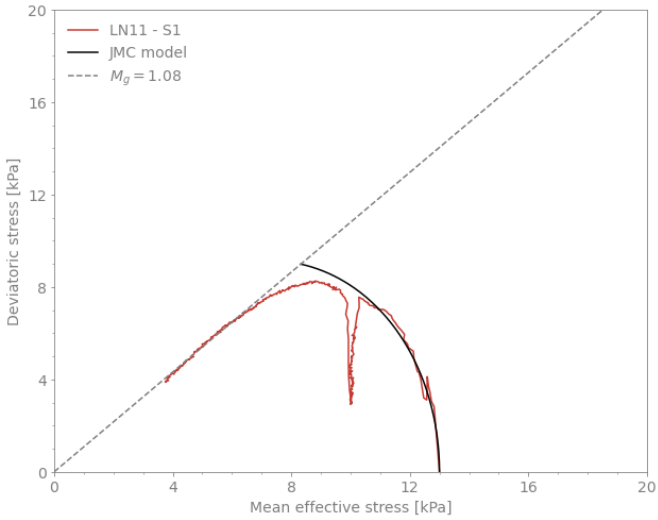

(a) S1 - Stress path

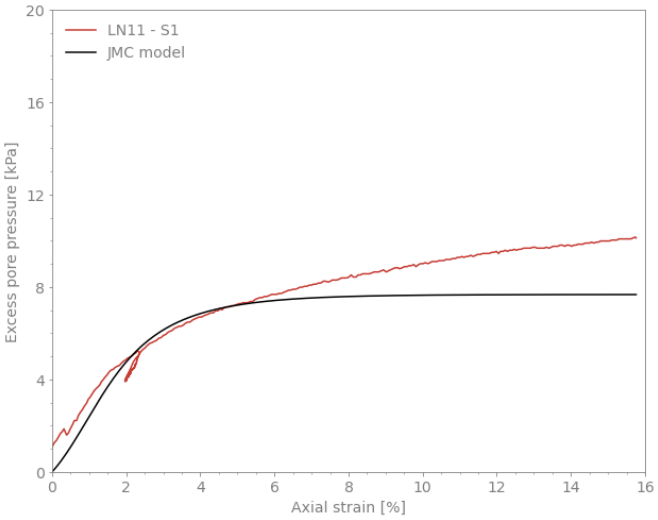

(b) S1 - Excess pore pressure - axial strain relation

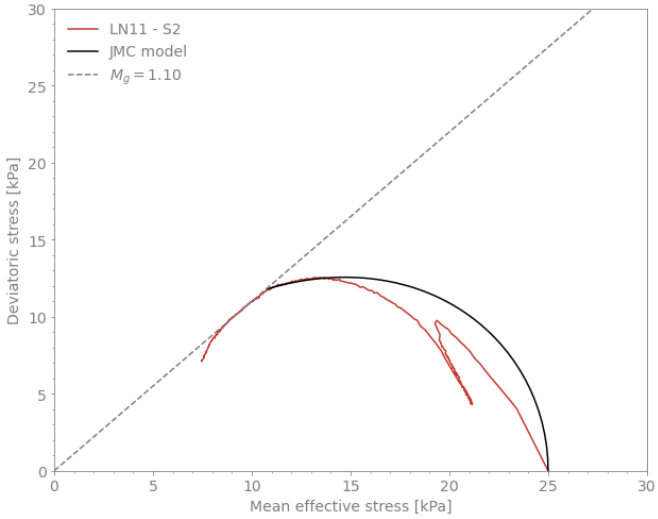

(c) S2 - Stress path

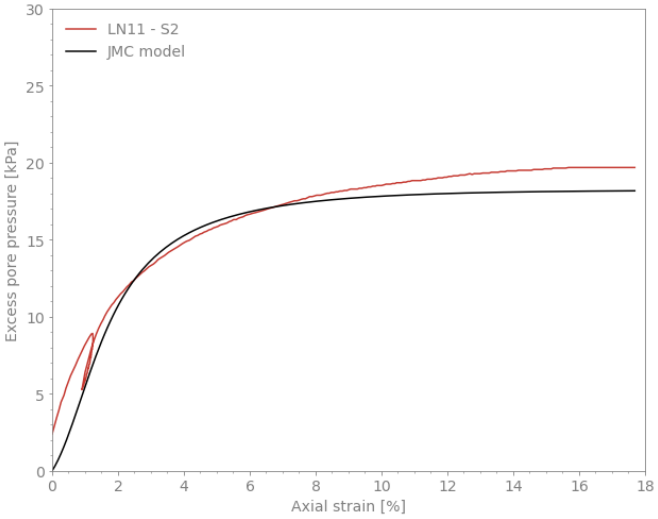

(d) S2 - Excess pore pressure - axial strain relation

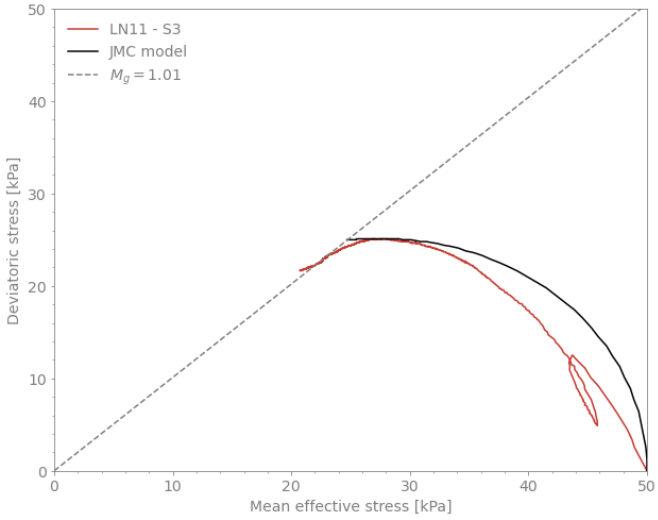

(e) S3 - Stress path

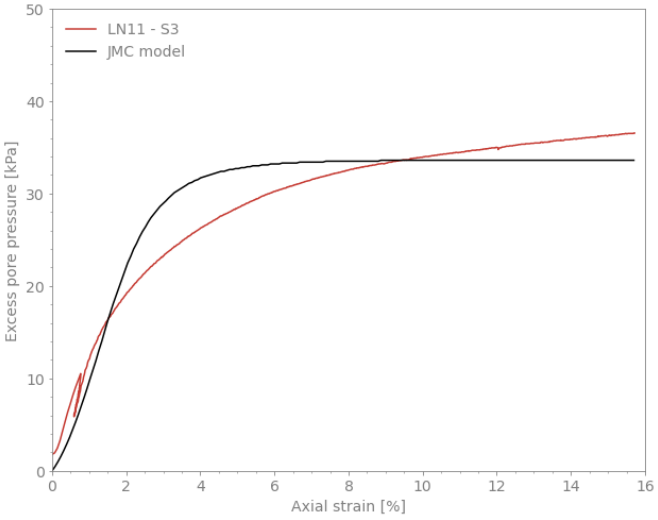

(f) S3 - Excess pore pressure - axial strain relation

Figure B.4: Simulation of CU triaxial test of sample LN11

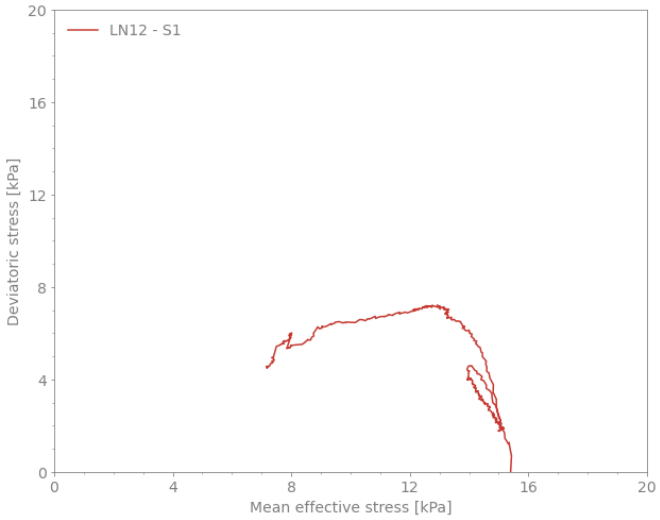

(a) S1 - Stress path

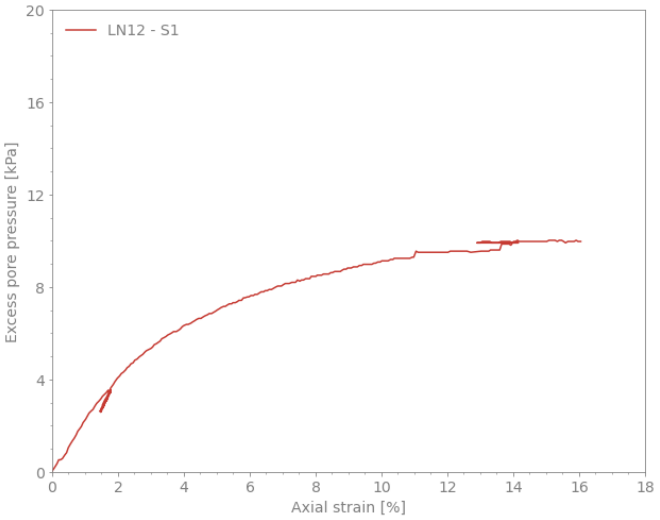

(b) S1 - Excess pore pressure - axial strain relation

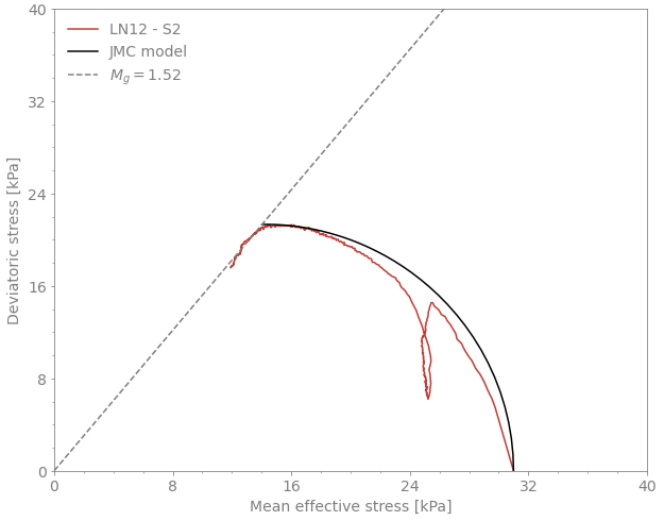

(c) S2 - Stress path

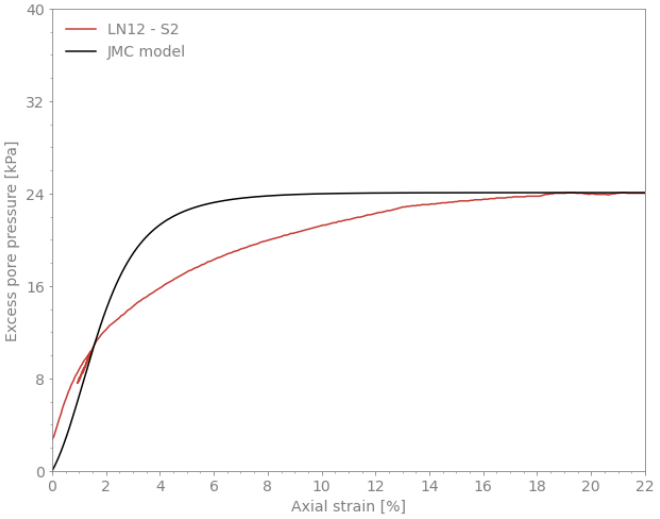

(d) S2 - Excess pore pressure - axial strain relation

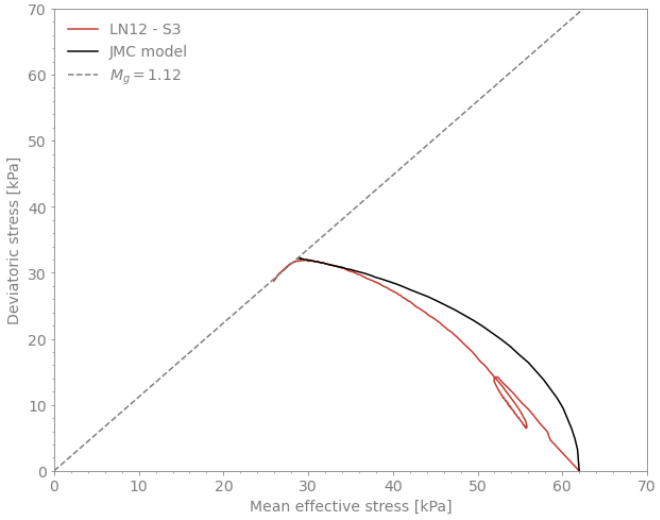

(e) S3 - Stress path

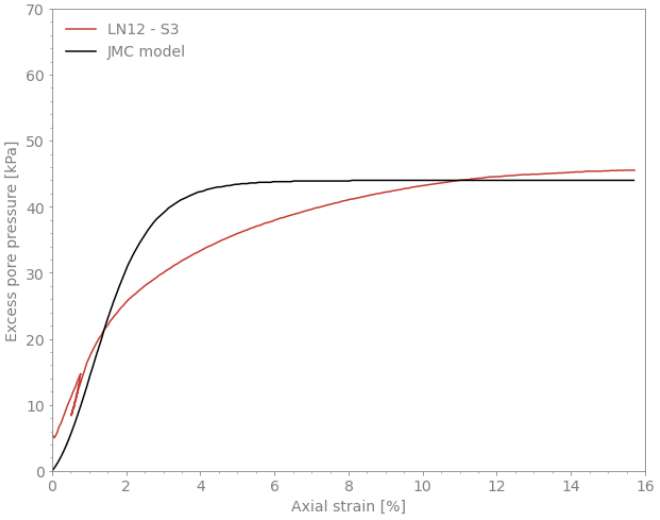

(f) S3 - Excess pore pressure - axial strain relation

Figure B.5: Simulation of CU triaxial test of sample LN12

C Simulation of constant displacement tests

When dealing with highly compressible soils, and more specifically with peat, an outstanding criticism of the K_0-CRS test is the variability of the perceived strain rates over the entire span of the test. Such materials will inevitably perceive a considerable restructuration of their matrix and as a consequence, the void ratio and the stiffness of the soil will vary greatly from their initial state. As a consequence, the strain rate corresponding to a prescribed displacement at the early stages of the test will be significantly different from that approaching the end of it.

Some of the sources of unreliability were also found in the reported stress conditions as they displayed two relevant limitations, the lack of a consistent initial stress point and an erratic measurement of the lateral stresses. Relative to the initial state, considering that the records begin with the initial movement of the cell, the lapse between this and the moment of contact with the sample introduces noise into the measurements (S. Muraro, personal communication). Parallely, the measurements of the horizontal stresses appear to be negative in some portions of the tests, which could signify a lack of contact between the apparatus and the sample. Because this registry is linked to the calculation of the K_0 and consequentially to the mean effective stress, these values are considered as unreliable.

In regards to the pore pressure measurements of the device, it can be argued that any reading at the lower threshold ($\approx$ 0.5 kPa) is subject to debate. This can be attributed to the fact that a low confinement levels, the condition of the soil might not be regarded as completely saturated. It is not until the voids within the soil are fully deprived of a gaseous phase that the behaviour of water is deemed characteristic of the material. Thus, these readings are only a reflection of the upper boundary of the actual hydraulic conductivity (C. Jommi, personal communication). Proof of this can be appreciated in the initial portion of various tests, where the trend of the pore pressure remains unchanged regardless of the linear increase in axial strain.

As a response to the uncertainty provided by these considerations, the present analysis makes use of a time-dependent consolidation FEM analysis employing the known data from the test. The usage of this numerical approximation to simulate the stress-strain conditions of which the input, output, and boundaries are known, provides a reliable framework to better evaluate the parametric values of the material and assure a better calibration of the model (Long, Paniagua, et al., 2022). Furthermore, doing so in the FEM environment of interest reassures the validity of the model's capabilities to replicate the behaviour of the soil within the software.

The use of a time-dependent consolidation assessment is possible by comparing the measurements of pore pressure and displacement throughout the K_0-CRS tests, as the evident correlation between the vertical deformation and the excess water pressure in the sample, is indicative of such process. Two distinct behaviours can be appreciated relative to this phenomenon: the accumulation of excess pore pressure as an undrained response to the vertical displacement acting on the soil; and the pore pressure dissipation during the so-called "relaxation phases", where the samples perceive no further deformation and the time-dependent restructuration of the matrix is the sole regulator. Each of these can then be further related to a fundamental component of the hydro-mechanical coupling, with the relaxation process as evidence of the stiffness of the material and the excess pore pressure generation proportionally related to the hydraulic conductivity (C. Jommi, personal communication).

C.1 Model

The three-dimensional models for the tests are assembled using a square prism of 0.1 by 0.1 meters, with a varying height that depends on the reported value of each case (Table C.3). Additional to the volume cluster, a surface element of equal area is introduced, to which a prescribed displacement can be later assigned. This *surface displacement* tool has a uniform distribution that allows to emulate the displacement perceived during the tests, without the need of translating those magnitudes into equivalent stress. On the other hand, the boundary conditions are constant throughout the phases and obey the specifications of Table C.1.

Table C.1: Model conditions for the emulation of K_0-CRS tests

Plane	XY_{min}	XY_{max}	XZ_{min}	XZ_{max}	YZ_{min}	YZ_{max}
Boundary	N.F.	Free	N.F.	N.F.	N.F.	N.F.
Flow	Open	Closed	Closed	Closed	Closed	Closed
Displacement	-	Varying	-	-	-	-

[1] N.F. - Normally fixed

The selected calculation type is *consolidation* using a *staged construction* type of loading, which is complemented with a *steady-state groundwater flow* pore pressure calculation. This allows to perform an elastoplastic consolidation analysis

based on the hydraulic conditions at the boundaries at the end of the previous calculation phase and thus enables a fully-coupled calculation in all steps (Plaxis, 2022b). In terms of the numerical control parameters, they are modified to favor precision over computational time. The *over-relaxation factor* is reduced to unity, the *tolerated error* for each iteration is set to 1.0 E^{-3} and the *load fraction per step* is limited to 0.05 to prevent inaccuracies in the numerical approximation.

For the input values of the Plaxis 3D model corresponding to each individual test, the present project makes use of the results from the testing equipment and the report by Deltares (2012). From the output data of the apparatus, it is possible to recover the maximum displacement at each loading phase of the K_0-CRS and the time it took to reach said magnitude. Also, the state properties included in the document are used to define the initial condition of the model. Also, the state properties included in the document are used to define the initial condition of the model. Moreover, because of the aforementioned uncertainties in the reported values of K_0 by Alink (2010), it is not possible to rely on the mean effective stress, and thus the models cannot be properly calibrated. Hence, a first estimation of the compression parameters for each model was made in their corresponding space and then a curve-fitting process in the $v - log(\sigma'_v)$ space improved on them.

By employing these values it is possible to replicate the stress history of the test and compare it with the pore pressure measurements. A parallel iterative approach is utilized to define the hydraulic conductivity (k_v) and the coefficient of permeability (c_k) that better describe said results. The overall procedure is presented in Figure C.1 and the relevant information for both portions of the consolidation process is presented hereafter.

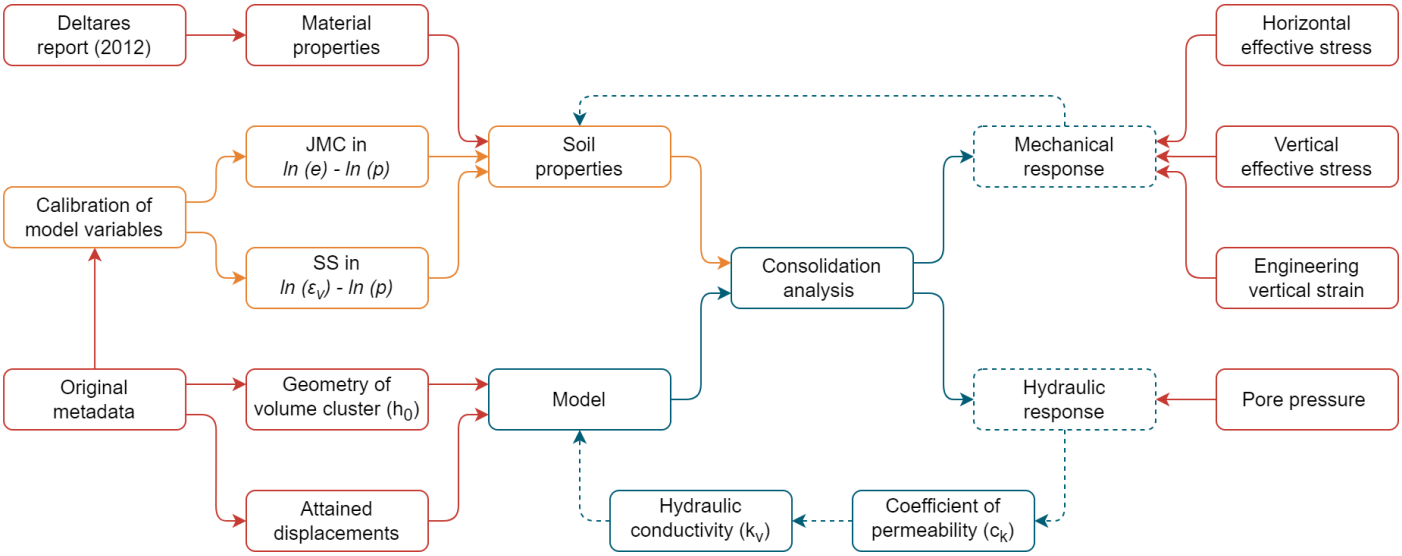

Figure C.1: Iterative procedure to define the adequate parameters

C.2 Mechanical response

The stress-strain relation as described by the Hook's Law axiom associates the deformation response solely to the stiffness of the material and the applied stress. Considering that two of those magnitudes are known in the form of the measured vertical stress and the corresponding applied displacement of each test, it can be said that an inverse problem analysis can yield the stiffness value that relates them. In the SS and JMC formulations, more components are introduced, however, the evaluation of this relation can be isolated if the complementary variables remain constant. Figures C.2 through C.11 display the variables employed to replicate each test, and further depict the distinction between the two constitutive models.

Regardless of the distinct advantages of the models of interest, the fidelity of the simulation is constrained by the fundamental assumptions made in their formulation and the actual measurement they're meant to replicate. On one hand, because the soft soil model is employed without the creep extension conceived by Vermeer and Neher (1999), both formulations are limited in how well the initial loading can be replicated, considering that they rely on a swelling index to describe this portion of the test. On the other, the models are equally affected by the erratic behaviour of the K_0 value that in consequence caused the mean effective stress (p') to fluctuate.

Additionally, it is worth noting the difference in the definition of the compression and swelling index between the soft soil and the JMC model. Regardless of the fact that both models follow the change in the mean effective stress, the latter is based on the change in the void ratio (or specific volume) and as such is calibrated in a $ln(v) - ln(p')$ space, while

the SS model is defined based on strain. An additional consideration must be made regarding the calibration of the soft soil variables, as their dependency on strain is also bound to the definition of the property itself, and therefore, using the natural or engineering strain effectively establishes the space in which the parameters are meant to be evaluated.

The definition of the mechanical properties uses the estimation of the compression (C_c) and swelling indices (C_s) as a starting point. This is of relevance as the extensive research using these variables allows to compare the material with a well-established frame of reference. On one hand, the values of C_c and C_s are a rough visualization of the consistency of the results at any given depth based on the corresponding engineering properties (Table C.2), while it aids in defining a precedent for their modified counterparts.

Table C.2: Estimation of compression and swelling indices

Sample	e_0	w_0	Compression Index (C_c)				Swelling Index (C_s)	
			MacFarlane	Mesri	Alink	Measured	Alink	Measured
	-	%	(1969)	(2007)	(2010)	-	(2010)	-
BT2-8B	10.01	609.8	6.01	6.10	-	4.60	-	0.65
BT1-2B	11.21	677.3	6.73	6.77	-	5.20	-	0.90
B30-2C	11.01	667.5	6.61	6.68	-	4.70	-	0.56
BT1-LN3	13.40	818.6	8.04	8.19	6.95	6.27	1.02	1.18
BT1-3D	15.96	971.5	9.58	9.72	-	6.70	-	0.95
BT2-LN10	16.18	994.1	9.71	9.94	7.48	7.75	0.98	1.07
B30-4C	18.88	1142.0	11.33	11.42	-	7.80	-	1.04
BT1-LN4	18.48	1059.7	11.09	10.60	9.37	9.94	1.22	1.16
BT1-4D	21.23	1258.6	12.74	12.59	-	9.00	-	1.30
B30-5B	24.62	1380.2	14.77	13.80	-	4.30	-	0.32
BT2-LN11	18.18	1017.4	10.91	10.17	9.59	9.35	1.18	1.08
BT2-11B	13.05	795.3	7.83	7.95	-	6.54	-	0.62
BT2-12B	15.36	932.0	9.22	9.32	-	6.20	-	0.90
B30-6D	6.27	392.9	3.76	3.93	-	3.20	-	0.25
BT2-LN12	2.43	109.7	1.46	1.10	0.79	0.75	0.08	0.16
Average	14.42	855.1	8.65	8.55	6.84	6.51	0.89	0.79
Estimation	14.70	880.7	8.82	8.80	8.35	6.90	1.10	0.92

Table C.2 shows the measured values compared to empirical relations based on the state parameters (MacFarlane, 1969; Mesri and Ajlouni, 2007) and to the values recovered in the original tests (Alink, 2010). In general, the values fall below the average values from the literature based on the void ratio ($0.6 \cdot e_0$) and the water content ($0.1 \cdot w_0$), although they're still within their lower bound ($0.42 \cdot e_0$ and $0.075 \cdot w_0$).

This comparison cannot be easily translated for the case of κ^*, as the magnitude of κ^* for each model is measured in their corresponding plane. On the other hand, comparing the estimation of this variable with the engineering correlations is intrinsically complicated, as most of the relations assume that the stress state during unloading is isotropic and thus, consider a K_0 value of 1. This is inconsistent with the expected response of K_0 and what was shown in the K_0-CRS tests.

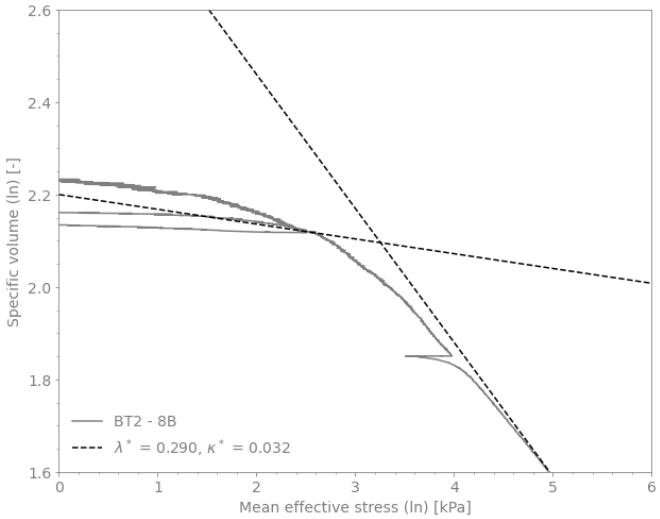

(a) Calibration in $ln(v) - ln(p')$ space

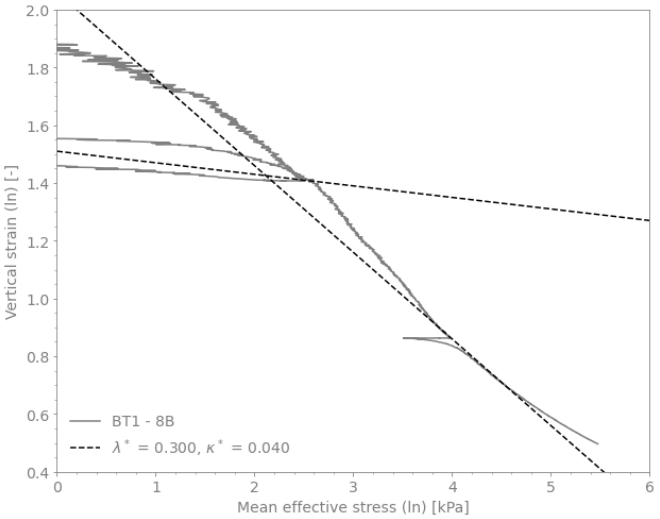

(b) Calibration in $ln(\epsilon_v) - ln(p')$ space

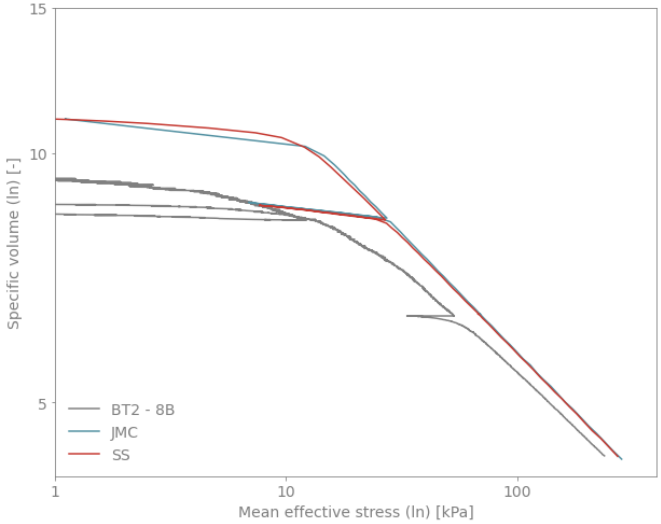

(c) Stress-strain relation in $ln(v) - ln(p')$ space

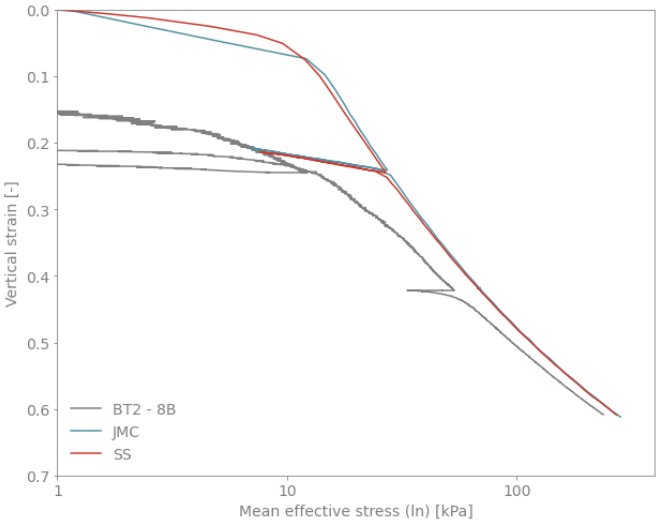

(d) Stress-strain relation in $\epsilon_v - ln(p')$ space

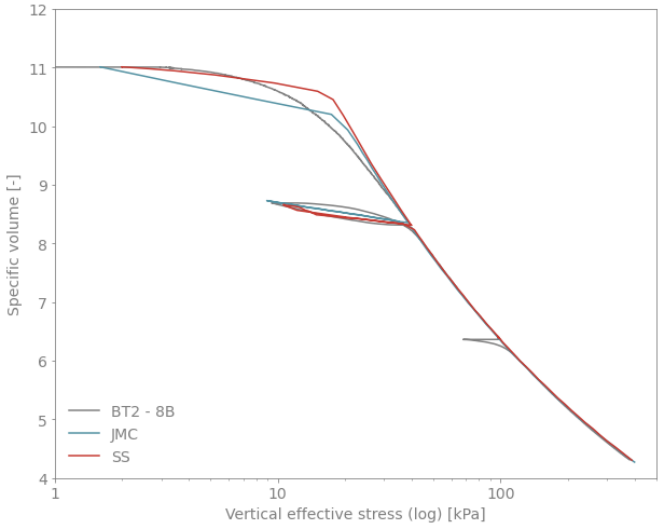

(e) Stress-strain relation in $v - log(\sigma'_v)$ space

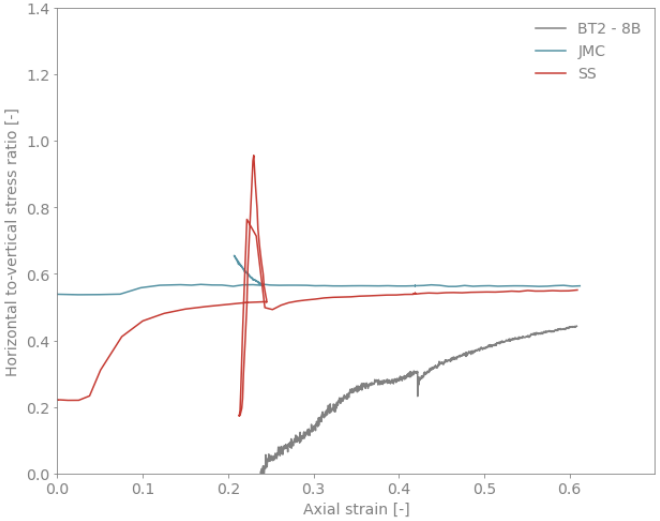

(f) K_0 behaviour

Figure C.2: Simulation of K_0-CRS for sample 8B

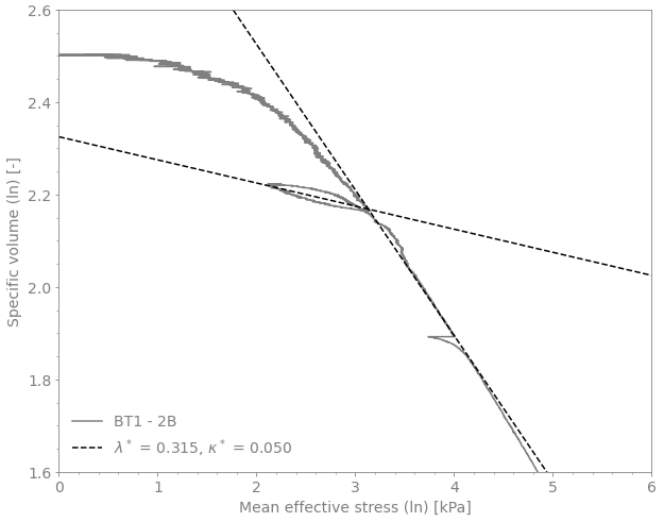

(a) Calibration in $ln(v) - ln(p')$ space

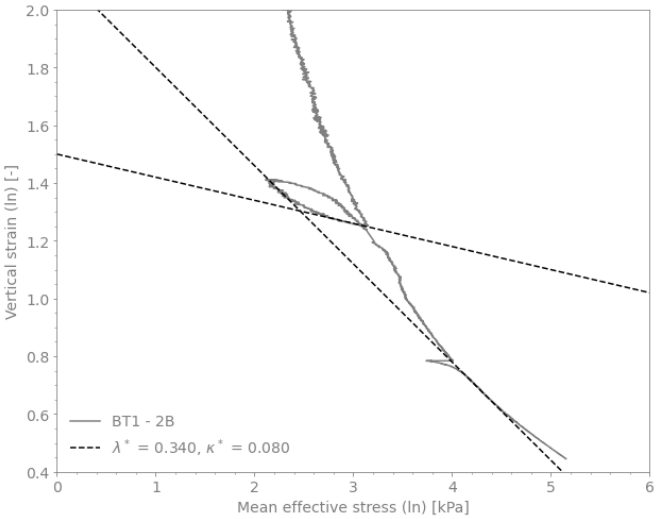

(b) Calibration in $ln(\epsilon_v) - ln(p')$ space

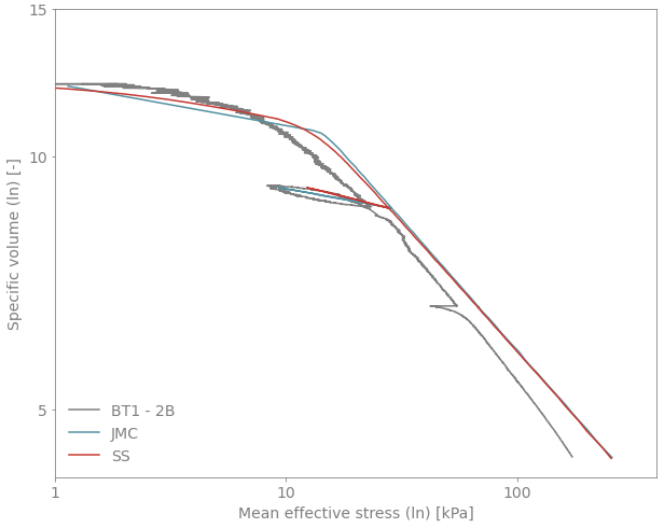

(c) Stress-strain relation in $ln(v) - ln(p')$ space

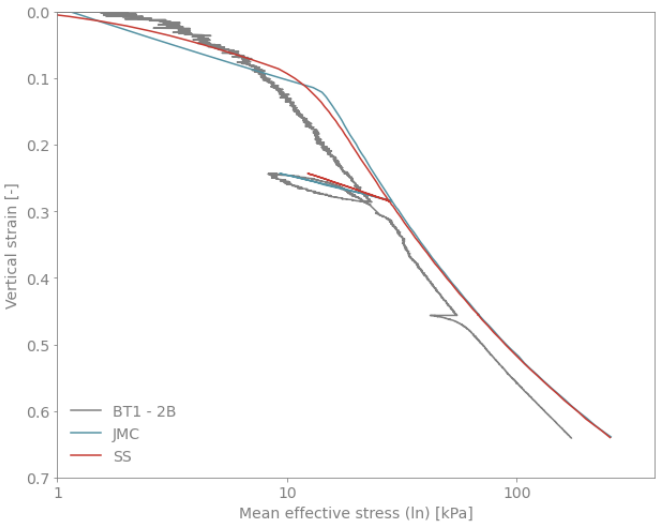

(d) Stress-strain relation in $\epsilon_v - ln(p')$ space

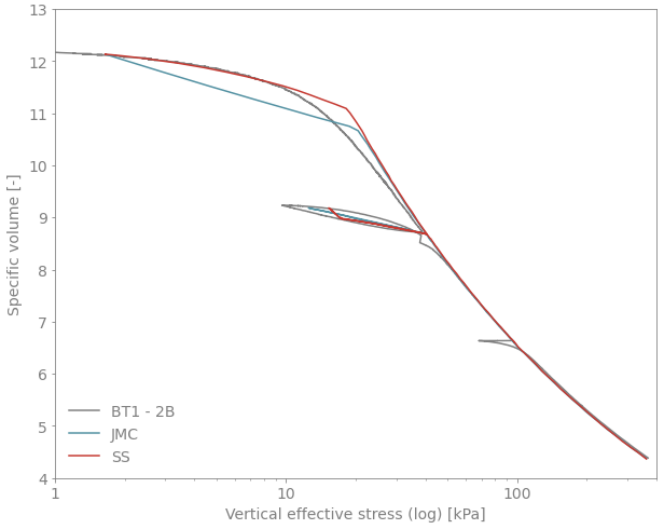

(e) Stress-strain relation in $v - log(\sigma'_v)$ space

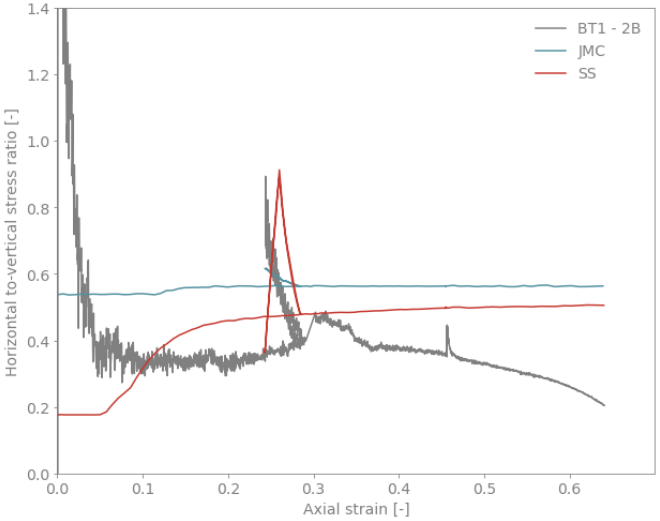

(f) K_0 behaviour

Figure C.3: Simulation of K_0-CRS for sample 2B

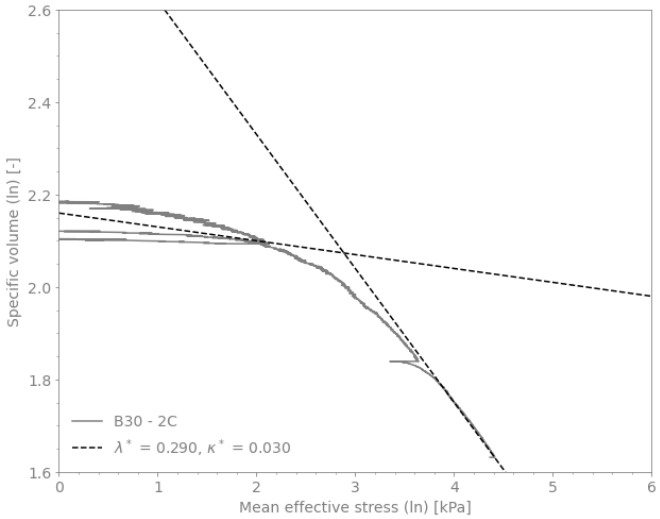

(a) Calibration in $ln(v) - ln(p')$ space

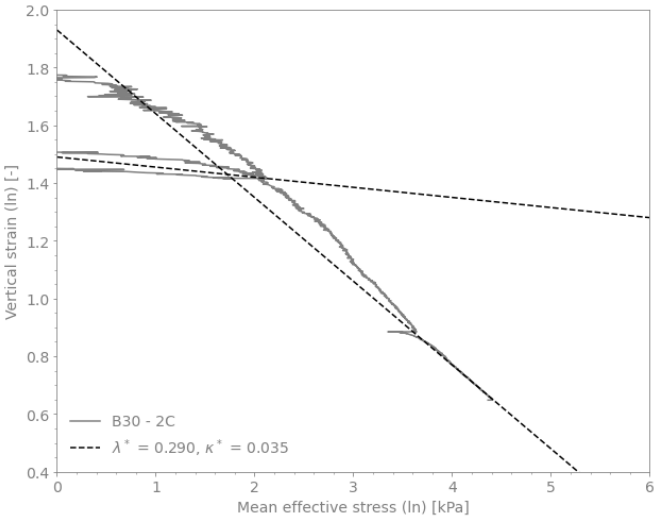

(b) Calibration in $ln(\epsilon_v) - ln(p')$ space

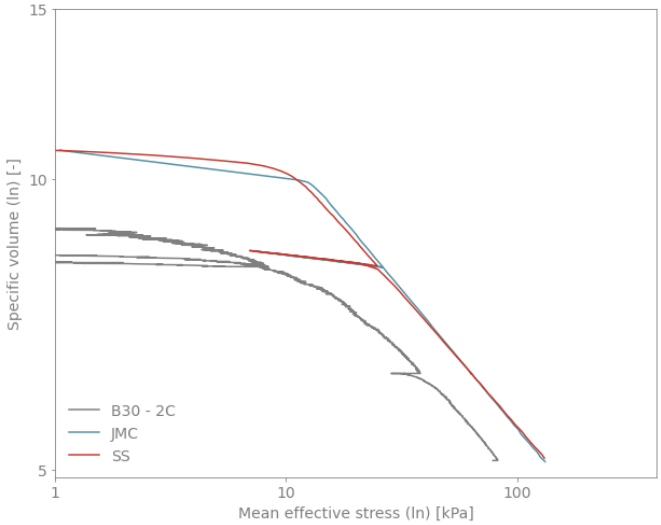

(c) Stress-strain relation in $ln(v) - ln(p')$ space

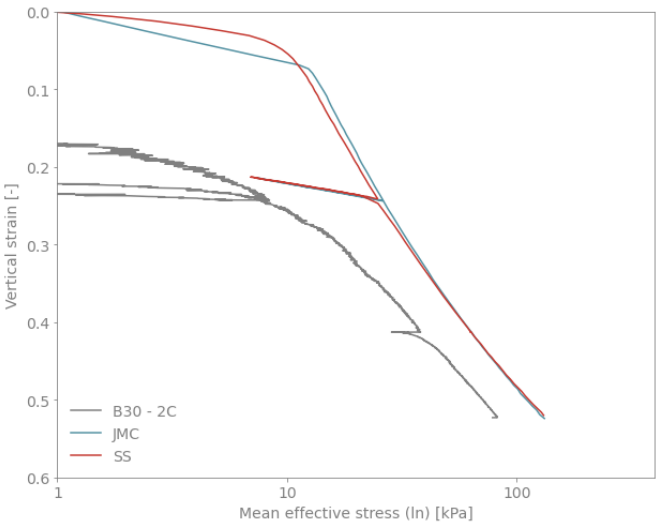

(d) Stress-strain relation in $\epsilon_v - ln(p')$ space

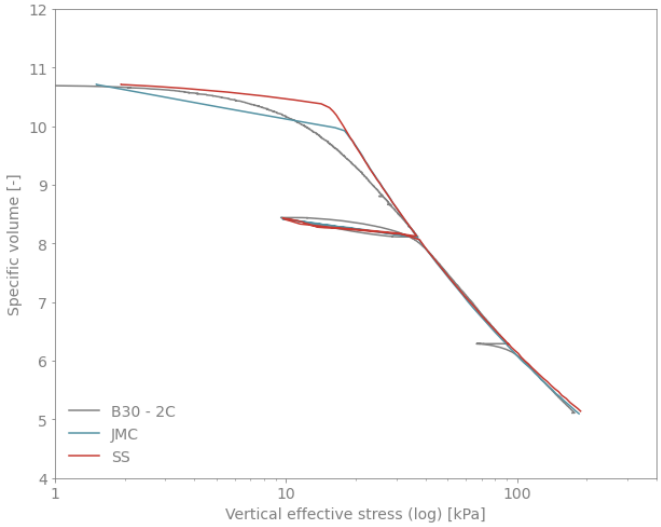

(e) Stress-strain relation in $v - log(\sigma'_v)$ space

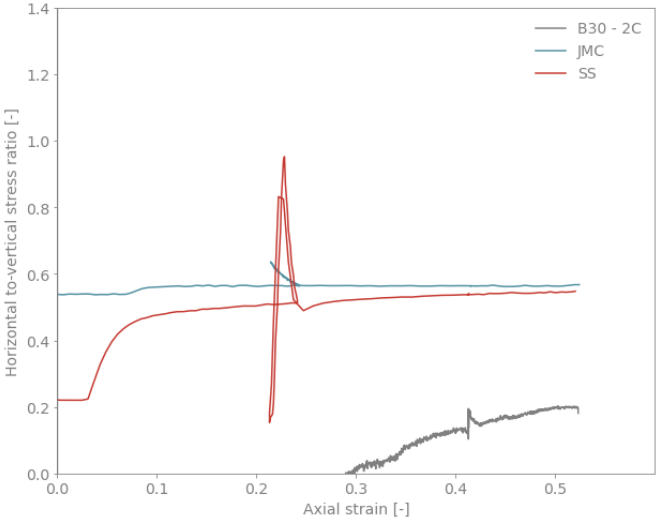

(f) K_0 behaviour

Figure C.4: Simulation of K_0-CRS for sample 2C

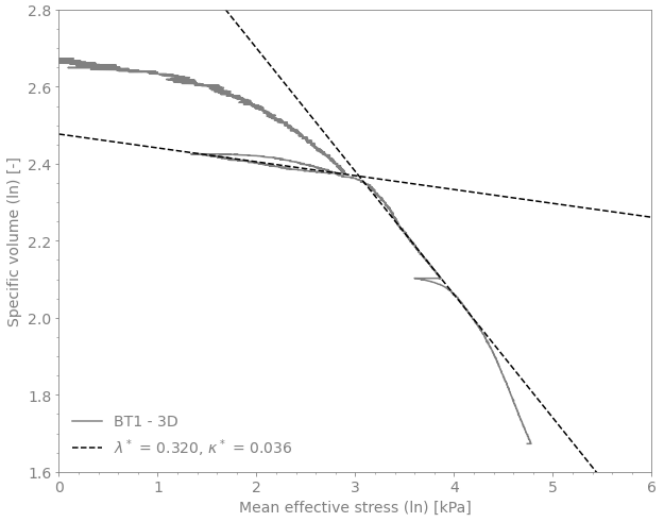

(a) Calibration in $ln(v) - ln(p')$ space

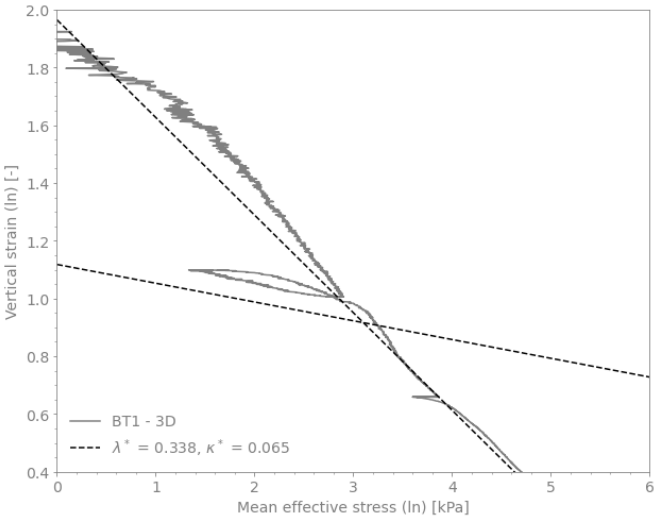

(b) Calibration in $ln(\epsilon_v) - ln(p')$ space

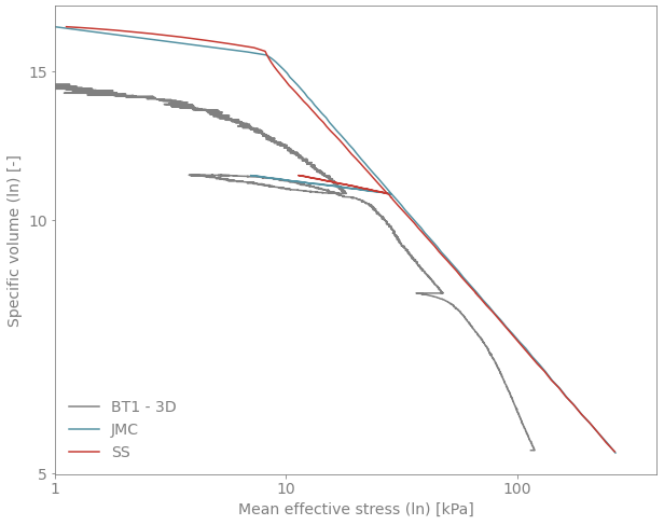

(c) Stress-strain relation in $ln(v) - ln(p')$ space

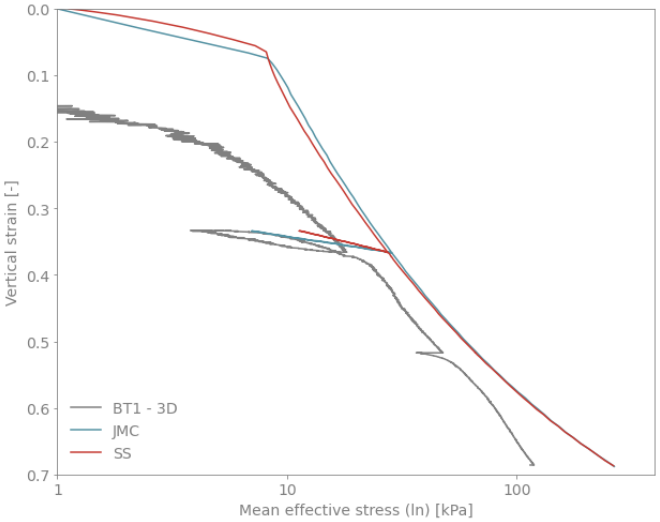

(d) Stress-strain relation in $\epsilon_v - ln(p')$ space

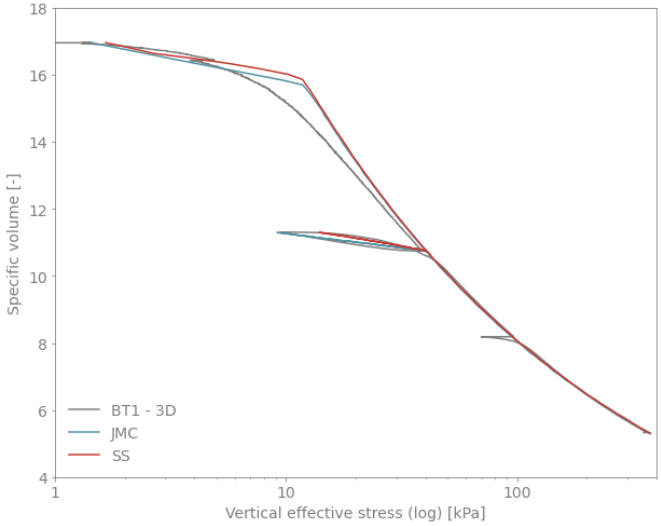

(e) Stress-strain relation in $v - log(\sigma'_v)$ space

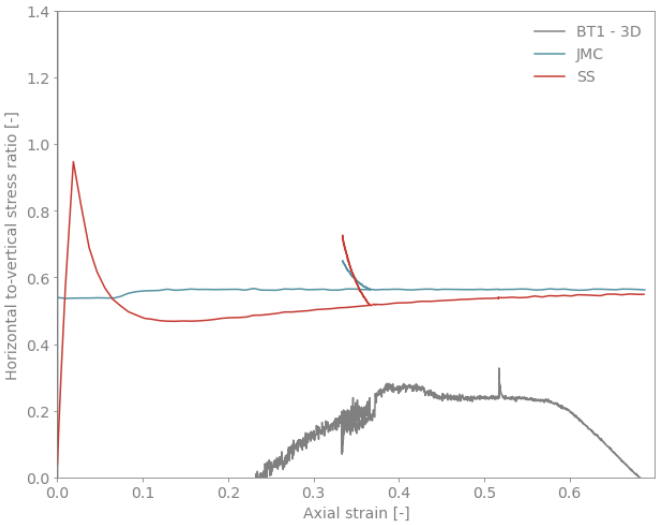

(f) K_0 behaviour

Figure C.5: Simulation of K_0-CRS for sample 3D

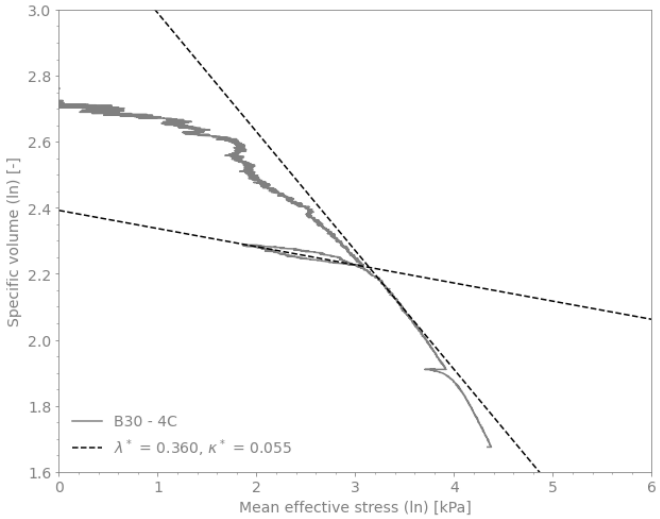

(a) Calibration in $ln(v) - ln(p')$ space

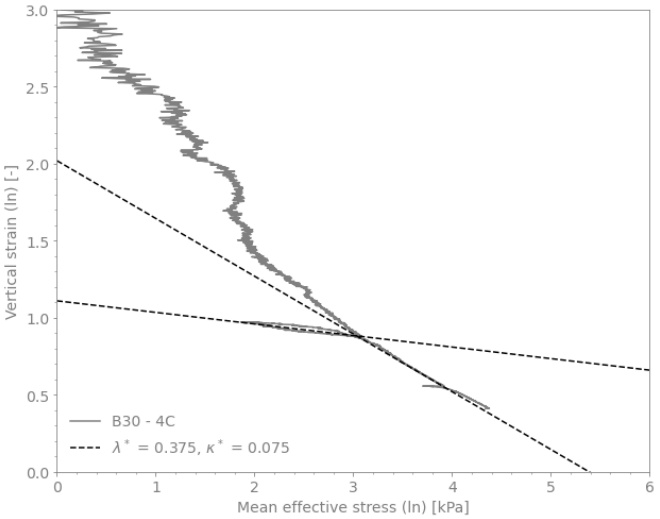

(b) Calibration in $ln(\epsilon_v) - ln(p')$ space

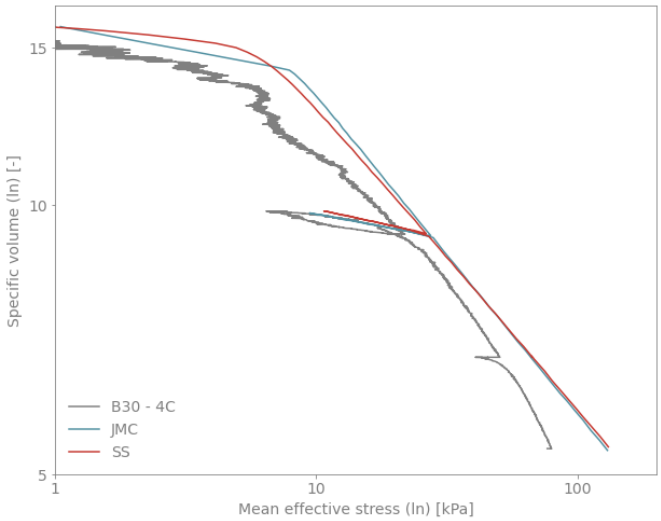

(c) Stress-strain relation in $ln(v) - ln(p')$ space

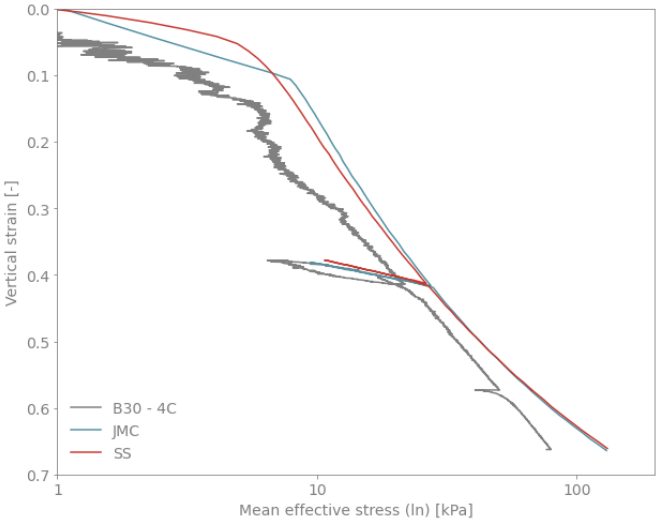

(d) Stress-strain relation in $\epsilon_v - ln(p')$ space

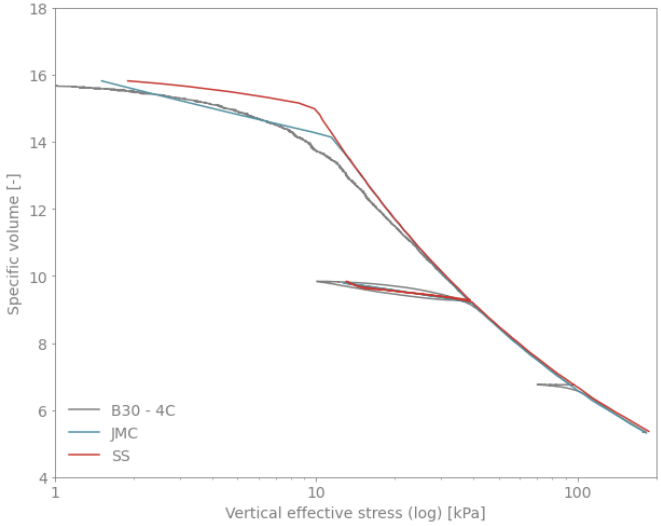

(e) Stress-strain relation in $v - log(\sigma'_v)$ space

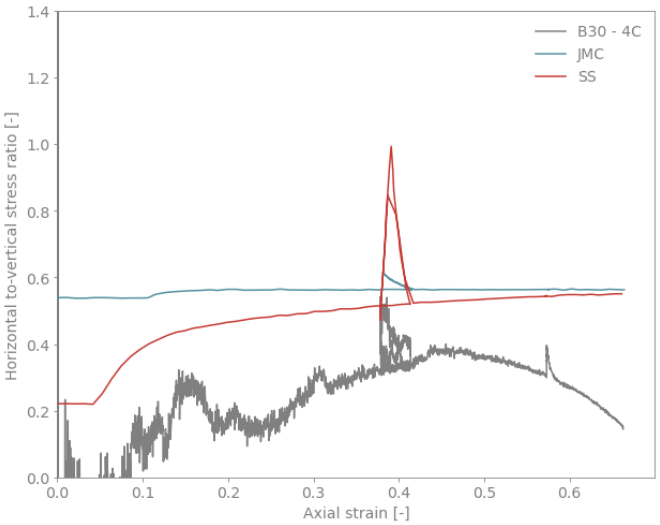

(f) K_0 behaviour

Figure C.6: Simulation of K_0-CRS for sample 4C

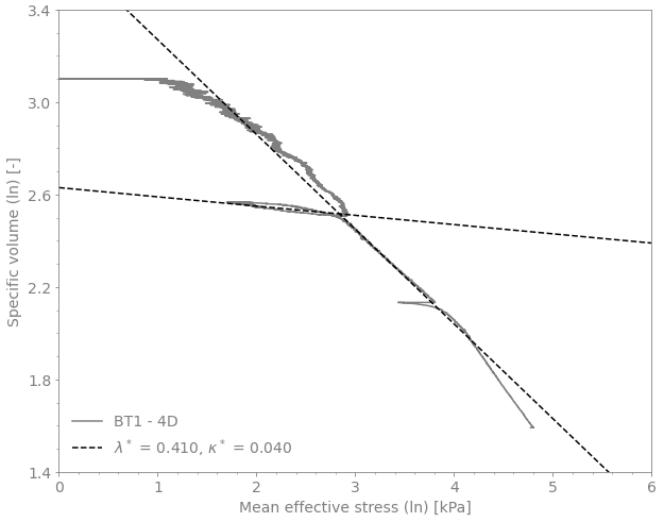

(a) Calibration in $ln(v) - ln(p')$ space

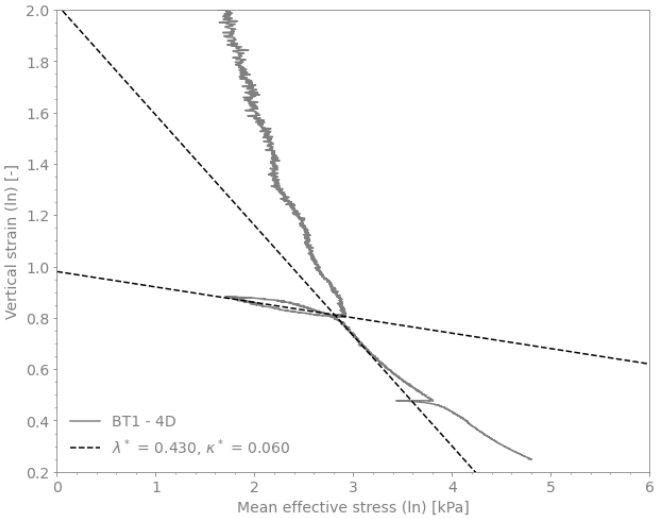

(b) Calibration in $ln(\epsilon_v) - ln(p')$ space

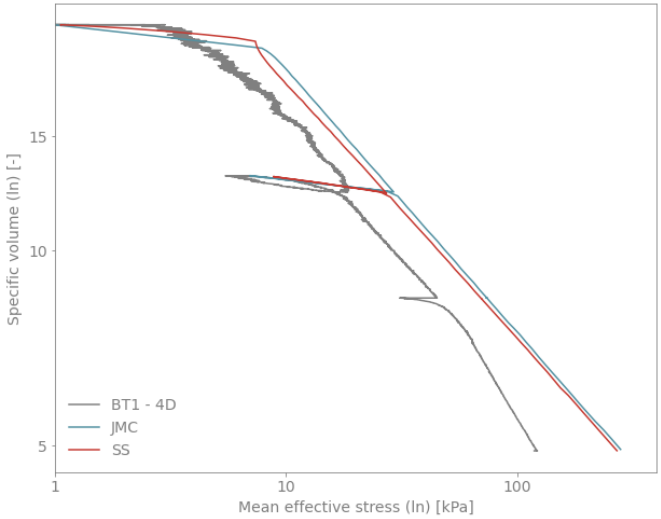

(c) Stress-strain relation in $ln(v) - ln(p')$ space

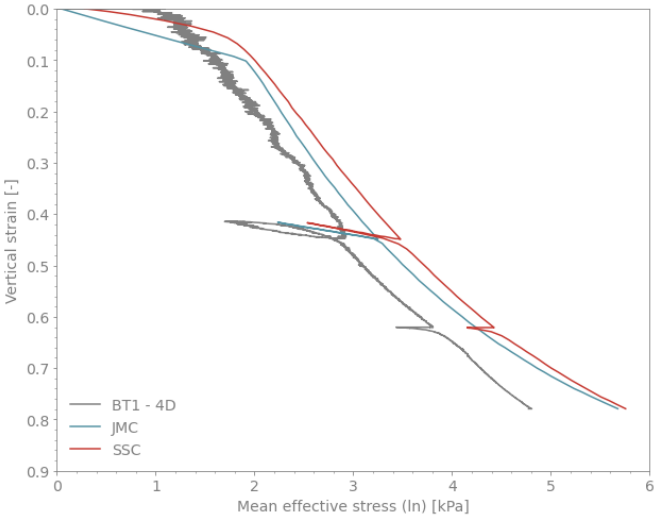

(d) Stress-strain relation in $\epsilon_v - ln(p')$ space

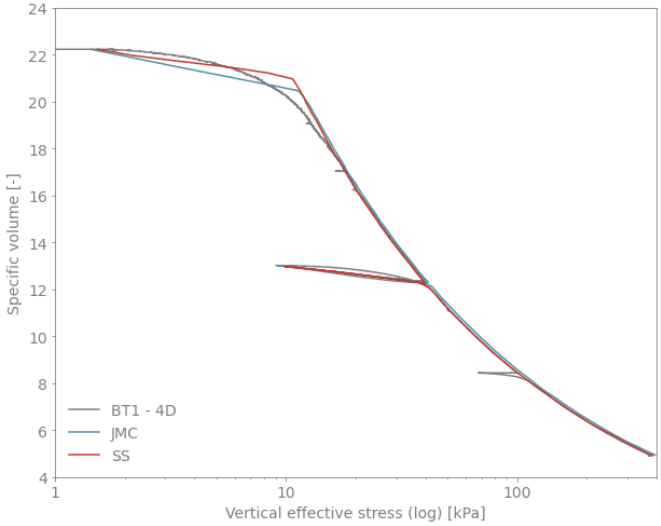

(e) Stress-strain relation in $v - log(\sigma'_v)$ space

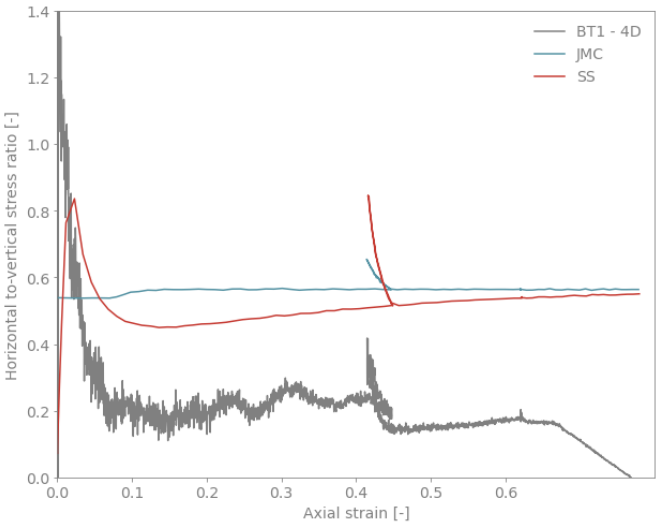

(f) K_0 behaviour

Figure C.7: Simulation of K_0-CRS for sample 4D

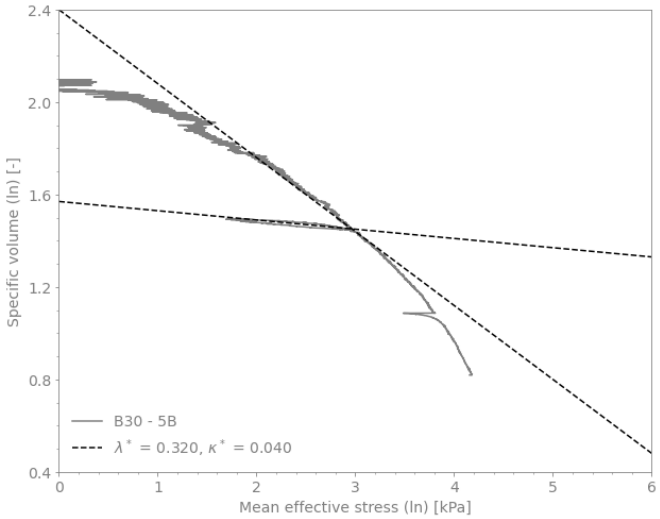

(a) Calibration in $ln(v) - ln(p')$ space

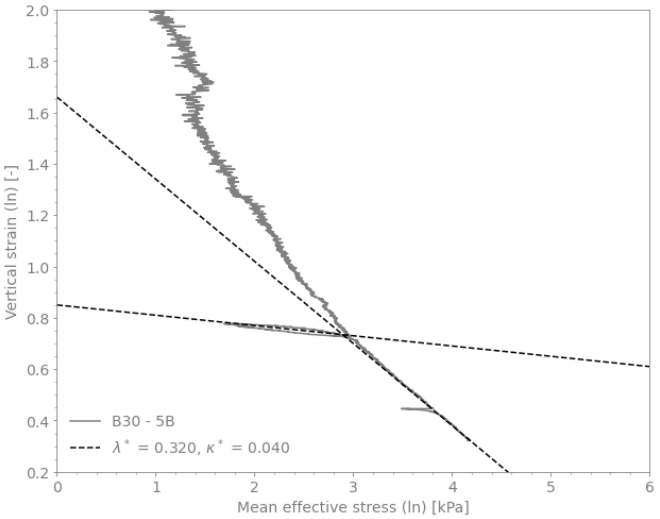

(b) Calibration in $ln(\epsilon_v) - ln(p')$ space

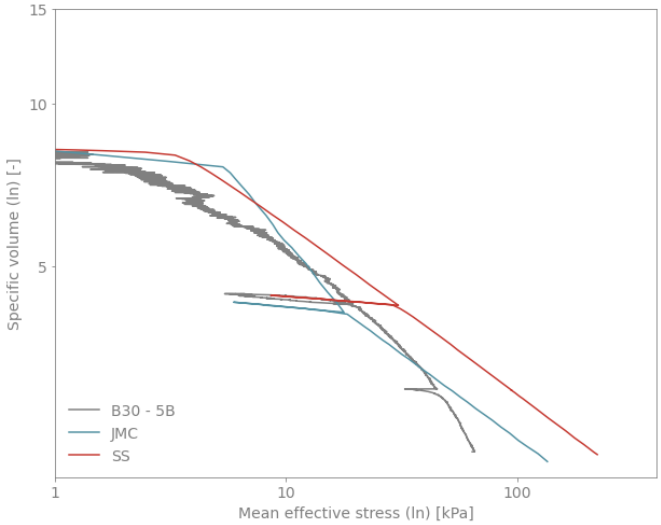

(c) Stress-strain relation in $ln(v) - ln(p')$ space

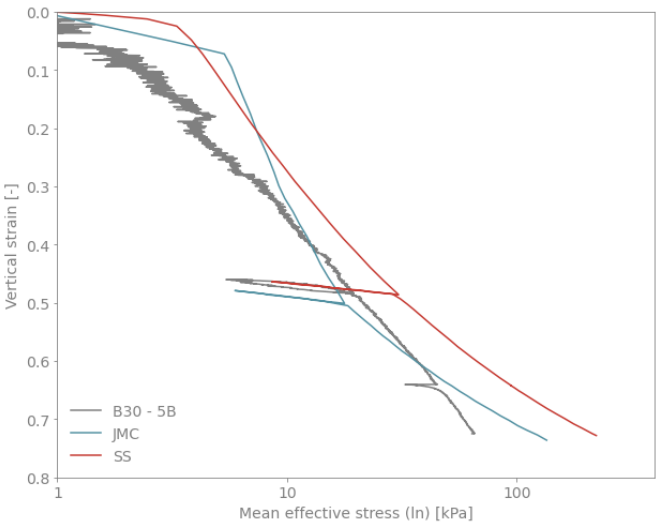

(d) Stress-strain relation in $\epsilon_v - ln(p')$ space

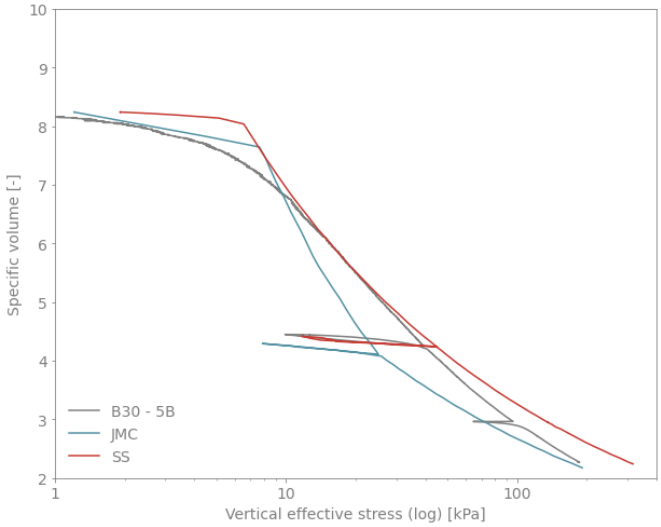

(e) Stress-strain relation in $v - log(\sigma'_v)$ space

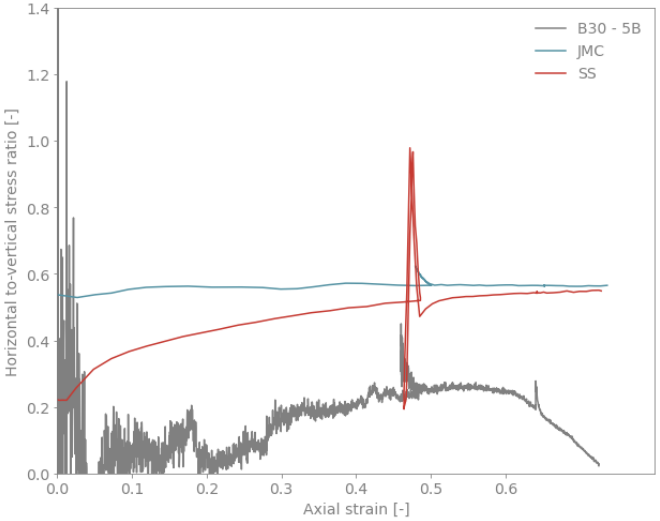

(f) K_0 behaviour

Figure C.8: Simulation of K_0-CRS for sample 5B

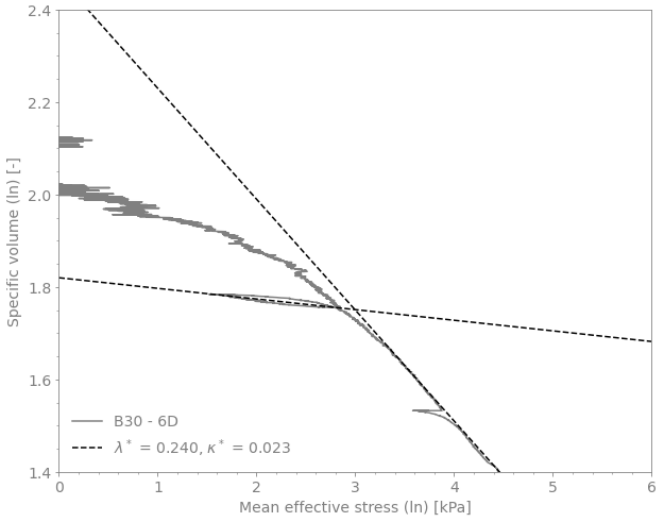

(a) Calibration in $ln(v) - ln(p')$ space

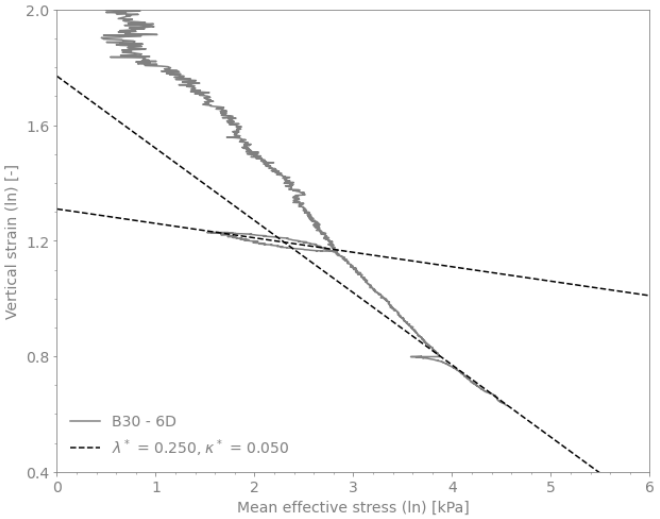

(b) Calibration in $ln(\epsilon_v) - ln(p')$ space

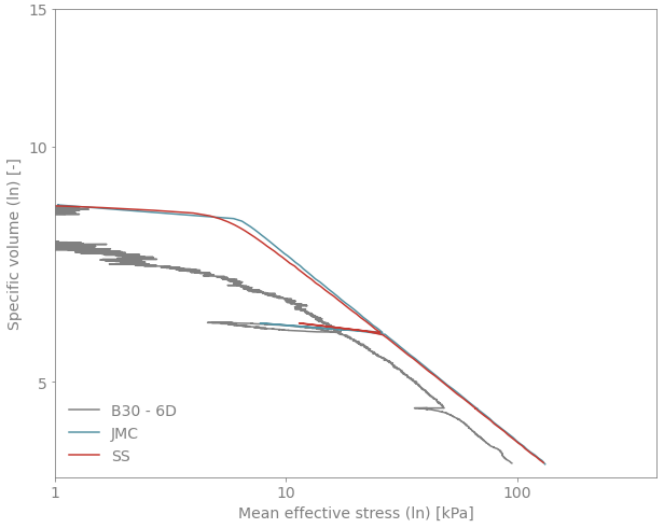

(c) Stress-strain relation in $ln(v) - ln(p')$ space

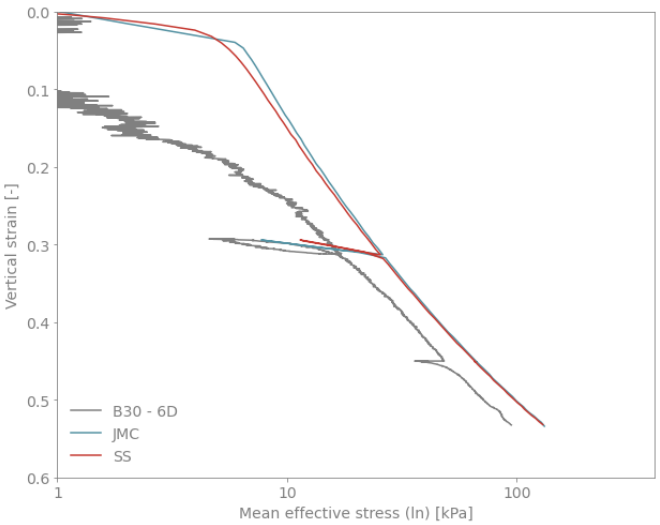

(d) Stress-strain relation in $\epsilon_v - ln(p')$ space

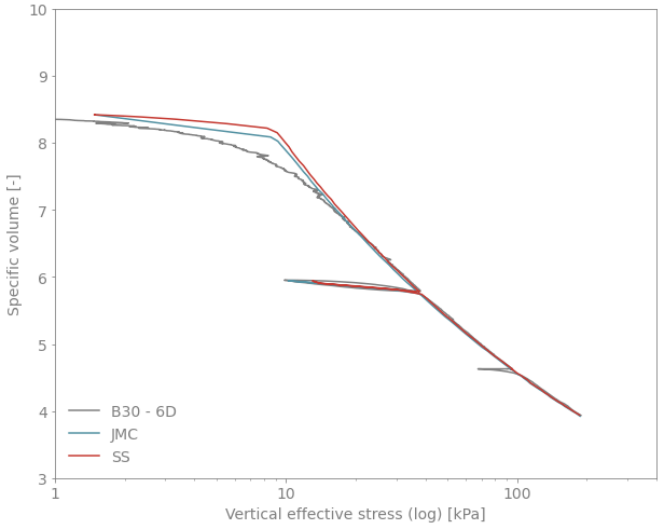

(e) Stress-strain relation in $v - log(\sigma'_v)$ space

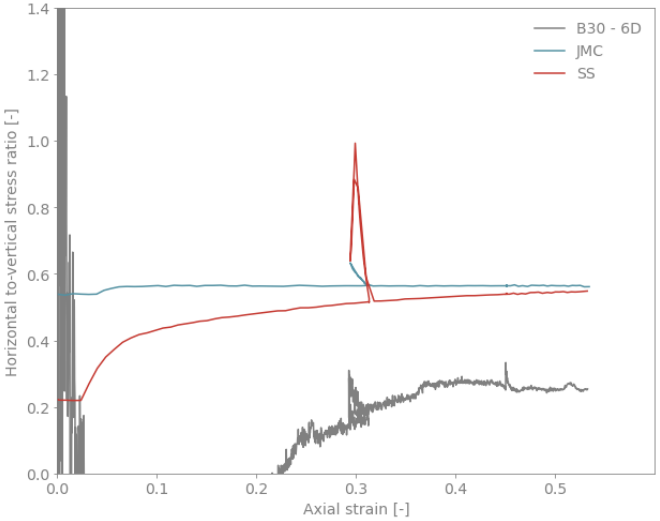

(f) K_0 behaviour

Figure C.9: Simulation of K_0-CRS for sample 6D

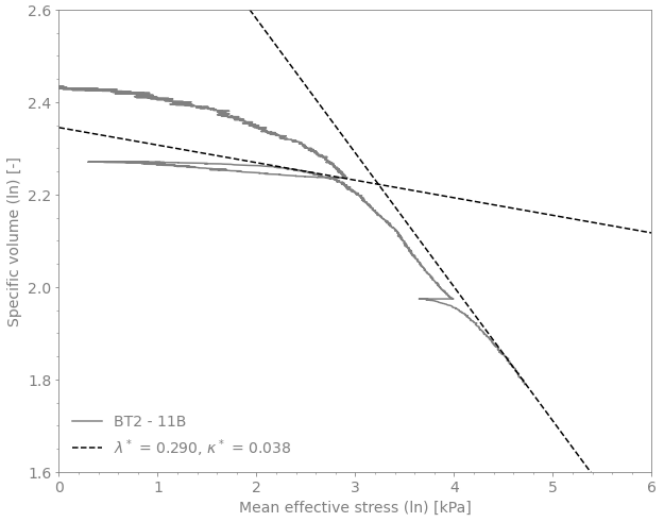

(a) Calibration in $ln(v) - ln(p')$ space

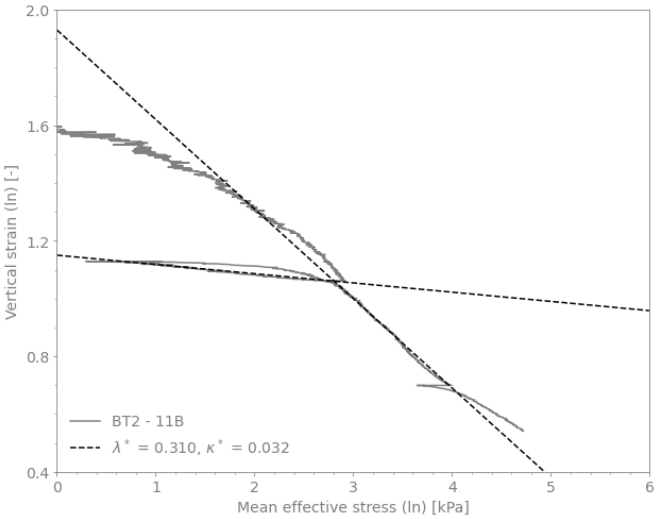

(b) Calibration in $ln(\epsilon_v) - ln(p')$ space

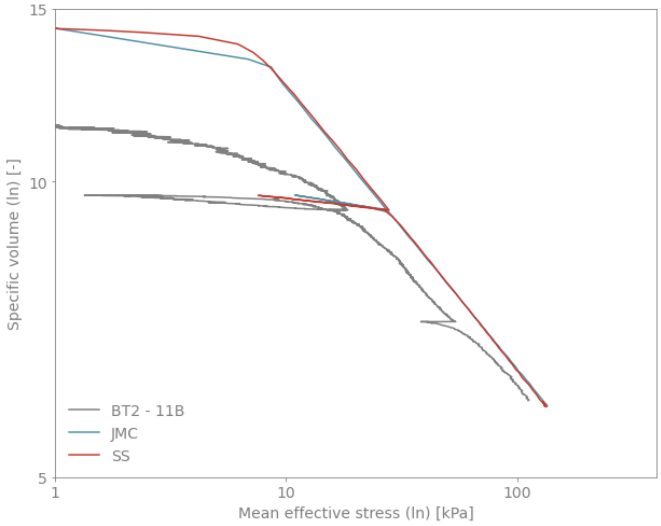

(c) Stress-strain relation in $ln(v) - ln(p')$ space

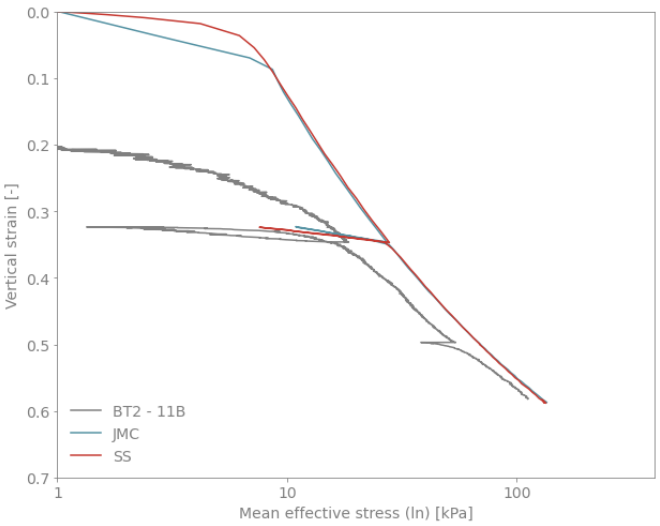

(d) Stress-strain relation in $\epsilon_v - ln(p')$ space

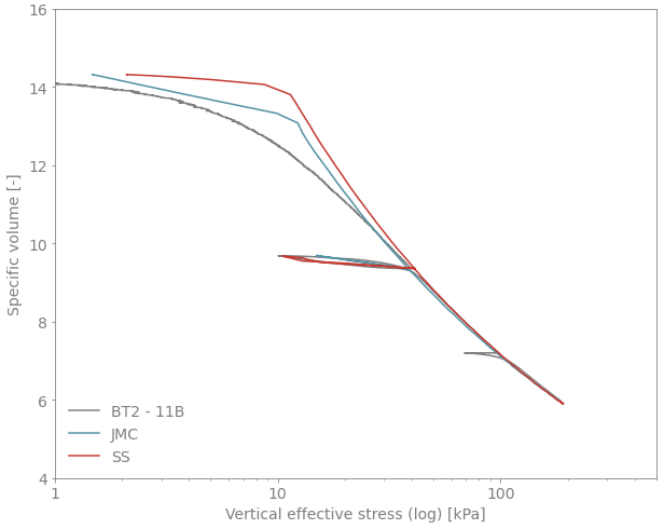

(e) Stress-strain relation in $v - log(\sigma'_v)$ space

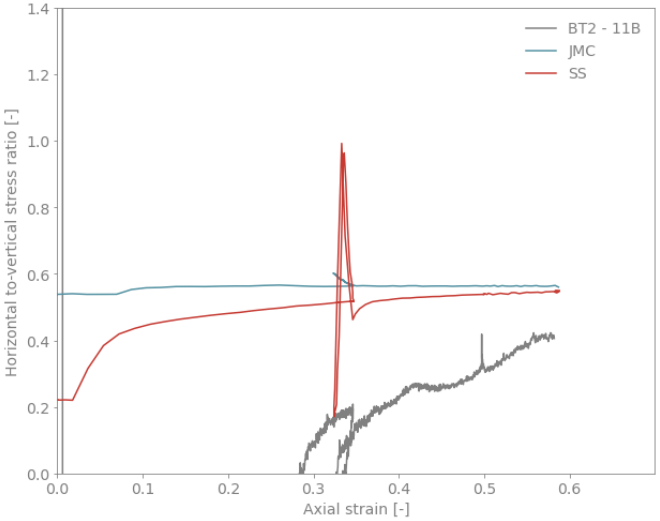

(f) K_0 behaviour

Figure C.10: Simulation of K_0-CRS for sample 11B

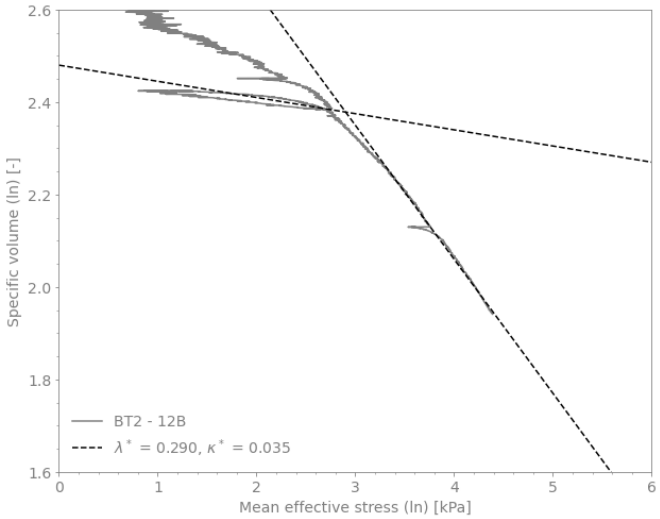

(a) Calibration in $ln(v) - ln(p')$ space

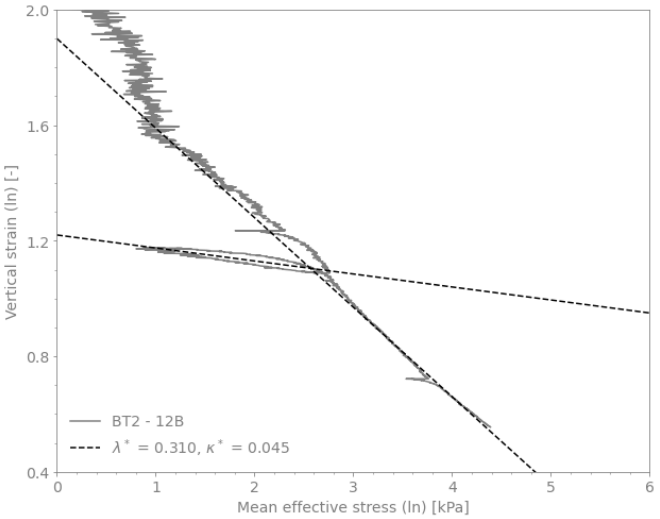

(b) Calibration in $ln(\epsilon_v) - ln(p')$ space

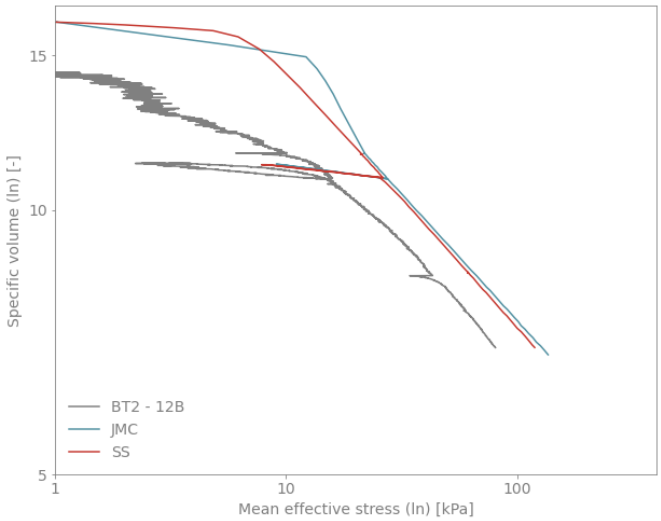

(c) Stress-strain relation in $ln(v) - ln(p')$ space

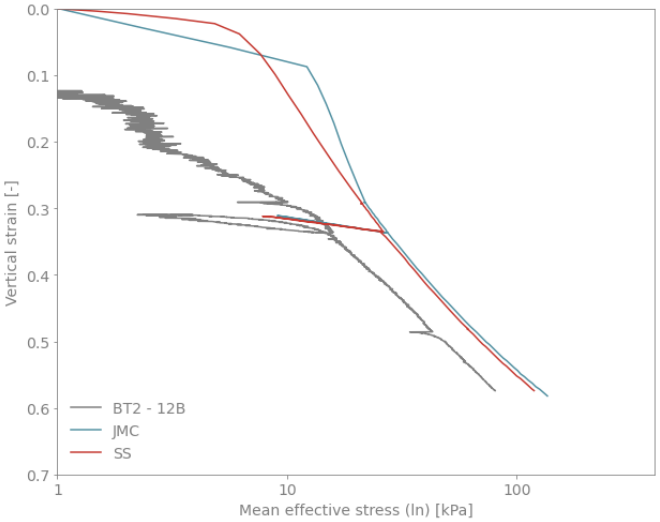

(d) Stress-strain relation in $\epsilon_v - ln(p')$ space

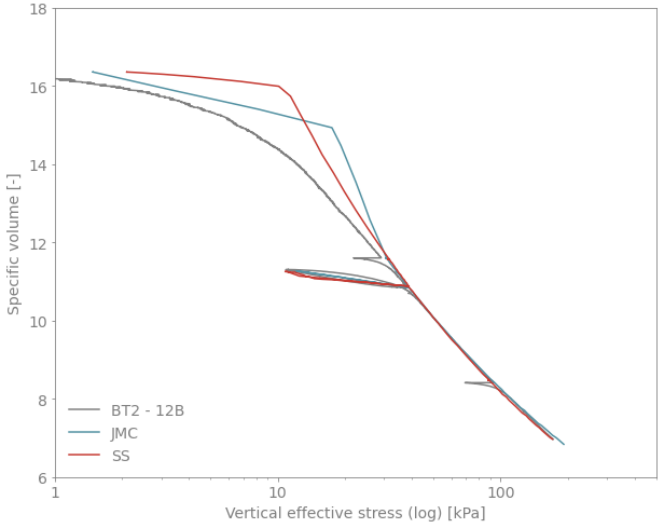

(e) Stress-strain relation in $v - log(\sigma'_v)$ space

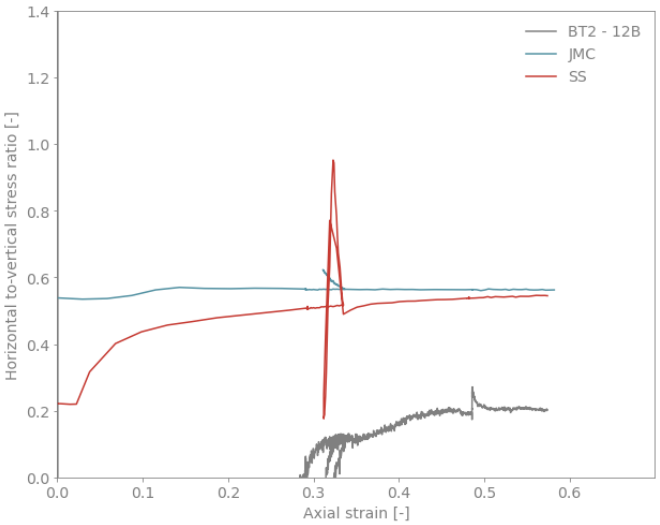

(f) K_0 behaviour

Figure C.11: Simulation of K_0-CRS for sample 12B

In practical terms, the description of the consolidation process, when seen in the traditional $\epsilon_v - ln(p')$ space by both methods, is adequate. As expected, neither model replicates the tests' response in their respective calibration planes, which is once again linked to the poor response of K_0. Nonetheless, the soft soil model does present two advantages over the JMC, the better adjustment of the loading stage before the pre-consolidation stage and the variation of K_0 based on the strain conditions. The source of the differences in the latter falls more so in the approach of Plaxis 3D to calculate the horizontal-to-vertical stress ratio in user-defined models, along with the additional built-in tools of the program to improve the estimation of the SS model.

Relative to the estimated parameters, the most recurrent magnitude for the JMC model was 0.320 for λ^* and 0.050 for κ^*. The homologous compression variable of the SS model varies by 5.0%, while the difference in κ^* is considerable. The ratio of λ^*/κ^* of the samples exceeds the typical range of 2.5 - 7.0 for the soft soil formulation (Plaxis, 2022a), suggesting reduced swelling capabilities of the material as it is common in amorphous peats. The estimated values are also smaller than those calculated by Siderius (2011) and Schadee (2012) based on the isotachen method.

Overall, the trend of values calculated through the FEM simulations diverges from the assumed depth-dependent increase shown by C_c and C_r. In the case of the modified compression parameters, the unique value of 0.32 and 0.34 is considered to be representative of a large portion of the strata, with only the tests close to the change in horizon having different values. Contrastingly, the modified swelling index does not show consistency in the attained magnitudes, with the estimation falling between 0.03 and 0.06 without a clear pattern. This can be attributed to the previously mentioned uncertainty in the p' planes and the relatively low degree of swelling potential.

Because the isotropic compression and K_0-CRS tests require more specialized equipment and technicians, estimating these indices based on one-dimensional compression tests is of relevance given their widespread availability and lower cost. The translation between the internationally normalized parameters is commonly carried out using Equation C.4 for both the $\kappa*$ and λ^* variables, which some slight variations in the case of the swelling index. However, this relation implies that the change in void ratio during the compression tests is negligible, which does not hold as a pertinent assumption in the case of peat. Comparatively, the use of the average value of void ratio during the test is hereby suggested as a better fit when dealing with peat. Table C.3 and C.4 display the use of these equations, along with an estimation based on the *isotachen* method (Equation C.2). Tables C.3 and C.4 summarize the variability between these approximations and the actual values recovered from the FEM simulations.

$$\kappa^* = 2 \cdot a \tag{C.1}$$

$$\lambda^* = b + 2 \cdot a \tag{C.2}$$

$$\lambda^* \parallel \kappa^* = \frac{C_c \parallel C_r}{2.303 \cdot (1 + e_0)} \tag{C.3}$$

$$\lambda^* \parallel \kappa^* = \frac{C_c \parallel C_r}{2.303 \cdot (1 + \bar{e})} \tag{C.4}$$

Table C.3: Estimation of modified compression index

Sample	C_c	Eq. C.2	Eq. C.3	Eq. C.4	JMC	SS
8B	4.60	0.352	0.181	0.290	0.290	0.300
2B	5.20	0.383	0.185	0.278	0.315	0.340
2C	4.70	0.383	0.191	0.273	0.290	0.290
3D	6.70	0.384	0.172	0.278	0.320	0.338
4C	7.80	0.456	0.357	0.214	0.360	0.375
4D	9.00	0.497	0.176	0.333	0.410	0.430
5B	4.30	0.382	0.227	0.416	0.320	0.320
11B	5.60	0.360	0.170	0.274	0.290	0.310
12B	6.20	0.391	0.165	0.241	0.290	0.310
6D	3.20	0.287	0.165	0.243	0.240	0.250

Table C.4: Estimation of modified swelling index

Sample	C_r	Eq. C.1	Eq. C.3	Eq. C.4	JMC	SS
8B	0.65	0.065	0.026	0.041	0.032	0.040
2B	0.90	0.090	0.032	0.048	0.050	0.080
2C	0.56	0.062	0.023	0.033	0.030	0.035
3D	0.95	0.076	0.024	0.039	0.036	0.065
4C	1.04	0.093	0.048	0.029	0.055	0.075
4D	1.30	0.087	0.025	0.048	0.040	0.060
5B	0.32	0.062	0.017	0.032	0.040	0.040
11B	0.59	0.052	0.018	0.029	0.038	0.032
12B	0.90	0.069	0.024	0.035	0.035	0.045
6D	0.25	0.044	0.013	0.019	0.023	0.050

As seen in Tables C.3 and C.4, the estimations made with these equations underestimate the actual magnitudes of the compression index for both models, however, the calculations based on the initial void ratio underperform to a greater extent when compared to the average void ratio. Between models, Equation C.4 appears as the best option to approximate the values of the JMC model, while the *isotachen* relations better adjust to the SS model. Evidently, the use of equation C.3 is highly conservative and would not provide a representative magnitude for either λ^* or κ^*.

C.3 Hydraulic response

Considering the overall interaction of the components in the K_0-CRS tests as a coupled mechanism, it can be said that evidence of a successful model implementation can be found in the adequate replication of the excess pore pressure evolution and the stress-strain relation. Having defined the mechanical properties with the SS and JMC models, the focus of this process shifts to the definition of the hydraulic conditions. In this step, an initial hydraulic conductivity and permeability coefficient are iteratively modified to replicate the pore pressure measurements of the K_0-CRS metadata. The starting values of the process are based on the laboratory results and the semi-logarithmic rule implemented in Plaxis 3D, which are further modified based on the *excess pore pressure* values that result from the model.

Although the emulation includes all the phases from the K_0-CRS tests, this step of the analysis is particularly focused on the second and third deformation ramps, given the uncertainty of the remaining portions. The disregard of the preceding stages is based on the assumption that the hydraulic conductivity and the pore pressure cannot be considered representative. Since the sample is not fully saturated at lower degrees of strain, the water phase is not completely engaged and the apparatus is incapable of grasping this partially-saturated condition. Hence, the measurements from these phases can be considered as inconclusive.

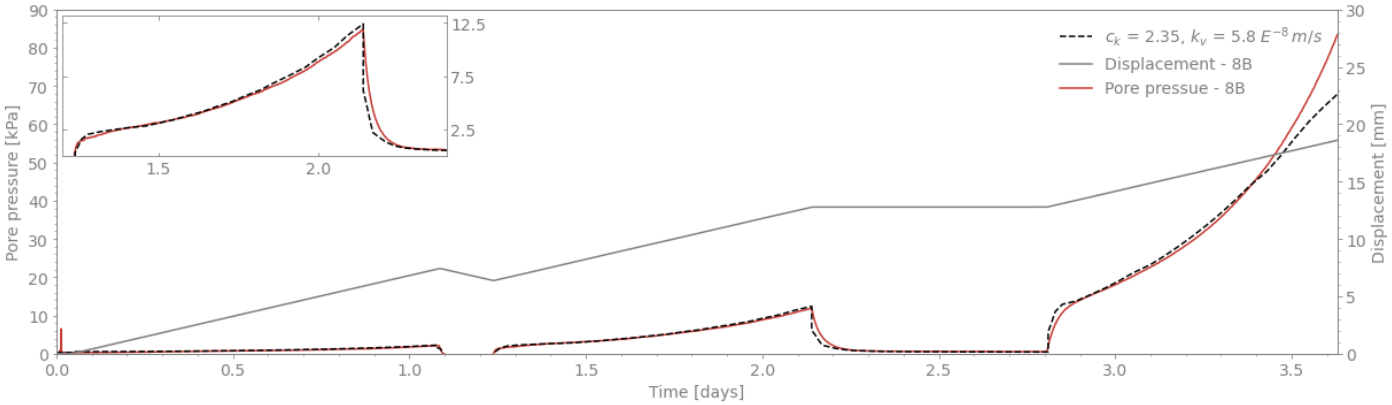

(a) Sample 8B

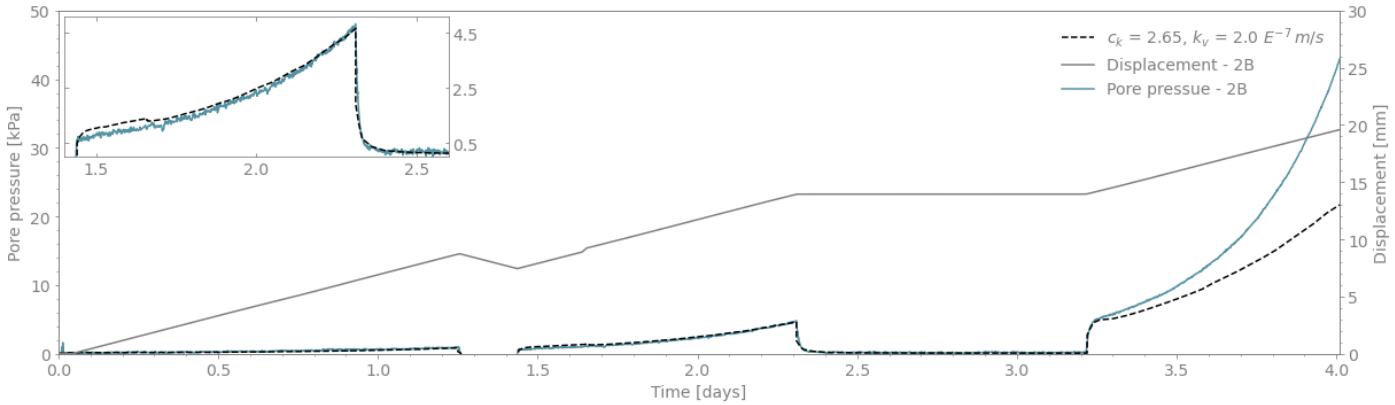

(b) Sample 2B

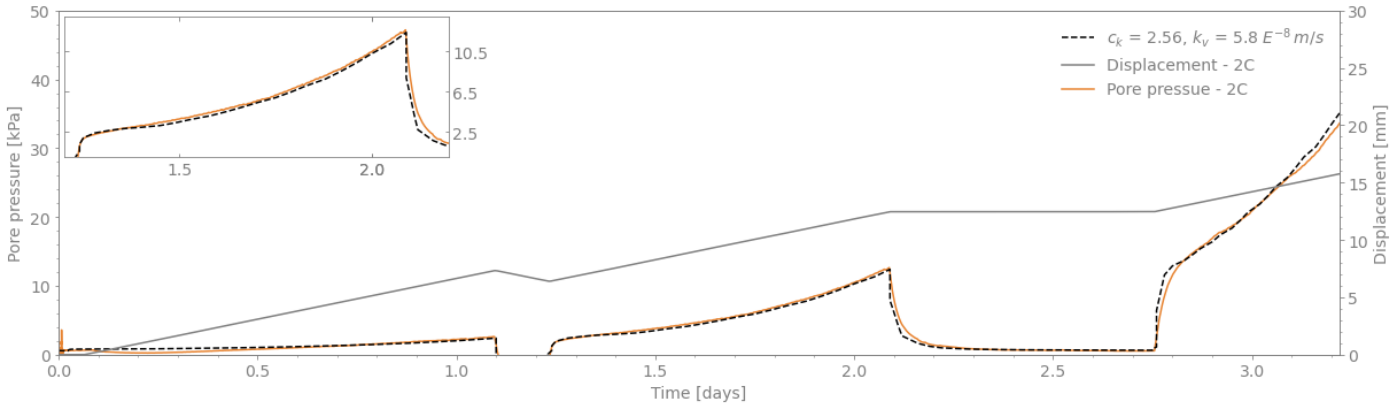

(c) Sample 2C

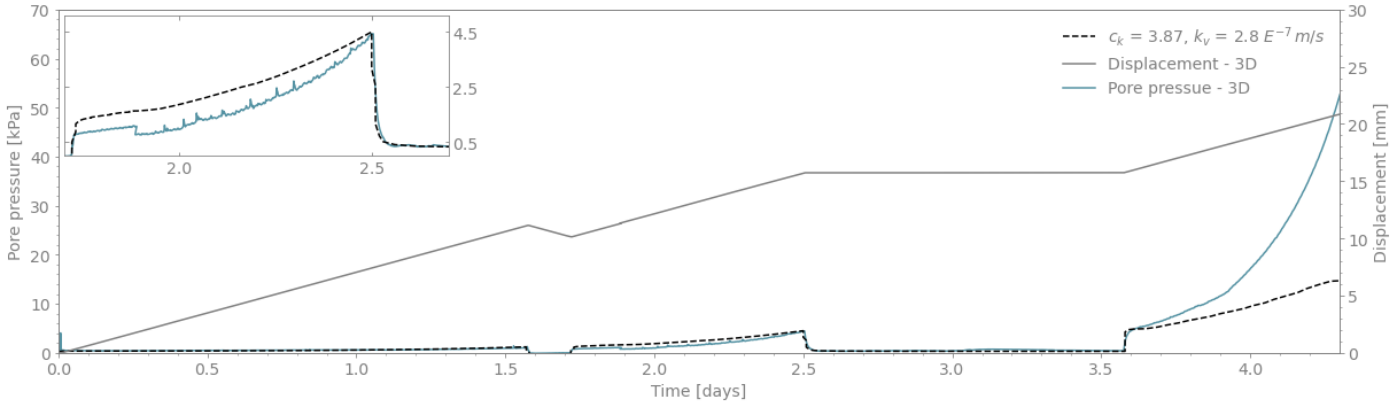

(d) Sample 3D

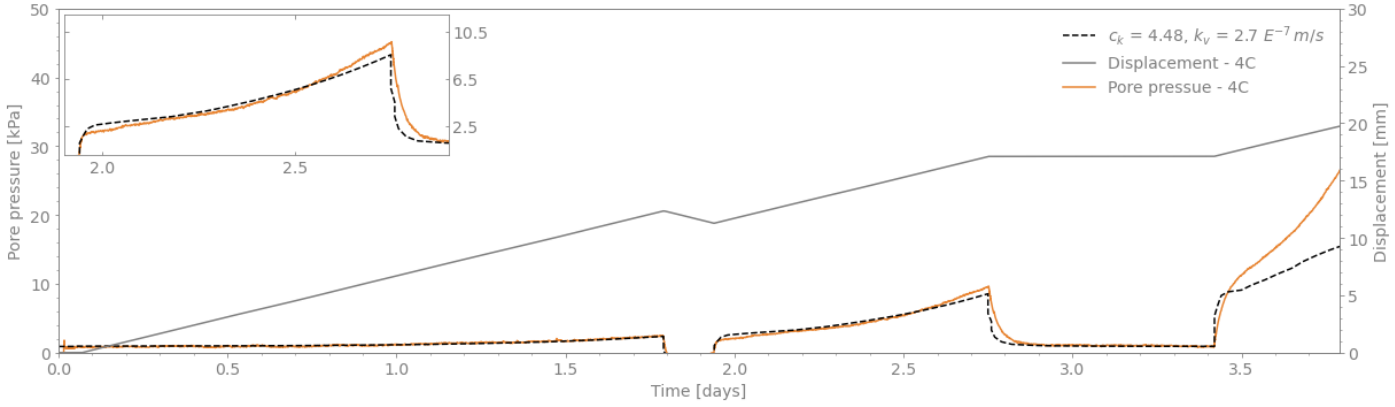

(e) Sample 4C

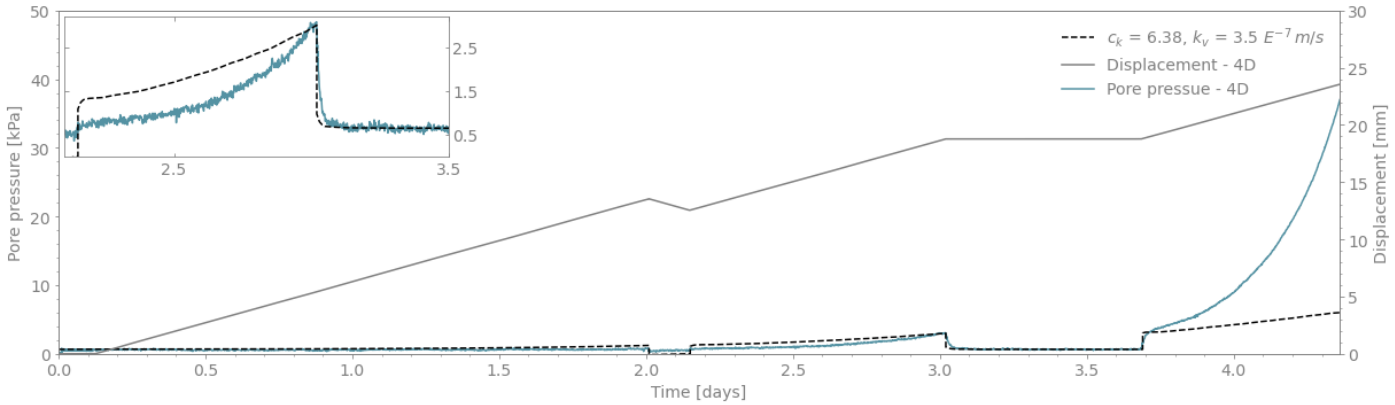

(f) Sample 4D

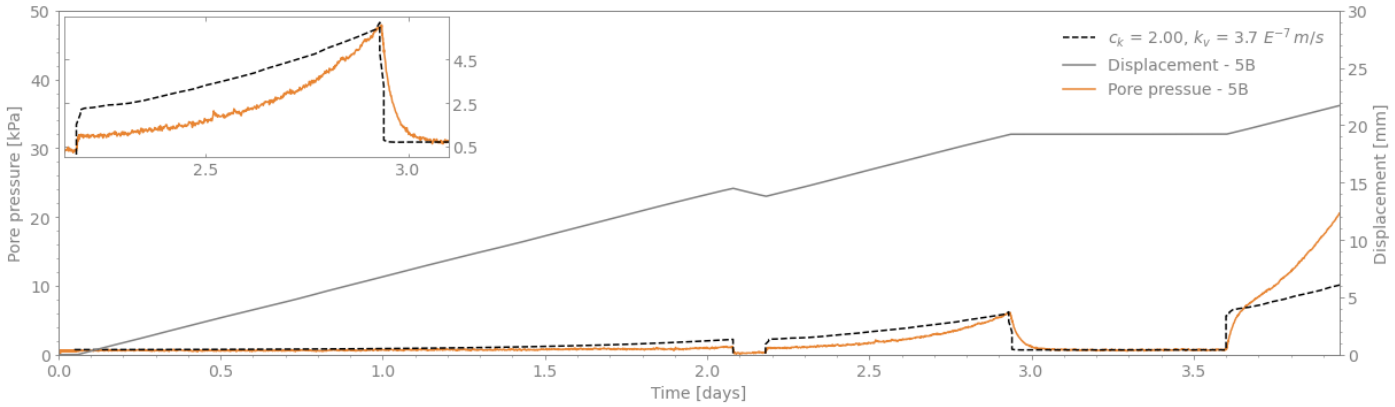

(g) Sample 5B

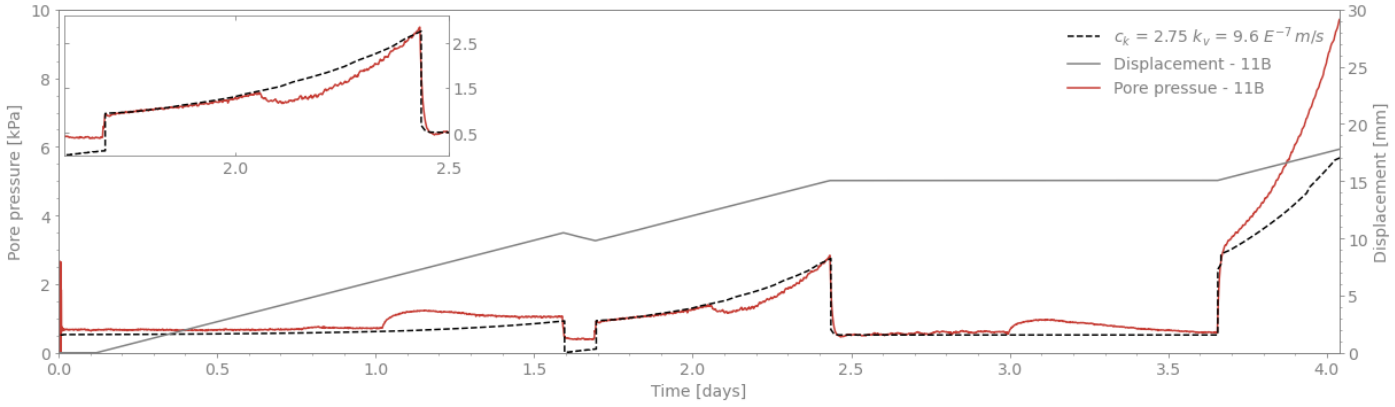

(h) Sample 11B

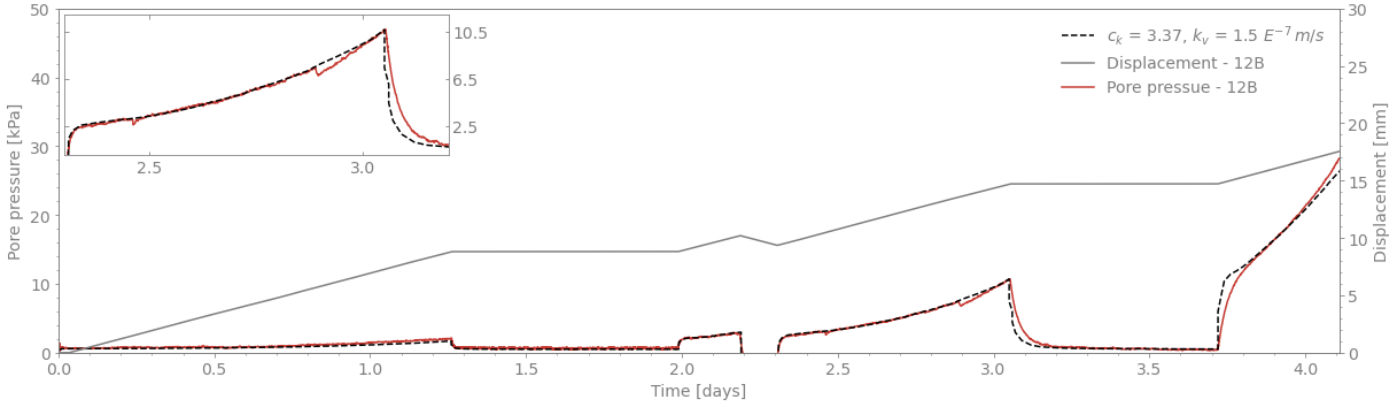

(i) Sample 12B

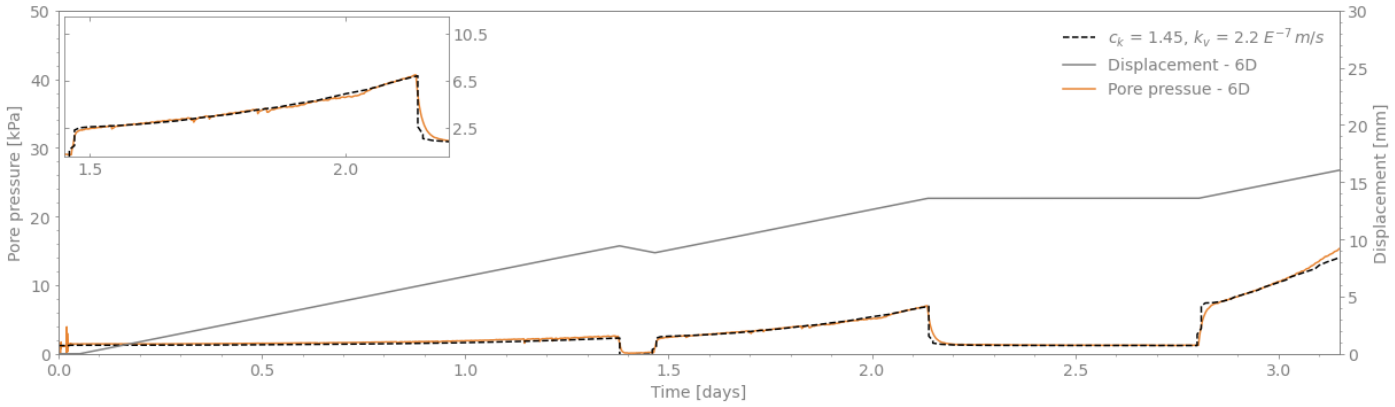

(j) Sample 6D

Figure C.12: Comparison of k_v during K_0-CRS tests

After defining the permeability parameters in Plaxis 3D, it is evident that in most of cases, the best fit of input values still fails to visualize the behaviour of the excess pore pressure in its entirety. Thus, it is relevant to contrast how the evolution of the parameters in the three-dimensional environment deviates from the response of the original data to define the limitations of the FEM tool (Figure C.13).

A major limitation of the procedure was the use of an inadequate tool to relate the void ratio dependency with the permeability throughout the analysis. As it is known, with the considerable deformation of the peat during consolidation, the state parameters are expected to also display a relevant variation in their newly found stress state. However, the only option in Plaxis 3D to follow this evolution is the semi-logarithmic formulation proposed by Taylor (1984) (equation C.5), which is not capable of providing the same level of variation.

$$log\left[\frac{k}{k_0}\right] = \frac{\Delta e}{c_k} \tag{C.5}$$

The estimation provided by the use of this equation aims to capture the latter stages of the consolidation process, and based on this portion, approximate feasible values for the permeability index and the initial hydraulic conductivity. This approach is based on the foregoing assumption that the output produced by the measuring equipment before the second loading ramp is not representative of the initial condition of the samples. Moreover, the usage of this logarithmic rule considers the characteristic initial void ratio of each sample as the magnitude declared in the metadata. Given this consideration and the final attained level of porosity, it is possible to estimate the magnitude of the hydraulic conductivity and consequentially the permeability coefficient that describes its evolution. As such, the values hereby presented are considered as the theoretical inceptive conditions which, after the consolidation process, would yield the final values of the metadata.

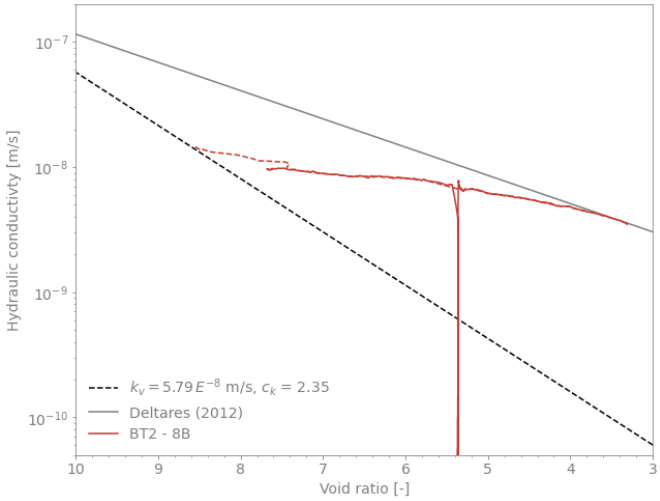

(a) Sample 8B

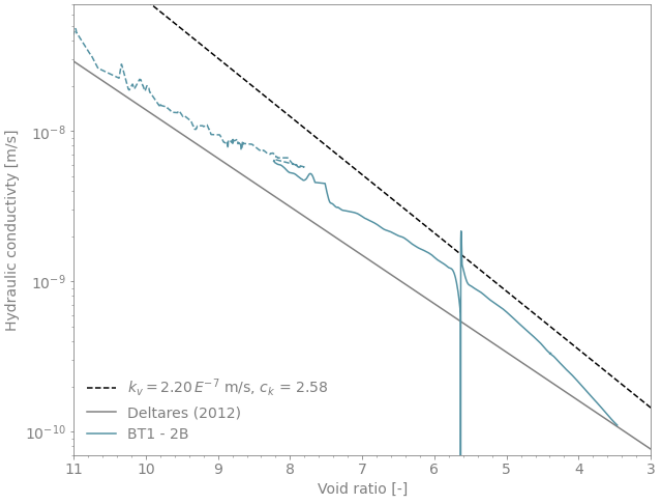

(b) Sample 2B

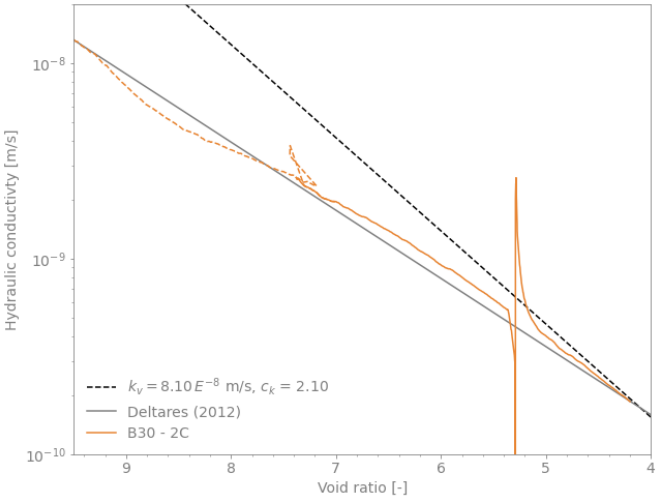

(c) Sample 2C

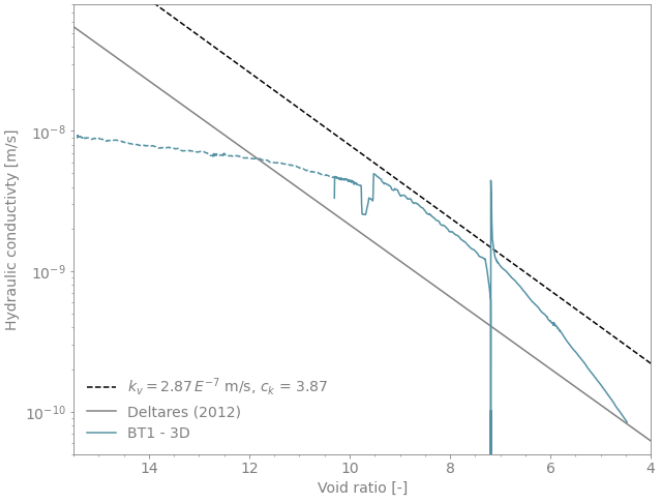

(d) Sample 3D

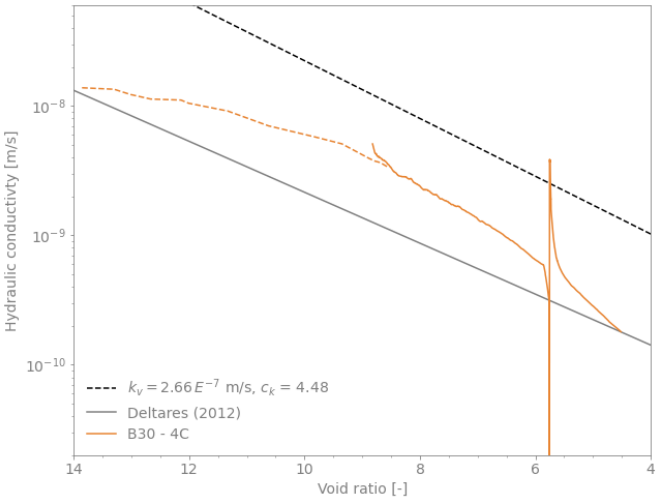

(e) Sample 4C

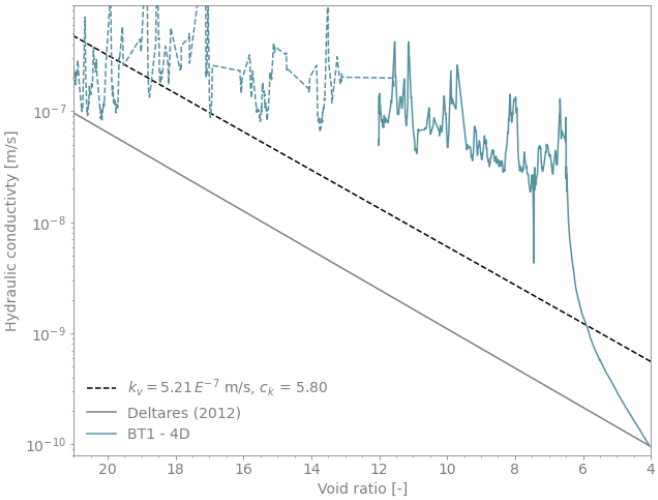

(f) Sample 4D

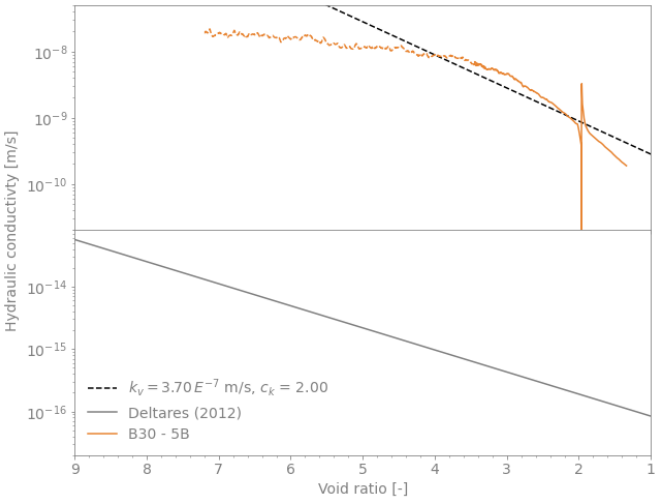

(g) Sample 5B

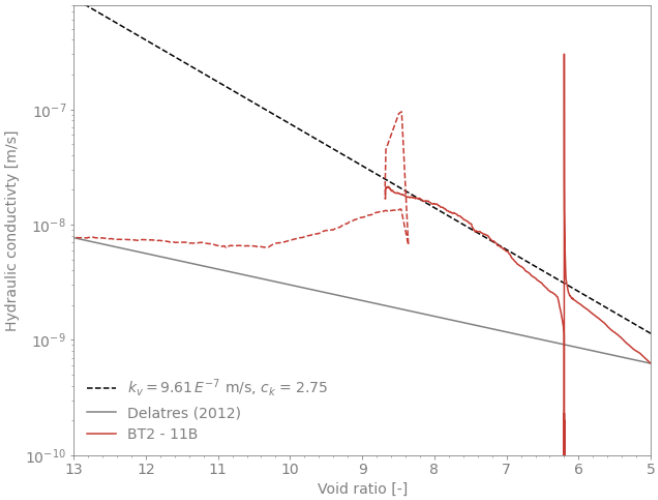

(h) Sample 11B

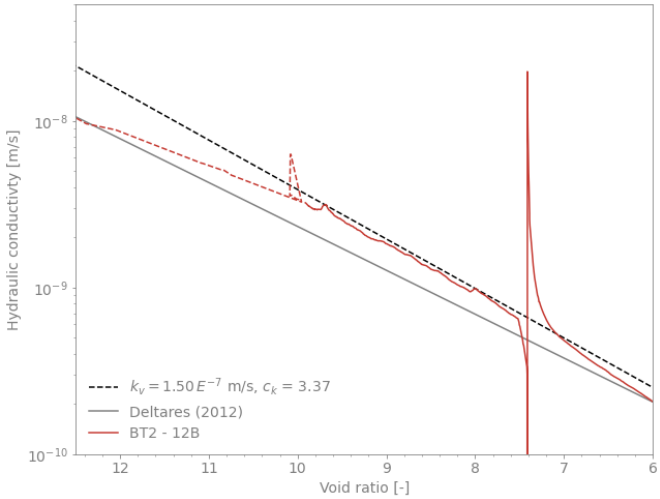

(i) Sample 12B

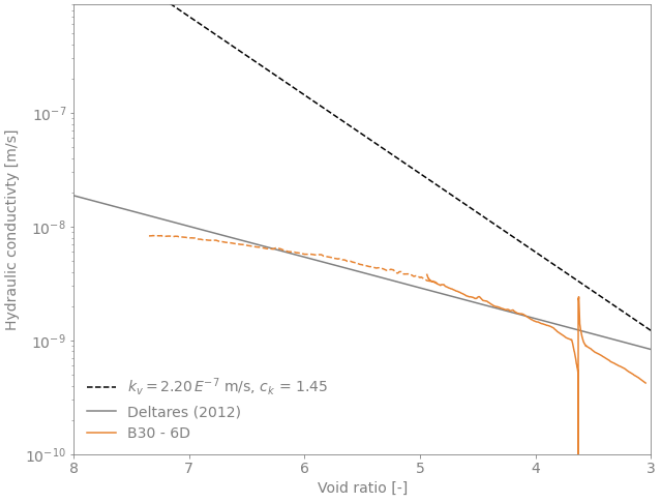

(j) Sample 6D

Figure C.13: Comparison of k_v during K_0-CRS tests

The results of the three methodologies in every K_0-CRS test are presented in Figure C.13, while Table C.5 provides a summary of the relevant magnitudes.

Table C.5: Estimation of hydraulic conductivity parameters

Sample	Deltares (2012)			Plaxis 3D		
	e_0	k_v	c_k	e_0	k_v	c_k
	-	m/s	-	-	m/s	-
8B	9.67	9.72 E^{-8}	4.43	10.21	5.79 E^{-8}	2.35
2B	11.21	3.41 E^{-8}	3.10	11.21	1.97 E^{-7}	2.65
2C	9.58	1.40 E^{-8}	2.87	11.01	5.79 E^{-8}	2.56
3D	15.45	5.36 E^{-8}	3.90	15.96	2.78 E^{-7}	3.87
4C	14.27	1.49 E^{-8}	5.08	18.88	2.66 E^{-7}	4.48
4D	21.21	1.05 E^{-7}	5.66	21.23	5.21 E^{-7}	5.80
5B	24.62	1.87 E^{-8}	2.83	7.24	3.70 E^{-7}	2.00
11B	13.05	7.81 E^{-9}	7.34	13.05	9.61 E^{-7}	2.75
12B	12.41	1.00 E^{-8}	3.80	15.36	1.50 E^{-7}	3.37
6D	6.27	6.38 E^{-9}	3.70	6.27	2.20 E^{-7}	1.45

D Measuring points in the FEM model

Having the precise location of the measuring devices, as reported by Alink (2010), means that the response of the model in a specific coordinate can be compared to the same location in the embankment. Nonetheless, for the meshing procedure to account for said locations it needs auxiliary elements that can dictate their position.

Following this, fictitious line elements are introduced into the meshing procedure to follow the role of the aforementioned devices. The line elements implicitly introduce nodes in the desired location, around which the mesh is elaborated. The original coordinates of the extensometers (HT), pressuremeter (WAT), hydraulic level (ZMS), and settlement plates (ZB) are translated into the local coordinate system of the model as shown in Table D.1.

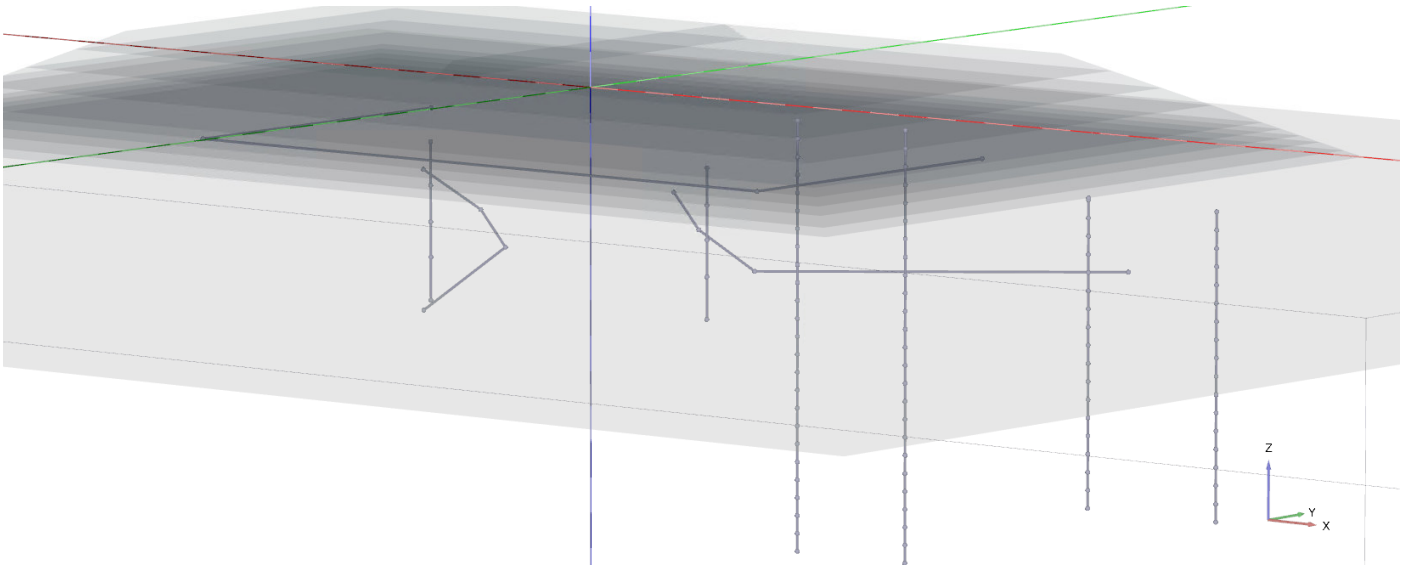

Figure D.1: Auxiliary line elements for meshing procedure

Table D.1: Location of auxiliary nodes for the evaluation of the measuring devices

Device	Type	X	Y	Z
WSM-T1-7A	Piezometer	-6.10	0.00	-2.76
WSM-T1-7B	Piezometer	-4.00	0.00	-3.74
WSM-T1-7C	Piezometer	-3.10	0.00	-4.74
WSM-T1-7D	Piezometer	-6.10	0.00	-6.76
WSM-T1-8A	Piezometer	3.00	0.00	-2.73
WSM-T1-8B	Piezometer	3.90	0.00	-3.72
WSM-T1-8C	Piezometer	5.90	0.00	-4.73
WSM-T1-10	Piezometer	19.00	0.00	-3.74
ZB-T1-1	Settlement plate	-10.00	5.00	-1.73
ZB-T1-3	Settlement plate	10.00	5.00	-1.73
ZB-T1-4	Settlement plate	-10.00	-5.00	-1.73
ZB-T1-6	Settlement plate	10.00	-5.00	-1.73
E-T1-7-0	Extensometer	-5.00	-1.00	-1.80
E-T1-7-5	Extensometer	-5.00	-1.00	-3.04
E-T1-7-4	Extensometer	-5.00	-1.00	-4.07
E-T1-7-3	Extensometer	-5.00	-1.00	-5.07
E-T1-7-2	Extensometer	-5.00	-1.00	-6.29

E-T1-8-0	Extensometer	5.00	-1.00	-1.81
E-T1-8-5	Extensometer	5.00	-1.00	-2.85
E-T1-8-4	Extensometer	5.00	-1.00	-3.83
E-T1-8-3	Extensometer	5.00	-1.00	-4.86
E-T1-8-2	Extensometer	5.00	-1.00	-6.05
H-T1-3-1	Inclinometer	18.00	0.00	-1.78
H-T1-3-2	Inclinometer	18.00	0.00	-2.28
H-T1-3-3	Inclinometer	18.00	0.00	-2.78
H-T1-3-4	Inclinometer	18.00	0.00	-3.28
H-T1-3-5	Inclinometer	18.00	0.00	-3.78
H-T1-3-6	Inclinometer	18.00	0.00	-4.28
H-T1-3-7	Inclinometer	18.00	0.00	-4.78
H-T1-3-8	Inclinometer	18.00	0.00	-5.28
H-T1-3-9	Inclinometer	18.00	0.00	-5.78
H-T1-3-10	Inclinometer	18.00	0.00	-6.28
H-T1-3-11	Inclinometer	18.00	0.00	-6.78
H-T1-3-12	Inclinometer	18.00	0.00	-7.28
H-T1-3-13	Inclinometer	18.00	0.00	-7.78
H-T1-3-14	Inclinometer	18.00	0.00	-8.28
H-T1-3-15	Inclinometer	18.00	0.00	-8.78
H-T1-3-16	Inclinometer	18.00	0.00	-9.28
H-T1-3-17	Inclinometer	18.00	0.00	-9.78
H-T1-3-18	Inclinometer	18.00	0.00	-10.28